Title
Vertical Mixing Processes in Temperate Lakes of Varying Depth

Author
Swann, Micah

Publication Date
2024

Peer reviewed|Thesis/dissertation

Vertical Mixing Processes in Temperate Lakes of Varying Depth

By

MICAH MANHEIM SWANN
DISSERTATION

Submitted in partial satisfaction of the requirements for the degree of

DOCTOR OF PHILOSOPHY

in

Civil and Environmental Engineering

in the

OFFICE OF GRADUATE STUDIES

of the

UNIVERSITY OF CALIFORNIA

DAVIS

Approved:

S. Geoffrey Schladow, Chair

Alexander Forrest

Steven Sadro

Committee in Charge

2024

Dedicated to my *cara* Erin

ABSTRACT

Lakes and reservoirs provide a wide range of socioeconomic benefits, serve as critical biodiversity hotspots, and are recognized as key sentinels of climate change. The seasonal evolution of lake thermal structure plays a central role in regulating the ecological health and productivity of these systems. During much of the year, thermal stratification inhibits the vertical exchange of oxygen, carbon, and nutrients between surface and deep layers. Conversely, when stratification weakens, complete vertical mixing (i.e., turnover) can transport nutrients to the surface for biotic uptake and ventilate deep layers with oxygen. However, climate change is altering the frequency and intensity of mixing events, threatening the trophic status of lakes globally. While one-dimensional hydrodynamic models are often utilized to investigate long-term changes in lake mixing regimes, they lack the ability to resolve both deep water mixing mechanistically and horizontal variations in temperature that can contribute to deep water renewal. Therefore, *in situ* temperature measurements and three-dimensional modeling serve as important tools for a comprehensive understanding of vertical mixing dynamics.

This dissertation examines the drivers and impacts of vertical mixing processes in three lakes varying in depth and mixing characteristics. The first study focuses on Clear Lake, a shallow, hypereutrophic, polymictic lake in Northern California beset by recurrent cyanobacteria blooms. Extensive field observations from 2019 – 2022 demonstrate how

intermittent periods of stratification and mixing induce internal phosphorus loading from sediments and alter nutrient limitation in favor of nitrogen-fixing cyanobacteria. The second study investigates Lake Tahoe, a deep, oligomictic, oligotrophic lake straddling the California-Nevada state border. Analysis of a multi-decadal record of winter mixing depth and winter thermal structure reveals that the occurrence of sporadic turnover events is primarily regulated by the serendipitous passage of cold fronts during the late winter. Temperature observations during deep mixing events indicate that three-dimensional transport processes likely contribute to deep water renewal in winter. The third study focuses on Lago Llanquihue a deep monomictic, oligotrophic lake in northern Patagonia, Chile. Utilizing a three-dimensional hydrodynamic model, the study explores the long-term response of the lake to climate change and watershed development. Predictions under a worst-case greenhouse gas emissions scenario indicate that the lake will warm more gradually than comparative Northern Hemisphere systems and will likely remain monomictic for decades, suggesting that the climate impacts on Southern Hemisphere lakes will be less severe throughout the 21st century. Collectively, these investigations significantly contribute to the understanding of how vertical mixing influences water quality in lakes and establishes a framework for predicting how such dynamics may evolve in the future.

ACKNOWLEDGMENTS

When I embarked on my graduate degree over five years ago, little did I know the opportunities and challenges that lay ahead. Originally, I planned to obtain a Masters degree at UC Davis and return to a career in the private sector shortly after. However, during that first year, while I helped to launch a new monitoring program in Clear Lake, I realized the wide range of modelling and analytical skills that I could learn by pursuing a PhD. Over the next four-plus years, my academic expedition has extended well beyond limnology. I've learned a diverse set of practical skills – from trailering a boat through mountain roads, to navigating international soil customs regulations, to conducting efficient team meetings, just to name a few. This journey, though, has not been without its obstacles. The COVID-19 pandemic disrupted much of my early field research plans, while disappearing instrumentation postponed the start of my data collection in Chile. Persevering through these challenges forced me to become a more adaptable and creative problem-solver and ultimately helped me develop into a more capable scientist. This dissertation is a testament to not only my efforts but also the encouragement and work of numerous individuals to whom I am greatly indebted.

I would like first to thank Geoffrey Schladow for his guidance, mentorship, and belief in me through the years. Your expertise and thoughtful advice during our weekly meetings have been pivotal to my professional growth and were instrumental in guiding my research. I am deeply grateful for the opportunities and resources that you provided me with to investigate lakes all over the world. I will always cherish the memories of our two trips to Chile and the friends, adventures, and piscos we shared. I would also like to thank my other committee members, Alex Forrest and Steve Sadro, for their willingness to discuss my research, insights on data exploration, and input on this dissertation. Your suggestions, particularly on my Clear Lake research, greatly helped to improve my scientific writing.

The field data collection in this research was made possible by numerous graduate students, researchers, technicians, and staff at the UC Davis Tahoe Environmental Research Center (TERC) and collaborations with Chile Lagos Limpios (ChLL). Clear Lake data were collected by graduate researchers Drew Stang, Nick Framsted, Ruth Thirkill, Samantha Sharpe, and Job Pinkankananavee, as well as many undergraduate volunteers. Thank you for your commitment and diligence in maintaining the monitoring program, even through wildfires and the pandemic, and for all the laughs we had along the way. Anne Liston, Steve Sesma, Lindsay Vaughan, and Helen Fillmore were instrumental in setting up the water quality monitoring program and analyzed many not-so-clear Clear Lake water samples. Raph Townsend was always just a phone call away whenever I needed help to fix a problematic monitoring site or a strange noise in the boat. I'm grateful to Alicia Cortés for overseeing all the aspects of the Clear Lake project and for your expertise and invaluable guidance on every aspect of my research—from coding to modeling to writing. I deeply admire your selfless and inclusive nature and the way you effectively communicate complex scientific ideas.

Data collection in Lake Tahoe was made possible by the tireless efforts of the TERC field team: Brant Allen, Brandon Berry, and Katie Senft. Thank you for your willingness to maintain thermistor chains in the heart of the winter to support my research efforts. Thank you to Sergio Valbuena for all our discussions on lake mixing processes and for teaching me novel ways to visualize 3D model simulations. I would also like to thank Shohei Watanabe for maintaining the Clear Lake and Lake Tahoe databases that served as the basis for much of my research and for your valuable writing advice.

The ChLL executive committee, Fernando Coz, Angela Delorenzo, and Cristóbal Valenzuela, helped facilitate my research in Chile. Thank you for all your hard work in getting our monitoring program off the ground and continuous optimism and creativity in the face of some early setbacks. I'd also like to thank Gonzalo Santamarina and Julio Alderete from Innovex for overseeing installation and maintenance of the Lago Llanquihue monitoring network.

Finally, thanks to all my family, especially to my parents, who have always unconditionally supported me in all my personal and academic pursuits. To my brother Noah, who has always been my biggest role model and biggest advocate. And most importantly, thanks to my wife, Erin Timony Bump, for her love, patience, companionship, and steadfast support through the most turbulent of times.

Funding for this research was provided by the California Department of Fish and Wildlife, the California Natural Resources Agency, a UC Davis Global Affairs seed grant, the ARCs foundation, the UC Davis Chile Life Sciences Innovation Center, and the generous support of Mary Ann Peoples.

CONTENTS

ABSTRACT III

ACKNOWLEDGMENTS V

CONTENTS IX

Table of Figures xvi

Table of Tables xx

Table of Appendix Figures xxi

1 INTRODUCTION AND MOTIVATION 1

1.1 Literature Review 1

1.1.1 Lake Mixing Regime 2

1.1.2 A Changing Climate 4

1.1.3 Physical Impacts of Climate Change 6

1.1.4 Ecosystem Impacts of Climate Change 8

1.1.5 Lake Models 10

1.2 Study Sites 11

1.3 Objectives and Organization of This Work 12

2 INTERNAL PHOSPHORUS LOADING ALTERS NUTRIENT LIMITATION AND CONTRIBUTES TO CYANOBACTERIA BLOOMS IN A POLYMICTIC LAKE 21

Abstract 21

2.1 INTRODUCTION 22
2.2 MATERIALS AND METHODS 26
2.2.1 Study Site 26
2.2.2 Field Data Collection 30
2.2.3 Cyanobacteria Dynamics 32
2.2.4 External Load Estimates 33
2.2.5 Mass Balance Models of Internal Loading 35
2.2.6 Stratification Metrics 40
2.2.7 Statistical Analyses 40
2.3 RESULTS 41
2.3.1 Spatial and Temporal Variability of Stratification and Hypoxia 41
2.3.2 Seasonal Nutrient Variability 44
2.3.3 External Loads 47
2.3.4 Internal Loads 49
2.3.5 Cyanobacteria Temporal and Spatial Variability 51
2.3.6 Drivers of Cyanobacterial Blooms 55
2.4 DISCUSSION 57
2.4.1 Contribution of External and Internal Loading 59
2.4.2 Contribution of Internal P Loading to Seasonal N limitation 60

2.4.3 Seasonal and Internannual Variability of HCBs 62

2.4.4 Comparative Estimates of Internal Load 66

2.4.5 Unresolved Internal Loading Mechanisms 71

2.5 Conclusions 74

References 75

3 DRIVERS AND DYNAMICS OF DEEP WINTER MIXING EVENTS IN A DEEP OLIGOMICTIC LAKE 81

Abstract 81

3.1 Introduction 82

3.2 Methods 86

3.2.1 Site Description 86

3.2.2 Observation Data 88

3.2.3 Estimates of Deep Mixing in Tahoe 91

3.2.4 Surface Heat Balance 93

3.2.5 Characterization of Mixing and Stability 94

3.2.6 Spectral Analysis 95

3.2.7 Correlation Analysis 96

3.3 Results 96

3.3.1 Meteorological Forcing 96

3.3.2 Characteristics of Lake Tahoe's Hypolimnion 98

3.3.3 Historical Record of Winter Mixing Depth (WMD) 100

3.3.4 Hydrodynamics of Deep Mixing 103

3.4 Discussion & Conclusions 115

3.4.1 Drivers of Deep Mixing Events 116

3.4.2 Evolution of Winter Lake Thermal Structure 118

3.4.3 Potential Effects of Climate Change on Deep Mixing 125

3.4.4 Future Research 128

References 130

4 THE RESILIENCE OF A DEEP SOUTHERN HEMISPHERE LAKE TO CLIMATE CHANGE 135

Abstract 135

4.1 Introduction 136

4.2 Materials and Methods 142

4.2.1 Study Site 142

4.2.2 Lake Monitoring Program 144

4.2.3 3D Hydrodynamic Model (Si3D) 145

4.2.4 1D Hydrodynamic Model (GLM) 148

4.2.5 Calibration and Validation 149

4.2.6 Forecasted Meteorological Data 150

4.2.7 Characteristics of Thermal Stratification 153

4.3 Results 154
4.3.1 Lake Observational Data 154
4.3.2 Model Calibration and Validation 156
4.3.3 Downscaled Climate Forecast Data 160
4.3.4 Sensitivity Analysis 163
4.3.5 Forecasted Changes in Lake Thermal Structure 166
4.3.6 Impacts of Clarity 171
4.4 Discussion 172
4.4.1 Model Performance and Limitations 172
4.4.2 Climate Change Effects on Heat Fluxes and Mixing Regime 174
4.4.3 Comparison to Forecasted Warming of Deep Lakes 179
4.4.4 Potential Implications for Lake Ecosystem and Water Quality 182
4.5 Conclusions 183
References 185

5 SUMMARY & CONCLUSIONS 191

Chapter 2 Concluding Remarks 192
Chapter 3 Concluding Remarks 195
Chapter 4 Concluding Remarks 197
Further Research 200

APPENDIX A – CHAPTER 2 SUPPLEMENTAL INFORMATION....... 203

A.1 Historical Metrological and Nutrient Data 203

A.2 Lake Temperature and Dissolved Oxygen Data 205

A.3 Constituents Analyzed During Water Quality Monitoring. 209

A.4 Clear Lake Cyanobacteria Index 210

A.5 Stream External Loading Calculations 212

A.6 Clear Lake Meteorology 213

A.7 Time Series Decomposition of Spatially-averaged CI 215

A.8 Distribution of Submersed Aquatic Vegetation in Clear Lake 216

References 216

APPENDIX B – CHAPTER 3 SUPPLEMENTAL INFORMATION....... 217

B.1 Characterization of Mixing and Water Column Stability 217

B.2 Monitoring Metadata 219

B.3 Thermistor Chain and CTD Data 221

B.4 Historical Observations 224

APPENDIX C – CHAPTER 4 SUPPLEMENTAL INFORMATION....... 226

C.1 Meteorological Data Downscaling Procedure Future Meteorological Data 226

C.2 Evaluating Uncertainty in Climate Projections 236

C.3 Observed Temperature and DO Data from Lago Llanquihue (2021 – 2022) 239

C.4 Characterization of Mixing and Water Column Stability....................................240

Table of Figures

Figure 1.1. Location of study lakes: Chapter 2 (Clear Lake – green), Chapter 3 (Lake Tahoe – purple), Chapter 4 (Lago Llanquihue – orange). 12

Figure 2.1. Subsurface instrument mooring, water column and sediment core sampling sites in Clear Lake, California with 2 m bathymetry contour lines. Two-character site prefix indicates location in Upper Arm (UA), Oaks Arm (OA), Lower Arm (LA), and Narrows (NR). Location of subsurface monitoring moorings marked with white circles and locations of shoreline meteorological stations are shown by black triangles. The insert to the right of the bathymetrical map shows the location of Clear Lake watershed in California, its extent, and the location of the main creeks. 29

Figure 2.2. Timing of hypolimnetic anoxia across Clear Lake sub-basins. Black dots indicate periods when hourly DO < $1 mgL^{-1}$. 43

Figure 2.3. a) Spatially-averaged, 7-day moving average of the trailing 10-day maximum modified cyanobacteria index Upper (dark grey), Oaks (light grey) and Lower (black) arms. B) Percent coverage of cyanobacteria of arm surface area. C) DO measured at 0.5m above sediment water interface at deepest point in each arm. Dashed line indicated 3.5 mgL^{-1} hypoxia threshold d) Average buoyancy frequency in the water column. Dotted line indicates threshold for stratification at $N = 0.015\ s^{-1}$ (2019 – 2021). 45

Figure 2.4. Mass of a) total phosphorus, b) total nitrogen, c) soluble reactive phosphorus, d) ammonium, e) chlorophyll-a in the epilimnion (grey) and hypolimnion (black) averaged across all monitoring sites [mgL^{-1}]; f) Biovolume of cyanobacteria in surface samples [$\mu m^3\ L^{-1}$]. Black arrows indicating timing of maximum external loading input. Error bars indicate the range of values measured across all sites. 46

Figure 2.5. a) Water year (i.e., Oct 1 – Sept 31) cumulative discharge from Middle Creek from 1980 – 2022. Water years from Oct 2018 to Sept 2022 are shown in bold. B) Monthly TP load estimates from gauged Clear Lake tributaries and precipitation data measured. 48

Figure 2.6. a-c) Total and d-f) proportional biovolume for major phytoplankton groups and g-i) proportional biovolume of major cyanobacteria genera across sub-basins from April to October (2019 – 2021). Asterix indicate N-fixing species. 54

Figure 2.7. Predictor rank calculated from MRMR algorithm. 57

Figure 2.8. Volume-averaged TN:TP molar ratios for each sub-basin. Dotted lines indicate 25:1 (Maranger, 2018) and 16:1 (Redfield, 1958) thresholds. 61

Figure 2.9. a) Seasonal cyanobacteria bloom magnitude (June – October) recorded by satellite imagery from 2004-2011 and 2016-2021. No satellite data was available from 2012-2015. Scatter plots comparing b) cumulative inflow from previous water year vs bloom magnitude and c) average summer TP concentration vs bloom magnitude. 65

Figure 2.10. Comparison of sediment composition with SRP release rates in lab incubation experiments. Sediment concentrations are units of $\mu g\ g^{-1}$ and are average of top 0-5 cm from duplicate oxic incubated cores while SRP release rates shown are from anoxic cores. Solid line indicates least-squares linear regression with 95% confidence interval (dotted line). 69

Figure 3.1. Location and bathymetric map of Lake Tahoe. Marker indicates type of monitoring data collected each site. Monthly CTD profiles are collected at MTLP. Grey lines indicate 50 meter depth contours. Wind rose denotes the prevailing wind direction from 2008 to 2023. 89

Figure 3.2. a) Daily average surface heat fluxes (2007 – 2022). Shaded areas indicated 95% confidence interval. B) Daily average air temperature (black) and lake surface water temperature (grey). C) Daily average wind speed. 97

Figure 3.3. a) Time series of temperature at surface (dotted) and at 400 m depth (solid) recorded at GBTC (black) and CTD profiles at MLTP (grey). Triangles indicate deep mixing events. B) DO measured at 460 m at the base of GBTC. 99

Figure 3.4. a) Annual mean winter (Dec – Mar) air temperature (T_{wntr}) recorded at Tahoe City (TC). Horizontal line is 50-year average. b) Maximum winter mixing depth from 1973 to 2023. Circles in a) and thick lines in b) indicate turnover years. c) Frequency distribution of maximum winter mixing depth... 100

Figure 3.5. a) Time series of cross correlation (lagged Pearson correlation) of WMD with daily Schmidt stability (S_T) and cumulative net surface heat flux (Q_{net_total}) at daily lags and cumulative monthly net surface heat flux (Monthly Q_{net}) at monthly lags between March 1 and preceding 9 months. b) Pearson correlation coefficients (r) between winter monthly cumulative sensible (Q_s), latent (Qe), net shortwave (Q_{sw}), net longwave (Q_{lw}), and cumulative (Q_{net}) heat fluxes, (AirT) air temperature, wind speed (Wx) , PNA index and ST with maximum winter mixing depth (Columns 1-4). Column 5 shows same calculations for the winter period of January 1 - March 31. * and ** indicates significant $p < 0.05$ and $p < 0.001$ respectively 103

Figure 3.6. Schematic overview of hypothesized evolution of Tahoe's thermal structure during deep mixing winters. a) Lake is thermally stratified with seasonal differential cooling in littoral zone generating shallow plunging density currents. b) Heat loss and wind stirring deepen surface mixed layer and weaken density gradient at thermocline. C) Lake becomes isothermal facilitating vertical mixing throughout the water column. d) Plunging cold water reaches lake bottom while epilimnion begins to reform. 104

Figure 3.7. a-b) Cumulative latent (Q_s) and net (Q_{net}) heat fluxes, c) Schmidt stability (S_T), d) mixed layer depth (h_{CML}), e) surface water temperature and f) cumulative TKE input during the mixed layer deepening period (December 1 – February 1). Asterix indicate years of full turnover. Dotted line from winter 2023 in d) is linearly interpolated when sensor was out of water. Dotted horizontal lines in e) indicate range of bottom temperatures. 107

Figure 3.8. IPE calculated for overlapping 30-day windows during the 2018/19 winter. Black arrow indicates the inertial frequency of the lake. 108

Figure 3.9. Time series of the ratio of the buoyancy frequency at base of the mixed layer to background stratification, Lake Number (black) and Wedderburn Number (red) and temperature structure with mixed layer depth highlighted by white line during the winters of 1997/99, 1998/99, 2018/19, 2022/23, 2017/18, and 2020/21. Black horizontal line on Lake Number and Wedderburn Number plots indicates a threshold of 1. 109

Figure 3.10. Boxplots of weekly averages of a) net surface heat fluxes, b) air temperature, c) wind speeds during From January – March (1998-1998, 2008-2023). Colored line shows weekly averages for selected winters. Arrows indicate date of turnover. 110

Figure 3.11. Surface and hypolimnion temperature and dissolved oxygen (460 m) in the deep hypolimnion during turnover events in February and March of a) 1998, b) 1999, c) 2019 and 2023. Temperatures were interpolated to 100 m depth intervals for comparison. 111

Figure 3.12. Thermal structure of lake during winters of a) 1998, b) 1999, c) 2019, d) 2023. Red vertical lines indicate onset of turnover. White isotherm denotes cold water observed to fill the deep hypolimnion from the bottom....... 113

Figure 3.13. Horizontal temperature variability during 2023 deep mixing event. a) nearshore surface temperature and b) derived water density measured at Tahoe City (black) and average offshore surface temperature measured at TB 1-4 (red). c) temperatures measured at depths of 65 m and 110 m at HWTC and 100 m and 460 m at GBTC. 115

Figure 3.14. Scatter plot of observed and predicted winter maximum mixing depth for 1998-1999 and 2008-2023. Dotted line indicates 1:1 line, black line indicates slope of model....... 118

Figure 3.15. Comparison of observed mixed layer depth, h_{CML}, (blue) and modeled h_{CML} (red) during three turnover winters. Vertical black indicates when the buoyancy frequency at the base of the mixed layer $<$ 1% greater than background stratification....... 120

Figure 3.16. One-day filtered time series of nearshore surface temperatures measured at Tahoe City (red), average offshore surface temperatures measured at TB 1-4 (blue) and lake bottom temperatures measured at the base of Glenbrook thermistor chain (black) and Blackwood Creek (black) from October 2017 to May 2023. Dashed line indicates the temperature of the maximum density of water. 123

Figure 3.17. Seasonal average air temperature for a) January through March, b) April through June, c) July through September, d) October through December from 1920 to 2022 measured at Tahoe City. Red line indicates linear trend for entire time period while black line indicates linear trend since 1980. e) Running standard deviation (10-year running window) of the mean seasonal air temperature. Colors correspond to season. 127

Figure 4.1. Lago Llanquihue site map indicating locations of thermistor chains (red markers) and meteorological stations (triangles). Black and grey contours indicate 100 m and 50 m isobaths. Dashed line is the watershed boundary. 143

Figure 4.2. a) Contour plot of the observed temperature at P7 during 2021-2022 deployment. Missing data was gap filled with data from P4 and P6 when possible and linearly interpolated otherwise. Magenta line indicates thermocline depth. Red dots on y-axis indicate location of thermistors. b) Time series of DO at 100 m at P4 and temperature at 300 m at P7. 155

Figure 4.3. Comparison of a) observed vertical temperature structure at P7 with b) calibrated Si3D and c) GLM simulations from September 2021 to August 2022. Red dots indicate locations of thermistors. White line denotes 10.75 °C isotherm. RMSE of Si3D (red) and GLM (black) at thermistor depths during d) calibration and e) validation period. 157

Figure 4.4. Predicted change in 12 month running mean relative to 2007-2021 baseline for a) air temperature, b) relative humidity, c) incoming shortwave radiation, d) incoming longwave radiation, and e) wind speed in Lago Llanquihue from REGCM4 RCP 8.5 simulation. Shaded grey region denote range across all six GCM RCM combinations. Black lines indicate the Sens slope estimate of the linear trend. 162

Figure 4.5. Seasonal variation in projected changes a) wind speed, b) air temperature, c) incoming longwave radiation under RCP 8.5 scenario relative to 2021-2022 baseline. 163

Figure 4.6. Comparison of forecasted a) volume-averaged lake temperature, b) epilimnion temperature between 1-20 m, c) hypolimnion temperature below 100 m, d) Schmidt Stability, e) thermocline depth for REGCM4 RCP 8.5 simulations using a constant k_d (black) and k_d increasing + 1% yr^{-1} (red). Boxes and

whiskers indicate quartile ranges for one year of simulation data, dots indicate mean and solid lines indicate linear trend determined via linear regression. 167

Figure 4.7. Monthly mean temperatures at a) surface b) 50 m c) 300 m and d) volume-averaged for 2021-2022 baseline (solid line with circles) and 2091-92 RCP 8.5 projection (dotted line with triangles). Error bars show the maximum and minimum of the baseline simulation. 168

Figure 4.8. Projections of long-term changes in a) onset (black) and end (red) of stratified season, b) onset (black) and end (red) of winter mixing period, c) duration of stratified season, d) duration of winter mixing period, e) temperature difference between epilimnion and hypolimnion during stratified season, f) minimum bottom temperature during mixing for RCP 8.5 projection. Solid lines indicate linear trend calculated via linear regression. 168

Figure 4.9. Comparison of depth of thermocline (Z_{thermo}) and thickness of metalimnion (h_{meta}) in baseline (black) and 2091-92 (red) RCP 8.5 simulation. 169

Figure 4.10. Results of wintertime numerical tracer experiments. A): Mixing Index (M_{idx}) and b) Schmidt Stability (S_T) for selected winters in RCP 8.5 simulation. 171

Figure 4.11. Comparison of monthly cumulative heat fluxes in mJ m^{-2} for baseline (red), 2041-42 (black) and 2091-92 (blue) RCP 8.5 simulations. a) Q_{net} is net surface, b) Q_{LW} is net longwave radiative, c) Q_{SW} is net shortwave radiative, d) Q_e is latent, e) Q_h is sensible heat flux. 177

Table of Tables

Table 2.1 Physical characteristics of Clear Lake and sub-basins. Values in parentheses indicate percentage of total lake. 27

Table 2.2. Annual totals of observed hypoxic days in the hypolimnion of each arm at three DO thresholds and the modeled active sediment area factor (equation 2.4, AA_{mod}). 42

Table 2.3. Comparison of external watershed (L_{ext}) and internal loading estimates for Clear Lake and sub-basins (2019 – 2021). All load estimates are presented as areal rates in mg TP m $^{-2}$ year $^{-1}$. Clear Lake nutrient TMDL is shown in right column for comparison. 48

Table 2.4. Comparison of estimated sediment P release rates [mg TP m^{-2} day^{-1}]. RR_{core} is average SRP diffusive flux measured in duplicate oxic and anoxic sediment cores. RR_{sed} is TP release rate modeled from linear regression with TP concentration in upper 5 cm sediment of duplicate oxic cores. RR_{TP} is the TP release rate modeled from linear regression with average summer TP concentration through water column for each study year. 50

Table 2.5. Spearman rank correlation coefficients for biovolumes of total cyanobacteria and selected cyanobacteria genera with environmental parameters measured in water column from all samples collected from 2019 – 2021 (n = 116). Correlations with $p < 0.001$ are bolded. 56

Table 2.6. Comparison of multiple linear regression models for predicting cyanobacteria biovolume. 57

Table 2.7. Internal and external TP load estimates (metric tons) for January to December (2019 - 2021). Internal load estimates are based on the observed increase in water column TP (L_{int_1}). Internal load estimates calculated from experimentally-determined releases rates are shown in parentheses. External load is sum of both watershed and atmospheric contributions. 58

Table 3.1. Main morphometric and hydrological characteristics of Lake Tahoe. 88

Table 3.2. Volumetric scaling analysis for deep water cooling during four deep mixing winters. $t_{turnover}$, t_{final} , and Δt indicate the temperature of the deep hypolimnion at turnover, at the end of the winter and the difference between the two. V4℃ indicates the volume of water at 4 ℃ that would be required to cause the observed cooling of the hypolimnion. Total inflow volume shows the estimated volume of water discharged into the lake from November 1 to April 1 when the inflow density was >-0.1 kg m^{-3} the density of the nearshore region. The percentage of the required volume is shown in parenthesis. Shoreline volume denotes the volume of water in the shallow littoral zone <15 m depth. τ_f is the theoretical littoral zone flushing rate. 125

Table 4.1. Thermistor chain array description. All depths are in meters. 145

Table 4.2. Specification of model parameters 149

Table 4.3. Comparison of performance metrics during calibration and validation of Si3D and GLM. 158

Table 4.4. Sensitivity of lake temperature, stratification strength, thermocline depth and duration of stratified and mixing seasons to changes in air temperature, clarity, and wind speed. 165

Table 4.5. Comparison of modeled and observed response of deep lakes to climate change. 181

Table of Appendix Figures

Figure A.1. Long term trends in summer (circle) and winter (triangle) Clear Lake surface temperatures from 1970 – 2020 (California Department of Water Resources). 203

Figure A.2. Dissolved inorganic nitrogen (DIN, nitrate plus ammonium) to orthophosphate (OP) molar ratio, concentrations of nitrate, ammonium, orthophosphate in mmol/L, Redfield ratio (N:P = 16:1), and N:P ratio = 25:1. (Source – Department of Water Resources). 204

Figure A.3. Hourly temperature data measured by moored thermistor chain at LA-03 and hypolimnetic DO measured 0.5m off lakebed (Apr 2019 – Dec 2021). 206

Figure A.4. Hourly temperature data measured by moored thermistor chain at OA-04 and hypolimnetic DO measured 0.5 m off lakebed (Apr 2019 – Dec 2021). 207

Figure A.5. Hourly temperature data measured by moored thermistor chain at UA-06 and hypolimnetic DO measured 0.5 m off lakebed (Apr 2019 – Dec 2021). 208

Figure A.6. Monthly averaged 10-day running maximum modified cyanobacteria index for May – October (2019-2021). 210

Figure A.7. Scatter plots comparing observed cyanobacteria biovolume and chlorophyll a concentration in surface grab samples against 10-day running maximum modified cyanobacteria index from March 2019 – December 2021. 211

Figure A.8. Left) Stream-specific linear regressions relating flow to TP concentration from Lake County Water Resources Department routine stream sampling program (2008-2018). Right) Daily and hourly hydrographs for gaged streams from January 2019 – December 2021. 212

Figure A.9. Frequency Distribution of observed summertime wind speeds (April – October) across Clear Lake subbasin from 2019-2021. 213

Figure A.10. 10 Day trailing average wind speed (a) and air temperature(b) and lake surface water temperature (c) measured at BKP station and 3 Day trailing average buoyancy frequency for UA from May to November 2019 – 2021. 214

Figure A.11. Time series of spatially averaged CI across Clear Lake and three sub-basins. Plots show observed (blue), long term trend (orange), seasonal trend (yellow) and residuals (purple). 215

Figure A.12. Aquatic vegetation bio-volume in Clear Lake, Sept-2002 (ReMetrix 2003). Majority of vegetation is located along the western and northern banks of UA. 216

Figure B.1. Time series of temperature measured at discrete depths in Lake Tahoe recorded at MLTP profiling site (grey) and GBTC thermistor chain (black). Deep mixing events occurred in the winters of 2007, 2008, 2011, 2019, and 2023. 221

Figure B.2. Profiles of temperature and DO collected at MLTC monitoring site and calculated buoyancy frequency (N^2) before and after turnover on February 10 2019. 222

Figure B.3. a-d) Thermal structure of Lake Tahoe events during deep mixing in the winters of 1998,1999,2019,and 2023. Red vertical lines indicate onset of turnover. Black lines show 0.05 °C isotherms. 223

Figure B.4. Monthly average wind speeds measured by on-water buoys at Lake Tahoe 2006-2022. Red lines indicate linear trend line. 224

Figure B.5. Comparison of daily average surface temperature from May 1 – Apr 30 (1997-1999 and 2008 – 2023). Colored lines denote deep mixing winters. 225

Figure C.1. Frequency plots comparing observed and down-scaled hourly data for a) air temperature, b) relative humidity, c) incoming shortwave radiation, d) longwave radiation, e) atmospheric pressure, f) wind speed and g) wind direction. 235

Figure C.2. Projected trends in monthly meteorological conditions for Lago Llanquihue under RCP 8.5 emissions scenario relative to 2006 to 2016 baseline. Six combinations of GCMs, RCMs and domains are shown in various color. Parameters shown include a) relative humidity, b) incoming longwave radiation, c) incoming shortwave radiation, d) average air temperature, e) maximum air temperature, f) minimum air temperature, g) zonal wind component, f) meridional wind component. Average of all simulation results is indicated by black dotted line. 237

Figure C.3. Observed temperature data from moored instrument arrays at a) p4, b) p6, and c) p7 buoys and d) observed DO fluctuations at three discrete depths. DO measurements from both depths at the p6 buoy and at 200 m from p7 buoy are not shown due to erroneous measurements and data gaps. White areas indicate periods when data was not properly transmitted. 239

1 INTRODUCTION AND MOTIVATION

1.1 Literature Review

There are over 100 million lakes and reservoirs on Earth (collectively referred to as lakes hereafter), which contain 87% of the planet's liquid surface fresh water (Musie & Gonfa, 2023; Verpoorter et al., 2014). These lakes provide a wide range of socioeconomic benefits including water supply, fisheries habitat, transportation, hydropower, flood control, tourism, and recreation. Despite covering a mere 2.3% of Earth's surface, these lentic ecosystems host 9.5% of the world's recognized animal species, making them crucial biodiversity hotspots (Reid et al., 2019). Lakes also serve as useful sentinels of climate change as they integrate the effects of perturbations in watershed use and climate (Adrian et al., 2009; Williamson et al., 2009). As such, they are listed as key indicators in the United Nations' Sustainable Development Goals committed to water resources (target 6.6, UN DESA 2023). Unlike oceans and estuaries, horizontal density gradients in freshwater lakes are typically relatively small; therefore, hydrodynamic and thermodynamic processes that govern vertical mixing and transport play a central role in regulating the dynamics of dissolved oxygen (DO), nutrients, sediments, and heat in these systems. Changes in climate and water clarity, which alter lake temperatures and vertical mixing regimes, can thus have a profound impact on lake trophic status and ecosystem health.

1.1.1 Lake Mixing Regime

Thermal stratification is a ubiquitous feature of lakes, because of the temperature dependence of the density of water. The seasonal evolution of stratification is determined by the balance between turbulence, which acts to enhance mixing, and buoyancy, which acts to suppress turbulence and results in vertical layering (Boehrer & Schultze, 2008). Throughout the year, the vertical thermal structure of lakes varies seasonally in response to variations in heating and wind shear at the air-water interface. Surface heat flux results from latent, sensible, and longwave radiative heat exchange and incoming shortwave radiation. Heat is also lost or gained below the surface due to sub-surface inflows, sediment heat exchange and the attenuation of penetrative shortwave radiation within the water column (Schmid & Read, 2022). During net heating periods, a homogenous surface layer of warm, less dense water (epilimnion) forms above a deeper, denser, stratified hypolimnion below. Between these layers, a metalimnion forms, containing a thermocline where a sharp vertical temperature gradient is present. The the relative thickness of each of these layers and the strength of the thermocline exerts a strong control on the transport of nutrients and oxygen between the surface and deep layers and the vertical distribution and composition of lake biota (Giling et al., 2017). When the surface heat flux is negative, turbulence induced by convection and wind shear increases the depth of the surface mixed layer and erodes the thermocline, ultimately culminating in isothermal conditions when vertical mixing (i.e., *turnover*) occurs throughout the water column.

Limnologists have long recognized that a lake's mixing regime—the annual number of turnover periods—is influenced by its morphometry, geographic setting, and climate (Hutchinson & Loffler, 1956; Lewis, 1983). In temperate lakes, where hypolimnion temperatures remain consistently above the temperature of maximum water density (4 °C), relatively shallow systems tend to be *polymictic*, stratifying and mixing multiple times throughout the year whereas, sufficiently deep systems are *monomictic*, where thermal stratification persists until cooling during autumn and winter induce a single period of deep water circulation. Many of the world's deepest lakes are classified as *oligomictic*, mixing less than once a year, with turnover only occurring during extreme winters when meteorological conditions align to create isothermal conditions. Permanently stratified lakes are classified as *meromictic*.

Vertical mixing plays a fundamental role in the availability of dissolved oxygen, thereby influencing various ecological processes and lake trophic status. The concentration of DO determines the availability of aquatic organism habitat, ecological niches, redox reactions at the sediment water interface, and the recycling of organic matter within the water column (Wetzel, 2001). The main sources of oxygen to a lake include transfer from the atmosphere, production via photosynthesis and advection from inflowing streams, whereas consumption of oxygen results from both biogeochemical processes within the water column (e.g., decomposition of organic material, oxidation, and respiration) and sediment oxygen demand (Bouffard et al., 2013; Straile et al., 2003). When stratified, the thermocline inhibits oxygen flux into the hypolimnion, leading to oxygen depletion at depth, whereas vertical mixing facilitates deep water oxygen renewal. In eutrophic systems, excessive phytoplankton production and the settling of biomass can rapidly deplete hypolimnetic DO, creating hypoxic (≤3.5 mgL^{-1}; Nürnberg et al., 2013) and anoxic (≤1 mgL^{-1}; Nürnberg, 1995) conditions at the depth. Hypolimnetic hypoxia limits aerobic biota habitat and enhances the release of nutrients, trace metals, and greenhouse gases from sediments (Aeppli et al., 2022; Grasset et al., 2018; Hupfer & Lewandowski, 2008). Thus, climate change-induced alterations to lake stratification and mixing regimes directly impact lake oxygen budgets and water quality (Adrian et al., 2009; Jane et al., 2022).

1.1.2 A Changing Climate

Since the start of the industrial revolution, Earth's global average temperature has risen rapidly, primarily in response to increasing anthropogenic emissions of heat-trapping greenhouse gases (GHGs). The decadal average global surface (land and ocean) temperature from 2011-2020 was the warmest on record, with global surface temperatures estimated to be 1.09 °C [0.95 to 1.20 °C] higher than in 1850-1900 (IPCC 2023). Global average temperature is expected to continue to rise and is likely to exceed 1.5-2 °C during the 21st century unless sharp reductions in GHG emissions occur in the coming decades (IPCC 2023). In addition to rising air temperature, climate change is affecting other meteorological parameters including humidity, solar radiation, and wind speed. Specific humidity, the amount of water vapor held in the atmosphere, has increased rapidly in response to rising air temperature in accordance with the Clausius–Clapeyron relationship. Global mean specific humidity increased by 0.07 g kg^{-1} from 1973-2002 (Willett et al., 2007). The trend in incoming solar radiation has been observed to vary decadally since the mid 20th century, decreasing (i.e., "dimming") from the 1950s to the 1980s and increasing (i.e. "brightening") from the 1980s through the mid 2000s. These variations have been associated with changes in atmsopheric transparency, such as clouds and aerosol concentrations (Wild, 2012). Incoming longwave radiation, thermal radiation emitted by the atmosphere and clouds, has also increased as it is proportional to atmospheric temperature due to the Stefan-Boltzmann law and the concentration of GHGs (Schmid & Read, 2022).

Long-term declines in near-surface wind speeds, referred to as atmospheric stilling, have been observed in many regions, with wind speeds declining on average by -0.014 ms^{-1} $year^{-1}$ over a 30-year period globally (McVicar et al. 2012). This decrease in wind speed can partly be attributed to increased land surface roughness and changes in global atmospheric circulation patterns (Torralba et al., 2017; Vautard et al., 2010). Changes in all these climate variables directly impact lake mixing by modifying the seasonality of surface heat fluxes and the mechanical energy available for mixing.

1.1.3 Physical Impacts of Climate Change

In response to these climatic changes, lake surface water temperatures (LSWT) warmed at an average rate of +0.29 °C decade^{-1} from 1981 to 2020 (Tong et al., 2023). However, at a global scale, warming rates are highly variable, with lakes in the Laurentian Great Lakes region and Northern Europe warming significantly faster than the global average (O'Reilly et al. 2015). In contrast, Southern Hemisphere (SH) lakes have warmed at a slower pace (Schneider and Hook 2010). The difference in warming between Northern Hemisphere (NH) and SH lakes has been attributed to a faster increase in NH air temperature since 1980 (Piccolroaz et al., 2020), partly due to the greater extent of land coverage in the NH and disproportionate melting of arctic sea ice (Bryan et al., 1988; Friedman et al., 2013). While increasing atmospheric temperatures are often seen as the main cause of lake warming, changes in wind speed can also play a role in amplifying or suppressing these effects (Bayer et al., 2013a; Sahoo et al., 2013). Atmospheric stilling, for example, reduces the magnitude of mechanical vertical mixing, leading to less heat transferred from the surface to greater depths and consequently an increase in LSWT and bottom water cooling (Woolway et al., 2019).

Spatial heterogeneity in lake warming rates has been observed regionally as well, as internal lake characteristics (e.g., water clarity, ice phenology, and morphology) influence an individual lake's response to climate change. Water clarity determines how much solar radiation is absorbed and how heat is distributed within the water column (Persson and Jones 2008; Read and Rose 2013). Decreasing clarity enhances surface water warming and thermal stratification, whereas increasing clarity has the opposite effect: amplifying whole-lake and bottom warming, while reducing surface warming (Rose et al., 2016). Ice-covered lakes have warmed twice as fast as overlying air temperatures, as a combination of a shorter ice duration and earlier summer stratification results in LSWT warming more rapidly than air (Austin & Colman, 2007). Warming rates are also modulated by lake morphology (Kraemer et al., 2015; Winslow et al., 2015). Shallow lakes have lower heat storage capacity, responding more directly to short-term variations in atmospheric conditions compared to deep lakes, where heat can be readily transferred through the water column by wind mixing. Deep lakes require stronger wind speed to completely mix (Magee & Wu, 2017) but large surface areas increase the effect of vertical wind mixing and vertical transfer of heat to the lake bottom (Rueda & Schladow, 2009). In response to climate-induced alterations to lake temperatures, lake stratification and mixing regimes are projected to shift through time. Warmer surface temperatures cause the stratified season to begin earlier in the spring and last longer into the fall, while the strength of stratification is increasing due to differential warming rates between surface and bottom waters (Livingstone, 2003). Thermocline depth has also been observed to decrease in many deep lakes that have warmed appreciably (Coats et al., 2006; Zhang et al., 2014). This changes are collectively increasing lake stability, the amount of work needed to completely mix a density stratified water column. As a result, the frequency and intensity of deep mixing events are declining across lakes globally, resulting in widespread shift in lake mixing regimes. Woolway (2019) used a one-dimensional lake model to forecast climate change impacts on the mixing regimes of 635 lakes worldwide and predicted that increasing winter LSWT will shift a significant percentage of monomictic lakes to an oligomictic or meromictic state. Many lakes that are currently classified as oligomictic (e.g., Lake Maggiore, Lake Garda) are also predicted to become permanently thermally stratified under future climate conditions (Fenocchi et al., 2018; Rogora et al., 2018). However, the frequency of deep winter mixing events in some oligomictic systems has remained consistent or increased, highlighting the complex response of deep lakes to climate change (Schladow et al., 2021; Swann et al., 2020).

1.1.4 Ecosystem Impacts of Climate Change

The effects of changing climate and thermal regimes on lake ecosystems have been observed globally. Warming LSWT promote shifts in the timing and magnitude of phytoplankton blooms and impact phytoplankton community composition (Winder &

Sommer, 2012). Spring phytoplankton blooms are occurring earlier in the year due to excess lake warming and an earlier onset of thermal stratification (Peeters et al., 2007). Cyanobacteria, many of which produce harmful toxins, have optimal growth rates at higher temperatures (often above 25 °C) compared to other phytoplankton groups such as diatoms or green algae (Berg & Sutula, 2015). This suggests that these species will have a competitive advantage under warmer conditions (Paerl & Huisman, 2008). Furthermore, many cyanobacteria species have the ability to regulate their buoyancy, giving them an advantage over other photosynthetic organisms in highly stratified environments by accessing light more efficiently (Oliver et al., 2012). The combination of changes in climate and lake thermal regime with increasing watershed nutrient loads has thus led to widespread expansion of harmful cyanobacteria blooms (Paerl, 2014).

Stronger lake stability and a longer duration of thermal stratification reduces vertical mixing, facilitating greater hypolimnetic oxygen depletion and increasing the prevalence of anoxia in deep waters (Foley et al., 2012; Jane et al., 2022; North et al., 2014). When benthic sediments become anoxic, they can release phosphorus (P) into the water column, increasing the amount of biologically available P and shifting limiting nutrient status from P to nitrogen (N) (Nikolai & Dzialowski, 2014; Wu et al., 2020). Changes in nutrient limitation can further promote cyanobacteria growth, many of which can fixate atmospheric N and outcompete other phytoplankton groups in N-limited environments (Orihel et al., 2015). In polymictic systems, intermittent stratification and mixing events throughout the summer regularly transport bioavailable P into the epilimnion when phytoplankton growth rates are high. This so-called *climatic eutrophication* (Sahoo et al., 2016) can also negatively affect the trophic status of deep oligomictic lakes. This can occur when deep lakes remain stratified for extended multi-year periods, resulting in deep water anoxia, a decrease in fish habitat, and an increase in the release of sedimentary nutrients into the hypolimnion (Beutel & Horne, 2018; Rogora et al., 2018).

1.1.5 Lake Models

Long-term monitoring programs are important to assess lake response to climate change because they establish baseline conditions and help identify trends. Numerical lake models driven by climate model outputs complement these observations by allowing scientists to predict the future response of lakes to environmental change and assess how management strategies can be developed to ensure sustainable water use for future generations. One-dimensional (1D) hydrodynamic lake models are frequently used to simulate lake response to climate change due to their computational efficiency, minimal input data requirements, and skill in simulating vertical lake thermal structure at seasonal and decadal timescales (Feldbauer et al., 2022; Ladwig et al., 2018). However, 1D models require extensive site-specific calibration to parametrize the complex interactions of basin morphology, wind, and surface forcings into a one-dimensional framework. Consequently, 1D models calibrated to current, baseline conditions may produce unrealistic predictions in the future if lake mixing regimes shift (Zamani et al., 2021). Furthermore, 1D models cannot resolve horizontal processes, such as upwellings, flows influence by Coriolis acceleration, and differential cooling/heating between shallow and deep waters, which can contribute to deep ventilation (Fer et al., 2002; Piccolroaz et al., 2019; Reiss et al., 2020; Valbuena et al., 2022). These limitations can be reduced with three-dimensional (3D) hydrodynamic models, which can resolve seiche activity, spatially heterogeneous geometries, and planetary rotational effects (Hodges et al., 2000; Rueda et al., 2003). Though 3D models require calibration as well, their ability to mechanistically simulate energetics, suggests that a well-calibrated model will continue to perform reasonably under changing lake thermal regimes.

1.2 Study Sites

This dissertation investigates three lakes varying in geographical location, morphometry, mixing regime, and trophic status. **Chapter 2** focuses on Clear Lake, located in Lake County, California. Clear Lake is a shallow, hypereutrophic, multi-basin, polymictic lake situated in the Coastal Range of Northern California (432 m.a.s.l). The lake experiences a Mediterranean climate characterized by dry, hot summers, and mild, wet winters with large interannual variability in precipitation. **Chapter 3** investigates

Lake Tahoe, straddling the California-Nevada state boundary within the Sierra Nevada Mountains (1897 m.a.s.l). Lake Tahoe is an extremely deep, oligomictic lake and world renowned for its high water clarity. The lake experiences an alpine climate with cold, snowy winters and warm, dry summers. **Chapter 4** examines Lago Llanquihue, located in the Los Lagos region of northern Patagonia, Chile. Llanquihue is a deep, oligotrophic, monomictic lake located at an elevation of 51 m.a.s.l. The lake's temperate climate is characterized by significant rainfall throughout the year.

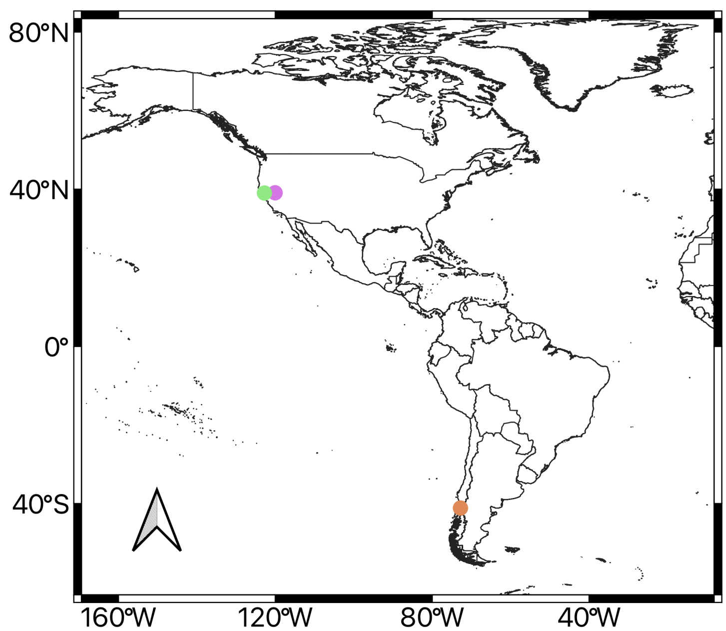

Figure 1.1. *Location of study lakes: Chapter 2 (Clear Lake – green), Chapter 3 (Lake Tahoe – purple), Chapter 4 (Lago Llanquihue – orange).*

1.3 Objectives and Organization of This Work

This dissertation aims to investigate the drivers and dynamics of deep mixing events, forecast how lake mixing regime may be impacted by climatic and watershed changes, and examine how resulting deep water hypoxia can influence nutrient cycling and ecosystem dynamics. While the impacts of climate change on lake mixing processes have been widely investigated through numerical modeling, 1D hydrodynamic models have been typically employed, which cannot resolve horizontal processes that may contribute to hypolimnetic renewal and mixing in weakly stratified, deep lakes. This dissertation instead utilizes both high-frequency measurements of temperature and oxygen and 3D numerical modeling to characterize the drivers, dynamics, and impacts of vertical mixing processes. The following chapters focus on three lakes greater than 100 km^2 that range in depth, mixing regime and trophic status. The research presented hereafter is organized as follows:

Stronger thermal stratification and reductions in turnover frequency, coupled with increasing watershed nutrient inputs, have led to a widespread deoxygenation of lakes and an increase in internal P loading (Jane et al., 2021, 2022). However, anoxia at the sediment surface and associated P releases often remain unnoticed in polymictic systems due to the lack of detailed observations (Tammeorg et al., 2020). **Chapter 2** seeks to quantify the contribution of internal P loading to the annual P budget and examine its impact on cyanobacteria blooms in hypereutrophic, multi-basin, polymictic Clear Lake, CA. This study combines near-bed measurements of temperature and oxygen from 2019 to 2021 with water quality measurements and experimental sediment P release rates to provide two comparative estimates of internal loads. The findings demonstrate that P released from anoxic sediments during stratified periods constitute the majority of P inputs to the lake on annual basis. This internal source increases the amount of bioavailable P for primary production and shifts the system towards N-limitation in favor of N-fixing cyanobacteria. This research highlights the importance of managing in-lake P along with external sources, especially in the context of changing stratification and mixing patterns.

One-dimensional numerical models predict that the majority of deep oligomictic lakes will become permanently stratified by the end of the 21st century, leading to widespread deoxygenation and shifts in lake trophic status (Woolway & Merchant, 2019). However, observations of winter mixing depths in deep, oligomictic Lake Tahoe, CA, indicate that the average winter mixing depth and turnover frequency has not declined in the past 50 years. This suggests that Tahoe may continue to experience deep mixing for longer than previously forecasted (Sahoo et al., 2013). While turnover events in oligomictic lakes have been widely documented with periodic temperature profiles, high-frequency, continuous observations of deep mixing events are rare due to their sporadic and infrequent occurrence (van Haren et al., 2021). Motivated by the need to better understand the factors that drive turnover in oligomictic systems, and the hydrodynamics processes the occur during deep mixing events, a multi-decadal record of winter mixing depths and high-frequency deep water temperature/DO measurements during four turnover winters from 1998 to 2023 was analyzed. **Chapter 3** demonstrates that whether or not oligomictic Lake Tahoe undergoes turnover is primarily determined by the meteorological conditions during a narrow window of time in the late winter. Field observations, indicate that while turnover is initiated by buoyancy-driven convection, convectively driven horizontal transport produced by differential cooling plays a significant role in cooling and ventilating the deep hypolimnion during subsequent weakly stratified conditions. The importance of this three-dimensional deep water transport process suggests that 1D models may not fully resolve how renewal of deep lakes will change under a warmer climate.

Though climate change is warming lakes and altering mixing regimes globally, there is considerable global and regional variation in warming rates as both external factors and internal lake characteristics modulate a system's specific response to climatic perturbations (O'Reilly et al., 2015). Changes in watershed land use can also influence these physical processes by altering water clarity. While long-term changes in European and North American lakes have been well documented, deep South American lakes have received less attention, due to the lack of high-resolution monitoring data. In **Chapter 4**, a 3D hydrodynamic model (Si3D) is employed to investigate the potential impacts that climate change and watershed development may have on stratification and deep water mixing in deep, monomictic Lago Llanquihue, Chile. A sensitivity analysis demonstrates that changes in clarity may be as important as rising air temperatures in determining how deep lakes respond to climate change. Long-term projections forecast that Llanquihue's mixing regime is not likely to change significantly during the 21st century, suggesting that climate change impacts on Southern Hemisphere lakes may not be as severe as in comparative Northern Hemisphere systems in the near term. **Chapter 5** summarizes the findings of the studies presented in this dissertation and highlights potential future research to extend the understanding of vertical mixing processes in lakes. The subsequent appendices A, B, and C provide supplementary information regarding the data and analytical methods used in Chapters 2, 3, and 4 respectively.

References

Adrian, R., O'Reilly, C. M., Zagarese, H., Baines, S. B., Hessen, D. O., Keller, W., Livingstone, D. M., Sommaruga, R., Straile, D., Van Donk, E., Weyhenmeyer, G. A., & Winder, M. (2009). Lakes as sentinels of climate change. *Limnol. Oceanogr.*, *54*(6), 2283–2297.

Aeppli, M., Schladow, G., Lezama Pacheco, J. S., & Fendorf, S. (2022). Iron reduction in profundal sediments of ultraoligotrophic lake tahoe under oxygen-limited conditions. *Environ. Sci. Tech.*, *57*.

Austin, J. A., & Colman, S. M. (2007). Lake Superior summer water temperatures are increasing more rapidly than regional temperatures: A positive ice-albedo feedback. *Geophys. Res. Lett.*, *34*(6).

Bayer, T. K., Burns, C. W., & Schallenberg, M. (2013). Application of a numerical model to predict impacts of climate change on water temperatures in two deep, oligotrophic lakes in New Zealand. *Hydrobiologia*, *713*(1), 53–71.

Berg, M., & Sutula, M. (2015). *Factors affecting the growth of cyanobacteria with special emphasis on the Sacramento-San Joaquin Delta.*

Beutel, M. W., & Horne, A. J. (2018). Nutrient fluxes from profundal sediment of ultra-oligotrophic Lake Tahoe, California/Nevada: Implications for water quality and management in a changing climate. *Water Resour. Res.*, *54*(3), 1549–1559.

Biemond, B., Amadori, M., Toffolon, M., Piccolroaz, S., Van Haren, H., & Dijkstra, H. A. (2021). Deep-mixing and deep-cooling events in Lake Garda: Simulation and mechanisms. *J. Limnol.*, *80*(2).

Boehrer, B., & Schultze, M. (2008). Stratification of lakes. *Reviews of Geophysics*, *46*(2), 1–27.

Bouffard, D., Ackerman, J. D., & Boegman, L. (2013). Factors affecting the development and dynamics of hypoxia in a large shallow stratified lake: Hourly to seasonal patterns. *Water Resour. Res.*, *49*(5), 2380–2394.

Bryan, K., Manabe, S., & Spelman MJ. (1988). Interhemispheric asymmetry in the transient response of a coupled ocean–atmosphere model to a CO2 forcing. *J. Phys. Oceanogr.*, *18*(6), 851–867.

Coats, R., Perez-Losada, J., Schladow, G., Richards, R., & Goldman, C. (2006). The warming of Lake Tahoe. *Clim. Change*, *76*(1–2), 121–148.

Feldbauer, J., Ladwig, R., Mesman, J. P., Moore, T. N., Zündorf, H., Berendonk, T. U., & Petzoldt, T. (2022). Ensemble of models shows coherent response of a reservoir's stratification and ice cover to climate warming. *Aquat. Sci.*, *84*(50).

Fenocchi, A., Rogora, M., Sibilla, S., Ciampittiello, M., & Dresti, C. (2018). Forecasting the evolution in the mixing regime of a deep subalpine lake under climate change scenarios through numerical modelling (Lake Maggiore, Northern Italy/Southern Switzerland). *Clim. Dyn.*, *51*(9–10), 3521–3536.

Fer, I., Lemmin, U., & Thorpe, S. A. (2002). Winter cascading of cold water in Lake Geneva. *J. Geophys. Res.*, *107*(C6).

Foley, B., Jones, I. D., Maberly, S. C., & Rippey, B. (2012). Long-term changes in oxygen depletion in a small temperate lake: Effects of climate change and eutrophication. *Freshw. Biol.*, *57*(2), 278–289.

Friedman, A. R., Hwang, Y. T., Chiang, J. C. H., & Frierson, D. M. W. (2013). Interhemispheric temperature asymmetry over the twentieth century and in future projections. *J. Clim.*, *26*(15), 5419–5433.

Giling, D. P., Nejstgaard, J. C., Berger, S. A., Grossart, H. P., Kirillin, G., Penske, A., Lentz, M., Casper, P., Sareyka, J., & Gessner, M. O. (2017). Thermocline deepening boosts ecosystem metabolism: Evidence from a large-scale lake enclosure experiment simulating a summer storm. *Glob. Change Biol.* , *23*(4), 1448–1462.

Grasset, C., Mendonça, R., Saucedo, G. V., Bastviken, D., Roland, F., & Sobek, S. (2018). Large but variable methane production in anoxic freshwater sediment upon addition of allochthonous and autochthonous organic matter. *Limnol. Oceanogr.*, *63*, 1488–1501.

Hodges, B. R., Imberger, J., Laval, B., & Appt, J. (2000). Modeling the hydrodynamics of stratified lakes. *Hydroinformatics 2000 Conference*, *July*, 23–27.

Hupfer, M., & Lewandowski, J. (2008). Oxygen controls the phosphorus release from lake sediments – A long-lasting paradigm in limnology. *Int. Rev. Hydrobiol.*, *93*(4–5), 415–432.

Hutchinson, G. E., & Loffler, H. (1956). The thermal classification of lakes. *Geophysics*, *42*, 84–86.

Jane, S. F., Hansen, G. J. A., Kraemer, B. M., Leavitt, P. R., Mincer, J. L., North, R. L., Pilla, R. M., Stetler, J. T., Williamson, C. E., Woolway, R. I., Arvola, L., Chandra, S., DeGasperi, C. L., Diemer, L., Dunalska, J., Erina, O., Flaim, G., Grossart, H. P., Hambright, K. D., ... Rose, K. C. (2021). Widespread deoxygenation of temperate lakes. *Nat.*, *594*(7861), 66–70.

Jane, S. F., Mincer, J. L., Lau, M. P., Lewis, A. S. L., Stetler, J. T., & Rose, K. C. (2022). Longer duration of seasonal stratification contributes to widespread increases in lake hypoxia and anoxia. *Glob. Change Biol.* , *29*(4), 1009–1023.

Ladwig, R., Furusato, E., Kirillin, G., Hinkelmann, R., & Hupfer, M. (2018). Climate change demands adaptive management of urban lakes: model-based assessment of management scenarios for Lake Tegel (Berlin, Germany). *Water*, *10*(188), 1–23.

Lee. H, & Romero .J. (2023). *IPCC, 2023: Summary for policymakers. In: Climate Change 2023: Synthesis Report.Contribution of Working Groups I, II and III to the Sixth Assessment Report of the Intergovernmental Panel on Climate Change.*

Lewis, W. M. (1983). A revised classification of lakes based on mixing. *Can. J. Fish. Aquat. Sci*, *10*, 1779–1787.

Livingstone, D. M. (2003). Impact of secular climate change on the thermal structure of a large temperate central European lake. *Clim. Change*, *57*, 205–225.

Magee, M. R., & Wu, C. H. (2017). Response of water temperatures and stratification to changing climate in three lakes with different morphometry. *Hydrol. Earth Sys. Sci.*, *21*(12), 6253–6274.

McVicar, T. R., Roderick, M. L., Donohue, R. J., Li, L. T., Van Niel, T. G., Thomas, A., Grieser, J., Jhajharia, D., Himri, Y., Mahowald, N. M., Mescherskaya, A. V., Kruger, A. C., Rehman, S., & Dinpashoh, Y. (2012). Global review and synthesis of trends in observed terrestrial near-surface wind speeds: Implications for evaporation. *J. Limnol.*, *416–417*, 182–205.

Musie, W., & Gonfa, G. (2023). Fresh water resource, scarcity, water salinity challenges and possible remedies: A review. *Heliyon*, *9*(8), e18685.

Nikolai, S. J., & Dzialowski, A. R. (2014). Effects of internal phosphorus loading on nutrient limitation in a eutrophic reservoir. *Limnologica*, *49*, 33–41.

North, R. P., North, R. L., Livingstone, D. M., Köster, O., & Kipfer, R. (2014). Long-term changes in hypoxia and soluble reactive phosphorus in the hypolimnion of a large temperate lake: Consequences of a climate regime shift. *Glob. Change Biol.* , *20*(3), 811–823.

Oliver, R., Hamilton, D., Brookes, J. D., & George, G. G. (2012). Physiology, Blooms and Prediction of Planktonic Cyanobacteria. In Whitton B.A. (Ed.), *Ecology of Cyanobacteria II: Their Diversity in Space and Time*. Springer-Verlag.

O'Reilly, C. M., Rowley, R. J., Schneider, P., Lenters, J. D., Mcintyre, P. B., & Kraemer, B. M. (2015). Rapid and highly variable warming of lake surface waters around the globe. *Geophys. Res. Lett.*, *42*, 10773–10781.

Orihel, D. M., Schindler, D. W., Ballard, N. C., Graham, M. D., O'Connell, D. W., Wilson, L. R., & Vinebrooke, R. D. (2015). The "nutrient pump:" Iron-poor sediments fuel low nitrogen-to-phosphorus ratios and cyanobacterial blooms in polymictic lakes. *Limnol. Oceanogr.*, *60*(3), 856–871.

Paerl, H. W. (2014). Mitigating harmful cyanobacterial blooms in a human- and climatically-impacted world. *Life*, *4*, 988–1012.

Paerl, H. W., & Huisman, J. (2008). Blooms like it hot. *Sci.*, *320*(5872), 57–58.

Peeters, F., Straile, D., Lorke, A., & Livingstone, D. M. (2007). Earlier onset of the spring phytoplankton bloom in lakes of the temperate zone in a warmer climate. *Glob. Change Biol.* , *13*(9), 1898–1909.

Persson, I., & Jones, I. D. (2008). The effect of water colour on lake hydrodynamics: A modelling study. *Freshw. Biol.*, *53*(12), 2345–2355.

Piccolroaz, S., Amadori, M., Toffolon, M., & Dijkstra, H. A. (2019). Importance of planetary rotation for ventilation processes in deep elongated lakes: Evidence from Lake Garda (Italy). *Sci. Rep.*, *9*(8290).

Piccolroaz, S., Woolway, R. I., & Merchant, C. J. (2020). Global reconstruction of twentieth century lake surface water temperature reveals different warming trends depending on the climatic zone. *Clim. Change*, *160*, 427–442.

Read, J. S., & Rose, K. C. (2013). Physical responses of small temperate lakes to variation in dissolved organic carbon concentrations. *Limnol. Oceanogr.*, *58*(3), 921–931.

Reid, A. J., Carlson, A. K., Creed, I. F., Eliason, E. J., Gell, P. A., Johnson, P. T. J., Kidd, K. A., Maccormack, T. J., Olden, J. D., Ormerod, S. J., Smol, J. P., Taylor, W. W., Tockner, K., Vermaire, J. C., Dudgeon, D., & Cooke, S. J. (2019). Emerging threats and persistent conservation challenges for freshwater biodiversity. *Biol. Rev.*, *94*, 849–873.

Reiss, R. S., Lemmin, U., Cimatoribus, A. A., & Barry, D. A. (2020). Wintertime coastal upwelling in Lake Geneva: An efficient transport process for deepwater renewal in a large, deep lake. *JGR: Oceans*, *125*(8), 1–18.

Rogora, M., Buzzi, F., Dresti, C., Leoni, B., Lepori, F., Mosello, R., Patelli, M., & Salmaso, N. (2018). Climatic effects on vertical mixing and deep-water oxygen content in the subalpine lakes in Italy. *Hydrobiologia*, *824*(1), 33–50.

Rose, K. C., Winslow, L. A., Read, J. S., & Hansen, G. J. A. (2016). Climate-induced warming of lakes can be either amplified or suppressed by trends in water clarity. *Limnol. Oceanogr. Lett.*, *1*, 44–53.

Rueda, F. J., & Schladow, S. G. (2009). Mixing and stratification in lakes of varying horizontal length scales: Scaling arguments and energy partitioning. *Limnol. Oceanogr.*, *54*(6), 2003–2017.

Rueda, F. J., Schladow, S. G., & Pálmarsson, S. Ó. (2003). Basin-scale internal wave dynamics during a winter cooling period in a large lake. *JGR: Oceans*, *108*(3), 1–16.

Sahoo, G. B., Schladow, S. G., Reuter, J. E., Coats, R., Dettinger, M., Riverson, J., Wolfe, B., & Costa-Cabral, M. (2013). The response of Lake Tahoe to climate change. *Clim. Change*, *116*(1), 71–95.

Sahoo, G. B., Forrest, A. L., Schladow, S. G., Reuter, J. E., Coats, R., & Dettinger, M. (2016). Climate change impacts on lake thermal dynamics and ecosystem vulnerabilities. *Limnol. Oceanogr.*, *61*(2), 496–507.

Schladow, S. G., Toy, A., & Watanabe, S. (2021). *Tahoe: State of the Lake Report.* https://tahoe.ucdavis.edu/stateofthelake

Schmid, M., & Read, J. (2022). Heat Budget of Lakes. In *Encyclopedia of Inland Waters, Second Edition* (Vol. 1, pp. 467–473). Elsevier.

Schneider, P., & Hook, S. J. (2010). Space observations of inland water bodies show rapid surface warming since 1985. *Geophys. Res. Lett.*, *37*(22).

Straile, D., Jöhnk, K., & Rossknecht, H. (2003). Complex effects of winter warming on the physicochemical characteristics of a deep lake. *Limnol. Oceanogr.*, *48*(4), 1432–1438.

Swann, G. E. A., Panizzo, V. N., Piccolroaz, S., Pashley, V., Horstwood, M. S. A., Roberts, S., Vologina, E., Piotrowska, N., Sturm, M., Zhdanov, A., Granin, N., Norman, C., Mcgowan, S., & Mackay, A. W. (2020). Changing nutrient cycling in Lake Baikal, the world's oldest lake. *PNAS*, *117*(44).

Tammeorg, O., Nürnberg, G., Horppila, J., Haldna, M., & Niemistö, J. (2020). Redox-related release of phosphorus from sediments in large and shallow Lake Peipsi: Evidence from sediment studies and long-term monitoring data. *J. Great Lakes Res.* , *46*(6), 1595–1603.

The Sustainable Development Goals Report 2023: Special Edition. (2023).

Tong, Y., Feng, L., Wang, X., Pi, X., Xu, W., & Woolway, R. I. (2023). Global lakes are warming slower than surface air temperature due to accelerated evaporation. *Nature Water*.

Torralba, V., Doblas-Reyes, F. J., & Gonzalez-Reviriego, N. (2017). Uncertainty in recent near-surface wind speed trends: A global reanalysis intercomparison. *Environ. Res. Lett.*, *12*(11).

Van Haren, H., Piccolroaz, S., Amadori, M., Toffolon, M., & Dijkstra, H. A. (2021). Moored observations of turbulent mixing events in deep Lake Garda, Italy. *J. Limnol.*, *80*(1).

Vautard, R., Cattiaux, J., Yiou, P., Thépaut, J.-N., & Ciais, P. (2010). Northern Hemisphere atmospheric stilling partly attributed to an increase in surface roughness. *Nat. Geosci.*, *3*, 756–761.

Verpoorter, C., Kutser, T., Seekell, D. A., & Tranvik, L. J. (2014). A global inventory of lakes based on high-resolution satellite imagery. *Geophys. Res. Lett.*, *41*(18), 6396–6402.

Wetzel, R. G. (2001). Oxygen. In *Limnology* (3rd ed., pp. 151–169). Academic Press.

Wild, M. (2012). Solar radiation versus climate change. *Encyclopedia of Sustainability Science and Technology* (pp. 9731–9740).

Willett, K. M., Gillett, N. P., Jones, P. D., & Thorne, P. W. (2007). Attribution of observed surface humidity changes to human influence. *Nat.*, *449*, 710–713.

Williamson, C. E., Saros, J. E., Vincent, W. F., & Smol, J. P. (2009). Lakes and reservoirs as sentinels, integrators, and regulators of climate change. *Limnol. Oceanogr.*, *54*(6), 2273–2282.

Winder, M., & Sommer, U. (2012). Phytoplankton response to a changing climate. *Hydrobiologia*, *698*(1), 5–16.

Woolway, R. I., & Merchant, C. J. (2019). Worldwide alteration of lake mixing regimes in response to climate change. *Nat. Geosci.*, *12*(4), 271–276.

Woolway, R. I., Merchant, C. J., Van, J., Hoek, D., Azorin-Molina, C., Nõges, P., Laas, A., Mackay, E. B., & Jones, I. D. (2019). Northern Hemisphere atmospheric stilling accelerates lake thermal responses to a warming world. *Geophys. Res. Lett.*, *46*(11), 11983–11992.

Wu, Z., Zou, R., Jiang, Q., Elser, J. J., Zhao, L., Ye, R., & Liu, Y. (2020). What maintains seasonal nitrogen limitation in hyper-eutrophic Lake Dianchi? Insights from stoichiometric three-dimensional numerical modeling. *Aquat. Sci.*, *82*(4).

Zamani, B., Koch, M., & Hodges, B. R. (2021). A potential tipping point in the thermal regime of a warm monomictic reservoir under climate change using three-dimensional hydrodynamic modeling. *Inland Waters*, *11*(3), 315–334.

Zhang, Y., Wu, Z., Liu, M., He, J., Shi, K., Wang, M., & Yu, Z. (2014). Thermal structure and response to long-term climatic changes in Lake Qiandaohu, a deep subtropical reservoir in China. *Limnology and Oceanography*, *59*(4), 1193–1202.

2 INTERNAL PHOSPHORUS LOADING ALTERS NUTRIENT LIMITATION AND CONTRIBUTES TO CYANOBACTERIA BLOOMS IN A POLYMICTIC LAKE[1]

Abstract

Clear Lake, a medium-sized hypereutrophic, polymictic lake in Northern California, has had recurring harmful cyanobacteria blooms (HCBs) for over a century despite reductions in external phosphorus (P) loadings. Internal P loading can alter nutrient availability and limitation supporting HCBs but is rarely quantified or compared with external loads. We have quantified external P loads from 2019-2021 for the three main tributaries (accounting for 46% of the flow) and internal loadings using two methods: a P mass balance and modeled release rates of soluble reactive phosphorus from oxic and anoxic sediments. In addition, we combined high-frequency *in situ* measurements of water temperature and dissolved oxygen, discrete grab sampling for nutrient chemistry, and remote sensing in order to explore the potential drivers of the observed variability and provide a comprehensive view of the spatiotemporal dynamics of HCBs. By understanding the relative contribution of external and internal nutrient loadings and the relationship

---

[1] This manuscript has been accepted for publication in *Aquatic Sciences*

between environmental parameters and HCBs, interannual bloom variability can be better predicted. Comparative estimates of external and internal phosphorus loading indicate that internal sources accounted for 70 – 95% of the total P input into the system during the study period. Contrary to other lakes, the intensity of the summer bloom season was correlated to the timing and duration of anoxia rather than the magnitude of spring runoff. Internally released P shifted the system from phosphorus to nitrogen limitation during the summer, potentially favoring the proliferation of nitrogen-fixing cyanobacteria.

2.1 Introduction

Eutrophication poses a grave threat to lentic ecosystems globally, promoting the proliferation of harmful cyanobacteria blooms (HCBs) that reduce aquatic biodiversity, yielding increased water treatment costs, and threatening human health through bloom-produced cyanotoxins (Aráoz et al., 2010; Chorus et al., 2000; Paerl et al., 2001; Svirčev et al., 2014). Phosphorus (P) has been historically viewed as the limiting nutrient for primary production in freshwater lakes (Dillon & Rigler, 1974; V. H. Smith, 1985; V. H. Smith & Schindler, 2009), and watershed P load reduction programs have been widely implemented to control HCBs (Schindler et al., 2016; Xu et al., 2015). While external nutrient loading (L_{ext}) ultimately regulates lake water quality over longer timescales, internal loading (L_{int}) from sediment nutrient pools defines the timeframe required for load abatement programs to result in improved water quality and can directly influence the intensity of the summer HCB season (Coveney et al., 2005; Isles et al., 2015; Søndergaard et al., 2003). Despite the potential for internal P loading to delay the recovery of eutrophicated lakes, L_{int} is rarely quantified and directly compared to L_{ext}, especially over time scales that adequately resolve the physiochemical and biological mechanisms which contribute to in-lake P cycling.

When P enters a lake, it can be cycled within food webs or retained in sediment. Under oxidizing conditions, P is adsorbed onto ferric oxy-hydroxides and deposited in sediments (Einsele 1936; Mortimer 1941). In summer, when thermal stratification prevents the vertical exchange of dissolved oxygen (DO), anoxic sediments release chemically bound P into porewater, which is eventually internally loaded into the overlying water column via advection and diffusion. Aerobic organic matter decomposition can also promote the release of inorganic and dissolved organic P into the water column (Hupfer & Lewandowski, 2008; K. Song & Burgin, 2017). While watershed L_{ext} can be directly quantified via stream discharge and nutrient concentration data, L_{int} is more difficult to assess because internal P sources cannot be easily measured *in situ* before biotic uptake (Nürnberg, 2009). Methods for quantifying L_{int} include regression analysis, mass-balance techniques, time-dynamic modeling, and coupled hydrodynamic-ecological modeling (Burger et al., 2008; Håkanson, 2004; Nürnberg, 1988, 2009).

In polymictic systems, L_{int} is frequently ignored or assumed negligible in mass balance studies since hypolimnetic DO concentrations in temporarily stratifying systems rarely remain consistently anoxic (DO < 1 mgL^{-1}) during the warm growing season (Molot et al., 2010; Nürnberg, 2005; Orihel et al., 2015; Winter et al., 2002). However, elevated total phosphorus (TP) concentrations have been observed in eutrophic, polymictic systems when bottom water DO is depleted (Burger et al. 2008; Nürnberg et al. 2013). Resolving the spatial and temporal extent of anoxia and hypoxia (DO < 3.5 mgL^{-1}) in frequently mixing systems remains challenging as hypolimnetic DO can rapidly decline during stratification and reoxygenation regularly occurs with mixing events (Nürnberg & LaZerte, 2016; Tammeorg et al., 2020).

Episodic summertime mixing events can make polymictic systems highly susceptible to HCBs when nutrient-enriched waters are transported vertically into the epilimnion during the warm growing season. In addition to increasing bioavailable nutrients, a surplus of P relative to nitrogen (N) in surface waters shifts the system towards nitrogen limitation, which favors the dominance of nitrogen-fixing cyanobacteria (Orihel et al., 2015; V. H. Smith, 1983). Non N-fixing cyanobacteria can subsequently dominate due to their ability to maintain net growth under low underwater irradiance (van Duin et al., 1995). A N:P molar ratio $<$ 16:1 is commonly proposed to indicate N limitation in marine environments (Redfield, 1958). However, this may be a poor approximation for nutrient limitation in freshwater systems as nutrient demands differ for inland and marine ecosystems (Domagalski et al., 2021). Guildford and Hecky (2000) suggested that in lakes, N limitation occurs at TN:TP molar ratios $<$ 20:1, though the molar TN:TP threshold indicating shifts in nutrient limitation is likely system specific (Klausmier et al. 2004).

This study explores the linkages between internal P loading and the interannual variability of HCB severity in a hypereutrophic, polymictic system. We combined data from a range of sources collected over a three-year period to quantify the internal and external nutrient loads and their relationship to the magnitude of the summer HCB season in Clear Lake, California. We estimated: (1) net annual internal P loads from observed changes in the integrated lake P during the dry season; and (2) gross P loads derived from experimental sediment soluble reactive phosphorus (SRP) release rates and estimates of hypolimnetic hypoxia. The terms net and gross respectively differentiate whether or not the P fraction removed from the water column via sedimentation is considered in the associated calculations. For the latter method, we applied a novel approach, comparing theoretical estimates of sediment anoxia (i.e., Nürnberg's anoxic factor [Nürnberg 2005]) with *in situ* hypolimnetic DO measurements to calibrate the system-specific threshold for which redox-mediated internal P loading will occur. In addition, we examined how interbasin and interannual variability in the timing and duration of mixing events influences the summer HCB season.

We hypothesize that: (1) P release from anoxic sediments is the primary source of phosphorus loading to Clear Lake; (2) internal P loading is one of the main drivers of blooms of nitrogen-fixing cyanobacteria by lowering N:P ratios, creating a nitrogen-limited environment; and (3) the annual variation in the timing and duration of hypoxia regulates the magnitude of the summer HCB season. We then compare the strengths and limitations of each internal loading estimate to provide insight for improving loading estimation methods in polymictic systems. Finally, the contribution of internal loading to Clear Lake's overall phosphorus budget is assessed to determine if current lake management policies can be expected to improve water quality in the long term.

2.2 Materials and Methods

2.2.1 Study Site

Clear Lake is a shallow, polymictic lake located in the Coastal Range of Northern California (39°00′N; 122°45′W). The lake has an average surface area (A_o) of 151 km^2, mean depth (Z_{mean}) of 8 m, and maximum depth (Z_{max}) of 15 m (**Table 2.1**). Annual precipitation variability and water releases result in year-to-year water surface elevation fluctuations from nearly 1 m below the natural rim of the lake to nearly 3 m above it. As a result of the lake's relatively shallow depth, long fetch, and the prevailing west/northwesterly winds, Clear Lake mixes to the bottom frequently during the summer months when the water column is thermally stratified. The lake has three distinct sub-basins: Upper, Oaks, and Lower Arm (**Figure 2.1**). The Upper Arm (UA) is the largest and shallowest basin and receives over 90% of the watershed runoff. This includes flows from the lake's three largest inlets: Middle, Scotts, and Kelsey Creek. A passage at the east end of the UA (the Narrows), connects to the two smaller and deeper basins. The Lower Arm (LA) discharges into the lake's only outflow, Cache Creek, while the Oaks Arm (OA) is the smallest basin and extends east of the Narrows. The residence time of the whole lake has been estimated at 4.5 years (Chamberlin et al., 1990).

Table 2.1 *Physical characteristics of Clear Lake and sub-basins. Values in parentheses indicate percentage of total lake.*

Characteristic	Upper (UA)	Oaks (OA)	Lower (LA)	Whole Lake
Station(s)	UA-01, UA-06, UA-08	OA-04	LA-03	All
Catchment area [A_o, km^2]	1031	89	83	1190
Surface Area [A_o, km^2]	106 (70%)	15 (10 %)	30 (20%)	151 (100%)
Max Depth [Z_{mean}, m]	11	14	15	15
Mean Depth [Z_{max}, m]	6	9	8.5	8
Volume [V, km^3]	0.66 (63%)	0.13 (12%)	0.27 (25%)	1.11 (100%)
Dynamic Ratio [DR, km/m]	1.7	0.4	0.7	1.5

The lake is naturally highly productive due to its large drainage basin area which contributes to a significant external load of mineral nutrients and the nutrient-rich volcanic soils within the watershed (Wilson, 2015). Paleolimnological evidence indicates that the lake has supported abundant phytoplankton production for the past 15,000 years (Sims, 1988). However, since the mid-1800s, anthropogenic modifications to the watershed (e.g., wetland conversion, shoreline development, agriculture, and mining) have significantly increased sediment and nutrient loading to the lake, exacerbating eutrophication, and promoting the proliferation of HCBs (Suchanek et al., 2002). The earliest lake nutrient measurements, collected from 1969 – 1972, recorded peak summer dissolved P concentrations up to 0.5 mgL^{-1}. Clear Lake has also warmed during this period; average summer surface temperatures increased by 1.39 (95% CI, ± 0.63) °C from 1970 – 2020 (**Figure A.1**) favoring cyanobacteria proliferation (Smucker et al., 2021). Monitoring of shoreline cyanobacteria and cyanotoxins is presently conducted by the Big Valley and Elem Indian Colony Environmental Protection Departments (https://bit.ly/ClearLakeCyanoProgram), which provides biweekly toxin risk assessment maps.

Cyanobacteria assemblages typically form between April and October and have been historically dominated by N-fixing cyanobacteria *Dolichospermum*, *Lyngbya*, and *Gloeotrichia* as well as the non-N fixing cyanobacteria *Microcystis, Planktothrix,* and *Pseudanabaena* (Richerson et al., 1994; Winder et al., 2010). All these genera are capable of producing cyanotoxins. Horne and Goldman (1972) determined that atmospheric fixation accounts for 40% of Clear Lake's annual nitrogen inputs. Blooms tend to first form and be most persistent in the eastern arms of the lake (OA and LA), where surface scums accumulate due to prevailing winds but can also frequently occur in natural coves within the UA (Richerson et al., 1994; Tetra Tech, 2004). The bloom season is generally defined by two peaks in biomass occurring in late spring and early fall, separated by a minimum in August (Horne, 1975). Wurtsbaugh and Horne (1983) hypothesized that the exhaustion of available iron during the midsummer, limited atmospheric nitrogen uptake, and catalyzed the die-off of N-fixing species in the late summer.

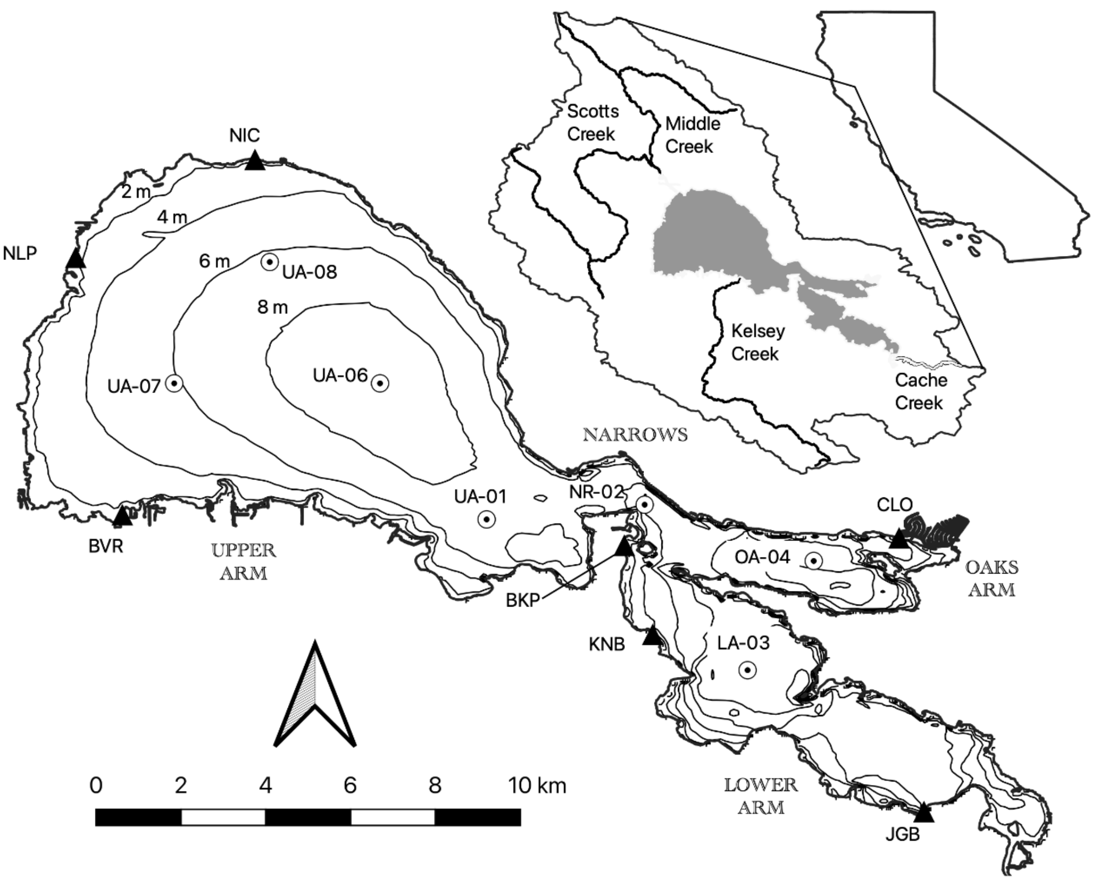

Figure 2.1. *Subsurface instrument mooring, water column and sediment core sampling sites in Clear Lake, California with 2 m bathymetry contour lines. Two-character site prefix indicates location in Upper Arm (UA), Oaks Arm (OA), Lower Arm (LA), and Narrows (NR). Location of subsurface monitoring moorings marked with white circles and locations of shoreline meteorological stations are shown by black triangles. The insert to the right of the bathymetrical map shows the location of Clear Lake watershed in California, its extent, and the location of the main creeks.*

To reduce the nutrient loads in Clear Lake, a total maximum daily load (TMDL) was established in 2006 limiting watershed inputs to a target TP load of 239.1 kg day^{-1} (548 mg m^{-2} year^{-1}; Tetra Tech 2004). In addition, a pipeline was completed in 2003 to divert wastewater discharges from the lake to nearby geothermal steam fields (Water Resources Department of Lake County 2010). While watershed restoration efforts (e.g., erosion control and wetland restoration) have been implemented to reduce external sources and attain TMDL targets, HCBs continue to regularly occur each summer and annual maximum lake TP concentrations have not declined in 17 years following the implementation of the regulation.

2.2.2 Field Data Collection

Six bottom-moored thermistor and oxygen sensor arrays were deployed in the three basins of the lake in March 2019, continuously measuring water temperature and dissolved oxygen (DO) through the water column (**Figure 2.1**). The moorings are comprised of RBR solo^{3}T thermistors (0.002 °C accuracy, 0.0002 °C resolution) spaced ~1 m apart with RBR codaT.ODO dissolved oxygen sensors (accuracy 0.26 mgL^{-1}, and resolution $<$0.03 mgL^{-1}) at a height (z) of 0.5 m above the lakebed. The deepest site in each arm (OA-04, LA-03 and UA-06) also contain RBR-DO loggers at z = 2 m and PME miniDOT dissolved oxygen sensors (accuracy 0.3 mgL^{-1}, and resolution of 0.01 mgL^{-1}) at ~4-5 m below the surface. Thermistors and RBR DO and PME DO loggers sampled at 10 second, 30 second, and 1 minute intervals respectively. A detailed description of the mooring set up can be found in **Appendix A.2** Lake Temperature and Dissolved Oxygen Data were collected using a peristaltic pump and silicon tubing lowered to 4 depths (0.5 m below the surface and z = 1, 2, and 4 m above the bottom) every ~8 weeks in winter and ~6 weeks in summer. Once collected, samples were stored in the dark on ice and transported to the laboratory for processing. Dissolved samples were filtered through a 0.45 µm filter within 24 hours of sampling to limit reabsorption of dissolved material. Samples were analyzed for a range of dissolved and particulate carbon, N and P forms, and chlorophyll using the analytical methods outlined in **Appendix A.3** Constituents Analyzed During Water Quality Monitoring.

Meteorological data were obtained from seven stations deployed along the perimeter of the lake at Nice (NIC), North Lakeport (NLP), Big Valley Rancheria, (BVR), Konocti Bay (KNB), Jago Bay (JGB), Buckingham Point (BKP), and Clearlake Oaks (CLO). Air temperature, relative humidity, incoming shortwave solar radiation, wind speed and direction were measured every 15 min with Davis Instruments Wireless Vantage Pro2 Plus® meteorological stations. At each site (except BVR), a surface water temperature sensor (Onset Water Temp Pros® with 0.2 °C accuracy, 0.02 °C resolution) was deployed ~0.5 m below the lake surface, sampling every 10 min. Hourly precipitation data were obtained from the Mt. Konocti Meteorological Station operated by the Western Regional Climate Center.

2.2.3 Cyanobacteria Dynamics

To quantify large scale variability of HCBs in Clear Lake we utilized remote sensing data collected by the Ocean Land Color Instrument on board the Copernicus Sentinel-3 satellite and post-processed by the National Oceanic and Atmospheric Association (San Francisco Estuary Institute, 2022). Satellite imagery estimates the abundance of cyanobacteria (i.e. Modified Cyanobacteria Index [CI]) by measuring the absorption of light by chlorophyll and phycocyanin, a photosynthetic pigment specific to cyanobacteria (Stumpf et al., 2009). Abundance data can be estimated for the top 1 meter of the water column with a pixel resolution of 300 m. We assessed 10-day running maximum composites of daily products to avoid data contaminated by clouds and glint. All pixels adjacent to the lake shoreline were excluded from this analysis as edge water pixels may be contaminated with spectra of adjoining land features (Iiames et al., 2021). While this remote sensing product has not formally been validated for Clear Lake's lake-specific cyanobacteria community, Lunetta (et al. 2015) demonstrated that this algorithm provided robust estimates for cyanobacteria cell counts in lakes spanning eight states in the Eastern US. We determined that this tool provided accurate quantitative information on the seasonal dynamics of cyanobacteria blooms in Clear Lake by comparing measured cyanobacteria biovolumes from surface samples with the modified *CI* from overlapping pixels collected on the same day (**Appendix A.4** Clear Lake Cyanobacteria Index). While the tool did not detect cyanobacteria below concentrations of 10^8 µm^3 L^{-1}, the modified *CI* was significantly correlated with biovolume above this threshold ($R^2 = 0.51$, $p < 0.01$, $n = 50$). We expect this correlation to improve once the remote sensing product is fully validated for Clear Lake's cyanobacteria community, as was initially conducted in Sharp et al., 2021. This data was assessed by calculating the spatially-averaged *CI* and percent coverage of blooms in each arm. To quantify the lake-wide and arm-specific severity of each summer HCB season, we calculated the bloom magnitude metric (*BM,* Mishra et al., 2019) by calculating the spatiotemporal mean *CI* from June to October each year as:

$$BM = \frac{1}{T}\sum_{t=1}^{T}\sum_{p=1}^{P} CI \tag{2.1}$$

where the indices P and T represent respectively the number of valid pixels with detectable *CI* in a basin and the number of composite time sequences in each month, respectively.

2.2.4 External Load Estimates

Annual external P loads (Jan to Dec) were quantified for the three primary tributaries (Kelsey, Middle, and Scotts Creek) using 15-minute stream gauging data collected by the California Department of Water Resources (DWR) and stream-specific linear regressions relating discharge to TP derived from routine stream monitoring data collected by the Lake County Water Resources Department from 2008-2018 (**Figure A.7**). While these streams account for 73% of the total inflow into Clear Lake (Richerson et al., 1994), gages are located several miles upstream of the lake inlet, therefore the gaged area accounts for 46% of the Clear Lakes inflows (Lake County Watershed Protection District, 2009; Tetra Tech, 2004). The cumulative nutrient load was multiplied by a factor of 2.18 to account for the ungauged portion of the watershed. P inputs from atmospheric deposition (L_{atm}) were calculated using wet (0.25 mg TP m^{-2} d^{-1}) and dry (2 mg TP m^{-2} d^{-1}) phosphorus deposition rates from Lake Tahoe (Jassby et al. 1994), located approximately 220 km east of Clear Lake. These rates are higher than the average of 38 North American sites (0.12 ± 0.11 mg TP m^{-2} d^{-1}) reported in Tipping et al. 2014. The deposition rates were the nearest available but introduce uncertainty, considering that rates can vary due to prevailing winds and sources (Boehme et al., 2011). However, given that atmospheric deposition accounted for less than 3% of the total load in all years (see section 2.3) the uncertainty introduced to P budget estimates was considered minimal. Rates were multiplied by lake surface area to calculate the daily atmospheric TP load, depending on the form of deposition determined from precipitation data. P inputs from groundwater were considered negligible as groundwater flows contributes less than <0.3% of the total inflow (Richerson et al., 1994). Wastewater effluent from the large population centers along the southern, eastern, and northern shores is collected and exported outside the watershed via a pipeline. Therefore, it was also assumed that the nutrient loads from wastewater would be minimal. P outputs to Cache Creek were calculated–from outflow discharge volume. Streamflow data were obtained from the US Geological Survey (USGS) Cache Creek Rumsey Gauge (USGS Site 11451800), located ~20 miles downstream from the Clear Lake outlet. No water quality data were collected from this stream, so outflow TP concentrations were assumed to be equivalent to LA surface concentrations.

2.2.5 Mass Balance Models of Internal Loading

We compared watershed and atmospheric TP loads against two estimates of internal P loading to determine the relative contributions of external and internal P loading to Clear Lake's P budget. The terminology of Nürnberg (2009) is used for consistency with the published literature. All internal loads are presented as areal annual loading rates (mg m^{-2} yr^{-1}) to enable comparison between sub-basins.

Method 1 – In situ Increase in Water Column Phosphorus

The net total and dissolved internal loads (L_{int_1}) were calculated as the observed increase within the water column during the dry season (May – October) of TP and SRP, respectively, with equation (2.2.

$$L_{int\_1} = \frac{\left(P_{t_2} \times V_{t_2}\right)}{A_{o_2}} - \frac{\left(P_{t_1} \times V_{t_1}\right)}{A_{o_1}} \tag{2.2}$$

Here t_1 and t_2 are the dates of the annual minimum and maximum water column TP and SRP concentrations respectively, P_t is the corresponding depth-averaged P concentration through the entire water column, V_t is basin volume (m^3) and A_o is basin surface area (km^2). Hydro-acoustic survey data (ReMetrix, 2003) was used in conjunction with the USGS Clear Lake level gauge at Lakeport (USGS Site 11450000) to determine basin surface areas and volumes at a daily timestep. Lake-wide loading rates were calculated from a surface area weighted average of the three arms. L_{int_1} yields a net estimate, integrating both inputs and losses to sedimentation and biotic uptake. While external loading was excluded in this method, most of Clear Lake's tributaries are seasonal, diminishing to a trickle during the dry season, and are not expected to impact loading estimates.

Method 2 – Modeled SRP Flux from Anoxic Sediments

Modeled estimates of gross internal P loading released from anoxic lake sediments (L_{int_2}) were quantified as the product of 2 component terms: days of active anoxic sediments (AA) presented in units of days per year that an entire basin's surface area is actively releasing P, and areal sediment P release rate (RR), (equation(2.3, Nürnberg 2009).

$$L_{int\_2} = AA \times RR \tag{2.3}$$

AA was directly estimated as the number of days that deepest near-sediment DO logger in the water of each arm recorded hypoxic conditions (AA_{obs}). When the hypolimnion is hypoxic, underlying sediments can become completely anoxic and release P into the water column (Eimers and Winter 2005; Nürnberg et al. 2013) as microbial mediated sediment anoxia does not require anoxia in the overlying water column (Holdren & Armstrong, 1980). Since the specific hypolimnetic DO threshold for which underlying sediment will become anoxic is not well defined, we calibrated the hypoxic threshold indicating elevated P release by comparing observed DO measurements against AA_{mod}, modeled from a log-linear regression previously applied to quantify hypoxia in polymictic systems, (equation 2.4, Nürnberg 1996).

$$AA_{mod} = -36.2 + 50.1\log(TP_{Jun\text{-}Oct}) + 0.762\frac{Z_{mean}}{Ao^{\ 0.5}} \tag{2.4}$$

Here, TP_{Jun_Oct} is the June to October volume-averaged TP concentration for each lake basin and $Z_{mean}/A_o^{0.5}$ is the basin morphometric factor with Z_{mean} in units of m and A_o in km^2. A hypoxic threshold of 3.5 mgL^{-1} was selected to calculated AA_{obs}, as this level minimized the error between modeled and observed hypoxic days (RMSE = 10.9 days). While this threshold for redox-dependent P flux is higher than employed in many internal P loading studies, elevated deep water TP concentrations have been observed at this DO concentration in comparable eutrophic polymictic systems (e.g., Lake Simcoe, Eimers and Winter 2005; Nürnberg et al. 2013).

Empirically Derived Sediment P Flux Rates

Arm-specific sediment SRP flux rates (RR_{core}) were quantified via incubations of quadruplicate sediment cores collected from all monitoring sites in November 2019.

Samples were collected with a large-bore gravity corer from Aquatic Research Instruments fitted with 0.5 m long, 9.5 cm diameter polycarbonate cores tubes and stored on ice during transport. Each core contained 15-25 cm of sediment and 25-35 cm of overlying water. To standardize within-site initial conditions, overlying water for each core set was siphoned off, filtered through a 0.45 µm membrane, and homogenized within a large carboy before being pumped back. Two duplicate cores were incubated under anoxic conditions, maintained by bubbling with nitrogen gas balanced with 350 ppm CO_2 for pH buffering (Moore et al., 1998; Ogdahl et al., 2014), and the remaining two were incubated under oxic conditions by bubbling with air. All incubations were maintained at a constant temperature of 15 °C and sampled approximately every three days for a 30-day period. Loading rates were calculated at an hourly timestep by applying either oxic or anoxic release rates to the entire surface area of each arm based on observed hypolimnion DO concentrations. To account for the temperature dependence of reaction rates, fluxes were modified by Van't Hoff's Q_{10} rule of 3 (i.e., a 10 °C temperature increase, corresponds to a tripling of the P flux rate, equation 2.5). This Q_{10} coefficient has been widely used to model temperature effects of diffusive P fluxes (Liikanen et al. 2002; Nürnberg 2009).

$$RR_{Temp} = RR_{core} \times Q_{10}^{(ti-15)/10} \tag{2.5}$$

Here RR_{Temp} is the average hourly P flux rate based on the deviation of observed sub-basin hypolimnetic temperature from incubation temperature (t_i -15) and $Q_{10} = 3$.

Experimentally determined RR values were compared against 2 other modeled RR estimates derived from water column and sediment TP concentrations. In a study of anoxic incubated sediment cores from 17 reservoirs across the US central plains, Carter and Dzialowski (2012) found that RR values were significantly correlated with trophic status and TP concentration in the water column and developed a log linear model to predict RR from summer TP concentrations (equation 2.6, R^2=0.37, p = 0.009, n = 17)

$$\log(RR_{TP}) = -0.540 + 0.827\log(TP_{Jun\text{-}Oct}) \tag{2.6}$$

Here $TP_{Jun\text{-}Oct}$ is the depth-averaged TP concentration in the photic zone. Unlike the original study, we chose to use the average TP concentration throughout the water column since intermittent mixing facilitates consistent vertical nutrient transport in Clear Lake throughout the summer. RR values are also correlated to sediment P composition (Nürnberg, 1988) and can be estimated via a regression with sediment TP concentration (equation 2.7, R^2=0.21, p <0.001, n = 63).

$$\mathrm{Log}(RR_{sed}) = 0.8 + 0.76\log(TP_{sed}) \tag{2.7}$$

Here TP_{sed} is the average concentration of TP in the upper 5 cm of lake sediment in mg g^{-1} of dry weight. Sediment TP concentrations were measured from oxic incubation cores following the November 2019 incubation.

2.2.6 Stratification Metrics

The timing of stratification events was determined based on the mean hour Brunt–Väisälä buoyancy frequency in the water column ($\overline{N}$ $[s^{-1}]$). We assumed Clear Lake was thermally stratified when $\overline{N} > 0.015$ s^{-1}, a threshold previously determined by Cortés et al. 2021.

2.2.7 Statistical Analyses

Ordinary least squares regression analyses between explanatory environmental factors (nutrient concentrations, daily average surface water temperature, and 3-day trailing average wind speed / DO) with cyanobacteria biovolume were performed in MATLAB to determine which set of parameters predicted the greatest variation in cyanobacteria intensity. A Box Cox transformation (*boxcox* MATLAB® function) was applied to each dataset to ensure normal distribution. Spearman Rank correlations were initially calculated to assess the strength and direction of the association between each predictor variable and cyanobacteria response. A minimum redundancy maximum relevance (MRMR) algorithm (*fsmrmr* MATLAB® function) was then applied to rank the importance of each predictor and determine the appropriate number of predictor variables to include in a regression. MRMR is a two-stage feature selection algorithm that finds the optimal set of predictors that are mutually and maximally dissimilar and can represent the response variable effectively (Peng et al., 2005). The algorithm first calculates the relevance of each predictor, based on the mutual information metric, and then calculates the redundancy between each predictor pair. Predictors are then ranked by subtracting redundancy from relevance. The optimal multiple linear regression model was then selected based on the adjusted R^2 and the Bayesian information criteria (BIC).

To assess the strength of long term and seasonal trends in HCB intensity, the time series of spatial averaged CI for each basin and the entire lake was decomposed (*trenddcomp* MATLAB function) into additive long-term trend (LT), seasonal trend (ST) and residual I components such that the observed $CI = LT + ST + R$. The strength of the long-term trend (F_T) and seasonality (F_s) between 0 and was evaluated via equation 2.8 and 2.9, Wang et al. 2006.

$$F_T = \max(0,1\text{-}\frac{\mathrm{Var}(R)}{\mathrm{Var}(LT{+}R)}) \tag{2.8}$$

$$F_S = \max(0,1\text{-}\frac{\mathrm{Var}(R)}{\mathrm{Var}(ST{+}R)}) \tag{2.9}$$

2.3 Results

2.3.1 Spatial and Temporal Variability of Stratification and Hypoxia

Thermistor chains recorded multiple intermittent cycles of thermal stratification and mixing from March to November each year with stratification periods ranging from daily to monthly timescales (**Figure A.3-Figure A.5**), surface temperatures ranging from 22-29 °C and vertical temperature differences exceeding 6 °C during the summertime.

Within a week of stratification onset, hypolimnetic DO concentrations rapidly declined to anoxic levels due to high oxygen demand in the hypolimnion but the timing and duration of these events differed in each of the three summers (**Table 2.2**). The lake was more consistently anoxic during May and June 2019 (31% of the time) than in 2020 (5%) or 2021 (12%). In contrast, the lake was less anoxic in July and August 2019 (37%) than in 2020 (45%) or in 2021 (73%). Similarly, anoxia rarely occurred in September and October 2019 (1%) but was more frequently observed in 2020 (15%) and 2021 (10%). Although the earliest anoxic period was observed in April 2019, the cumulative duration of anoxia and hypoxia increased across all arms each subsequent year of the study (**Figure 2.2**).

Table 2.2. *Annual totals of observed hypoxic days in the hypolimnion of each arm at three DO thresholds and the modeled active sediment area factor (equation 2.4, AA_{mod}).*

		2019	**2020**	**2021**
UA (Average)	HDO <= 1 mgL^{-1}	28	39	49
	HDO <= 2 mgL^{-1}	61	56	61
	HDO <= 3.5 mgL^{-1}	88	93	88
	AA_{mod}	84	93	101
OA-04	HDO <= 1 mgL^{-1}	25	37	41
	HDO <= 2 mgL^{-1}	39	52	56
	HDO <= 3.5 mgL^{-1}	73	77	91
	AA_{mod}	78	88	95
LA-03	HDO <= 1 mgL^{-1}	23	24	37
	HDO <= 2 mgL^{-1}	35	36	50
	HDO <= 3.5 mgL^{-1}	59	71	82
	AA_{mod}	82	92	99

In 2020 and 2021, the lake remained continuously thermally stratified throughout much of the mid-summer resulting in multi-week hypoxic periods in all 3 arms in July and August.

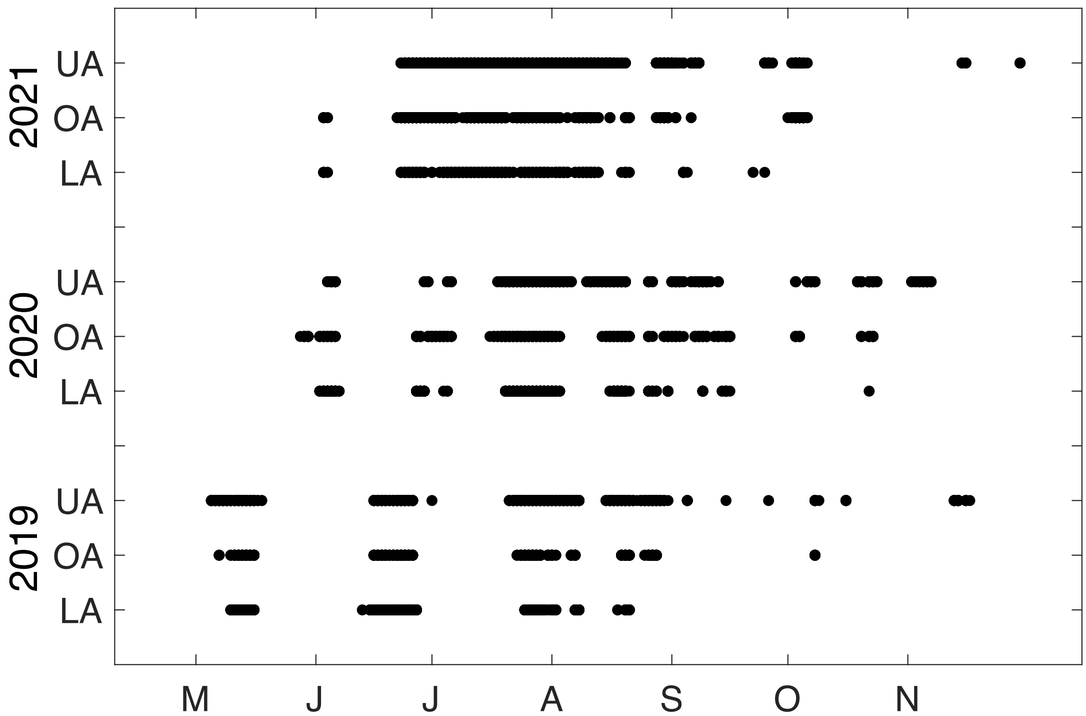

Figure 2.2. *Timing of hypolimnetic anoxia across Clear Lake sub-basins. Black dots indicate periods when hourly DO < 1mgL^{-1}.*

Clear Lake's spatially variable wind field drove interbasin variability in the duration of summertime stratification and hypoxia. Winds blow predominantly along a northwesterly axis and the orographic effect of Mount Konocti focuses winds through the Oaks and Lower Arms, resulting in more intense winds in the eastern side of the lake relative to the west (Rueda, 2001). As a result, the UA experienced longer periods of stratification and hypoxia than the other two arms, despite its comparatively shallow depth. A frequency distribution of summertime wind speeds highlights the interbasin variability in wind forcing (**Figure A.9**). In the UA, summer winds averaged between 0.81

and 0.98 ms^{-1} and rarely exceeded 5 ms^{-1}, while winds in the two eastern arms averaged between 1.30 and 3.02 ms^{-1}, with gusts up to 10 ms^{-1}. These stronger winds provided more mechanical energy to surface of the eastern two arms, frequently eroding the thermocline of these arms days before the UA mixed. For example, at the end of stratification periods in August 2020 and 2021, $\overline{N}$ in the UA remained above the 0.015 s^{-1} stratification threshold for 3 and 5 days longer respectively than in the other two arms (***Figure** 2.3*).

2.3.2 Seasonal Nutrient Variability

Lake-wide TP concentrations followed a consistent seasonal pattern in all 3 arms with annual minimums observed each spring (< 0.05 mgL^{-1}), increasing throughout the summer, and peaking in early fall (**Figure 2.4**). The annual peak concentrations were observed simultaneously in all three arms, with the highest concentrations occurring in the UA (0.5 – 0.8 mgL^{-1}) during September 2019 as well as in October 2020 and 2021. The maximum concentrations in the deeper OA and LA sites were comparatively lower, ranging from 0.3 to 0.7 mgL^{-1}. The summer TP increase was primarily comprised of SRP, which accounted for 75-95% of TP in the water column from July to October. Elevated TP and SRP concentrations in the hypolimnion in early summer preceded increases in the epilimnion in early fall. Average TN concentrations followed a similar seasonal pattern with annual minimums in the spring (~0.35 mgL^{-1}), increasing throughout the summer and reaching a peak in the fall/winter (0.5 – 1.1 mgL^{-1}). NH_4,

Figure 2.3. *a) Spatially-averaged, 7-day moving average of the trailing 10-day maximum modified cyanobacteria index Upper (dark grey), Oaks (light grey) and Lower (black) arms. B) Percent coverage of cyanobacteria of arm surface area. C) DO measured at 0.5m above sediment water interface at deepest point in each arm. Dashed line indicated 3.5 mgL^{-1} hypoxia threshold d) Average buoyancy frequency in the water column. Dotted line indicates threshold for stratification at $\overline{N}$ = 0.015 s^{-1} (2019 – 2021).*

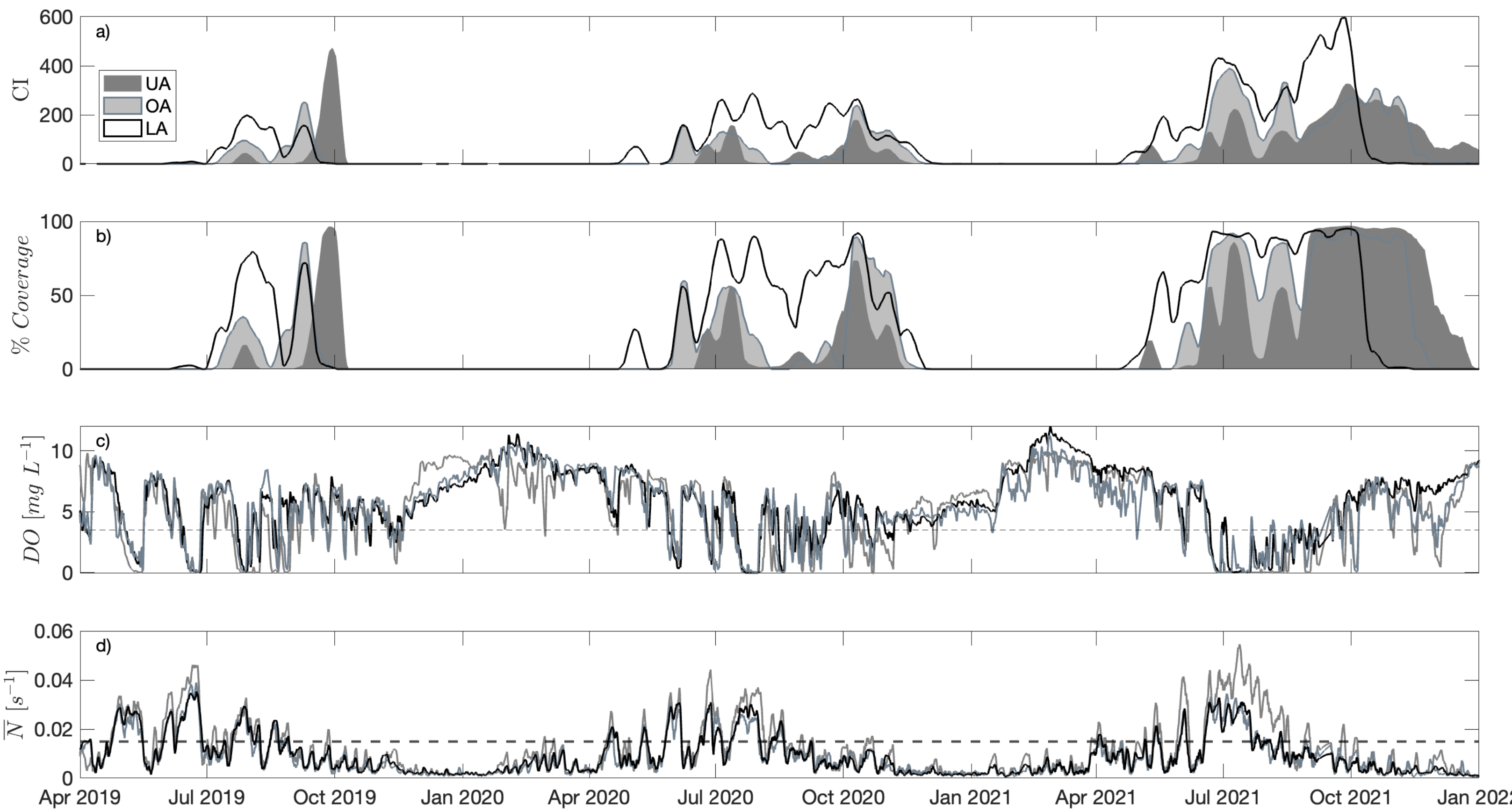

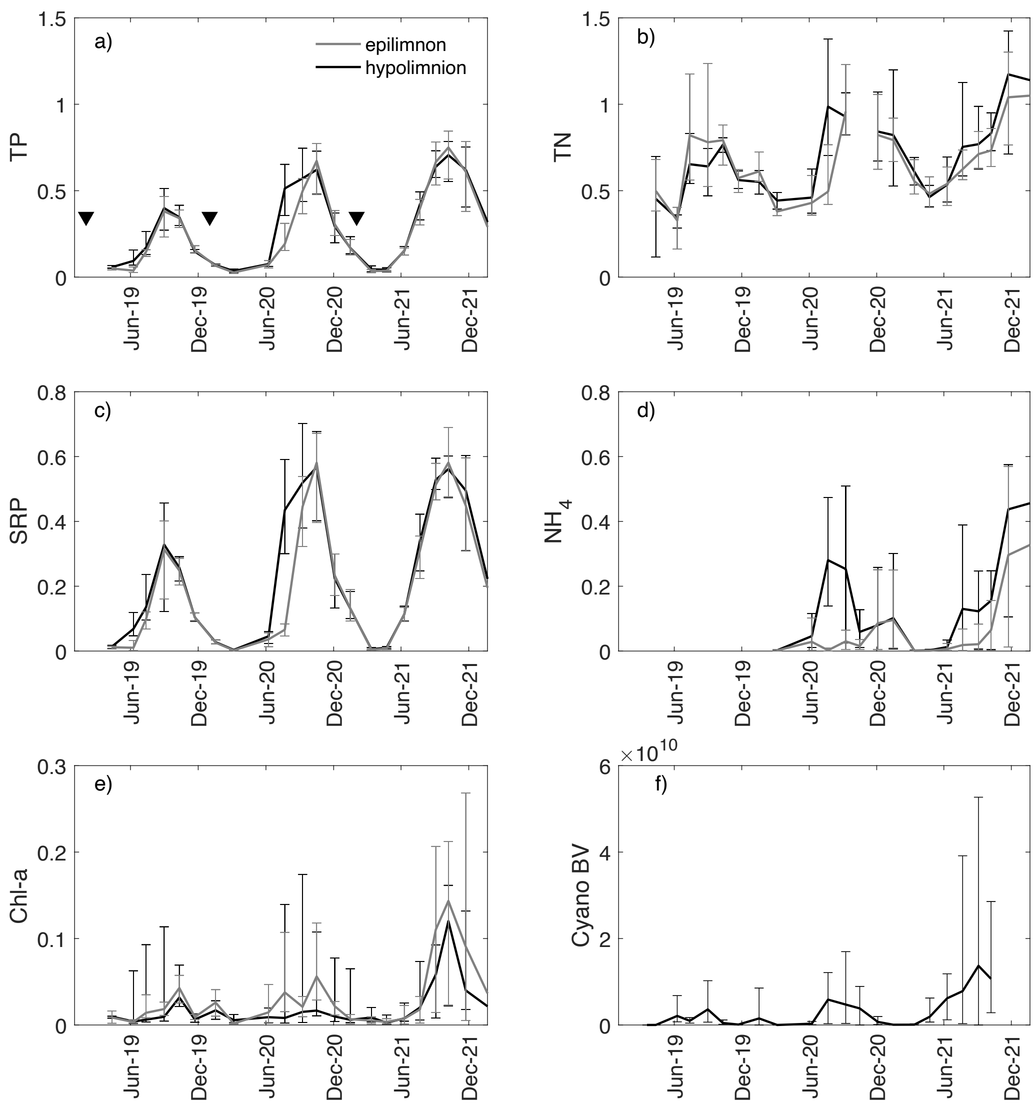

Figure 2.4. *Mass of a) total phosphorus, b) total nitrogen, c) soluble reactive phosphorus, d) ammonium, e) chlorophyll-a in the epilimnion (grey) and hypolimnion (black) averaged across all monitoring sites [mgL^{-1}]; f) Biovolume of cyanobacteria in surface samples [µm^3 L^{-1}]. Black arrows indicating timing of maximum external loading input. Error bars indicate the range of values measured across all sites.*

Measured from March 2020 onwards, was higher in the summer and fall (0.125 mgL^{-1}) than in winter and spring (~0.002 mgL^{-1}) with the highest concentrations observed in the LA and the OA. Like SRP, NH_4 concentrations increased sharply near the lakebed during the summer, indicating internal N release. In contrast, NO_2-NO_3 concentrations were higher in the fall and winter (0.08 – 0.14 mgL^{-1}) and lower (0.001 mgL^{-1}) during spring and summer, suggesting that algal uptake and denitrification was occurring during stratification. The seasonality of NH_4 and NO_2-NO_3 accounts for the variability in TN. In addition, external loading of N following winter storms likely contributed to higher wintertime TN concentrations.

2.3.3 External Loads

Total external areal TP loads from the watershed to Clear Lake during 2019, 2020 and 2021 were 72, 40, and 80 mg TP m^{-2} respectively, while areal TP loads from atmospheric deposition (L_{atm}) were 78, 84, 80 mg TP m^{-2} in each respective year (**Table 2.3**). The interannual variation in L_{ext} resulted from the extreme variability in the region's precipitation, with 2019 being a wetter-than-average year, while 2020 and 2021 were two of the driest years on record (**Figure 2.5**a). External TP inputs from tributaries are primarily conveyed to UA (>90% of watershed inflows) and varied seasonally. External loads were greatest during the winter (October to March), declined throughout the spring and reached near zero during the summer.

Table 2.3. *Comparison of external watershed (L_{ext}) and internal loading estimates for Clear Lake and sub-basins (2019 – 2021). All load estimates are presented as areal rates in mg TP m $^{-2}$ year $^{-1}$. Clear Lake nutrient TMDL is shown in right column for comparison.*

Year	L_{ext}	L_{atm}	**Basin**	L_{int_1} **TP**	L_{int_1} **SRP**	$L_{int\_2\_Core}$ RR_{temp}	$L_{int\_2\_TP}$ RR_{TP}	**TMDL**
2019	721	78	UA	2,830	2,690	1,770	2,900	548
			OA	2,550	2,400	2,950	1,810	
			LA	1,960	1,590	2,020	1,350	
			Clear Lake	2,630	2,440	1,960	2,500	
2020	40	84	UA	3,840	3,840	2,300	4,510	
			OA	4,120	3,860	4,640	2,780	
			LA	3,540	3,320	3,350	2,270	
			Clear Lake	3,800	3,740	2,810	3,910	
2021	80	80	UA	3,790	3,110	2,290	4,780	
			OA	4,680	4,140	5,440	4,060	
			LA	3,730	3,510	4,820	3,240	
			Clear Lake	3,860	3,280	3,240	4,400	

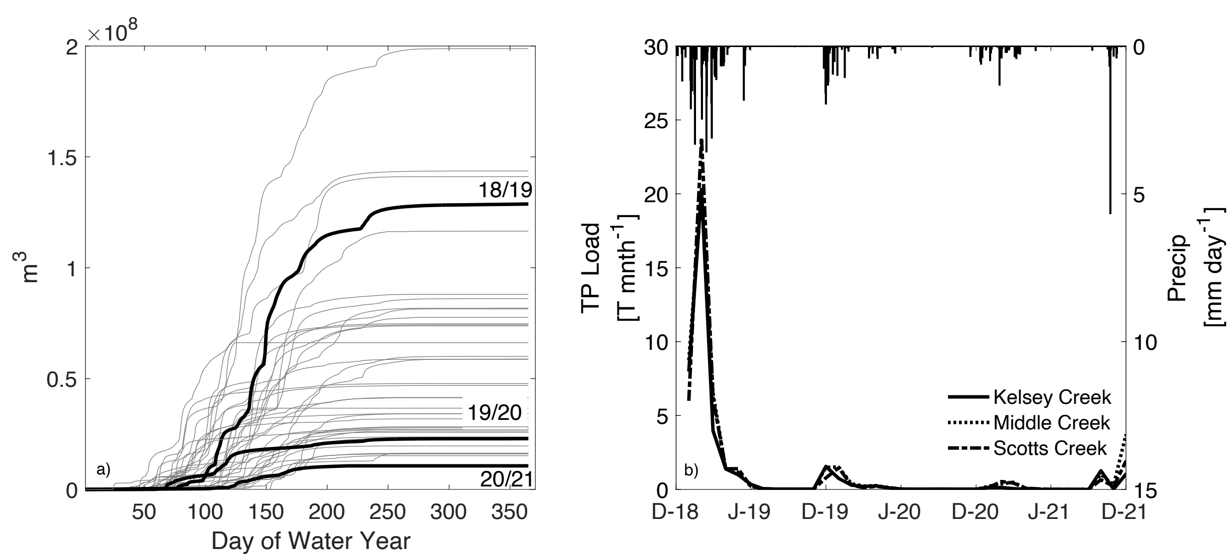

Figure 2.5. *a) Water year (i.e., Oct 1 – Sept 31) cumulative discharge from Middle Creek from 1980 – 2022. Water years from Oct 2018 to Sept 2022 are shown in bold. B) Monthly TP load estimates from gauged Clear Lake tributaries and precipitation data measured.*

2.3.4 Internal Loads

2.3.4.1 In situ increase in water column phosphorus (***L_{int_1}***)

Net lake-wide, annual, internal TP loading estimates derived from water column measurements were 2,630, 3,800, and 3,860 mg TP m^{-2} in 2019, 2020, and 2021 respectively, with more than 40% variation in loading rates observed between arms (**Table 2.3**). L_{int_1} estimates for SRP fluxes were similar in magnitude with rates of 2,440, 3,740 and 3,280 mg SRP m^{-2} during each respective summer. The timings of the TP and SRP internal loads were consistent with one another. The lowest areal loading rates consistently occurred in the LA while the highest rates were observed in the UA in 2019 and in the OA in 2020 and 2021. Despite lower observed TP concentrations in the OA, its surface area is 88% smaller than the UA, resulting in comparative areal release rates between the 2 arms.

2.3.4.2 Modeled P Flux from Anoxic Sediments (***L_{int_2}***)

Mean estimates for basin-specific anoxic sediment SRP release rates in incubations ranged from 10.5 – 24.6 mg SRP m^{-2} d^{-1} while oxic release rates were an order of magnitude smaller, ranging from 0.17 – 0.6 mg SRP m^{-2} d^{-1} (**Table 2.4**). Release rates from UA ranged from 8.8 ± 0.09 (UA-08) to 11.6 ± 0.94 mg m^{-2} d^{-1} (UA-01) and were more than 50% lower than those observed in the Narrows (26.7 ± 3.86 mg m^{-2} d^{-1}), the OA (24.9 ± 0.86 mg m^{-2} d^{-1}), or in the LA (21.4 ± 1.61 mg m^{-2} d^{-1}). RR rates calculated from sediment

TP concentrations (RR_{sed}) were significantly lower than observed in lab incubations and ranged from 6.1 – 7.9 mg m^{-2} d^{-1}, while fluxes modeled from lake summertime TP concentrations (i.e., RR_{TP}) ranged from 22.9 – 30.9 mg TP m^{-2} d^{-1} in 2019, 34.1 – 45.0 mg TP m^{-2} d^{-1} in 2020, and 39.5 – 54.4 mg TP m^{-2} d^{-1} in 2021 across arms. RR_{TP} estimates in 2019 were consistent with RR_{core} estimates for the OA and the LA but predicted a substantially larger RR in the UA than was experimentally determined.

Table 2.4. *Comparison of estimated sediment P release rates [mg TP m^{-2} day^{-1}]. RR_{core} is average SRP diffusive flux measured in duplicate oxic and anoxic sediment cores. RR_{sed} is TP release rate modeled from linear regression with TP concentration in upper 5 cm sediment of duplicate oxic cores. RR_{TP} is the TP release rate modeled from linear regression with average summer TP concentration through water column for each study year.*

Method	UA (mean)	OA	LA
Oxic RR_{core}	0.17	0.55	0.61
Anoxic RR_{core}	10.5	24.6	21.4
RR_{sed}	6.1	6.1	7.9
RR_{TP_2019}	30.9	25.7	22.9
RR_{TP_2020}	45.0	38.1	34.1
RR_{TP_2021}	54.4	44.6	39.5

The lake-wide gross internal SRP loads estimated from the incubation release rates ($L_{int\_2\_core}$) were 1,960, 2,810, and 3,240 mg SRP m^{-2} yr^{-1} in 2019, 2020, and 2021 respectively. Modeled internal TP load estimates utilizing RR_{TP} ($L_{int\_2\_TP}$) were 28-36% larger than predicted by core incubations: 2,500, and 3,910 and 4,400 mg TP m^{-2} yr^{-1} in

2019, 2020, and 2021 respectively. Greater loading rates predicted from RR_{TP} were due to higher predicted sediment flux rates in the UA.

2.3.5 Cyanobacteria Temporal and Spatial Variability

Satellite imagery recorded two peaks in cyanobacteria biomass in Clear Lake each summer though there was significant interannual variability in the timing and intensity of the HCB season (***Figure** 2.3*, **Figure A.6**) The bloom magnitude metric indicated that the HCB was increasingly intense each summer, with the bloom magnitude, BM = 8,115, 16,848, and 37,572 in 2019, 2020, and 2021, respectively. Time series decomposition of the CI time series further demonstrated that there was a strong long-term increasing trend in the HCB intensity across all three arms (F_T = 0.56, 0.58, 0.60 in UA, OA ,and LA respectively, **Figure A.11**). In 2019, the spatial extent of the bloom was relatively small, with large patches only detected from July through early October in each arm and peak cyanobacteria biovolumes detected in samples collected in late August. An early summer bloom began forming in the LA on July 4, 2019, following a 12-day stratified period and subsequent mixing event on June 26. The LA bloom increased in size from July 18-31 while the lake remained thermally stratified, reaching a maximum extent of 80% of the arm's surface area on July 31 before declining through mid-August following a mixing event on August 1, indicated by a decreasing $\overline{N}$ and a sudden increase in bottom DO. A subsequent fall bloom began forming in the OA and the LA on August 22, shifting to the

UA two weeks later on September 10. The fall bloom continued to grow, reaching a spatial coverage 97% of the UA's surface in late September while water temperatures declined, and the lake became increasingly well-mixed. The fall bloom rapidly declined from its peak on September 28, covering less than 2% of the UA surface by Oct 8.

In 2020, blooms began to form in the LA and the OA on May 30 during a stratification period that lasted from May 26 – June 5. This bloom, only observed in the two smaller arms, reached a peak on June 4 (~50% coverage) and began to decrease in size following a mixing event on June 6. Blooms were detected in all three arms on June 18, growing in extent until July 15 before declining to near levels in the OA and the UA by August 8 and in the LA by August 26. Unlike the previous summer, this decline occurred while they lake was stably stratified from July 17 to August 1. From August 26 to October 5 blooms began to proliferate in all three arms covering ~85% of the lake by early October. As in 2019, the blooms continued to grow through the early fall despite decreasing lake stability. The 2020 fall bloom declined slowly from its peak, continuing to cover at least 50% of the OA and the LA through early November. Peak cyanobacteria biovolumes for the 2020 season were observed in late July samples in the UA and in September in the OA and the LA.

The 2021 bloom season was the most severe observed during the monitoring period. Blooms in the LA started to form in late April prior to the onset of stratification. From

June 13 – July 29, blooms began to grow in extent across all 3 arms, covering nearly 90% of each arm at its peak while the lake remained predominantly stratified and hypolimnetic DO concentrations were consistently <1 mgL^{-1}. This early summer bloom decreased in intensity in all 3 arms from July 13 – 29 but continue to cover more than 60% of the LA. Blooms began to rebound in all 3 arms on August 1 and increased in coverage throughout August until ~92% of the lake was covered on August 31. This late summer bloom continued covering the majority of the lake until October 8 when the bloom disappeared from the LA, followed by a declined in the OA a month later on November 11. A bloom continued to wain in the UA but persisted until January 2022. The highest cyanobacteria biovolumes detected in summer 2021 were observed in the LA on July 22, in the OA on September 3 and in the UA on October 7. Despite interannual variation in intensity, the blooms followed an analogous bimodal seasonal evolution with peaks in bloom coverage in early summer and fall separated by a mid-summer minimum. The seasonal component of the *CI* time series showed the strongest seasonal trend in the LA (F_S= 0.53) while the strength of the seasonal trend in the OA (F_S= 0.38) and UA (F_S= 0.28) was weaker (**Figure A.11**). The early summer peak was most prevalent in the LA while the fall peak was primarily observed in the UA.

Spatial and temporal variation in cyanobacteria community composition highlights the complexity of Clear Lake's phytoplankton ecology (**Figure 2.6**). During each summer,

Figure 2.6. *a-c) Total and d-f) proportional biovolume for major phytoplankton groups and g-i) proportional biovolume of major cyanobacteria genera across sub-basins from April to October (2019 – 2021). Asterix indicate N-fixing species.*

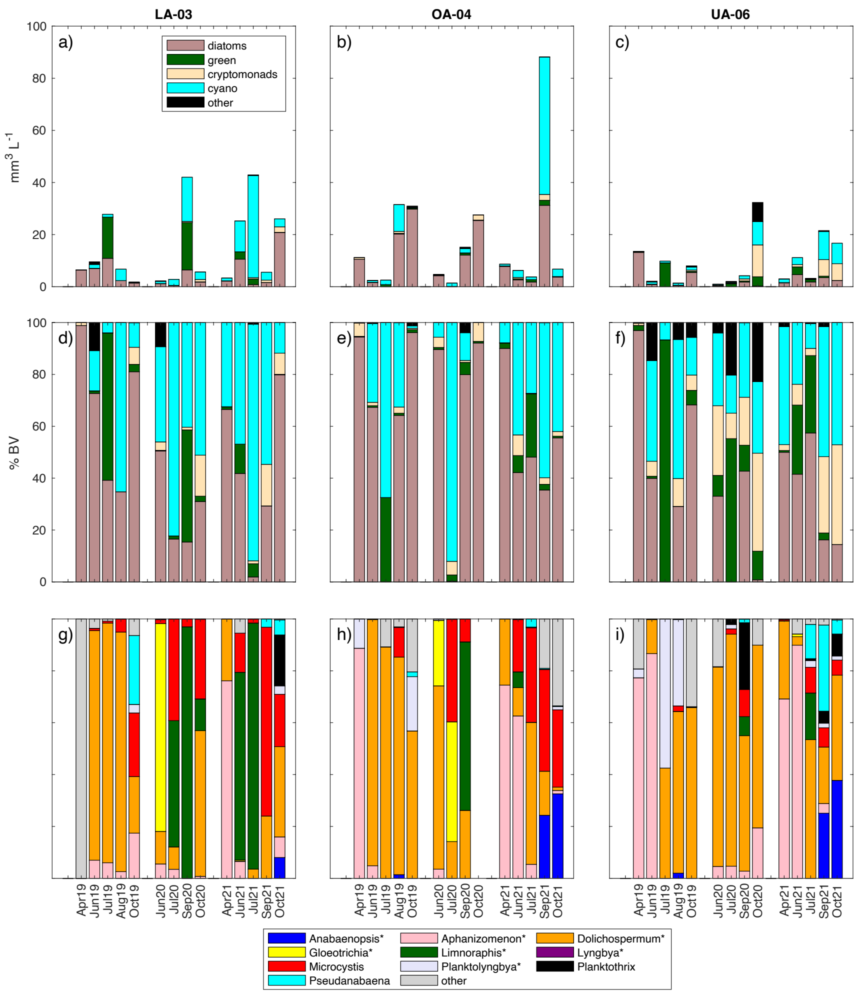

The early season peak was dominated by N-fixing cyanobacteria, while the fall peak contained both N-fixing and non N-fixing genera. In summer 2019, *Aphanizomenon* and *Dolichospermum* dominated from June to August, comprising 22-92% of the total cyanobacteria biovolume. In comparison, in 2020, the early summer peak was dominated by *Gloetrichia* and *Dolichospermum*, while *Aphanizomenon*, *Limnopharis*, and *Dolichospermum* dominated in June and July of 2021. In contrast, non N-fixing

Microcystis and *Pseudanabaena* were observed September and October. *Microcystis* was predominantly observed in the LA, the OA and the Narrows. Unlike other genera, *Microcystis* cannot fix nitrogen and must utilize in-lake sources of N. Since bioavailable nitrate and nitrite concentrations are very low in the summer due to denitrification and algal uptake, this genus tends to form where there is available NH_4, such as the OA and the LA. The interbasin variability in cyanobacteria ecosystem composition highlights the spatial heterogeneity of cyanobacteria blooms across Clear Lake's three arms.

2.3.6 Drivers of Cyanobacterial Blooms

Table 2.5 details the spearman rank correlations between environmental predictor variables and cyanobacteria biovolume for 116 samples collected throughout the entire year from 2019 to 2021. Significant and positive correlations were observed between surface temperature ($\rho = 0.53$, $p < 0.001$), TP ($\rho = 0.52$, $p < 0.001$), and TN ($\rho = 0.48$, $p < 0.001$) while TN:TP was negatively correlated ($\rho = -0.40$, $p < 0.001$). No significant correlations were observed between DO, Chla, or wind speed with biovolume. The rank of each predictor variable, based on the MRMR algorithm, indicated that TN:TP and water temperature were the two most important predictors (**Figure 2.7**), followed by DO, TP and TN. The drop in importance score between each term represents the confidence of feature selection. While there was a large decrease in the importance score after the first two terms, the decrease in score for subsequent predictors was relatively small, implying that the difference in predictor importance for these latter terms was not significant. A linear model incorporating both TN:TP and water temp explained 43% of the variance in cyanobacteria biovolume (**Table 2.6**). Adding an additional DO term improved the adjusted R^2 of the model to 0.45, however BIC of the three-parameter model also increased, indicating that a multiple linear regression using only TN:TP and water temperature is preferred as it provides a simpler and more parsimonious explanation of the data.

Table 2.5. *Spearman rank correlation coefficients for biovolumes of total cyanobacteria and selected cyanobacteria genera with environmental parameters measured in water column from all samples collected from 2019 – 2021 (n = 116). Correlations with p < 0.001 are bolded.*

	Chla	**TP**	**TN**	**TNTP**	**Temp**	**DO**	**WS**
cyano	0.25	**0.52**	**0.48**	**-0.40**	**0.53**	-0.22	0.26
micro	0.24	**0.38**	0.27	**-0.30**	0.21	-0.01	-0.07
anab	0.04	0.06	0.02	-0.07	0.14	0.06	0.15
lyng	-0.10	0.07	0.02	-0.09	0.10	**-0.37**	0.09
doli	**0.30**	**0.51**	0.27	**-0.48**	**0.79**	-0.28	0.29
gloeo	0.03	0.03	0.06	0.01	0.25	-0.19	0.27

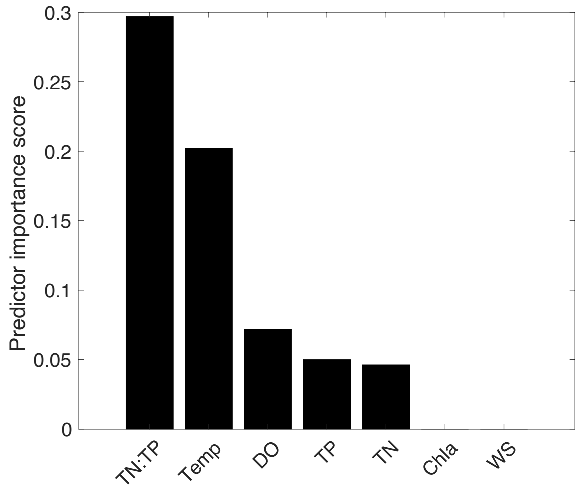

Figure 2.7. *Predictor rank calculated from MRMR algorithm.*

Table 2.6. *Comparison of multiple linear regression models for predicting cyanobacteria biovolume.*

Model	**R^2**	**Adj R^2**	***p***	**BIC**
$\log(cyano\ bv) = 252.8 - 39.4 \log(TNTP)$	0.26	0.25	<0.001	1258
$\log(cyano\ bv) = -89.4 + 96.0 \log(Temp) - 16.1 \log(TNTP)$	0.46	0.43	<0.001	1226
$\log(cyano\ bv) = -82.4 + 94.9 \log(Temp) - 14.9 \log(TNTP) - 3.76 \log(DO)$	0.46	0.45	<0.001	1231

2.4 Discussion

Clear Lake's morphometry (i.e., its shallow depth and large surface area to volume ratio), warm in-lake summer temperatures, and high rates of primary production make the system conducive to internal P loading. In this study we hypothesized that (1) diffusive P fluxes from anoxic sediments was the primary source of phosphorus loading to Clear Lake, (2) internal P loading created an N-limiting environment during the summer promoting blooms of nitrogen-fixing cyanobacteria and (3) annual variation in the timing and duration of hypoxia regulated the magnitude of the summer HCB season. During the three-year monitoring period we observed large increases in lake TP each summer which were an order of magnitude larger than watershed P inputs from preceding winters with internal sources accounting for 70%, 97% and 96% of the total TP load in 2019, 2020, and 2021 respectively (**Table 2.7**). Moreover, the largest increases in the water column TP occurred in the late summer and early fall each year, when external loading from tributaries was lowest, further supporting hypothesis (1). Nutrient measurements corroborated hypothesis (2), indicating that increased summertime TP lowered the N:P ratio below the 16:1 Redfield ratio, shifting the nutrient limitation from P to N (**Figure 2.8**). While the largest wintertime external TP loading occurred prior to summer 2019, the highest peak in-lake TP concentrations were observed in 2021, resulting in the most severe HCB season recorded since 2004 (**Figure 2.9**). Through our high-frequency measurements of temperature and oxygen we demonstrated the validity of hypothesis (3)

Table 2.7. *Internal and external TP load estimates (metric tons) for January to December (2019 – 2021). Internal load estimates are based on the observed increase in water column TP (L_{int_1}). Internal load estimates calculated from experimentally-determined releases rates are shown in parentheses. External load is sum of both watershed and atmospheric contributions.*

Year	Internal TP Load	External TP Load	Internal Load Contribution (% total)
2019	412 (306)	130	70 (59)
2020	605 (432)	22	96 (95)
2021	597 (492)	27	97(95)

attributing the high concentrations of TP observed in 2021 to warmer air temperatures, prolonged periods of stratification and resultant hypolimnetic hypoxia that persisted throughout the summer. The following sections will provide further supporting evidence for each of these hypotheses. While many eutrophic lakes, that experience regular HCBs, have high internal P loading rates due to oxygen depletion at the sediment-water interface (SWI) and high rates of organic matter production (Søndergaard et al., 2001; Spears et al., 2012), it is rare for it to dominate P cycling to such a large extent.

2.4.1 Contribution of External and Internal Loading

While TP loads from the watershed were greatest during the wet winter season, the highest water column TP concentrations were observed during each summer and fall demonstrating the prevalence of internal P loading in the system. In summer 2019 and 2020, TP increased in the hypolimnion faster than in the epilimnion further indicating that the sediments acted as major internal source of TP. By subtracting external load contributions from the observed increase in water column TP during the dry season (i.e., L_{int_1}) we determined that internal sources accounted for more than 70% of the TP in the lake each summer (**Table 2.7**). While atmospheric load estimates varied interannually by less than 10%, watershed loads were significantly less in 2020 and 2021 due to lower-than-average stream inputs as a result of a prolonged drought resulting in a higher relative contribution of internal loading to the overall P budget. The overwhelming influence of internal loadings on P cycling in Clear Lake suggests that focusing on managing in-lake internal P sources (e.g., dredging, hypolimnetic oxygenation, alum application) is more likely to result in improved water quality than focusing on non-point source pollution from the watershed (De Palma-Dow et al., 2022).

2.4.2 Contribution of Internal P Loading to Seasonal N limitation

While many freshwater systems have been historically viewed as P-limited environments, the release of P from sediments in eutrophic systems can increase phosphorus availability in the water column, thereby reducing N:P ratios and shifting the system towards N-limitation (Ding et al., 2018; Wu et al., 2020). As a result of the large mass of P released from sediment pools during hypoxic periods, Clear Lake experienced N-limitation at least 8 months each year with TN:TP molar ratios remaining consistently $<$25 from June through January (**Figure 2.8**). Our findings align with historical monitoring data which show persistently low TN:TP ratios in Clear Lake since the early 1970s (**Figure A.2**). Florea (2022) likewise observed consistent N-limitation across 10 Clear Lake monitoring sites in 2020 and 2021. These results agree with an analysis of 369 German lakes, which found that shallow polymictic lakes are predominantly N-limited during the summer (Dolman et al., 2016).

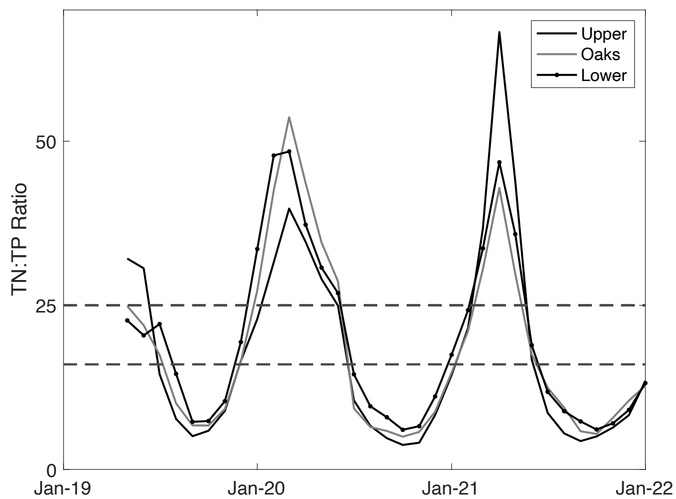

Figure 2.8. *Volume-averaged TN:TP molar ratios for each sub-basin. Dotted lines indicate 25:1 (Maranger, 2018) and 16:1* (Redfield, 1958) *thresholds.*

When ratios of N:P are low, cyanobacteria often dominate phytoplankton assemblages as their ability to fixate nitrogen provides a competitive advantage over other N-limited groups (Smith 1983). With the exception of *Microcystis and Pseudanabaena*, all dominant cyanobacteria genera in Clear Lake are N-fixing, allowing them to thrive in N-limited environments. The strong negative correlation between TN:TP and cyanobacteria biovolume supports our hypothesis that the relative abundance of cyanobacteria increases as N:P ratio decreases. The MRMR predictor rank further highlights that TN:TP ratio is the single most important predictor of cyanobacteria bloom intensity. TN:TP ratio was higher ranked than either TN or TP alone, likely because the ratio incorporates both the amount of TP available to cyanobacteria and the amount of N limiting growth of other phytoplankton groups. Thus, this statistically significant correlation provides further evidence that internal P release from lake sediment promotes the proliferation of HCBs by both increasing bioavailable limiting nutrients and altering the nutrient balance in favor of N-fixing cyanobacteria.

2.4.3 Seasonal and Internannual Variability of HCBs

While there was variability in the intensity and duration of each summer bloom season, there were commonalities in their temporal evolution. In each year, the bloom season could be separated into three periods: (1) an early summer bloom in June and July predominantly in the LA, (2) a late summer minimum in August, and (3) a large fall bloom in September and October predominantly in the OA and the UA. This bimodal pattern corroborates the findings of Horne (1975) who documented a seasonal succession of cyanobacteria species in Clear Lake with peaks of *Aphanizomenon* in early summer and *Anabaena* in early fall separated by a minimum in cyanobacteria biomass in late summer. Horne hypothesized that the mid-summer decline was due to iron depletion, a trace element integral to the nitrogenase enzyme required for N-fixation, limiting the growth of diazatrophs. Iron limitation on nitrogen fixation has been widely observed in both freshwater and marine systems (Hanington et al. 2016; Mills et al. 2004; Wurtsbaugh and Horne 1983). Dissolved iron measurements collected from 1970 to 2020 in Clear Lake show a decrease In the monthly average and minimum concentrations from June through September indicating that the system was likely iron limited in the late summer (Summary Report on Metals and Metalloids in Clear Lake 2022). Seasonal cyanobacteria succession can also be regulated by zooplankton grazing pressure, light availability, and water temperature (Abrantes et al., 2006).

Cyanobacteria community composition data further demonstrates that the seasonal pattern in bloom intensity is a result of shift in the dominant genera. For example, during June and July of 2020, *Gloetrichia* was detected in all monitoring sites, except for UA-06, but completely disappeared from the fall bloom, replaced by *Limnopharis* as the dominant species in the September 2020 sampling event. Similarly, *Aphanizomenon* was prevalent in April and June samples in 2021 but was succeeded by *Psuedanabaena* and *Microcystis* as the dominant genera in September 2021 samples. Neither *Psuedanabaena or Microcystis* can fix nitrogen, so their appearance in the fall is likely driven by increasing availability of TN, which increased throughout the summer each year (Florea et al. 2022).

In comparison to all bloom seasons since 2004, BM in 2019 and 2020 was below average, whereas the 2021 BM was the most severe on record (**Figure 2.9**). The highest cyanotoxin levels ever documented in the lake were observed August 2021, providing further evidence of the exceptional bloom magnitude in that summer (Big Valley EPA, 2021). Annual bloom magnitudes in Clear Lake show a significant, positive linear correlation with summertime TP concentrations in the lake ($R^2 = 0.47$, $p = 0.007$). However, contrary to observations from many eutrophic systems (Kane et al. 2014), high wintertime external loading rates were not correlated with the magnitude of the subsequent HCB season. While discharge from Middle Creek was linearly correlated with BM during years with cumulative discharge less than 0.05 km^3 ($R^2 = 0.35$, $p = 0.074$), for high flow years, the relationship is non-linear. In fact, during this 3-year study we observed an inverse relationship to discharge, with years of low external loading corresponding to more severe blooms. This result is consistent with the observations of De Palma - Dow (2022) which found that summer TP concentrations in Clear Lake were negatively correlated with precipitation during the previous winter. While this study covers only 3 summers, we were able to observe HCB seasons following both extremely wet and extremely dry water years. Precipitation accumulations during the 2018-19, 2019-2020 and, 2020-21 water years were respectively 170%, 55% and 30% of the average rainfall from 1997-2021. While P loading from sediments is primarily driven by internal processes, TN concentrations each year were highest in the early winter following major storm events. This pattern suggests that external loading may be more important in controlling N availability than P availability and is supported by the fact that the UA, which receives the majority of stream inflows, had an N:P ratio <20 in July 2019 but dropped below this threshold a month earlier in both 2020 and 2021 when inflows during the previous winters were low (**Figure 2.8**).

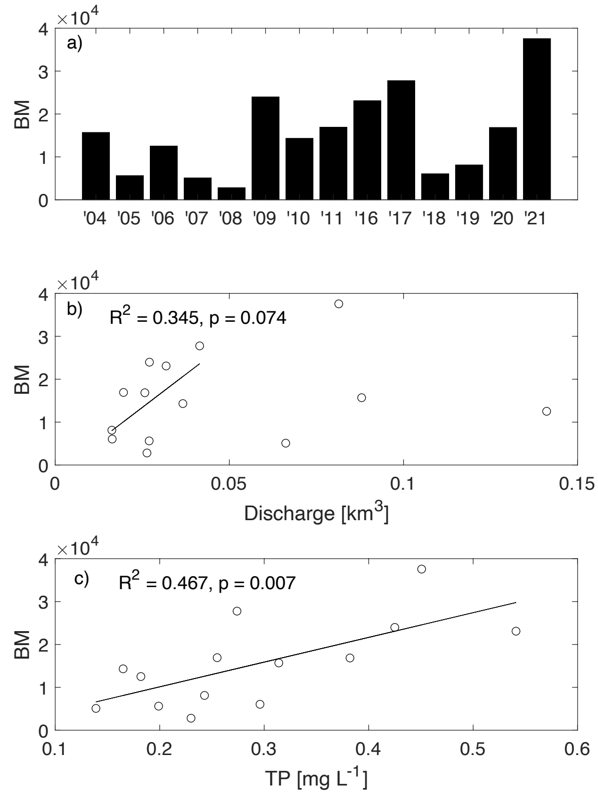

Figure 2.9. *a) Seasonal cyanobacteria bloom magnitude (June – October) recorded by satellite imagery from 2004-2011 and 2016-2021. No satellite data was available from 2012-2015. Scatter plots comparing b) cumulative inflow from previous water year vs bloom magnitude and c) average summer TP concentration vs bloom magnitude.*

In contrast to external loading, we observed that the timing and duration of stratification events, resulting from variability in summer meteorological conditions, strongly influenced in-lake TP concentrations and the severity of summer HCB season in Clear Lake. From June to September of 2019 and 2020, the 10-day averaged wind speeds fluctuated between 2 and 5 ms^{-1} while monthly average air temperatures ranged from 16.0 – 24.5 °C in 2019 and 17 – 25.6 °C in 2020 (**Figure A.10**). In 2021, on the other hand, wind speeds declined from a peak in June throughout the summer and remained consistently below 3 ms^{-1}. Monthly air temperatures were warmer than in both previous years, with July (27.2 °C) and August (26.2 °C) being particularly hot. The combination of lower wind speeds and warmer air temperatures in 2021 resulted in the longest stratification event observed during the three summers, June 18 – July 21. When a lake is stably stratified, cyanobacteria can use their buoyancy control ability to rise to the surface and outcompete other photosynthetic organisms for sunlight (Oliver et al., 2012). During this particularly long stratification event cyanobacteria covered over 85% of the lake's surface area (***Figure** 2.3*). In contrast, during the previous two summers, stratification periods ranged from only 3 – 10 days when the HCB seasons were relatively mild. Furthermore, thermal stratification, isolated the hypolimnion from oxygenated surface waters leading to rapid oxygen depletion at depth and longer periods of time for anoxic P fluxes from lake sediments. As a result, TP concentrations were higher in 2021 than in previous summers. Low spring discharge followed by warm stably stratified summers appear to influence interannual HCB variability in Clear Lake.

2.4.4 Comparative Estimates of Internal Load

The discrepancy in L_{int} estimates (**Table 2.3**) highlights the fundamental differences and limitations of each method (Burnet & Wilhelm, 2021; Nürnberg, 2009). L_{int_1} provides the most direct and intuitive quantification of internal P loading as it is based on measured increases in water column nutrient concentrations during the dry season. However, this method aggregates all potential internal P sources (e.g., mineralization of organic P, mechanical resuspension, and redox-dependent sediment fluxes) obfuscating the relative contribution and timing of each mechanism. Furthermore, this method may underestimate the internal load if sampling events are not frequent enough to capture peak nutrient concentrations in the water column. L_{int_1}, though, does provide an observation-based benchmark to compare theoretical estimates against.

In contrast, L_{int_2} quantifies the theoretical gross internal load released from sediments, excluding other mechanical or biological release mechanisms. In the OA and the LA, 2019 $\mathrm{L_{int\_2}}$ calculated with RR_{core} and RR_{TP} agreed closely with one another, corroborating our hypothesis that despite frequent vertical mixing events, redox-dependent diffusive flux from lake sediments is the primary mechanism of internal loading in these two arms of the lake. Compared with published release rates from other hypereutrophic reservoirs (n = 21, Carter and Dzialowski 2012; Nürnberg 1988),the UA sites have relatively low release rates while the other sites were about average. However, $L_{int\_2\_TP}$ estimates for UA were 60% (2019) – 110% (2021) larger than $L_{int\_2\_Core}$. Duplicate cores from all 3 UA sites had lower RR values than in the other arms so this discrepancy is not likely the result of higher spatial heterogeneity than found in the other arms. Lower diffusive flux from UA sites may partially be explained by variation in sediment P composition (**Figure 2.10**). UA cores contained the lowest concentrations of both TP and Fe/Al bound P, the most labile P form, in the top 5 cm of profundal sediments. Previous research has shown that concentration of Fe-bound P (Messer et al., 1984) and TP (Nürnberg, 1988) in sediment is closely correlated with anoxic P release rates. Therefore, the lower observed RR values in UA cores, likely reflect a smaller mobile P pool in UA sediments available for release. In addition, there was significant negative correlation between percent solids of the sediment (i.e., the total amount of solid material remaining after desiccating the sample), and SRP fluxes ($R^2 = 0.78$, $p < 0.001$). With a greater percentage of solids in sediments there is less interstitial pore space where high rates of diffusion of P from solid to aqueous phase can occur. In 2020 and 2021, on the other hand, estimates from $L_{int\_2\_core}$ were significantly less than $L_{int\_2\_TP}$ in all arms, suggesting seasonal variation in sediment P-pools need be considered, especially in polymictic lakes; highlighting the limitations when modeling multi-year internal loads from an individual incubation experiment. While the magnitude of the internal loading varied by up to 40% depending on the method employed, both the gross and net estimates demonstrate that internal P loading during the summer/fall, not external loading, is the primary factor driving seasonal nutrient fluctuations in Clear Lake.

Monitoring the response of Clear Lake to management and restoration programs requires accurately capturing the spatial and temporal variation of water quality, hypoxia,

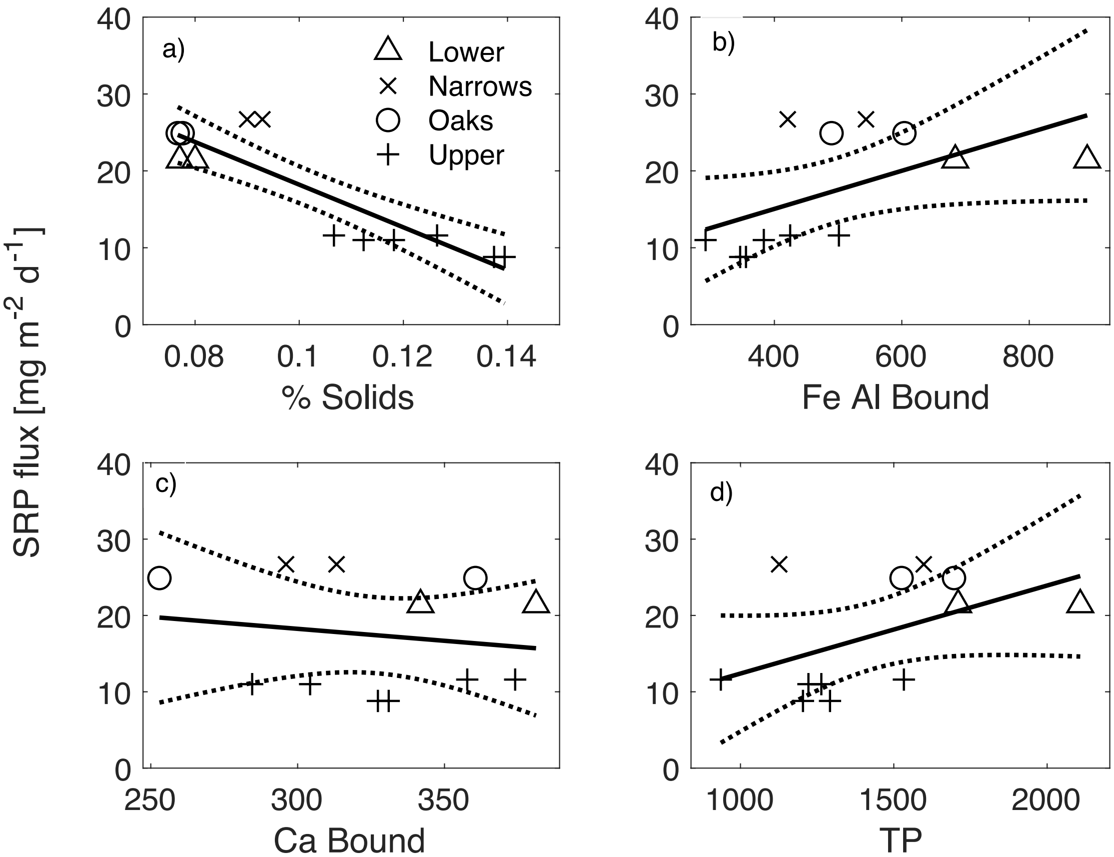

Figure 2.10. *Comparison of sediment composition with SRP release rates in lab incubation experiments. Sediment concentrations are units of μg g^{-1} and are average of top 0-5 cm from duplicate oxic incubated cores while SRP release rates shown are from anoxic cores. Solid line indicates least-squares linear regression with 95% confidence interval (dotted line).*

And nutrient loadings across the lake. Examining the strengths and limitations of the various methods we employed to quantify basin-wide gross and net internal loads can be instructive for improving loading estimates in other polymictic systems. Due to labor and financial constraints, L_{int_1} is often the preferred method for determining loading rates in reservoirs (Burnet & Wilhelm, 2021). However, this method assumes that measurements from monitoring sites are representative. In the UA, we observed within-basin variation in peak TP and SRP concentrations up to 23% and 24% respectively. In contrasts net loading calculations for OA and LA were estimated from one monitoring site each and thus there is uncertainty when assuming spatially homogenous concentrations across each sub-basin. Previous tracer studies have indicated that when stratified, baroclinic gradients and wind forcing can drive high dispersion rates and interbasin exchange of constituents throughout Clear Lake (Rueda et al. 2008). As a result, there can be significant intra- and inter-basin variability in nutrient concentrations. While individual point measurements may be sufficient for detecting long-term trends in eutrophication, distributed sampling strategies are necessary to accurately quantify internal loads in shallow lakes that are strongly influences by advective processes.

In addition, correctly determining the extent and duration of sediment anoxia can be challenging in shallow lakes with complex morphometry. In deep, stratified environments, the anoxic/hypoxic zone evolves in a predictable manner, forming first in the deep pelagic zone and growing vertically towards the shoreline until fall turnover ventilates the hypolimnion. When stably stratified, periodic vertical DO profiles are sufficient to determine the spatial extent of the actively releasing sediment area. However, in shallow polymictic systems, intermittent periods of stratification and mixing can deplete the hypolimnion of oxygen or rapidly reaerate it such that routine profile sampling may fail to accurately capture these changes. High-frequency *in situ* DO measurements, on the other hand, provide a more precise record of the timing and inter-basin variability of hypoxia. While AA_{mod} is frequently used to estimate the seasonal extent of sediment anoxia in polymictic system, it does not indicate the timing of hypoxic events at timescales relevant to ecosystem processes. By utilizing *in situ* measurements, we were able precisely determine at an hourly timestep when hypolimnetic DO concentrations would promote redox-dependent sediment P releases and when mixing events occurred that facilitated the transport of nutrient-enriched hypolimnetic waters to the photic zone for biotic uptake. Such high-frequency data can help to better quantify the physical and biogeochemical process influence interannual variability in cyanobacteria blooms in polymictic systems.

2.4.5 Unresolved Internal Loading Mechanisms

The discrepancy between modeled and experimentally determine loading rates in the UA suggests that additional mechanisms are contributing to internal P loading in this arm. Despite containing the lowest sediment concentrations of TP and Fe/Al bound P (**Figure 2.10**), peak TP concentrations were consistently observed in the UA sites each summer. This may appear counter-intuitive, as diffusive P fluxes are generally correlated with sediment P content (Nürnberg, 1988). However, this trend is consistent with routine water quality and sediment sampling data collected by LCWRD over the last 15 years (County of Lake Water Resources Department, 2022) which measured lower sediment TP concentrations throughout the year and higher peak water column TP concentrations in the UA when compared with OA and LA sites. Increased loading in the UA can be partially explained by the longer periods of thermal stratification and a higher surface area to volume ratio. However, the discrepancy between experimental (RR_{core}) and modeled (RR_{TP}) sediment release rates in the UA indicate that additional mechanical (resuspension), chemical (pH), and biological (decomposition) processes are contributing P cycling in this arm specifically.

In shallow lakes, physical processes such as wind stirring, wave action, boat wakes, benthivorous fish activity, and bioturbation by benthic infauna can disturb sediment, redistributing P-enriched water through the water column, enhancing P exchange (Steinman & Spears, 2020). Wind-driven sediment resuspension has been identified as an important physical P loading mechanism in many shallow, eutrophic systems, (Havens et al. 2007; Huang et al. 2016; Tammeorg et al. 2013) and experiments have shown that P fluxes from resuspended material can be 20-30 times greater than from undistributed sediments (Søndergaard et al., 1992). The dynamic ratio (i.e., inverse of the morphometric factor, DR) quantifies the susceptibility of a basin to wind-driven resuspension, with basins above a threshold of 0.8 generally being classified as highly susceptible (Havens et al. 2007). At Clear Lake, only the UA exceeds this threshold (**Table 2.1**), adding credibility to the hypothesis that sediment resuspension, during the summer and fall, may release TP in the shallow littoral regions. During the dry 2020 and 2021 years, summertime water level declined by more than a meter from 2019 significantly increasing the surface area susceptible to wind-driven resuspension (Laenen et al. 1996). Higher rates of sediment resuspension may in part have contributed to higher TP concentrations during a drought in the early 1990's.

Another potential mechanism is photosynthetically elevated pH driving higher release rates in littoral zones, as the pH of a waterbody influences the capacity of sediment to bind P. At high pH values, hydroxyl ions replace P on iron particle binding sites leading to a decline in the capacity of oxidized surfaces to bind P (Jensen & Andersen, 1992; Orihel et al., 2017). As photosynthesis results in elevated pH, high productivity events can increase P release (Koski-Vähälä & Hartikainen, 2001). However, pH varied by less than 1 (7.7 – 8.7) between basins during the summer indicating that this mechanism is unlikely to drive higher release rates in the UA specifically.

In addition, the decomposition of organic material can constitute a significant organic P input as phosphorus is incorporated into numerous biomolecules (Orihel et al., 2017). Surface-catalyzed hydrolysis, photolysis and mineralization by microbial activity can in turn mobilize and convert this solid organic P into an aqueous phase (Orihel et al., 2017; Reitzel et al., 2007). A biological survey of Clear Lake documented that the majority of rooted aquatic vegetation is found along the northern and western shallow regions of the UA (**Figure A.12**, ReMetrix 2003), indicating that there is potential for higher rates of mineralization of aquatic vegetation in the UA relative to the deeper arms. However, few measurements of organic matter in Clear Lake sediments have been collected to date. Future research should focus on investigating the role that each of these factors play in contributing to P cycling in Clear Lake.

2.5 Conclusions

Net and gross internal P loads for Clear Lake were calculated for a 3-year period using 2 comparative methods to determine the relative contribution of external and internal loading to the system. Internal P loading accounted for 70-95 % of the TP mass observed in Clear Lake annually with higher loading observed during drought years. The release of P during hypoxic periods shifted the system towards N-limitation favoring the proliferation of HCBs. With climate change expected to promote longer and more intense periods of thermal stratification in temperate lakes, state and federal agencies should prioritize funding of in-lake strategies to mitigate HCBs in impaired water bodies. Engineering solutions such as hypolimnetic oxygenation, sediment dredging, and alum application are clearly needed in conjunction with watershed restoration projects to limit the availability of in-lake nutrients fueling these blooms in the short and long term.

References

Abrantes, N., Antunes, S. C., Pereira, M. J., & Gonçalves, F. (2006). Seasonal succession of cladocerans and phytoplankton and their interactions in a shallow eutrophic lake (Lake Vela, Portugal). Acta Oecologica, 29(1), 54–64.

Aráoz, R., Molgó, J., & Tandeau de Marsac, N. (2010). Neurotoxic cyanobacterial toxins. Toxicon, 56(5), 813–828.

Big Valley EPA. (2021). 2021 Clear Lake Cyanotoxin Monitoring Program. https://www.bvrancheria.com/_files/ugd/f2d74c_13159c520c1d44ab8a112876ae6a6593.pdf

Boehme, J., Schulhauser, R., & Bejankiwar, R. (2011). Atmospheric deposition of phosphorus to freshwater lakes.

Burger, D. F., Hamilton, D. P., & Pilditch, C. A. (2008). Modelling the relative importance of internal and external nutrient loads on water column nutrient concentrations and phytoplankton biomass in a shallow polymictic lake. Ecol. Model., 211(3–4), 411–423.

Burnet, S. H., & Wilhelm, F. M. (2021). Estimates of internal loading of phosphorus in a western US reservoir using 3 methods. Lake Reserv. Manag., 37(3), 261–274.

California Department of Water Resources. (n.d.). Clear Lake Monitoring Program. Retrieved May 31, 2022, from https://wdl.water.ca.gov/waterdatalibrary/

Carter, L. D., & Dzialowski, A. R. (2012). Predicting sediment phosphorus release rates using landuse and water-quality data. Freshw. Sci., 31(4), 1214–1222.

Chamberlin, C. E., Chaney, R., Finney, B., Hood, M., Lehamn, P., Mckee, M., & Willis, R. (1990). Abatement and Control Study: Sulphur Bank Mine and Clear Lake.

Chorus, I., Falconer, I. R., Salas, H. J., & Bartram, J. (2000). Health risks caused by freshwater cyanobacteria in recreational waters. J. Toxicol. Environ. Health – B: Crit. Rev., 3(4), 323–347.

Cortés, A., Forrest, A. L., Sadro, S., Stang, A. J., Swann, M., Framsted, N. T., Thirkill, R., Sharp, S. L., & Schladow, S. G. (2021). Prediction of hypoxia in eutrophic polymictic lakes. Water Resour. Res., 57(6).

County of Lake Department of Public Works Water Resources Divison. (2010). Clear Lake Integrated Watershed Management Plan. https://www.lakecountyca.gov/1130/Clear-Lake-Integrated-Watershed-Manageme

County of Lake Water Resources Department. (2022, May 20). Clear Lake Limnological Ambient Water Quality Monitoring Program (CLLAMP). https://ceden.waterboards.ca.gov

Coveney, M. F., Lowe, E. F., Battoe, L. E., Marzolf, E. R., & Conrow, R. (2005). Response of a eutrophic, shallow subtropical lake to reduced nutrient loading. Freshw. Biol., 50(10), 1718–1730.

De Palma-Dow, A., McCullough, I. M., & Brentrup, J. A. (2022). Turning up the heat: Long-term water quality responses to wildfires and climate change in a hypereutrophic lake. Ecosphere, 13(12).

Dillon, P. J., & Rigler, F. H. (1974). The phosphorus-chlorophyll relationship in lakes. Limnol. Oceanogr., 19(5), 767–773.

Ding, S., Chen, M., Gong, M., Fan, X., Qin, B., Xu, H., Gao, S. S., Jin, Z., Tsang, D. C. W., & Zhang, C. (2018). Internal phosphorus loading from sediments causes seasonal nitrogen limitation for harmful algal blooms. Sci. Total Environ., 625, 872–884.

Dolman, A. M., Mischke, U., & Wiedner, C. (2016). Lake-type-specific seasonal patterns of nutrient limitation in German lakes, with target nitrogen and phosphorus concentrations for good ecological status. Freshw. Biol., 61(4), 444–456.

Domagalski, J. L., Morway, E., Alvarez, N. L., Hutchins, J., Rosen, M. R., & Coats, R. (2021). Trends in nitrogen, phosphorus, and sediment concentrations and loads in streams draining to Lake Tahoe, California, Nevada, USA. Sci. Total Environ., 752.

Eimers, M. C., & Winter, J. G. (2005). State of Lake Simcoe water quality 2000-2013.

Einsele, W. (1936). Über die Beziehungen des Eisenkreislaufs zum Phosphatkreislauf im eutrophen. Archi. Hydrobiol., 29, 664–686.

Florea, K., Stewart, B., Webb, E., Caron, D., & Smith, J. (2022). Environmental Drivers of Cyanobacterial Harmful Algal Blooms and Cyanotoxins in Clear Lake: 2020-2021. https://ftp.sccwrp.org/pub/download/DOCUMENTS/TechnicalReports/1261_ClearLakeHABs.pdf

Guildford, S. J., & Hecky, R. E. (2000). Total nitrogen, total phosphorus, and nutrient limitation in lakes and oceans: Is there a common relationship? Limnol. Oceanogr., 45(6), 1213–1223.

Håkanson, L. (2004). Break-through in predictive modelling opens new possibilities for aquatic ecology and management – A review. Hydrobiologia, 518(1–3), 135–157.

Hanington, P., Rose, A., & Johnstone, R. (2016). The potential of benthic iron and phosphorus fluxes to support the growth of a bloom forming toxic cyanobacterium Lyngbya 76scillato, Moreton Bay, Australia. Mar. Freshw. Res., 67(12), 1918–1927.

Havens, K. E., Jin, K. R., Iricanin, N., & James, R. T. (2007). Phosphorus dynamics at multiple time scales in the pelagic zone of a large shallow lake in Florida, USA. Hydrobiologia, 581(1), 25–42.

Holdren, G. C., & Armstrong, D. E. (1980). Factors affecting phosphorus release from intact lake sediment cores. Environ. Sci. Tech., 14(1), 79–87.

Horne, A. J. (1975). The Ecology of Clear Lake Phytoplankton.

Horne, A. J., & Goldman, C. R. (1972). Nitrogen fixation in Clear Lake, California. I. Seasonal variation and the role of heterocysts. Limnol. Oceanogr., 17(5), 678–692.

Huang, L., Fang, H., He, G., Jiang, H., & Wang, C. (2016). Effects of internal loading on phosphorus distribution in the Taihu Lake driven by wind waves and lake currents. Environ. Pollut., 219, 760–773.

Hupfer, M., & Lewandowski, J. (2008). Oxygen controls the phosphorus release from lake sediments – A long-lasting paradigm in limnology. Int. Rev. Hydrobiol., 93(4–5), 415–432.

Iiames, J. S., Salls, W. B., Mehaffey, M. H., Nash, M. S., Christensen, J. R., & Schaeffer, B. A. (2021). Modeling anthropogenic and environmental influences on freshwater harmful algal bloom development detected by MERIS over the central United States. Water Resour. Res., 57(10).

Isles, P. D. F., Giles, C. D., Gearhart, T. A., Xu, Y., Druschel, G. K., & Schroth, A. W. (2015). Dynamic internal drivers of a historically severe cyanobacteria bloom in Lake Champlain revealed through comprehensive monitoring. J. Great Lakes Res. , 41(3), 818–829.

Jassby, A. D., Reuter, J. E., Axler, R. P., Goldman, C. R., & Hackley, S. H. (1994). Atmospheric deposition of nitrogen and phosphorus in the annual nutrient load of Lake Tahoe (California-Nevada). Water Resour. Res., 30(7), 2207–2216.

Jensen, H. S., & Andersen, F. O. (1992). Importance of temperature, nitrate, and pH for phosphate release from aerobic sediments of four shallow, eutrophic lakes. Limnol. Oceanogr., 37(3), 577–589.

Kane, D. D., Conroy, J. D., Peter Richards, R., Baker, D. B., & Culver, D. A. (2014). Re-eutrophication of Lake Erie: Correlations between tributary nutrient loads and phytoplankton biomass. J. Great Lakes Res. , 40(3), 496–501.

Koski-Vähälä, J., & Hartikainen, H. (2001). Assessment of the risk of phosphorus loading due to resuspended sediment. J. Environ. Qual., 30(3), 960–966.

Lake County Watershed Protection District. (2009). Clear Lake Watershed TMDL Monitoring Program.

Lemmin, U., Mortimer, C. H., & Bäuerle, E. (2005). Internal seiche dynamics in Lake Geneva. Limnol. Oceanogr., 50(1), 207–216.

Liikanen, A., Murtoniemi, T., Tanskanen, H., Väisänen, T., & Martikainen, P. J. (2002). Effects of temperature and oxygen availability on greenhouse gas and nutrient dynamics in sediment of a eutrophic mid-boreal lake. Biogeochem., 59, 269–286.

Lunetta, R. S., Schaeffer, B. A., Stumpf, R. P., Keith, D., Jacobs, S. A., & Murphy, M. S. (2015). Evaluation of cyanobacteria cell count detection derived from MERIS imagery across the eastern USA. Remote Sens. Environ., 157, 24–34.

Messer, J. J., Ihnat, J. M., & Wegner, D. L. (1984). Phosphorus release from the sediments of Flaming Gorge Reservoir, Wyoming, U. S. A. Verh. Internat. Verein. Limnol., 22(3), 1457–1464.

Mills, M. M., Ridame, C., Davey, M., La Roche, J., & Geider, R. J. (2004). Iron and phosphorus co-limit nitrogen fixation in the eastern tropical North Atlantic. Nat., 429(6989), 292–294.

Molot, L. A., Young, J., Dillon, P. J., Hakanson, L., & Soliman, C. (2010). Intermin report on phosphorus and dissolved oxygen modelling of Lake Simcoe.

Moore, P. A., Reddy, K. R. Jr., & Fisher, M. M. (1998). Phosphorus Flux between Sediment and Overlying Water in Lake Okeechobee, Florida: Spatial and temporal variations. J. Environ. Qual., 27(6), 1428–1439.

Mortimer, C. H. (1941). The exchange of dissolved substances between mud and water in lakes. J. Ecol., 29, 280–329.

Nürnberg, G. K. (1988). Prediction of phosphorus release rates from total and reductant-soluble phosphorus in anoxic lake sediments. Can. J. Fish. Aquat. Sci, 45(3), 453–462.

Nürnberg, G. K. (1996). Trophic state of clear and colored, soft- and hardwater lakes with special consideration of nutrients, anoxia, phytoplankton and fish. Lake Reserv. Manag., 12(4), 432–447.

Nürnberg, G. K. (2005). Quantification of internal phosphorus loading in polymictic lakes. Verh. Internat. Verein. Limno, 29(2), 623–626.

Nürnberg, G. K. (2009). Assessing internal phosphorus load – Problems to be solved. Lake Reserv. Manag., 25(4), 419–432.

Nürnberg, G. K., & LaZerte, B. D. (2016). More than 20 years of estimated internal phosphorus loading in polymictic, eutrophic Lake Winnipeg, Manitoba. J. Great Lakes Res. , 42(1), 18–27.

Nürnberg, G. K., Lazerte, B. D., Sun Loh, P., & Molot, L. A. (2013). Quantification of internal phosphorus load in large, partially polymictic and mesotrophic Lake Simcoe, Ontario. J. Great Lakes Res. , 39, 271–279.

Nürnberg, G. K., Molot, L. A., O'Connor, E., Jarjanazi, H., Winter, J., & Young, J. (2013). Evidence for internal phosphorus loading, hypoxia and effects on phytoplankton in partially polymictic Lake Simcoe, Ontario. J. Great Lakes Res. , 39(2), 259–270.

Ogdahl, M. E., Steinman, A. D., & Weinert, M. E. (2014). Laboratory-determined phosphorus flux from lake sediments as a measure of internal phosphorus loading. J. Vis. Exp., 85, 1–9.

Oliver, R., Hamilton, D., Brookes, J. D., & George, G. G. (2012). Physiology, Blooms and Prediction of Planktonic Cyanobacteria. In Whitton B.A. (Ed.), Ecology of Cyanobacteria II: Their Diversity in Space and Time. Springer-Verlag.

Orihel, D. M., Baulch, H. M., Casson, N. J., North, R. L., Parsons, C. T., Seckar, D. C. M., & Venkiteswaran, J. J. (2017). Internal phosphorus loading in Canadian fresh waters: A critical review and data analysis. Ca. J. Fish. Aquat. Sci., 74(12), 2005–2029.

Orihel, D. M., Schindler, D. W., Ballard, N. C., Graham, M. D., O'Connell, D. W., Wilson, L. R., & Vinebrooke, R. D. (2015). The "nutrient pump:" Iron-poor sediments fuel low nitrogen-to-phosphorus ratios and cyanobacterial blooms in polymictic lakes. Limnol. Oceanogr., 60(3), 856–871.

Paerl, H. W., Fulton, R. S., Moisander, P. H., & Dyble, J. (2001). Harmful freshwater algal blooms, with an emphasis on cyanobacteria. Sci. World J., 1, 76–113.

Peng, H., Long, F., & Ding, C. (2005). Feature selection based on mutual information: criteria of max-dependency, max-relevance, and min-redundancy. IEEE Trans. Pattern Anal. Mach. Intell., 27(8), 1226–1238.

Redfield, A. C. (1958). The biological control of chemical factors in the environment. Am. Sci., 46(3), 205–221.

Reitzel, K., Ahlgren, J., DeBrabandere, H., Waldebäck, M., Gogoll, A., Tranvik, L., & Rydin, E. (2007). Degradation rates of organic phosphorus in lake sediment. Biogeochem., 82(1), 15–28.

ReMetrix. (2003). Assessment of Clear Lake, CA For Submersed Aquatic Vegetation, Morphology, and Sediment.

Rice, E. W., Bridgewater, L., & American Public Health Association. (2012). Standard methods for the examination of water and wastewater (Vol. 10). American public health association.

Richerson, Why, S. J., & Suchanek, T. H. (1994). The Causes and Control of Algal Blooms in Clear Lake, California.

Rueda, F., Schaldow, G., & Clark, J. (2008). Mechanisms of contaminant transport in a multi-basin lake. Ecol. App. Supp., 18(8), 72–88.

San Francisco Estuary Institute. (2022). HAB Satelite Analysis Tool. https://fhab.sfei.org

Schindler, D. W., Carpenter, S. R., Chapra, S. C., Hecky, R. E., & Orihel, D. M. (2016). Reducing phosphorus to curb lake eutrophication is a success. Environ. Sci. Tech., 50(17), 8923–8929.

Sharp, S. L., Forrest, A. L., Bouma-Gregson, K., Jin, Y., Cortés, A., & Schladow, S. G. (2021). Quantifying scales of spatial variability of cyanobacteria in a large, eutrophic lake ssing multiplatform remote sensing tools. Front. Environ. Sci.. , 9(April), 1–19.

Sims, J. D. (1988). Diatom biostratigraphy and the paleolimnology of Clear Lake, Lake County, California. GSA Special Papers, 214.

Smith, V. H. (1983). Low nitrogen to phosphorus ratios favor dominance by blue-green algae in lake phytoplankton. Sci., 221(4611), 669–671.

Smith, V. H. (1985). Predictive models for the biomass of blue-green algae in lakes. J. Clim., 21(3), 433–439.

Smith, V. H., & Schindler, D. W. (2009). Eutrophication science: where do we go from here? In Trends in Ecology and Evolution (Vol. 24, Issue 4, pp. 201–207).

Smucker, N. J., Beaulieu, J. J., Nietch, C. T., & Young, J. L. (2021). Increasingly severe cyanobacterial blooms and deep water hypoxia coincide with warming water temperatures in reservoirs. Glob. Change Biol. , 27(11), 2507–2519.

Søndergaard, M., Jensen, J. P., & Jeppesen, E. (2001). Retention and Internal Loading of Phosphorus in Shallow , Eutrophic Lakes. Sci. World, 1, 427–442.

Søndergaard, M., Jensen, J. P., & Jeppesen, E. (2003). Role of sediment and internal loading of phosphorus in shallow lakes. Hydrobiologia, 506–509, 135–145.

Søndergaard, M., Kristensen, P., & Jeppesen, E. (1992). Phosphorus release from resuspended sediment in the shallow and wind-exposed Lake Arreso, Denmark. In Hydrobiologia (Vol. 228).

Song, K., & Burgin, A. J. (2017). Perpetual Phosphorus Cycling: Eutrophication Amplifies Biological Control on Internal Phosphorus Loading in Agricultural Reservoirs. Ecosystems, 20(8), 1483–1493.

Spears, B. M., Carvalho, L., Perkins, R., A, K., & DM, P. (2012). Long-term variation and regulation of internal phosphorus loading in Loch Leven. Hydrobiologia, 681, 23–33.

Steinman, A. D., & Spears, B. M. (2020). Internal phosphorus loading in lakes : causes, case studies, and management. J. Ross Publishing.

Stumpf, R. P., Tomlinson, M. C., Calkins, J. A., Kirkpatrick, B., Fisher, K., Nierenberg, K., Currier, R., & Wynne, T. T. (2009). Skill assessment for an operational algal bloom forecast system. J. Marine. Sys., 76(1–2), 151–161.

Suchanek, T. H., Richerson, P. J., Nelson, D. C., Eagles-Smith, C. A., Anderson, D. W., Cech, J. J., Zierenberg, R., Schladow, G., Mount, J. F., McHatton, S. C., Slotton, D. G., Webber, L. B., Swisher, B. J., Bern, A. L., & Sexton, M. (2002). Evaluating and managing a multiply stressed ecosystem at clear lake, California: A holistic ecosystem approach. Managing for Healthy Ecosystems: Case Studies, 1233–1265.

Summary Report on Metals and Metalloids in Clear Lake Based on Historical Data. (2022).

Svirčev, Z. B., Tokodi, N., Drobac, D., & Codd, G. A. (2014). Cyanobacteria in aquatic ecosystems in Serbia: effects on water quality, human health and biodiversity. Systematics and Biodiversity, 12(3), 261–270.

Tammeorg, O., Niemistö, J., Möls, T., Laugaste, R., Panksep, K., & Kangur, K. (2013). Wind-induced sediment resuspension as a potential factor sustaining eutrophication in large and shallow Lake Peipsi. Aquat. Sci., 75(4), 559–570.

Tammeorg, O., Nürnberg, G., Horppila, J., Haldna, M., & Niemistö, J. (2020). Redox-related release of phosphorus from sediments in large and shallow Lake Peipsi: Evidence from sediment studies and long-term monitoring data. J. Great Lakes Res. , 46(6), 1595–1603.

TetraTech. (2004). Total Maximum Daily Load for Nutrients in Clear Lake , Lake County , California Technical Report.

Tipping, E., Benham, S., Boyle, J. F., Crow, P., Davies, J., Fischer, U., Guyatt, H., Helliwell, R., Jackson-Blake, L., Lawlor, A. J., Monteith, D. T., Rowe, E. C., & Toberman, H. (2014).

Atmospheric deposition of phosphorus to land and freshwater. Environ. Sci. Process. Impacts, 16(7), 1608–1617.

Van Duin, E. H. S., Aalderink, R. H., & Lijklema, L. (1995). Light adaptation of 80scillatoria agardhii at different time scales. Water Sci. Tech., 32(4), 35–48.

Wang, X., Smith, K., & Hyndman, R. (2006). Characteristic-based clustering for time series data. Data Min. Knowl. Disc., 13(3), 335–364.

Wilson, S. G. (2015). Soil Genesis, Mineralogy and Phosphorus Dynamics of the Clear Lake Volcanic Field. University of California, Davis.

Winder, M., Reuter, J., & Schladow, G. (2010). Clear Lake Historical Data Analysis. https://www.waterboards.ca.gov/rwqcb5/water_issues/tmdl/central_valley_projects/clear_lake_nutrients/load_allo_status/cl_lakeco_enc_2.pdf

Winter, J. G., Dillon, P. J., Futter, M. N., Nicholls, K. H., Scheider, W. A., & Scott, L. D. (2002). Total Phosphorus Budgets and Nitrogen Loads : Lake Simcoe , Ontario (1990 to 1998). Journal of Great Lakes Research, 28(3), 301–314.

Wu, Z., Zou, R., Jiang, Q., Elser, J. J., Zhao, L., Ye, R., & Liu, Y. (2020). What maintains seasonal nitrogen limitation in hyper-eutrophic Lake Dianchi? Insights from stoichiometric three-dimensional numerical modeling. Aquat. Sci., 82(4).

Wurtsbaugh, W. A., & Horne, A. J. (1983). Iron in eutrophic Clear Lake, California: Its importance for algal nitrogen fixation and growth. Can. J. Fish. Aquat. Sci, 40(9), 1419–1429.

Xu, H., Paerl, H. W., Qin, B., Zhu, G., Hall, N. S., & Wu, Y. (2015). Determining critical nutrient thresholds needed to control harmful cyanobacterial blooms in eutrophic Lake Taihu, China. Environ. Sci. Tech., 49(2), 1051–1059.

3 DRIVERS AND DYNAMICS OF DEEP WINTER MIXING EVENTS IN A DEEP OLIGOMICTIC LAKE[2]

Abstract

Deep mixing events (turnover) in temperate lakes provide a critical link between the epilimnion and hypolimnion, transporting nutrients to the surface and ventilating deep layers below. In this study, we utilized a 50-year record of winter mixing in Lake Tahoe (USA) combined with high-frequency temperature and dissolved oxygen measurements to determine the factors influencing the extent of winter vertical mixing and the hydrodynamic processes that occur during turnover. Winter mixing depth is primarily determined by intense episodic cooling events during late winter. Complete mixing is triggered when cold fronts serendipitously pass over the lake during the end of the limnological winter. Measurements show that ventilation at the sediment-water interface occurs almost simultaneously with the water column attaining isothermal conditions. Following this initiation of turnover, bottom waters continue to cool, even after the onset of spring stratification, suggesting that littoral water impacted by differential cooling is transported to the deep hypolimnion. The importance of this inherently three-dimensional process suggests that one-dimensional models may not

[2] This manuscript is being submitted to *Limnology & Oceanography* for publication.

adequately capture how hypolimnetic mixing in deep lakes occurs and may be of limited use for predicting how deep mixing may change under future climate conditions.

3.1 Introduction

Episodic extreme events, which induce rapid physical and biochemical responses, contribute to the internal variability of lake ecosystems. In oligomictic lakes, infrequent deep mixing (i.e., turnover) is a critical mechanism that regulates lake trophic status, facilitating the exchange of heat, nutrients, contaminants, and dissolved gases between the surface and deep layers (Goldman & Jassby, 1990; Straile et al., 2003).

Though oligomictic lakes can remain thermally stratified for timescales ranging from years to decades, episodic deep vertical mixing plays a central role in recycling nutrients from deep waters to the surface, where they are available for biotic uptake (Salmaso et al., 2003). While shallow, short retention period lakes often receive the majority of nutrient inputs from the watershed, nutrient transport from the hypolimnion can be the predominant nutrient source in deep lakes (Schwefel et al., 2019). Turnover facilitates deep water ventilation, acting as a first-order process that regulates hypolimnetic hypoxia (Crawford & Collier, 2007). Multiple years of continuous stratification can result in significant depletion of hypolimnetic dissolved oxygen (DO) (Dresti et al., 2023; Schwefel et al., 2016), promoting methanogesis from methantrophic microbes (Saarela et al., 2020), the release of phosphorus (Anderson et al., 2021; Beutel and Horne, 2018) and iron (Friedrich et al., 2014) from sediments, and the production of nitrous oxide in deep layers (Salk et al., 2016). Rapid deterioration of lake health can occur when these hypolimnetic waters are mixed into the epilimnion, where they can contribute to impacts such as the proliferation of harmful cyanobacteria and fish kills (Krishna et al., 2021). Thus, the frequency and intensity of turnover directly influence lake trophic status, biogeochemical cycling, and cold-water fish habitat (Nelligan et al., 2019; Salmaso et al., 2003).

Lake morphometry, heat fluxes, and local wind conditions determine a lake's mixing regime (Hutchinson & Loffler, 1956b; Imboden & Wuest, 1995); therefore, climatic changes that alter surface heat exchange and stratification patterns can modify the frequency of deep mixing. Woolway and Merchant (2019) predicted that under a forecasted warmer climate, all modeled oligomictic lakes would become permanently thermally stratified by the end of the 21st century, threatening the ecological status of many of the world's deepest lakes. The ecological effects of shifting lake mixing regimes are already apparent in deep lakes across climate zones (Adrian et al., 2009). Rogora (2018) linked declining winter mixing depth to the increasing extent of anoxia in six deep subalpine European lakes. Increasing thermal stability of tropical Lake Tanganyika and Lake Malawi has reduced vertical nutrient fluxes and lake productivity (Verburg & Hecky, 2009). Phytoplankton community composition in Lake Garda has shifted in response to lower nutrient concentrations in surface waters due to a decline in deep mixing (Salmaso et al., 2018). In Lake Tahoe (Winder et al., 2009) and Great Slave Lake (Rühland et al., 2023), there has been a shift to smaller diatoms in response to warming and altered mixing regimes. In contrast, deep water oxygen content in Lake Tovel has increased, where reductions in ice cover and a more extended fall mixing period have shifted the lake from a meromictic to a dimictic regime (Flaim et al., 2020). Long-term variability in wind stress can also impact the occurrence of deep mixing events. In Lake Baikal, paleolimnological records indicate that changing wind dynamics and reduced ice cover have dramatically increased nutrient supply from deep waters to the photic zone since the mid-19th century (Swann et al., 2020).

In temperate lakes, where hypolimnion temperatures exceed the temperature of maximum density (4 °C), deep mixing events have been associated with vertical, buoyancy-driven convection due to seasonal surface cooling (Michalski & Lemmin, 1995). As cooler, denser water plunges, the surface mixed layer deepens, culminating in complete lake turnover. Strong winds can accelerate this mixing through the introduction of turbulent kinetic energy (Fischer et al. 1979). The deepening rate of the convectively mixed surface layer (h_{CML}) is determined both by the strength of stratification and the intensity of surface cooling (Spigel et al., 1986). While global warming is clearly increasing lake thermal stability globally (Sahoo et al., 2016), the impact on winter heat fluxes is less consistent (Eichelberger et al., 2008).

One-dimensional (1D) lake models are frequently employed to simulate lake thermal structure and predict the long-term evolution of mixing regimes (Fenocchi et al., 2018; Woolway & Merchant, 2019). While the seasonal variations in surface temperature can be modeled with sufficient accuracy, 1D lake models often poorly resolve vertical mixing and the evolution of deep water temperature in large lakes (Stepanenko et al., 2010) due to overestimates of the amount of wind energy transferred to the deep hypolimnion under weakly stratified conditions (Gaudard et al., 2017). Furthermore, 1D models inherently neglect horizontal processes. In winter, vertical temperature gradients are small and vertical and horizontal turbulent diffusivities are on the same order of magnitude. Under these coniditions horizontal circulation induced by plunging stream inflows (Dresti et al., 2023), differential rates of cooling/heating between littoral and pelagic zones (Ambrosetti et al., 2010; Peeters et al., 2003), and wind-induced up and downwelling events (Fer et al., 2002; Piccolroaz et al., 2019; Reiss et al., 2020; Valbuena et al., 2022) can drive mixing and ventilation of deep waters.

While turnover events in oligomictic lakes have been widely documented with periodic CTD profiles, high-frequency, field observations of deep mixing events are rare due to their sporadic and infrequent occurrence (van Haren et al., 2021). Such data can help identify the important mixing and transport processes that occur during near-isothermal conditions.

This study demonstrates that a) episodic late winter cooling events drive interannual variability in deep lake mixing depth and b) differential cooling of littoral waters can be a key mechanism of deep water ventilation. We investigate the drivers and hydrodynamic processes associated with deep mixing events in Lake Tahoe, California-Nevada, a lake predicted to become permanently thermally stratified by 2065 (Sahoo et al., 2013). Long-term trends in the frequency and distribution of deep winter mixing events are first assessed by analyzing a 50-year record of maximum winter mixing depths. Correlations between stratification strength, and winter meteorological parameters, and mixing depth are calculated to evaluate the relative contribution of each term to the intensity of winter mixing. Finally, we compare high-frequency temperature and DO measurements from six contrasting winters, four with complete turnover and two with only partial mixing, to examine the physical processes that contribute to vertical mixing and deep water renewal.

3.2 Methods

Deep winter mixing processes in Lake Tahoe, are first examined through a correlation analysis of mixed layer depth and winter meterological forcing parameters. High frequency thermistor chain data is then analyzed to observe how lake thermal structure evolves during partial and deep mixing winters. Lastly a mass-balance scaling is conducted to investigate the potential contribution of plunging density currents from rivers inflows and differentially cooled littoral waters to deep water cooling following turnover.

3.2.1 Site Description

Lake Tahoe (39.097°, -120.032°) is a moderately-sized, deep lake at 1897 m.a.s.l within the Sierra Nevada mountains, straddling the California-Nevada border (**Figure 3.1**). The lake has a surface area of 501 km^2, a volume of 156 km^3, and a maximum depth of 501 m (**Table 3.1**), making it the third deepest lake in North America and the 11th deepest in the world (Coats et al., 2006). Lake Tahoe's volume is large relative to its watershed size (800 km^2), resulting in a long theoretical residence time of 650 years and low levels of external nutrient inputs that maintain its oligotrophic status and world-renowned water clarity. The lake is classified as warm oligomictic and the extent of winter mixing has a strong positive correlation with spring primary productivity (Goldman et al., 1989). Furthermore, water clarity can dramatically increase for days following turnover events when hypolimnetic waters are upwelled to the surface (Watanabe, 2023). Long-term monitoring indicates that the lake has warmed significantly in recent decades with the average surface water temperature warming by 0.70 °C $decade^{-1}$ (Coats et al. 2006), and the stratification season increasing in duration by 31 days between 1968 and 2021 (Sahoo et al., 2016; Schladow et al., 2021).

Table 3.1. *Main morphometric and hydrological characteristics of Lake Tahoe.*

Latitude /Longitude	°	39.097 / -120.032
Elevation of Lake Surface	m.a.s.l	1897
Lake Surface Area	km^2	501
Watershed Area (excluding lake)	km^2	800
Shoreline	km	120
Max Depth	m	501
Mean Depth	m	305
Volume	km^3	156
Theoretical Residence Time	yr	650

3.2.2 Observation Data

Thermistor chains recorded *in situ* temperatures throughout the water column at two locations: (1) a mid-lake site (MLTP) from 1997-1999 and (2) an eastern site near Glenbrook, Nevada (GBTC) from 2013-present (**Figure 3.1**).

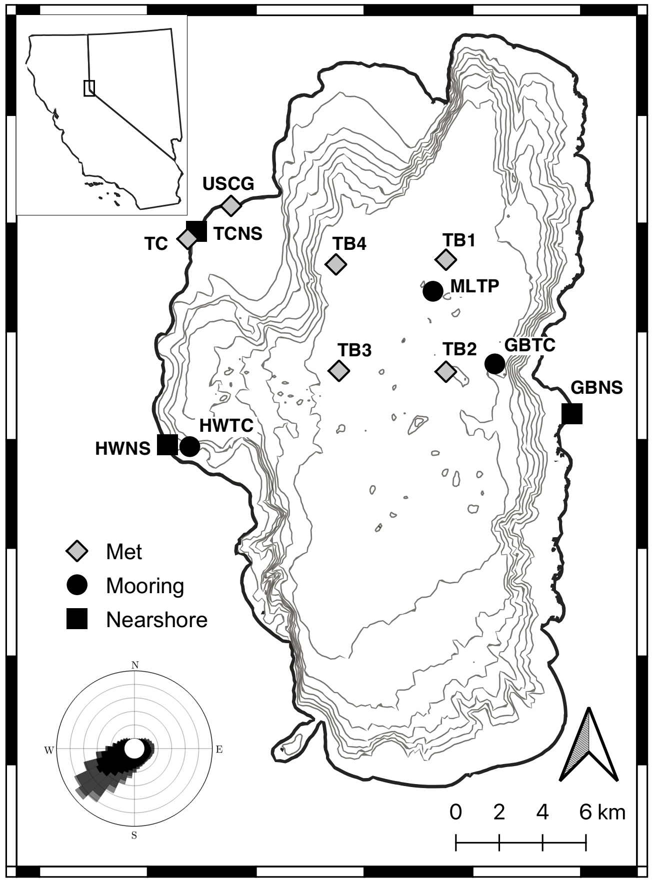

Figure 3.1. *Location and bathymetric map of Lake Tahoe. Marker indicates type of monitoring data collected each site. Monthly CTD profiles are collected at MTLP. Grey lines indicate 50 meter depth contours. Wind rose denotes the prevailing wind direction from 2008 to 2023.*

Both locations were over 460 m depth. The MLTP thermistor chain comprised a mix of 22 OEI 9311 and RBR TR-1000F (0.003°C accuracy, 0.001°C resolution) thermistors spaced at 10 to 40 m intervals from 0.5 – 460 m sampling every 2 minutes. The GBTC thermistor chain contained 18 RBR SoloT and TR 1060 thermistors (0.002°C accuracy, 0.0002°C resolution) spaced at 5 to 40 m intervals from 5 – 460 m sampling at 30-second intervals. The GBTC also contained an RBR concerto CTD equipped with a RINKO optical DO sensor (2% accuracy, <0.04% resolution) at 460 m recoding at 10 min intervals.

The DO sensor was calibrated pre / post-deployment in 0% and 100% solutions and data corrected for drift as necessary. During the 2022-2023 winter, data from an additional thermistor chain on the west side of the lake near Homewood (HWTC), which recorded temperatures down to 135.5 m, was used (**Table B.2** Monitoring Metadata). Nearshore surface temperature data was recorded by a network of RBR concerto CTDs deployed at a depth of 2 m around the perimeter of the lake since 2014, of which three are used in this study: Tahoe City (TCNS), Homewood (HWNS), and Glenbrook (GBNS). Monthly temperature, conductivity, and DO profiles were collected via a Seabird 19+ / 25+ at MLTP since 2006. Density was calculated using the Chen and Millero (1986) equation, accounting for temperature, salinity (conductivity), and pressure effects. Wintertime salinity profiles showed negligible variation with depth (**Figure B.3** Thermistor Chain and CTD Data, ±0.002 PSU), so a constant salinity of 0.042 PSU throughout the water column was used in calculations.

Air temperature, relative humidity, atmospheric pressure, short- and long-wave radiation, and wind were measured at the US Coast Guard Station (USCG) since November 1998 at 10 min intervals. Since 2006, four moored buoys (TB1-TB4) operated by the NASA-JPL have also recorded on-water wind speed and direction. Data from all locations were used to create a continuous meteorological record from 1998 to 2023. Wind speeds measured at the offshore NASA buoys were 35% greater than the shoreline USCG measurements, so a correction factor of 1.35 was applied to the USCG records. Historical daily air temperatures (1920-2023) were obtained from a meteorological station in Tahoe City (TC, USC00048758).

Estimates of winter inflow volume were calculated to determine the extent to which stream inflows contributed to deep water cooling during the late winter. We calculated daily inflows from November 1 to April 1 as a mass balance of the change in lake level (USGS 10337000), minus the daily evaporation rate estimated from the latent heat flux (Brutsaert 1982), and outflow discharge to the Truckee River (USGS 10337500), Tahoe's only outlet.

3.2.3 Estimates of Deep Mixing in Tahoe

The timing and depth of maximum winter mixing (WMD) in Lake Tahoe has been quantified annually since 1973. Historically, the WMD was estimated from the depth of the nitracline (Goldman et al., 1989; Paerl et al., 1975) as the resolution on thermistors was insufficient to resolve temperature differences in the hypolimnion. The WMD was considered to be the deepest sampling point that the nitrate gradient measured from a depth of 10 m was <0.02 µgL^{-1} m^{-1}. However, due to the 50 m vertical resolution of water sampling and the monthly frequency, these estimates had uncertainties of two weeks and a depth of 50 m. In the last two decades, high accuracy thermistors have enabled more precise estimates of WMD, as well as the timing and duration of deep mixing, from water temperature. While the depth of the maximum density gradient is frequently used to delineate the base of the mixed layer (Wilhelm and Adrian 2007), this threshold can yield unrealistic fluctuations in the convectively mixed layer depth (h_{CML}) during weakly stratified conditions when a clearly defined thermocline is absent. Instead, we employed a temperature threshold of 0.02 °C difference from the surface to define h_{CML} (Augusto-Silva and MacIntyre 2019). A 3-Day zero phase filter (*filtfilt* MATLAB® function) was applied to temperature data when calculating h_{CML} in order to remove the influence of isotherm oscillations due to internal waves, which have expected periods 16 to 60 hours (Rueda et al., 2023).

Estimates from multiple datasets were combined to determine WMD for 50 years: the seasonal nitracline (1973-1997, 2000-2006) and h_{CML} from MLTP (1998-1999, 2007-2022) and GBTC (2023). During the four winters for which thermistor chains were deployed during turnover events (1998, 1999, 2019, 2023), we defined the onset of deep mixing as when the deepest thermistor recorded a sudden cooling of -0.02 °C, indicating the arrival of surface waters at the bottom of the lake. The end of the deep mixing period was defined as when the temperature difference between the surface and bottom of the lake consistently exceeded 0.15 °C for more than a 24 hour period.

3.2.4 Surface Heat Balance

Surface heat fluxes were calculated at an hourly timestep from 1998-1999 and 2008-2023 to determine the relative contribution of heat and momentum fluxes to h_{CML} deepening and changes in the lake's thermal energy during winter. Heat flux components were calculated with the Lake Heat Flux Analyzer MATLAB® package (Woolway et al., 2015). Given Tahoe's long residence time, the impact of inflows on the lake's daily heat budget can be ignored, and the effective surface heat flux (Q_{net}, W m^{-2}) can be expressed as:

$$Q_{net} = Q_s + Q_e + Q_{lw} + Q_{sw} \tag{3.1}$$

where Q_s is sensible heat flux, Q_e is latent heat flux, Q_{lw} is net longwave radiative heat flux, and Q_{sw} is the absorbed incoming shortwave radiation accounting for the albedo at the water surface. The cumulative heat flux (Q_{net_total}) over monthly and seasonal timescales was calculated as:

$$Q_{net\_total} = \int_{t_1}^{t_2} Q_{net}\ dt \tag{3.2}$$

where t_1 and t_2 are the starting and ending dates respectively. The surface buoyancy flux (B_0, $m^2\ s^{-3}$), representative of the potential energy produced within the convectively mixed surface layer, was estimated as:

$$B_0 = g\frac{agQ_{net}}{\varrho_w C_p} \tag{3.3}$$

where g is the acceleration due to gravity (m s^{-2}), C_p is the specific heat capacity of water (4190 J kg^{-1} $°C^{-1}$), a is the thermal coefficient for the expansion of water ($°C^{-1}$), and ϱ_w is the density of the mixed layer (kg m^{-3}). Negative values of B_0 indicate destabilizing surface buoyancy fluxes (i.e., plunging down). The wind-induced surface shear velocity (u_*, m s^{-1}) was calculated as:

$$u_* = \sqrt{\frac{\tau_S}{\rho_w}} \tag{3.4}$$

where τ_s (kg m^{-1} s^{-2}) is the shear stress at the water surface parameterized as:

$$\tau_s = \varrho_a C_D u_{10}^2 \tag{3.5}$$

where ρ_a is the density of air (kg m^{-3}), C_D is the surface drag coefficient, and u_{10} is the wind speed at a height of 10 m (m s^{-1}). Time-varying estimates of C_D and ρ_a were calculated as a function of wind speed and air temperature/pressure respectively (Woolway et al. 2015).

3.2.5 Characterization of Mixing and Stability

Water column stability was evaluated with the square of the Brunt–Väisälä buoyancy frequency (N^2), Schmidt stability (S_T), Lake Number (L_N), and Wedderburn Number (W), using the Lake Analyzer MATLAB® toolbox (Read et al. 2011; see S1 for derivations). Turbulent kinetic energy (TKE) is a measure of the intensity of turbulence which provides energy for mixing and deepening of h_{CML} (Kraus & Turner, 1967). The relative contributions of both convective cooling and wind shear to vertical mixing and deepening of the surface mixed layer was evaluated by comparing $\mathbf{u}_*$ to the Deardorff vertical convective velocity scale (w_*), calculated during cooling periods as:

$$w_* = (h_{CML} B_0)^{1/3} \text{ for } B_0 < 0 \tag{3.6}$$

In this study TKE input to the mixed layer (TKE_{total}) was estimated from the kinetic energy imparted from gravitational instabilities generated by surface cooling (TKE_{conv}) and wind-driven shear (TKE_{wx}) defined by Imberger (1985) as:

$$TKE_{total} = TKE_{conv} + TKE_{wx} = \frac{1}{2}\left(w_*^3 + C_N^3 u_*^3\right) \tag{3.7}$$

where $C_N = 1.33$ is an empirical coefficient related to wind energy utilization for turbulent mixing. The Monin-Obukhov length scale (L_{MO}) provides an estimate of the depth to which wind-induced shear dominates the production of TKE, below which turbulent fluctuations are controlled by buoyancy fluxes, and defined as (Thorpe, 2007):

$$L_{MO} = -\frac{u_*^3}{k\, B_0} \tag{3.8}$$

where k is the von Karman Constant (0.41).

3.2.6 Spectral Analysis

The internal wave field was characterized using power spectra of the integrated potential energy (IPE) (IPE) at time t defined in Antenucci et al. (2000) as:

$$\text{IPE}(t) = \int_{z_0}^{z_1} \varrho(z,t)\, g\ z\ dz \tag{3.9}$$

where z is depth (m) with z_0 and z_1 representing the surface and deepest layers, respectively, and $\varrho(z,t)$ indicates the water density at a given depth and time. The IPE gives an indication of the frequency content of the internal wave field and the relative distribution of potential energy among frequencies.

3.2.7 Correlation Analysis

The significance of meteorological conditions and lake stability on WMD was assessed via Pearson's correlation coefficient between WMD and monthly integrated heat fluxes, mean air temperature, wind speed, and S_T for winters of 1998-1999 and 2008-2023. These subsets of years were selected because WMD could be more precisely determined from temperature data. The impact of large-scale climate variability was also assessed by including the monthly Pacific North American Index (PNA) as a predictor variable. PNA is a measure of the atmospheric circulation patterns in the Pacific Ocean off North America and is related to the El Niño-Southern Oscillation (ENSO). During El Niño events, the PNA index tends to be positive leading to a greater likelihood of warm and dry conditions in the western United States (Rodionov & Assel, 2001).

3.3 Results

3.3.1 Meteorological Forcing

Lake Tahoe's surface heat flux fluctuates seasonally (**Figure 3.2**). Monthly mean air temperature (± S.D.) ranged from 1.2 ± 2.6 °C in January to 18.3 ± 1.2 °C in August, while monthly wind speeds varied inversely with a minimum of 2.74 ± 0.8 m s^{-1} in August to a maximum of 5.5 ± 3.1 m s^{-1} in October.

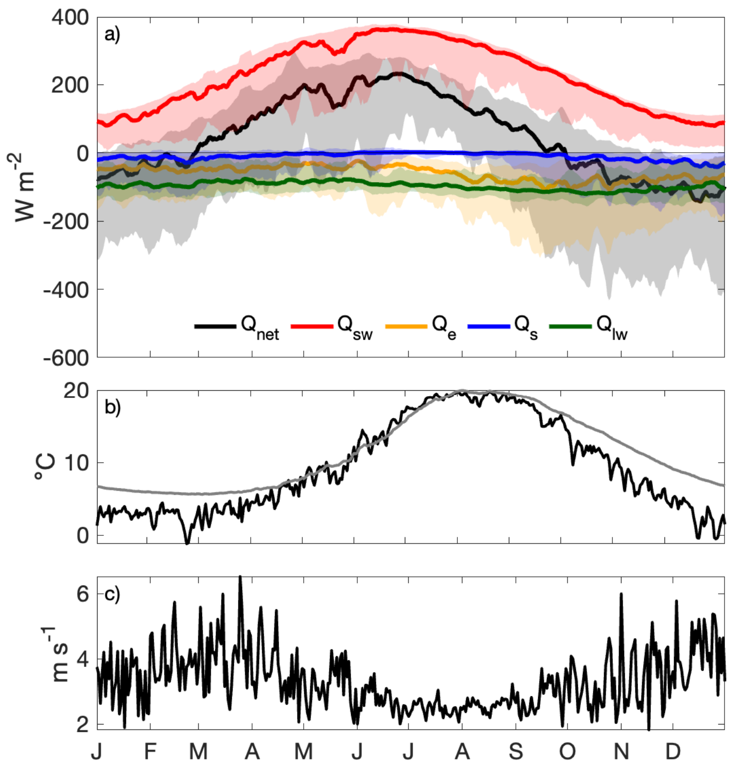

Figure 3.2. *a) Daily average surface heat fluxes (2007 – 2022). Shaded areas indicated 95% confidence interval. B) Daily average air temperature (black) and lake surface water temperature (grey). C) Daily average wind speed.*

From March through August, air temperatures were consistently warmer than the lake surface temperatures and shortwave radiation yielded a net heat flux into the lake. While maximum Q_{net} occurred in June, the lake continued to gain heat through August. September through March had a negative surface heat flux as declining air temperatures and higher wind speeds increased sensible and latent heat losses. While outgoing longwave radiation was consistently the largest heat loss mechanism throughout the year (-120 to -

76 W m^{-2}), sensible (-44 to 2 W m^{-2}) and latent heat (-107 to -23 W m^{-2}) losses were higher during the autumn and winter than in summer.

3.3.2 Characteristics of Lake Tahoe's Hypolimnion

Deep water temperatures display a "sawtooth" pattern, frequently observed in oligomictic lakes (Livingstone 1997), with multi-year periods of warming punctuated by abrupt cooling events during isothermy (**Error! Reference source not found.**). Vertical m ixing generally extended to a depth of <250 m. Below this depth, the hypolimnion remained stably stratified in the absence of turnover. A linear regression of bottom water temperatures indicates the hypolimnion warming rate was 0.037 ± 0.0013 °C year^{-1} between 2008 and 2019. The hypolimnion warmed faster during the autumn and winter when stratification was weakest. Sub-daily oscillations in hypolimnion temperature occurred throughout the year, with temperature fluctuations on the order of 0.01 °C, with isotherm amplitudes of 10 m, in the summer and 0.1 °C, with amplitudes of 100 m, in the winter, indicative of internal waves (Lemmin 2020). The dominant wintertime temperature oscillations in the deep hypolimnion fluctuated in the subinertial range of 16.5-19 hours, consistent with Poincaré waves (Rueda et al., 2003a; Sprague, 2013, McInerney et al., 2019).

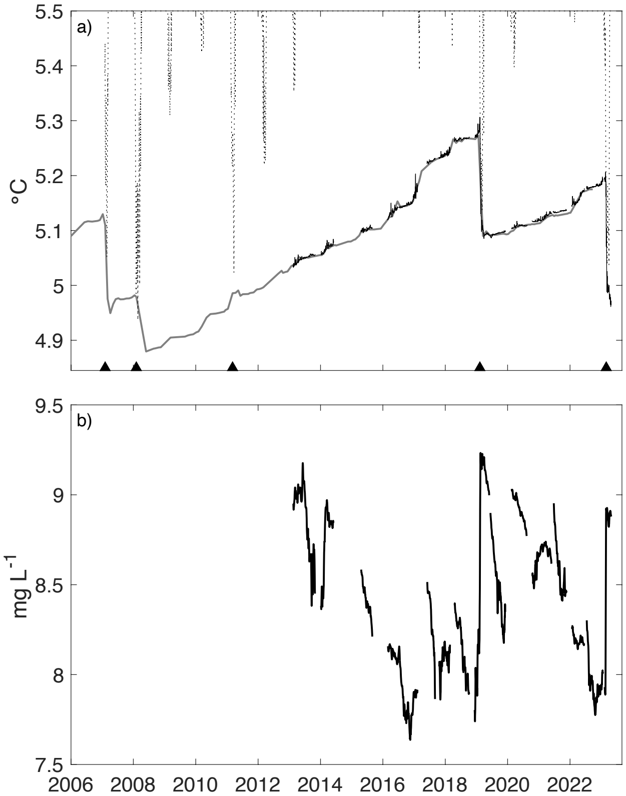

Figure 3.3. *a) Time series of temperature at surface (dotted) and at 400 m depth (solid) recorded at GBTC (black) and CTD profiles at MLTP (grey). Triangles indicate deep mixing events. B) DO measured at 460 m at the base of GBTC.*

Hypolimnion DO declined during consecutive years of warming and rebounded to near-saturated levels following deep mixing events. DO was continuously depleted from March to September each year, at rates ranging from -0.1 to -0.3 mgL^{-1} month^{-1}. DO increased during autumn and winter when either partial or complete vertical mixing occurred, offsetting much of the summer decline. The DO increases during partial deep mixing suggest mechanisms other than vertical convective mixing can contribute to deep water ventilation during weekly stratified conditions. *In situ* observations and modeling results have shown that wind-driven upwellings/downwellings ventilate the lake to depths of at least 135 m (Valbuena, in review).

3.3.3 Historical Record of Winter Mixing Depth (WMD)

Between 1973 and 2023, WMD ranged from 80 m (2015) to the full depth with a median depth of 270 m ± 130 m (Error! Reference source not found.). The WMD typically o ccurred in February through early March when surface temperatures reached their annual minimum and thermal stratification was weakest.

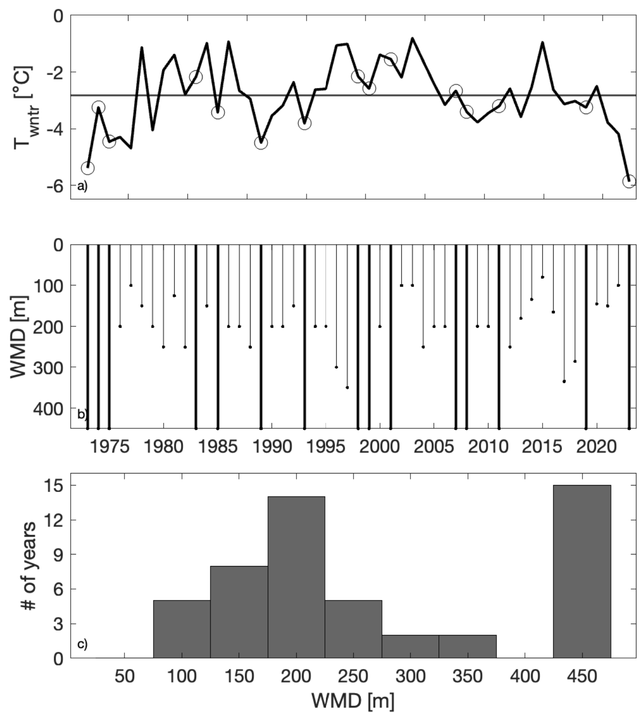

Figure 3.4. *a) Annual mean winter (Dec – Mar) air temperature (T_{wntr}) recorded at Tahoe City (TC). Horizontal line is 50-year average. b) Maximum winter mixing depth from 1973 to 2023. Circles in a) and thick lines in b) indicate turnover years. c) Frequency distribution of maximum winter mixing depth.*

Complete turnover occurred 15 times during this 50-year span with a return period of 1 – 8 years. Average winter (December-April) air temperatures at Tahoe City (TC) were 0.8 °C cooler during deep mixing years (2.35 °C) compared to partial mixing years (3.16 °C). A Mann-Kendall trend test indicated that long-term trends in WMD and the frequency of turnover were not statically significant. A Runs test for randomness indicated that WMD was not autocorrelated and that the return period of deep mixing events was not significantly different from a random distribution, suggesting that WMD was not related to climatic periodicity. WMD was bimodally distributed with peaks at 200 m and 450 m (the maximum sampling depth, and assumed to be complete turnover). There were only four observations of mixing depths between 250 and 350 m and no observations at 400 m. Thus, the lake mixed down to a depth <350 m in approximately 70% of winters, but when WMD exceeded this depth, complete turnover inevitably occurred.

Correlation analysis revealed that WMD is strongly dependent on the intensity of cooling during the late winter and less sensitive to initial winter stratification conditions (i.e., the lake's thermal structure at the end of autumn).Error! Reference source not found.**a** depicts how the cross correlation of WMD with S_T and Q_{net_total} varies at daily lag increments during the preceding 8 months. While the correlation between S_T from the preceding summer and WMD is not significant, correlation strength progressively increases throughout the autumn and early winter, and asymptotes near the highest correlation 30 days prior to March 1 (r = -0.71, p = 0.003). Q_{net_total}, which represents the cumulative heat flux between a given date and March 1, similarly shows the strongest correlation at a lag of 64 days (r = -0.81, p < 0.001). We therefore focus on the winter months (December–March) for further analysis.

Both winter air temperature and wind speed were strongly linearly correlated to WMD (**Figure 3.5b**). Monthly averages from December through February showed progressively stronger correlations to WMD, with February air temperature (r = -0.86, p < 0.001) and wind speeds (r = 0.65, p = 0.003) being the most significantly correlated. Except for the winters of 2008 and 2017, turnover occurred each winter when the mean February $AirT$ <0 °C or when February Wx > 5 m s^{-1}. Consequently, there was a strong correlation between the cumulative monthly sensible and latent heat fluxes, with the February Q_s displaying the highest correlation (r = -0.78, p < 0.001). Correlations of winter air temperature with mixing depth have previously been seen for Lake Geneva (Schwefel et al. 2016) and Lake Zug (Schwefel et al. 2019), though wind speed was more strongly correlated in Tahoe than in these lakes. As previously noted, the lake's thermal stability at the start of winter was weakly correlated with WMD (r = -0.23, p = 0.4). The PNA non-significantly correlated (p > 0.2) throughout all winter months, suggesting that climatic oscillations associated with ENSO may not influence deep mixing in Lake Tahoe.

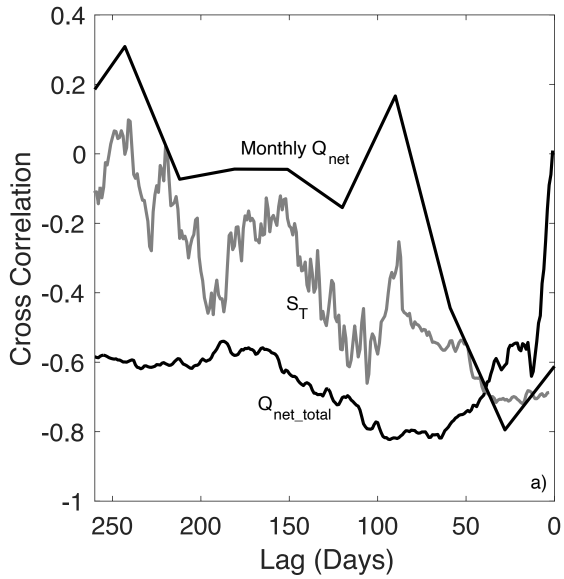

	Dec	Jan	Feb	Mar	JFM
Q_s	-0.07	-0.54*	-0.78**	-0.48*	-0.83**
Q_e	0.05	-0.38	-0.54*	-0.31	-0.59*
Q_{sw}	0.01	-0.20	-0.42	-0.20	-0.35
Q_{lw}	0.02	-0.23	-0.23	-0.05	-0.22
Q_{net}	-0.08	-0.54*	-0.81**	-0.61*	-0.83**
AirT	0.26	-0.62*	-0.86**	-0.64*	-0.84**
Wx	-0.26	0.48*	0.65*	0.38	0.69*
PNA	0.06	-0.22	-0.31	0.17	-0.12
S_T	-0.23	-	-	-	- b)

]

***Figure 3.5**. a) Time series of cross correlation (lagged Pearson correlation) of WMD with daily Schmidt stability (S_T) and cumulative net surface heat flux (Q_{net_total}) at daily lags and cumulative monthly net surface heat flux (Monthly Q_{net}) at monthly lags between March 1 and preceding 9 months. b) Pearson correlation coefficients (r) between winter monthly cumulative sensible (Q_s), latent (Qe), net shortwave (Q_{sw}), net longwave (Q_{lw}), and cumulative (Q_{net}) heat fluxes, (AirT) air temperature, wind speed (Wx) , PNA index and ST with maximum winter mixing depth (Columns 1-4). Column 5 shows same calculations for the winter period of January 1 - March 31. * and ** indicates significant $p < 0.05$ and $p < 0.001$ respectively*

3.3.4 Hydrodynamics of Deep Mixing

The hydrodynamic response was assessed by comparing the thermal structure of the lake during four winters during which complete turnover occurred (1998, 1999, 2019, and 2023) against two years in which the WMD was comparatively shallow (2018 and 2021, Error! Reference source not found.). **Figure 3.6** provides a schematic of four periods identified during deep mixing winters as characterizing deep mixing: (1) deepening of the surface mixed layer in early winter, (2) a transitional period with high amplitude internal waves and the disappearance of a distinct thermocline, (3) turnover and deep water renewal when the lake is briefly isothermal (4) continued bottom cooling lake due to the arrival of cold littoral water. The following sections describe the processes occurring during each stage.

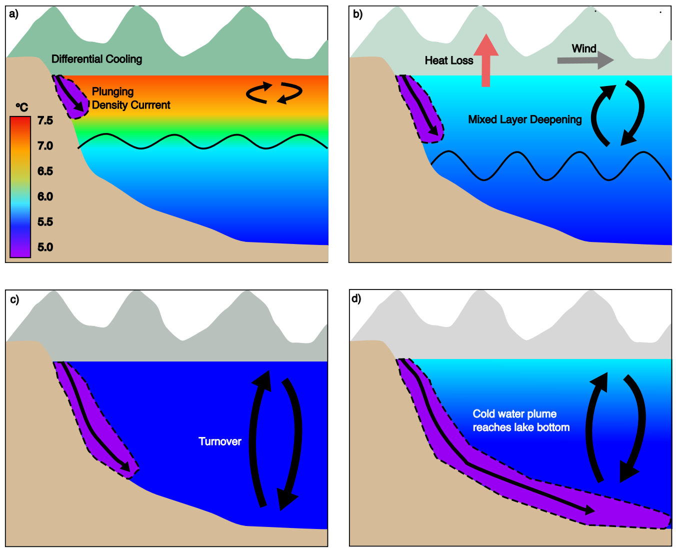

Figure 3.6. *Schematic overview of hypothesized evolution of Tahoe's thermal structure during deep mixing winters. a) Lake is thermally stratified with seasonal differential cooling in littoral zone generating shallow plunging density currents. b) Heat loss and wind stirring deepen surface mixed layer and weaken density gradient at thermocline. C) Lake becomes isothermal facilitating vertical mixing throughout the water column. d) Plunging cold water reaches lake bottom while epilimnion begins to reform.*

(1) Surface Layer Deepening

At the start of each winter, Lake Tahoe exhibited a classic thermal structure (**Figure B.2**) with a mixed surface layer extending to a depth of 40-50 m. The lower bound is delineated by a temperature difference >0.15 °C from the surface and corresponds with $N^2_{max} \approx 10^{-4}$ s^{-2}. DO concentrations; however, remained uniform down to a depth of 75 m. The hypolimnion was weakly thermally stratified with a vertical temperature gradient of 0.0004 °C m^{-1}. In all winters, initial surface water temperatures were within a degree (7.71

°C – 8.70 °C), except December 1998 when temperatures were considerably cooler (6.30 °C). Bottom temperatures ranged from 5.05 °C (December 1998) to 5.27 °C (December 2018), with higher temperatures reflecting prior years of incomplete winter mixing. Initial daily average Schmidt stability ranged from 4,000 J m^{-2} in 1998 to 12,000 J m^{-2} in 2021.

Throughout December and January, the surface mixed layer cooled at a quasi-linear mean rate ranging from 0.30 – 0.65 °C day^{-1} across the six winters (**Figure 3.7**). As h_{CML} deepened, temperatures below the thermocline initially rose and then cooled. The mixed layer deepened faster during complete turnover years (1.91 – 3.76 m day^{-1}) than in partial mixing years (0.99 – 1.11 m day^{-1}), due to a greater net loss of heat and higher input of TKE (**Figure 3.7d,f**). During the four deep mixing winters, the net heat loss from December through January ranged from 907 – 1,066 mJ m^{-2} compared with 737 – 877 mJ m^{-2} during the partial mixing winters (**Figure 3.7b**). While the rate of heat loss was similar for all years in December, surface temperatures during the deep mixing winters were lower in January because of increasing sensible heat losses (**Figure 3.7a**). Total TKE input through February 1 during the four turnover winters exceeded that during the partial mixing winters. Turbulence induced by convection was the dominant source of TKE driving mixed layer deepening during the early winter in all years as TKE_{CONV} = 56 – 76% of the total TKE input from December through January (**Figure 3.7f**).

During this phase, internal waves continued to propagate through the stratified hypolimnion with spectral density peaks of the IPE just below the lake's inertial frequency of 19 hours (Rueda et al., 2003). As the hypolimnetic stratification decreased the internal waves increased in amplitude, with isotherm oscillations up to 40 m. **Figure 3.8** displays the evolution of the internal wave field as the mixed layer deepened in winter 2018/19 by comparing IPE during consecutive overlapping 30-day windows. At the beginning of December, a clear superinertial peak at 17 hours was evident. As stratification declined, this spectral peak gradually shifted from 17 to 19 hours, the inertial frequency defining the lower limit for inertial wave propagation and was progressively dampened. By February, a clear peak in the IPE was no longer evident.

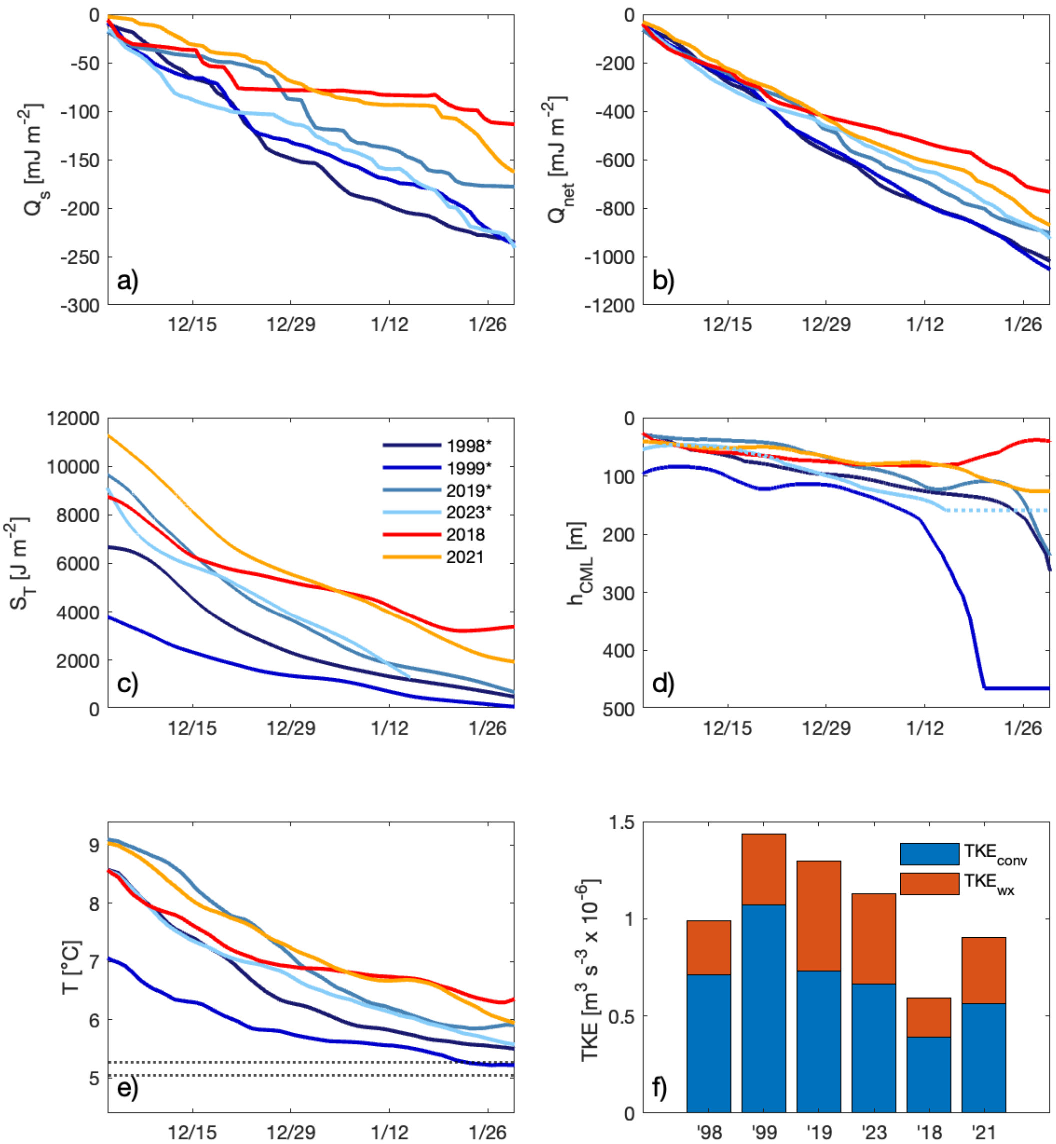

Figure 3.7. *a-b) Cumulative latent (Q_s) and net (Q_{net}) heat fluxes, c) Schmidt stability (S_T), d) mixed layer depth (h_{CML}), e) surface water temperature and f) cumulative TKE input during the mixed layer deepening period (December 1 – February 1). Asterix indicate years of full turnover. Dotted line from winter 2023 in d) is linearly interpolated when sensor was out of water. Dotted horizontal lines in e) indicate range of bottom temperatures.*

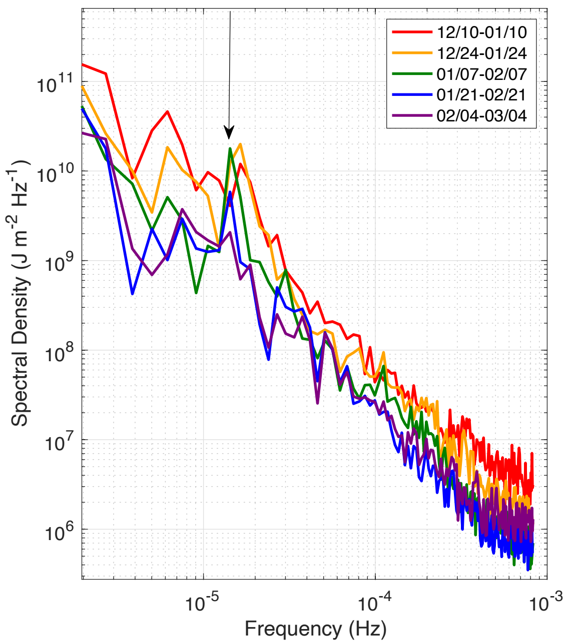

Figure 3.8. *IPE calculated for overlapping 30-day windows during the 2018/19 winter. Black arrow indicates the inertial frequency of the lake.*

(2) Transition to turnover

During the deep mixing winters, the h_{CML} deepening rate accelerated through February, (11.1 – 28.6 m day^{-1}). When the mixed layer surpassed a depth of 250 m, the local buoyancy frequency at the thermocline was within 1% of the background stratification (**Figure 3.9**), and thus a distinct separation of the epilimnion and hypolimnion was no longer apparent. We use this 1.01 threshold of the ratio of local to background stratification to denote the transition between the stably stratified period and onset of turnover. During this period, regular sinusoidal isotherm oscillations were no longer apparent and density stratification was primarily maintained by pressure effects. While the Wedderburn remained on the order of 10, the Lake Number frequently dropped below 1 during this transitional period (**Figure 3.9**), indicating shear induced by wind was sufficient to cause upwelling or deep mixing through water column (MacIntyre et al., 2009). Since W does not account for a lake's bathymetry, increasing mixed layer depth under weakly stratified conditions can result in large W relative to L_N (Saber et al., 2020). This transitional period lasted for between 4 and 14 days before vertical mixing penetrated to the deepest layers of lakes.

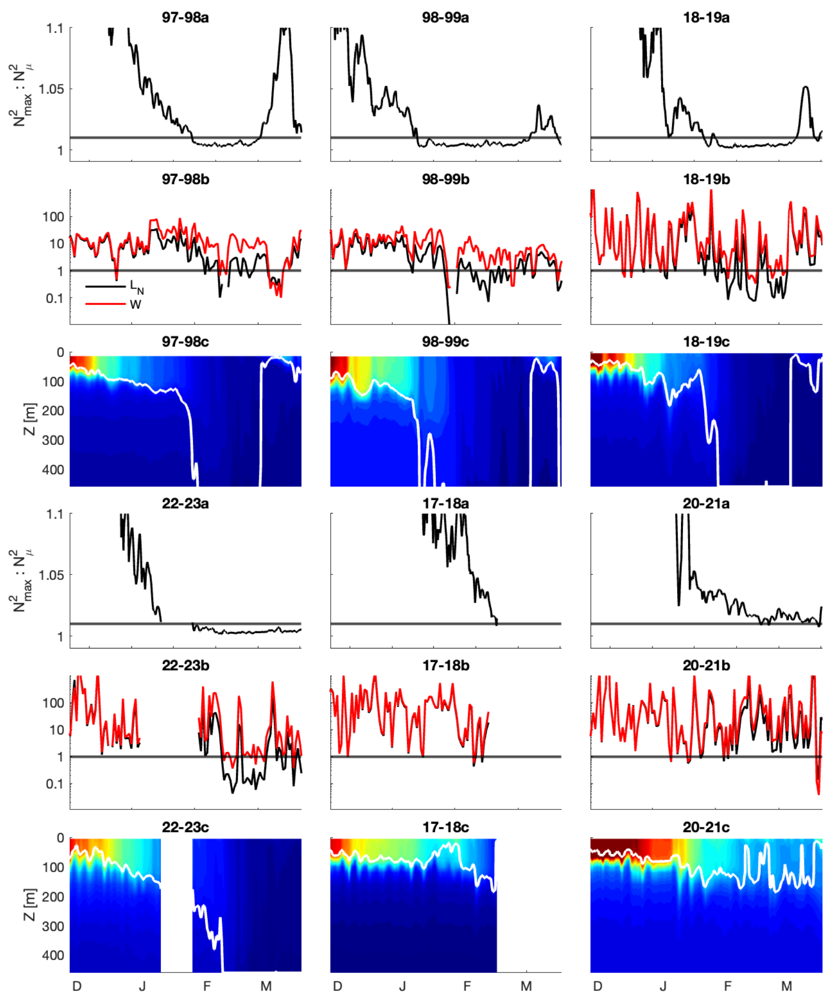

Figure 3.9. *Time series of the ratio of the buoyancy frequency at base of the mixed layer to background stratification, Lake Number (black) and Wedderburn Number (red) and temperature structure with mixed layer depth highlighted by white line during the winters of 1997/99, 1998/99, 2018/19, 2022/23, 2017/18, and 2020/21. Black horizontal line on Lake Number and Wedderburn Number plots indicates a threshold of 1.*

(3) Turnover and Renewal

Temperature and DO measurements below 450 m confirm that the mixed layer reached the lake bottom and turnover occurred on four specific dates: February 25, 1998; February 14, 1999; February 10, 2019; and February 24, 2023. Each event was preceded by a week during which average air temperatures <0 °C and, except for 1998, persistently high winds above 6 m s^{-1} (**Figure 3.10**). These combined factors resulted in distinct episodes of strongly negative heat fluxes during late winter.

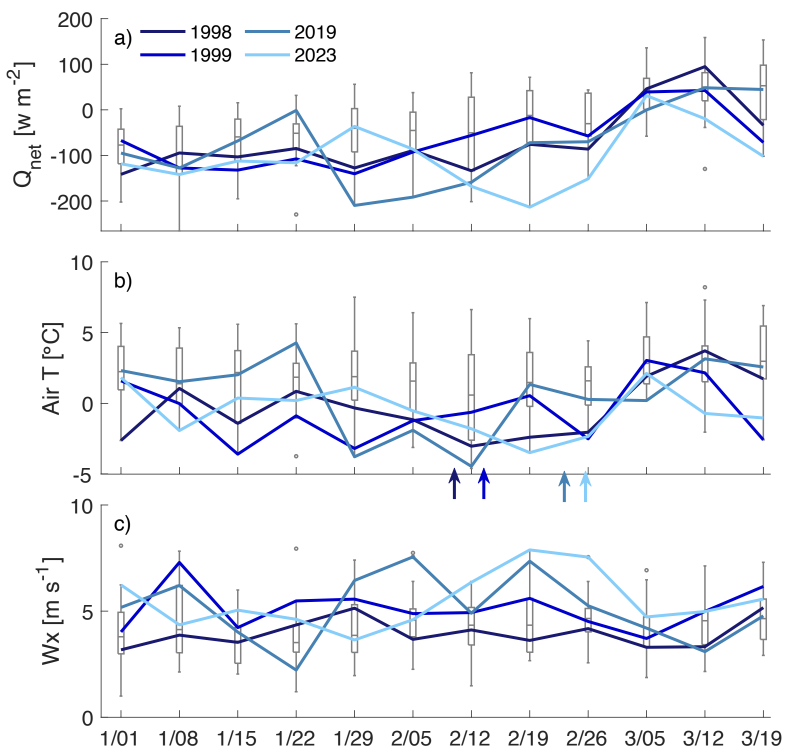

Figure 3.10. *Boxplots of weekly averages of a) net surface heat fluxes, b) air temperature, c) wind speeds during From January – March (1998-1998, 2008-2023). Colored line shows weekly averages for selected winters. Arrows indicate date of turnover.*

Prior to turnover, bottom temperatures remained steady with fluctuations on the order of 0.005 °C. Approximately six hours before each deep mixing event, lower temperatures were progressively observed at each thermistor below 300 m, eventually reaching the lake bottom (**Figure 3.11**). The sequential cooling at progressively deeper depths strongly suggests that mixing at this stage was primarily due to vertical, convectively-driven processes.

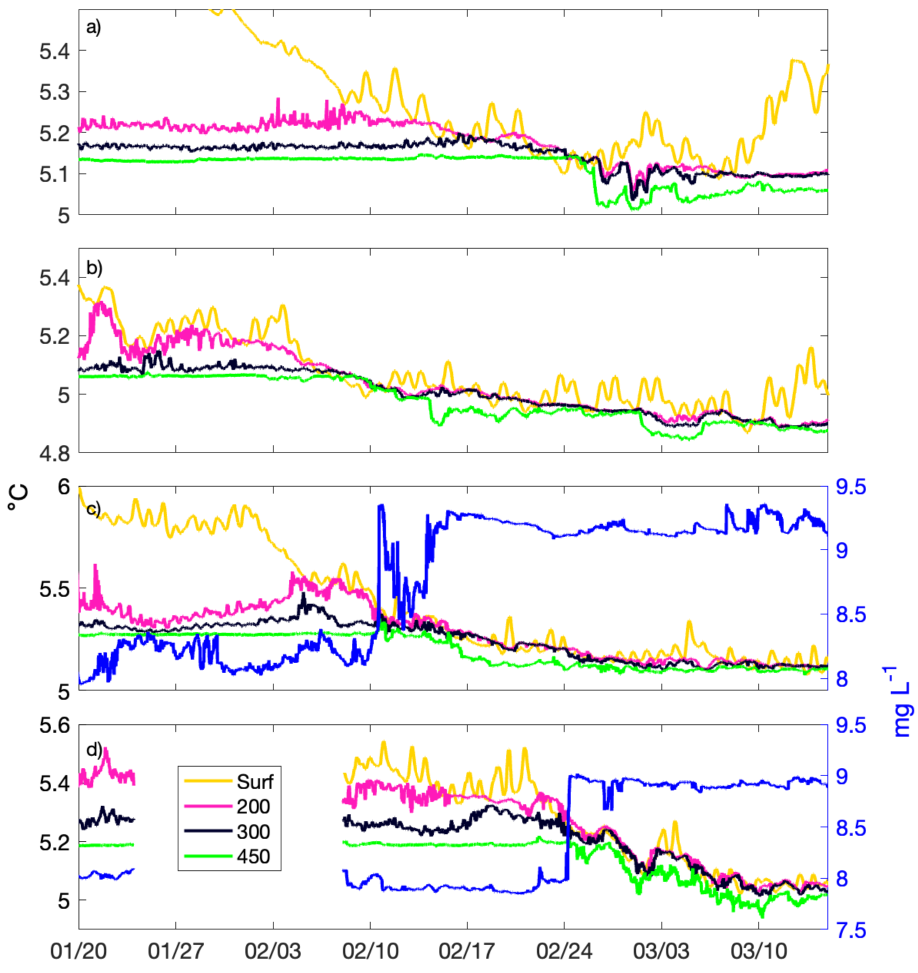

Figure 3.11. *Surface and hypolimnion temperature and dissolved oxygen (460 m) in the deep hypolimnion during turnover events in February and March of a) 1998, b) 1999, c) 2019 and 2023. Temperatures were interpolated to 100 m depth intervals for comparison.*

The onset of turnover was initially signaled by a small increase in bottom temperature, due to the entrainment, subsequently followed by cooling of the entire water column. Once the lake was isothermal, bottom DO increased to near-saturation levels within hours. On February 10, 2019, bottom DO, which typically fluctuates by <0.1 mgL^{-1} day^{-1}, increased sharply from 8.41 to 9.35 mgL^{-1} in the four hours immediately after the mixed layer reached the lake bottom, while on February 24, 2023, DO rose from 7.99 to 8.96 mgL^{-1} over the same time span.

(4) Littoral Convection and Deep Cooling

Isothermal conditions persisted for less than 48 hours after turnover in all years before bottom temperatures cooled below that of the overlying water. This period, when the temperature difference from top to bottom remained <0.15 °C, lasted between 11 (1998) and 57 days (1999). The deep hypolimnion continued to cool despite the absence of isothermal conditions above, as had been observed prior to turnover. For example, after turnover on February 26, 1998, the entire water column was 5.12 ± 0.003 °C. While temperatures above 300 m stabilized at this temperature, temperatures at 450 m continued to cool reaching a final temperature of 5.06 °C by the end of March. **Figure 3.12** illustrates that during each winter this cold water, initially detected at the bottom of the lake, was gradually observed at shallower depths, filling the deep hypolimnion from the bottom up. A plausible rationale for this observation is the presence of lateral flows generated from cool water formation in the shallow shelves and littoral regions.

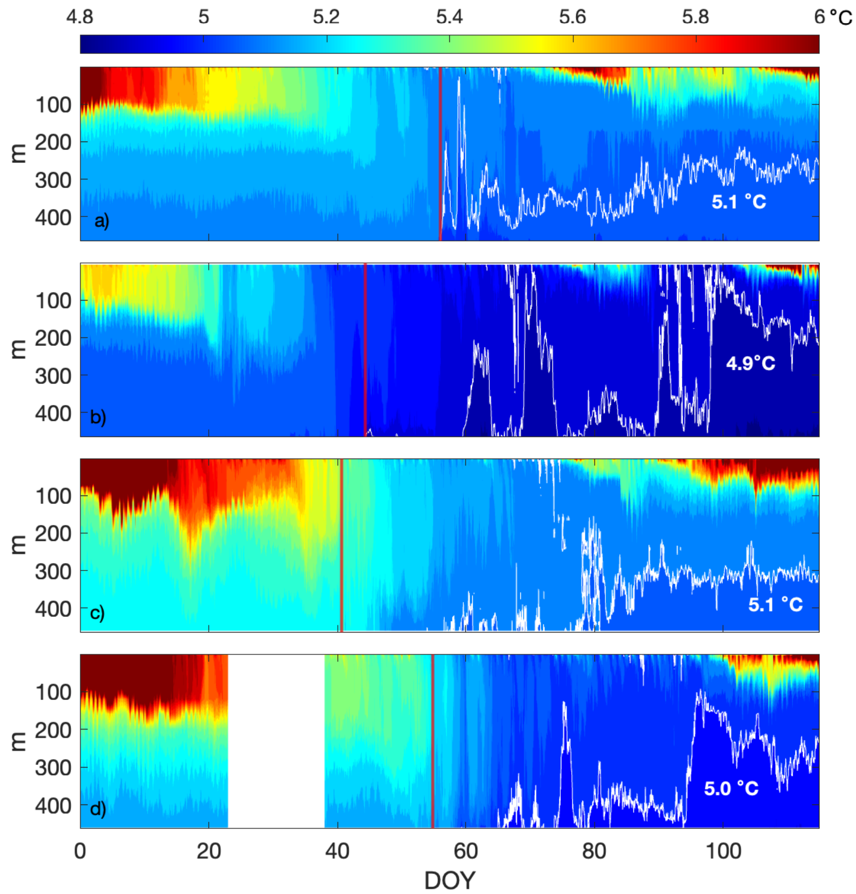

Figure 3.12. *Thermal structure of lake during winters of a) 1998, b) 1999, c) 2019, d) 2023. Red vertical lines indicate onset of turnover. White isotherm denotes cold water observed to fill the deep hypolimnion from the bottom.*

During the 2022/23 winter, lateral temperature differences were observed in both surface waters and deeper in the water column confirming the potential for horizontal density currents (**Figure 3.13a,b**). Throughout December 2022 and January 2023, surface temperatures measured at Tahoe City (TC), where a relatively shallow shelf extends out approximately 4.5 km, remained colder than offshore surface temperatures by ~1 °C. By February, nearshore surface temperatures cooled significantly, dropping below 4 °C when deep mixing occurred. This cool, littoral water had the potential to plunge to the lake bottom, entraining ambient water as it did so. Horizontal temperature differences were also observed between Tahoe's shallower western shoreline (HWTC) and deeper eastern shoreline (GBTC, **Figure 3.13c**). Temperatures at 110 m depth at HWTC were consistently 0.1 °C colder than at a comparative 100 m depth at GBTC throughout the winter. Following turnover, water at 100 m at HWTC cooled below the water at 450 m at GBTC. The 100 m HWTC thermistor also record several events where bottom water temperatures cooled dramatically while overlying layers remained warmer (e.g., February 7, 12, 15) suggesting lateral intrusions of plunging cold water passing by the lake bottom at Homewood. Observations of the horizontal variability of both surface and deep water temperatures indicate significant spatial variations in cooling rates across the lake due to heterogenous lake bathymetry which provide the potential for convectively driven density currents.

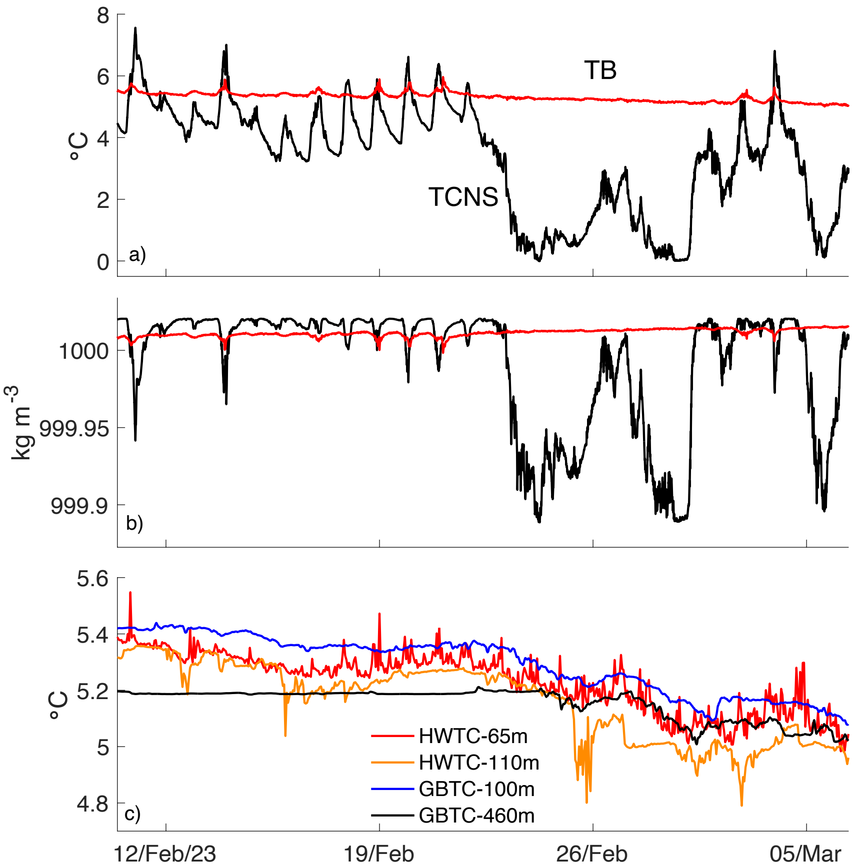

Figure 3.13. *Horizontal temperature variability during 2023 deep mixing event. a) nearshore surface temperature and b) derived water density measured at Tahoe City (black) and average offshore surface temperature measured at TB 1-4 (red). c) temperatures measured at depths of 65 m and 110 m at HWTC and 100 m and 460 m at GBTC.*

3.4 Discussion & Conclusions

The analysis of 50-years of monitoring data from Lake Tahoe indicates that there has not been a significant decline in the frequency of deep mixing events despite increasing water temperatures and increasing stability of the water column (Schladow et al., 2021). As a result, deep water DO concentrations have continued to remain relatively high in recent decades. Correlation analysis showed that late winter meteorology, particularly air temperature and wind speed, affected lake mixing patterns while the net heat flux during the summer and fall were weakly correlated. This finding suggests that the timing of the heat loss during the winter, rather than cumulative heat flux throughout the year determine whether or not the lake overturns. As the lake approaches isothermal conditions, three-dimensional process including lateral convectively-driven flows become increasingly important pathways for transporting cold oxygen-rich waters into the deep hypolimnion.

3.4.1 Drivers of Deep Mixing Events

The extent of WMD in Lake Tahoe was bimodally distributed, with peaks occurring at depths of 250 m and 450 m. As the h_{CML} deepens, S_T declines. At a depth of approximately 300 m, S_T approaches 0 (**Figure 3.7c**), implying that the amount of work required for complete mixing becomes vanishingly small far above the lakebed, and suggesting that the energy flux from even a single event (e.g., the passage of a cold front) could be sufficient to mix the water column to the lake bottom. Therefore, as previously suggested by Goldman (1989), complete mixing is primarily determined by the conditions during a narrow window of time in the late winter.

Correlations between February sensible and latent heat fluxes with WMD further suggest that the intensity of cooling at the end of the limnological winter largely determines the extent of deep mixing in Lake Tahoe. The lack of correlation with the

PNA index further indicate that deep mixing is largely determined by the serendipitous timing of storms at the end of the winter, not large-scale climatic oscillations. Similar observations have been made in Lake Maggiore (Ambrosetti & Barbanti, 1999) where the winter mixed layer depth was estimated as a linear function of solar radiation, wind speed and air-water temperature difference during winter months, with more weight given to meteorological conditions in the late winter. In Lake Tahoe, February meteorological conditions alone showed a stronger predictive power than including data from the entire winter (Error! Reference source not found.**b**). A simple multiple linear regression was d eveloped to predict WMD as a function of February air temperature and wind speed from 18 winters when the WMD could be precisely determined from lake temperature profiles (**Figure 3.14**). Due to the bimodal distribution of WMD, a stepwise threshold was applied so that when the modeled WMD exceeded 350 m it was assumed to extend down to the bottom. The observed and predicted mixing depths agreed well and the correlation was highly significant, (R^2 = 0.74, slope p <0.001, y-intercept p = 0.3, n = 18) further emphasizing the degree to which deep mixing in Lake Tahoe is primarily determined by late winter meteorology. The model fit did not improve when the initial thermal stability in December or shortwave radiation were included as additional explanatory variables. The lack of correlation of both the cumulative heat flux at lags greater than 90 days before March 1 and the stratification strength at the onset of winter with WMD suggests that while increasing warming and lake stability may make the lake less prone to deep mixing, turnover will likely continue to occur if the late winter meteorological conditions remain sufficiently cold and windy.

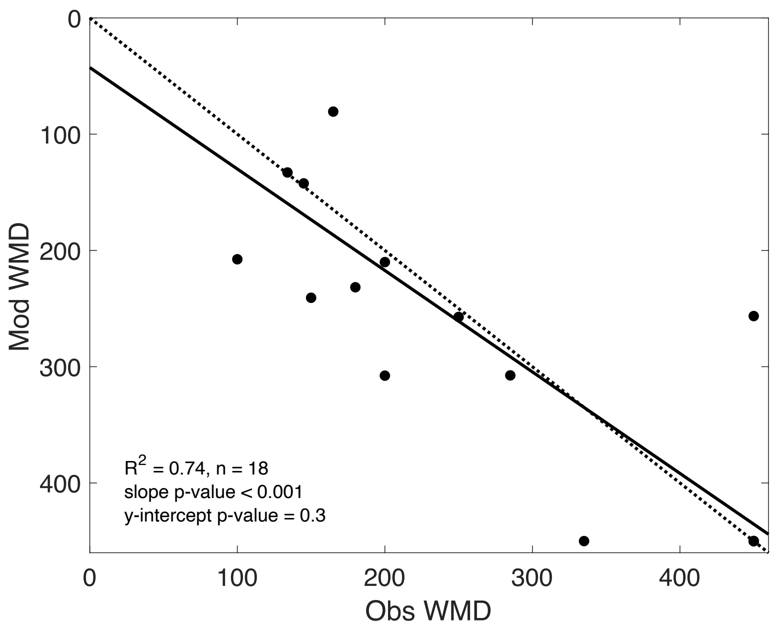

Figure 3.14. *Scatter plot of observed and predicted winter maximum mixing depth for 1998-1999 and 2008-2023. Dotted line indicates 1:1 line, black line indicates slope of model.*

3.4.2 Evolution of Winter Lake Thermal Structure

While winter mixing and transport of heat and oxygen in lakes can initially be described as a 1D vertical process, as stratification weakens 3D processes become increasingly important. Cooling, observed at progressively deeper depths, indicates the dominance of vertical penetrative convection in the early winter. For the six winters investigated, between 56-78% of the total TKE input during the first two months of the winter was contributed by convective cooling. Interannual variability in the rate of mixed layer deepening can be primarily attributed variations air temperature, and wind speed to a lesser extent. The Monin-Obukhov length scale was primarily between 10-50 m during the early winter, indicating the effects of turbulent mixing by wind are generally limited to the upper 50 m of the water column. We compared observed h_{CML} against a simple mixed layer model using the formulation of Batchvarova and Gryning (1991) where the deepening of h_{CML} is parameterized as a function of convective and wind-driven forcing:

$$\frac{dh_{CML}}{dt} = \frac{(1+2A)w_*^3 + Bu_*^3}{N^2 h_{CML}^2} \tag{3.10}$$

where the entrainment coefficients are $A = 0.2$ (Zilitinkevich, 1991) and $B = 2.5$ (Gryning & Batchvarova, 1990)and N^2 is the Brunt-Väisälä frequency at the mixed-layer interface. **Figure 3.15** shows a comparison of the observed and modelled mixed layer depth for three deep mixing winters. During the first two months, when the mixed layer deepens at a linear rate, the modelled and observed h_{CML} are in relatively close agreement (RMSE = 19 – 34 m). However, the two estimates of h_{CML} begin to diverge in the late winter when a distinct thermocline disappears. Once the strength of stratification at base of the mixed layer <1% greater than background stratification (denoted by vertical black line on **Figure 3.15**), the observed h_{CML} deepens at an increasing rate to the bottom of the lake, while the modeled mixing depth remains significantly shallower. The increasing discrepancy between the model and observed highlights the weakness of 1D models to accurately simulated lake thermal structure under weakly stratified conditions. During this transition period both Lake Number and Wedderburn numbers drop below 3.

Near-bed DO quickly rebounded to near saturated levels almost immediately after the lake became isothermal and oxygenated mixed layer water arrived at the bottom of lake. The rapidity with which bottom DO increases once the lake reaches isothermal conditions suggest that ventilation is occurring throughout the mixed layer as h_{CML} deepens. During the four deep mixing winters, the lake was isothermal for less than 48 hours each event, though the total difference in temperature between surface and bottom waters remained <0.15 °C for a subsequent 1 - 57 days following turnover. While the duration of this weakly stratified period following turnover may become shorter under a future, warmer climate, this data suggests that even if the lake remains isothermal for a few hours during a single frigid winter night, deepening of the h_{CML} during the preceding winter months can sufficiently oxygenate much of the deep hypolimnion, whereas ventilation at the sediment-water interface can occur quickly once the water column is isothermal.

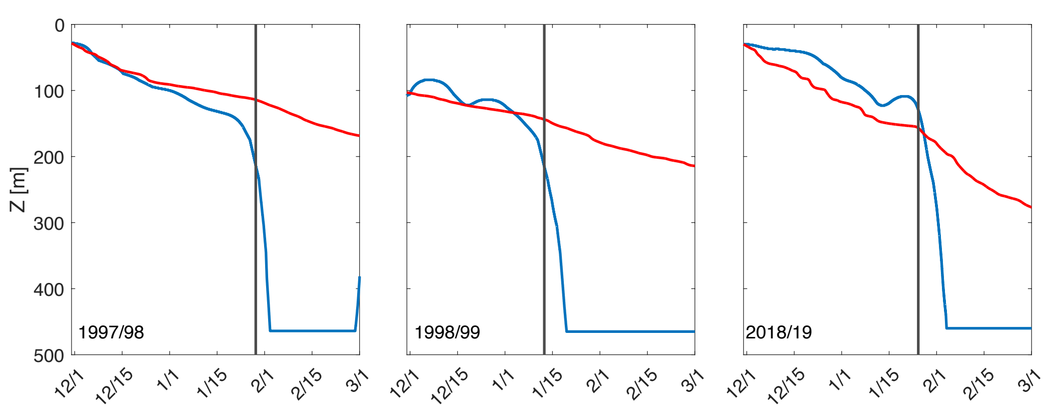

Figure 3.15. *Comparison of observed mixed layer depth, h_{CML}, (blue) and modeled h_{CML} (red) during three turnover winters. Vertical black indicates when the buoyancy frequency at the base of the mixed layer < 1% greater than background stratification.*

Following the initial vertical turnover of the lake, the bottom of the lake continued to cool below the temperature of the overlying water column. This cold water appeared first near the lakebed and then gradually "filled" the hypolimnion from the bottom upwards. Since the surface of the lake remained warmer than the bottom throughout this entire deep cooling period, this cold water could not have been transported by vertical convection alone. Two potential sources for this cold water include plunging density currents from stream inflows (Dresti et al., 2023; Fink et al., 2016) or differentially cooled littoral waters (Biemond et al. 2021; Peeters et al. 2003). Inflows to Lake Tahoe are colder than the lake bottom from November through May (**Figure 3.16**) and thus have the potential to plunge to significant depth when the lake is weakly stratified (Roberts et al., 2018). Observations of horizontal temperature gradients between littoral and deep waters throughout much of the 2022/23 winter indicate that differential rates of cooling could also induce plunging density from the littoral zone through much of the winter.

While both plunging stream flows and differential cooling of nearshore waters likely play a mechanistic role in deep water cooling, the following mass balance demonstrates that differential cooling is the primary mechansism of depth water renewal. The impacts of inflows and shelf-cooling flows, were estimated from the volume of 4 °C water that would be needed to reach the deep hypolimnion to produce the observed deep water cooling. For each winter, the required volume was estimated from the difference in temperature at the bottom of the lake immediately after turnover and at the end of the limnological winter (**Table 3.2**). Cold water was observed to fill the lake from the bottom to 300 m corresponding to a volume of 43 km^3. Temperature measurements from one of Tahoe's largest tributaries, Blackwood Creek (USGS 10336660), indicate that inflows remained cooler than the lake bottom from early November through the spring and thus had the potential to plunge to the bottom of the lake. Inflows were assessed as capable of plunging when the density difference between stream and littoral waters ($\Delta\varrho$) $\leq$ -0.1 kg m^{-3} (Roberts et al., 2018). Volumes of plunging winter inflows were thus calculated from a daily lake water mass balance from November 1 to April 1 when $\Delta\varrho$ was below this threshold. The depth of the littoral zone affected by differential cooling is system-specific and can be defined as the shallow plateau region extending out from the lake shoreline (Sturman et al., 1999; Wells & Sherman, 2001). In Lake Tahoe, a gently sloping plateau extends to a depth of 15 m beyond which the bed slope steepens dramatically, so the volume of the littoral zone was calculated for all regions where $z \leq 15$ m.

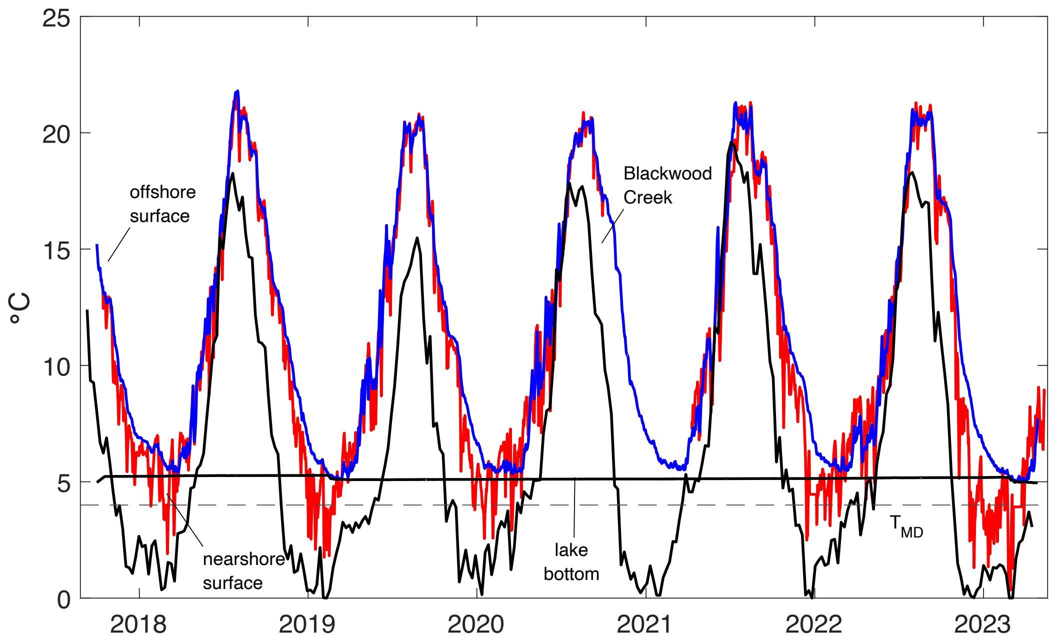

Figure 3.16. *One-day filtered time series of nearshore surface temperatures measured at Tahoe City (red), average offshore surface temperatures measured at TB 1-4 (blue) and lake bottom temperatures measured at the base of Glenbrook thermistor chain (black) and Blackwood Creek (black) from October 2017 to May 2023. Dashed line indicates the temperature of the maximum density of water.*

During the four deep mixing winters, temperatures below 450 m cooled by 0.02 – 0.06 °C in the weeks following turnover. This would have required 0.79 – 2.44 km^3 of 4 °C water, or ~1–2% of the lake's total volume. The cumulative stream discharge when $\Delta\varrho \leq$ -0.1 kg m^{-3} during each of the corresponding winters ranged from 0.09 – 0.17 km^3 accounting for 7-18% of the required volume. In comparison, the volume of the littoral region is 0.25 km^3 and would need to have been flushed at least 5-18 times throughout the winter to induce the level of cooling observed. To estimate a time scale required for differentially cooled water to travel from nearshore and arrive at the base of the GBTC site, we calculated a characteristic velocity scale for a plunging convectively driven flow based on the classic lock exchange flow problem in a sloping channel (Birman et al., 2007) as:

$$U_b = \frac{\sqrt{g'H}}{cos\vartheta} \ , \ g' = g\frac{\varrho_1 - \varrho_2}{\varrho_1} \tag{3.11}$$

Where U_b is the flow velocity (m s^{-1}), H is the thickness of the flow (15 m), ϑ is the slope (<< 1), and ϱ_1 and ϱ_2 are the densities of the plunging density current and the convectively mixed lake layer. A flushing timescale (τ_f), representing the time required for a convectively-driven flow with a unit-width velocity q, (m^2 s^{-1}) to flush the littoral region of unit-width volume V_{llit} (m^2) can be estimated as (Sturman et al., 1999):

$$\tau_f \sim \frac{V_{lit}}{q} \tag{3.12}$$

where $q \sim U_b \, z_{lit}$, and z_{lit} is the average depth of the littoral zone (5 m). For a flow at 4 °C plunging into a lake at 5 °C , $U_b = 0.025$ m s^{-1}, consistent with cross-shore velocities driven by differential cooling observed in other lakes (Doda et al., 2021; Ramón et al., 2022) and the theoretical $\tau_f = 18$ hours. Thus, under these idealized conditions, the littoral zone would be flushed 79 times between January and March and transport 19.75 km^3 of 4 °C water, 2 orders of magnitude larger than stream inputs. At this velocity, a parcel flowing from the lake's shallow northwestern shoreline to GBTC would take 8.5 days, moving in a straight line. The deep hypolimnion began filling with cold water, typically 1-2 weeks after turnover (**Figure 3.12**). This suggests that the estimated timescale of the convectively driven horizontal flow is consistent with this delay. Thus, differential cooling is likely driving horizontal convection and continued cooling in the deep hypolimnion following turnover.

Table 3.2. *Volumetric scaling analysis for deep water cooling during four deep mixing winters. $t_{turnover}$, t_{final}, and Δt indicate the temperature of the deep hypolimnion at turnover, at the end of the winter and the difference between the two. V4℃ indicates the volume of water at 4 ℃ that would be required to cause the observed cooling of the hypolimnion. Total inflow volume shows the estimated volume of water discharged into the lake from November 1 to April 1 when the inflow density was >-0.1 kg m^{-3} the density of the nearshore region. The percentage of the required volume is shown in parenthesis. Shoreline volume denotes the volume of water in the shallow littoral zone <15 m depth. τ_f is the theoretical littoral zone flushing rate.*

Winter	$t_{turnover}$	t_{final}	Δt	$V_{4℃}$	**Total Inflow Volume**	**Shoreline Volume (z < 15 m)**	τ_f
	℃	℃	℃	km^3	km^3 (%)	km^3	hr
1997/98	5.12	5.06	-0.06	2.44	N/A	0.25	18
1998/99	4.91	4.86	-0.05	2.51	0.17 (7%)		
2018/19	5.11	5.09	-0.02	0.79	0.14 (18%)		
2022/23	5.01	4.98	-0.03	1.32	0.09 (7%)		

3.4.3 Potential Effects of Climate Change on Deep Mixing

Unlike many deep lakes across the globe, (Fichot et al., 2019; Mosello et al., 2018; Rogora et al., 2018) the frequency of turnover in Lake Tahoe has not noticeably declined in recent decades as a result of climate change. Many oligomictic lakes are both thermally and chemically stratified because of high solute concentrations in deep waters due to eutrophication (Ambrosetti & Barbanti, 2005). The presence of chemical gradients in these lakes makes them more stable and less prone to turnover compared to Lake Tahoe, where no salinity gradient exists. Moroever, while winter air temperatures in the Lake Tahoe basin have risen at an average rate of 0.22 °C decade^{-1} over the last century (1920-2022), they have declined by -0.19 °C decade^{-1} since a peak in the mid 1980s (**Figure 3.17**). Winter air temperatures <0 °C, when deep mixing has been historically observed, occurred during 24% of years between 1980-2000, but the frequency has risen to 43% of years between 2000-2022. This stands in contrast to summer temperatures which have been warming at an increasingly accelerating pace (Coats 2006). Inter-annual variability in winter air temperature has also been steadily declining with extremely warm and cold winters becoming less frequent. An increase in wind speed in January and February has also been observed since 2006, which could continue to drive high sensible/latent heat losses and wind-induced surface mixing during winter (**Figure B.4**). Using a 1D numerical model, Sahoo (2013) predicted that under the A2 emissions scenario Lake Tahoe would transition to a meromictic state in coming decades, ceasing to completely mix after 2065. With the hypolimnion permanently disconnected from oxygenated surface waters, deep water anoxia could develop within a decade of this transition. While trends over the last 50 years are not necessarily predictive of the next 50, climate change has not appeared to impact deep mixing in Lake Tahoe to the same extent as similar deep European lakes. Furthermore, evidence of convectively-driven flows during the winter suggest that 3D numerical modelling is needed to improve long-term forecasts of deep mixing and renewal.

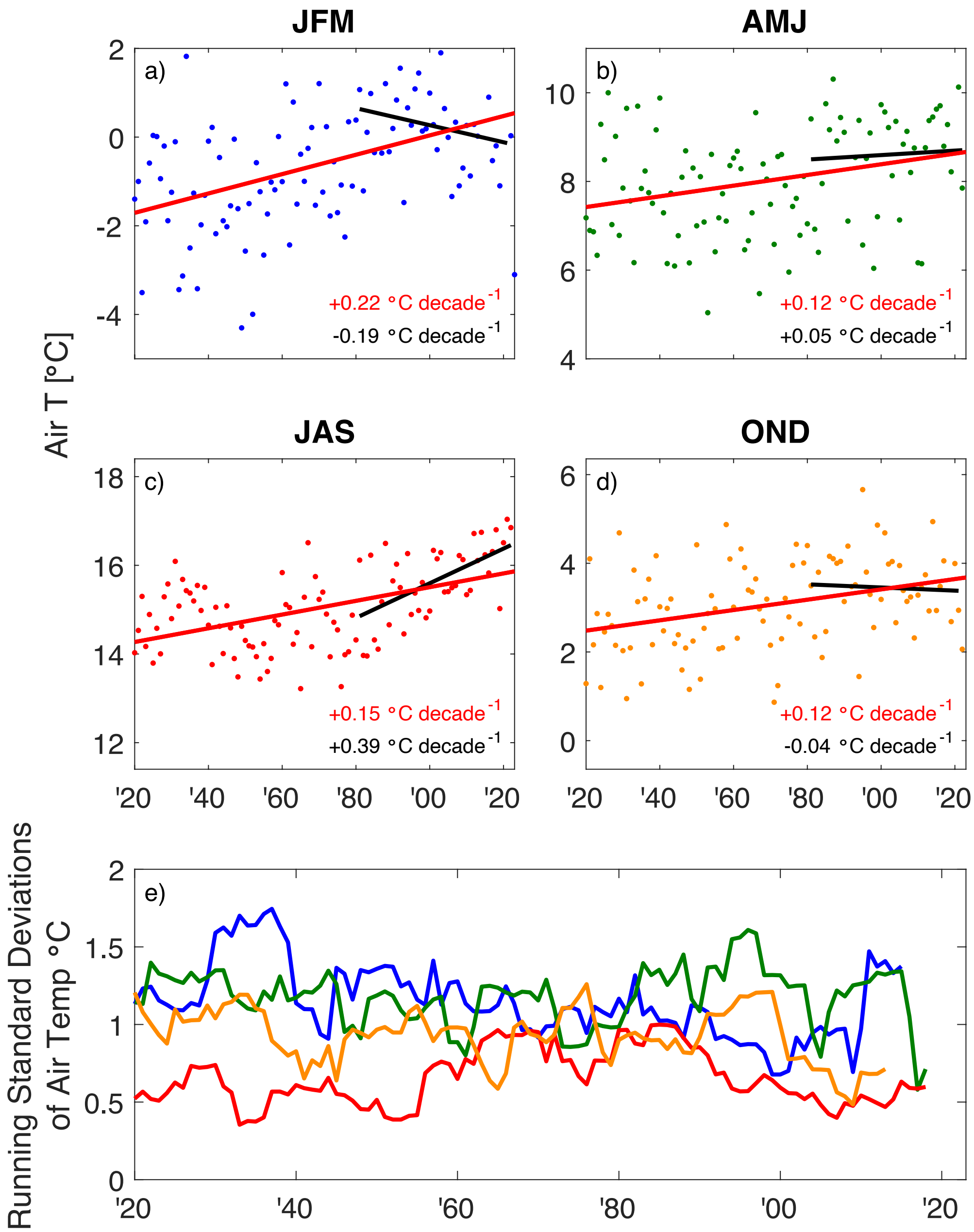

Figure 3.17. *Seasonal average air temperature for a) January through March, b) April through June, c) July through September, d) October through December from 1920 to 2022 measured at Tahoe City. Red line indicates linear trend for entire time period while black line indicates linear trend since 1980. e) Running standard deviation (10-year running window) of the mean seasonal air temperature. Colors correspond to season.*

3.4.4 Future Research

We find that the occurrence of complete turnover in Lake Tahoe is primarily determined by the occurrence of discrete periods of strongly negative heat flux in the late winter. Those years when such an event is absent, the lake never deepens below 250 m. When such events occur, mixing through the lower half of the hypolimnion is rapid, and ventilation of the lake bottom is achieved in a matter of hours after isothermy. When full turnover does occur, the process is characterized by four distinct phases. The first three phases are essentially one-dimensional and dominated by natural convection driven by sensible and latent heat fluxes. The final phase, the filling of the deep hypolimnion by cold water derived from differential cooling on the shallow shelves, is three-dimensional.

Through temperature measurements and scaling analysis, this research provides clear evidence that differential cooling contributes to deep mixing in Lake Tahoe, motivating further investigations along this line of research. While horizontal temperature variations throughout the winter indicate the potential for convectively-driven horizontal flows, there has been no measurement of seasonal and diurnal variation in current velocities. Future field efforts could focus on measuring the magnitude and timing of such currents in the lake's shallow littoral zones (e.g. southern and northern shorelines) during weakly stratified winter conditions. Additionally, the depth to which these gravity-driven flows travel downslope is uncertain and conducting 3D numerical tracer experiments could help clarify this intrusion region. Lastly, by running 3D numerical modeling forced by climate change scenarios, it would be possible to identify how these important renewal processes may be affected by climate change.

References

Augusto-Silva, P., MacIntyre, S., 2019. Stratification and mixing in large floodplain lakes along the lower Amazon River. *J. Gt. Lakes*

Ambrosetti, W., & Barbanti, L. (1999). Deep water warming in lakes: an indicator of climatic change. *J. Limnol.*, *58*(1), 1–9.

Ambrosetti, W., & Barbanti, L. (2005). Evolution towards meromixis of Lake Iseo (Northern Italy) as revealed by its stability trend. *J. Limnol.*, *64*(1), 1–11.

Ambrosetti, W., Barbanti, L., & Carrara, E. A. (2010). Mechanisms of hypolimnion erosion in a deep lake (Lago Maggiore, N. Italy). *J. Limnol.*, *69*(1), 1.

Anderson, H. S., Johengen, T. H., Godwin, C. M., Purcell, H., Alsip, P. J., Ruberg, S. A., & Mason, L. A. (2021). Continuous in situ nutrient analyzers pinpoint the onset and rate of internal p loading under anoxia in Lake Erie's central basin. *ACS ES&T Water*, *1*(4), 774–781.

Antenucci, J. P., Imberger, J., & Saggio, A. (2000). Seasonal evolution of the basin-scale internal wave field in a large stratified lake. *Limnol. Oceanogr.*, *45*(7), 1621–1638.

Batchvarova, E., & Gryning, S.-E. (1991). Applied Model for the Growth of the Daytime Mixed Layer. *Boundary-Layer Meteorol.*, *56*(3), 261–274.

Beutel, M. W., & Horne, A. J. (2018). Nutrient fluxes from profundal sediment of ultra-oligotrophic Lake Tahoe, California/Nevada: Implications for water quality and management in a changing climate. *Water Resour. Res.*, *54*(3), 1549–1559.

Biemond, B., Amadori, M., Toffolon, M., Piccolroaz, S., Van Haren, H., & Dijkstra, H. A. (2021). Deep-mixing and deep-cooling events in Lake Garda: Simulation and mechanisms. *J. Limnol.*, *80*(2).

Birman, V. K., Battandier, B. A., Meiburg, E., & Linden, P. F. (2007). Lock-exchange flows in sloping channels. *J. Fluid Mech.*, *577*, 53–77.

Brutsaert, W. (1982). Evaporation Into the Atmosphere: Theory, History and Applications. In *Environmental Fluid Dynamics* (1st ed.). Springer.

Chen, C. T. A., & Millero, F. (1986). Precise thermodynamic properties for natural waters covering only the limnological range. *Limnol. Oceanogr.*, *31*(3), 657–661.

Coats, R., Perez-Losada, J., Schladow, G., Richards, R., & Goldman, C. (2006). The warming of Lake Tahoe. *Clim. Change*, *76*(1–2), 121–148.

Crawford, G. B., & Collier, R. W. (2007). Long-term observations of deepwater renewal in Crater Lake, Oregon. *Hydrobiologia*, *574*(1), 47–68.

Doda, T., Ramón, C. L., Ulloa, H. N., Wüest, A., & Bouffard, D. (2021). Seasonality of density currents induced by differential cooling. *Hydrol. Earth Syst. Sci.*, *26*, 331–353.

Dresti, C., Rogora, M., & Fenocchi, A. (2023). Hypolimnetic oxygen depletion in a deep oligomictic lake under climate change. *Aquat. Sci.*, *85*(1), 4.

Eichelberger, S., McCAA, J., Nijssen, B., & Wood, A. (2008). Climate change effects on wind speed. *North American Wind Power*. www.nawindpower.com.

Fenocchi, A., Rogora, M., Sibilla, S., Ciampittiello, M., & Dresti, C. (2018). Forecasting the evolution in the mixing regime of a deep subalpine lake under climate change scenarios through numerical modelling (Lake Maggiore, Northern Italy/Southern Switzerland). *Clim. Dyn.*, *51*(9–10), 3521–3536.

Fer, I., Lemmin, U., & Thorpe, S. A. (2002). Winter cascading of cold water in Lake Geneva. *J. Geophys. Res.*, *107*(C6).

Fichot, C. G., Matsumoto, K., Holt, B., Gierach, M. M., & Tokos, K. S. (2019). Assessing change in the overturning behavior of the Laurentian Great Lakes using remotely sensed lake surface water temperatures. *Remote Sens. Environ.*, *235*.

Fink, G., Wessels, M., & Wüest, A. (2016). Flood frequency matters: Why climate change degrades deep-water quality of peri-alpine lakes. *J. Hydrol.*, *540*, 457–468.

Fischer H.B., List E.J., Koh R.C., Imberger J., & Brooks N.H. (1979). *Mixing in Inland and Coastal Waters* (1st ed.). Academic Press Inc.

Flaim, G., Andreis, D., Piccolroaz, S., & Obertegger, U. (2020). Ice cover and extreme events determine dissolved oxygen in a placid mountain lake. *Water Resour. Res.*, *56*(9).

Friedrich, J., Janssen, F., Aleynik, D., Bange, H. W., Boltacheva, N., Çagatay, M. N., Dale, A. W., Etiope, G., Erdem, Z., Geraga, M., Gilli, A., Gomoiu, M. T., Hall, P. O. J., Hansson, D., He, Y., Holtappels, M., Kirf, M. K., Kononets, M., Konovalov, S., ... Wenzhöfer, F. (2014). Investigating hypoxia in aquatic environments: Diverse approaches to addressing a complex phenomenon. *Biogeosci.*, *11*(4), 1215–1259.

Gaudard, A., Schwefel, R., Räman Vinnä, L., Schmid, M., Wuëst, A., & Bouffard, D. (2017). Optimizing the parameterization of deep mixing and internal seiches in one-dimensional hydrodynamic models: A case study with Simstrat v1.3. *Geosci. Model Dev.*, *10*(9), 3411–3423.

Goldman, C. R., & Jassby, A. D. (1990). Spring mixing and annual primary production at Lake Tahoe, California-Nevada. *Verh. Internat. Verein. Limnol.*, *24*(1), 504–504.

Goldman, C. R., Jassby, A., & Powell, T. (1989). Interannual fluctuations in primary production: Meteorological forcing at two subalpine lakes. *Limnol. Oceanogr.*, *34*(2), 310–323.

Gryning, S. E., & Batchvarova, E. (1990). Analytical model for the growth of the coastal internal boundary layer during onshore flow. *Quarterly Journal of the Royal Meteorological Society*, *116*(491), 187–203.

Hutchinson, G. E., & Loffler, H. (1956). The thermal classification of lakes. *Geophysics*, *42*, 84–86. https://www.pnas.org

Imberger, J. (1985). The diurnal mixed layer. *Limnol. Oceanogr.*, *30*(4), 737–770.

Imberger, J., & Patterson J. (1989). Physical Limnology. In *Advances in Applied Mechanics* (Vol. 27, pp. 303–475). Elsevier.

Imboden, D. M., & Wuest, A. (1995). Mixing Mechanisms in Lakes. In *Physics and Chemistry of Lakes* (Issue March 2018, pp. 83–130). Springer-Verlag.

Kraus, E. B., & Turner, J. S. (1967). A one-dimensional model of the seasonal thermocline II. The general theory and its consequences. *Tellus*, *19*(1), 98–106.

Krishna, S., Ulloa, H. N., Kerimoglu, O., Minaudo, C., Anneville, O., & Wüest, A. (2021). Model-based data analysis of the effect of winter mixing on primary production in a lake under reoligotrophication. *Ecol. Model.*, *440*.

Lemmin, U. (2020). Insights into the dynamics of the deep hypolimnion of Lake Geneva as revealed by long-term temperature, oxygen, and current measurements. *Limnol. Oceanogr.*, *65*(9), 2092–2107.

Livingstone, D. M. (1997). An example of the simultaneous occurrence of climate-driven "sawtooth" deep-water warming/cooling episodes in several Swiss lakes. *Verh. Internat. Verein. Limnol.*, *26*(2), 822–828.

MacIntyre, S., Fram, J. P., Kushner, P. J., Bettez, N. D., O'Brien, W. J., Hobbi, J. E., & Kling, G. W. (2009). Climate-related variations in mixing dynamics in an Alaskan arctic lake. *Limnol. Oceanogr.*, *54*(6, part 2), 2401–2417.

McInerney, J. B. T. , Forrest A. L., Schladow S. G. & Largier J. L., "How to fly an autonomous underwater glider to measure an internal wave," OCEANS 2019 MTS/IEEE SEATTLE, Seattle, WA, USA, 2019, pp. 1-8

Michalski, J., & Lemmin, U. (1995). Dynamics of vertical mixing in the hypolimnion of a deep lake: Lake Geneva. *Limnol. Oceanogr.*, *40*(4), 809–816.

Mosello, R., Bruni, P., Rogora, M., Tartari, G., & Dresti, C. (2018). Long-term change in the trophic status and mixing regime of a deep volcanic lake (Lake Bolsena, Central Italy). *Limnologica*, *72*, 1–9.

Nelligan, C., Jeziorski, A., Rühland, K. M., Paterson, A. M., & Smol, J. P. (2019). Long-term trends in hypolimnetic volumes and dissolved oxygen concentrations in boreal shield lakes of south-central Ontario, Canada. *Can. J. Fish. Aquat. Sci*, *76*(12), 2315–2325.

Paerl, H. W., Richards, R. C., Leonard, R. L., & Goldman, C. R. (1975). Seasonal nitrate cycling as evidence for complete vertical mixing in Lake Tahoe, California-Nevada. *Limnol. Oceanogr.*, *20*(1), 1–8.

Peeters, F., Finger, D., Hofer, M., Brennwald, M., Livingstone, D. M., & Kipfer, R. (2003). Deep-water renewal in Lake Issyk-Kul driven by differential cooling. *Limnol. Oceanogr.*, *48*(4), 1419–1431.

Piccolroaz, S., Amadori, M., Toffolon, M., & Dijkstra, H. A. (2019). Importance of planetary rotation for ventilation processes in deep elongated lakes: Evidence from Lake Garda (Italy). *Sci. Rep.*, *9*(8290).

Ramón, C. L., Ulloa, H. N., Doda, T., & Bouffard, D. (2022). Flushing the Lake Littoral Region: The Interaction of Differential Cooling and Mild Winds. *Water Resour. Res.*, *58*(3).

Read, J. S., Hamilton, D. P., Jones, I. D., Muraoka, K., Winslow, L. A., Kroiss, R., Wu, C. H., & Gaiser, E. (2011). Derivation of lake mixing and stratification indices from high-resolution lake buoy data. *Environ. Model. Soft.*, *26*(11), 1325–1336.

Reiss, R. S., Lemmin, U., Cimatoribus, A. A., & Barry, D. A. (2020). Wintertime coastal upwelling in Lake Geneva: An efficient transport process for deepwater renewal in a large, deep lake. *JGR: Oceans*, *125*(8), 1–18.

Roberts, D. C., Egan, G. C., Forrest, A. L., Largier, J. L., Bombardelli, F. A., Laval, B. E., Monismith, S. G., & Schladow, S. G. (2021). The setup and relaxation of spring upwelling in a deep, rotationally influenced lake. *Limnol. Oceanogr.*, *66*(4), 1168–1189.

Roberts, D. C., Forrest, A. L., Sahoo, G. B., Hook, S. J., & Schladow, S. G. (2018). Snowmelt timing as a determinant of lake inflow mixing. *Water Resour. Res.*, *54*(2), 1237–1251.

Rodionov, S., & Assel, R. (2001). A new look at the Pacific/North American Index. *Geophys. Res. Lett.*, *28*(8), 1519–1522.

Rogora, M., Buzzi, F., Dresti, C., Leoni, B., Lepori, F., Mosello, R., Patelli, M., & Salmaso, N. (2018). Climatic effects on vertical mixing and deep-water oxygen content in the subalpine lakes in Italy. *Hydrobiologia*, *824*(1), 33–50.

Rueda, F. J., Schladow, S. G., & Pálmarsson, S. Ó. (2003). Basin-scale internal wave dynamics during a winter cooling period in a large lake. *JGR: Oceans*, *108*(3), 1–16.

Rühland, K. M., Evans, M., & Smol, J. P. (2023). Arctic warming drives striking twenty-first century ecosystem shifts in Great Slave Lake (Subarctic Canada), North America's deepest lake. *Proc. R. Soc. B*, *290*.

Saarela, T., Rissanen, A. J., Ojala, A., Pumpanen, J., Aalto, S. L., Tiirola, M., Vesala, T., & Jäntti, H. (2020). CH4 oxidation in a boreal lake during the development of hypolimnetic hypoxia. *Aquat. Sci.*, *82*(2).

Saber, A., James, D. E., & Hannoun, I. A. (2020). Effects of lake water level fluctuation due to drought and extreme winter precipitation on mixing and water quality of an alpine lake, case study: Lake Arrowhead, California. *Sci. Total Environ.*, *714*.

Sahoo, G. B., Forrest, A. L., Schladow, S. G., Reuter, J. E., Coats, R., & Dettinger, M. (2016). Climate change impacts on lake thermal dynamics and ecosystem vulnerabilities. *Limnol. Oceanogr.*, *61*(2), 496–507.

Sahoo, G. B., Schladow, S. G., Reuter, J. E., Coats, R., Dettinger, M., Riverson, J., Wolfe, B., & Costa-Cabral, M. (2013). The response of Lake Tahoe to climate change. *Clim. Change*, *116*(1), 71–95.

Salk, K. R., Ostram, P. H., Biddanda Bopaiah A, Weinke Anthony D, Kendall Scott T, & Ostrom Nathaniel E. (2016). Ecosystem metabolism and greenhouse gas production in a mesotrophic northern temperate lake experiencing seasonal hypoxia. *Biogeochem.*, *131*, 303–319.

Salmaso, N., Boscaini, A., Capelli, C., & Cerasino, L. (2018). Ongoing ecological shifts in a large lake are driven by climate change and eutrophication: evidences from a three-decade study in Lake Garda. *Hydrobiologia*, *824*(1), 177–195.

Salmaso, N., Mosello, R., Garibaldi, L., Decet, F., Brizzio, M. C., & Cordella, P. (2003). Vertical mixing as a determinant of trophic status in deep lakes: A case study from two lakes south of the Alps (Lake Garda and Lake Iseo). *J. Limnol.*, *62*(SUPPL), 33–41.

Schladow, S. G., Toy, A., & Watanabe, S. (2021). *Tahoe: State of the Lake Report.* https://tahoe.ucdavis.edu/stateofthelake

Schwefel, R., Gaudard, A., Wüest, A., & Bouffard, D. (2016). Effects of climate change on deepwater oxygen and winter mixing in a deep lake (Lake Geneva): Comparing observational findings and modeling. *Water Resour. Res.*, *52*(11), 8811–8826.

Schwefel, R., Müller, B., Boisgontier, H., & Wüest, A. (2019). Global warming affects nutrient upwelling in deep lakes. *Aquat. Sci.*, *81*(3).

Spigel, R. H., Imberger, J., & Rayner, K. N. (1986). Modeling the diurnal mixed layer. *Limnol. Oceanogr.*, *31*(3), 533–556.

Sprague, H. M. (2013). *Identifying Effects of Basin-Scale Waves on Hypolimnetic Dissolved Oxygen : A Coherence Analysis.* University of California, Davis.

Stepanenko, V. M., Goyette, S., Martynov, A., Perroud, M., Fang, X., & Mironov, D. (2010). First steps of a lake model intercomparison project: LakeMIP. *Boreal Environ. Res.*, *15*, 191–202.

Straile, D., Jöhnk, K., & Rossknecht, H. (2003). Complex effects of winter warming on the physicochemical characteristics of a deep lake. *Limnol. Oceanogr.*, *48*(4), 1432–1438.

Sturman, J. J., Oldham, C. E., & Ivey, G. N. (1999). Steady convective exchange flows down slopes. *Aquat. Sci.*, *61*, 267–278.

Swann, G. E. A., Panizzo, V. N., Piccolroaz, S., Pashley, V., Horstwood, M. S. A., Roberts, S., Vologina, E., Piotrowska, N., Sturm, M., Zhdanov, A., Granin, N., Norman, C., Mcgowan, S., & Mackay, A. W. (2020). Changing nutrient cycling in Lake Baikal, the world's oldest lake. *PNAS*, *117*(44).

Thorpe, S. A. (2007). *An Introduction to Ocean Turbulence*. Cambridge University Press.

Valbuena, S. A., Bombardelli, F. A., Cortés, A., Largier, J. L., Roberts, D. C., Forrest, A. L., & Schladow, S. G. (2022). 3D flow structures during upwelling events in lakes of moderate size. *Water Resour. Res.*, *58*(3).

Valbuena, S. A., Bombardelli, F. A., Largier, J. L., & Schladow, G. (2003). Deep water re-oxygenation from lake upwelling. *JGR: Oceans (In Review)*.

van Haren, H., Piccolroaz, S., Amadori, M., Toffolon, M., & Dijkstra, H. A. (2021). Moored observations of turbulent mixing events in deep Lake Garda, Italy. *J. Limnol.*, *80*(1).

Verburg, P., & Hecky, R. E. (2009). The physics of the warming of Lake Tanganyika by climate change. *Limnol. Oceanogr.*, *54*(6 PART 2), 2418–2430.

Watanabe, S. 2023. Lake Tahoe Historic Secchi depth ver 6. Environmental Data Initiative. https://doi.org/10.6073/pasta/31095ad19b63d890be67815333ad2b2b.

Wells, M. G., & Sherman, B. (2001). Stratification produced by surface cooling in lakes with significant shallow regions. *Limnol. Oceanogr.*, *46*(7), 1747–1759.

Winder, M., Reuter, J. E., & Schladow, S. G. (2009). Lake warming favours small-sized planktonic diatom species. *Proc. R. Soc. B*, *273*, 427–435.

Woolway, R. I., Jones, I. D., Hamilton, D. P., Maberly, S. C., Muraoka, K., Read, J. S., Smyth, R. L., & Winslow, L. A. (2015). Automated calculation of surface energy fluxes with high-frequency lake buoy data. *Environ. Model. Soft.*, *70*, 191–198.

Woolway, R. I., & Merchant, C. J. (2019). Worldwide alteration of lake mixing regimes in response to climate change. *Nat. Geosci.*, *12*(4), 271–276.

Zilitinkevich, S. S. (1991). *Turbulent Penetrative Convection* (B. Henderson-Sellers, Ed.). Avebury.

4 THE RESILIENCE OF A DEEP SOUTHERN HEMISPHERE LAKE TO CLIMATE CHANGE[3]

Abstract

The climate change responses of Lago Llanquihue in northern Patagonia, Chile, are investigated through hydrodynamic model simulations for selected years throughout the 21st century. Results from a three-dimensional (3D) hydrodynamic model are compared against those from a one-dimensional (1D) model to highlight the importance of more fully capturing the complex hydrodynamic processes in a deep lake. The models were calibrated and validated using in situ mooring and meteorological data collected over a one-year period. In contrast to earlier studies, we evaluate both the impacts of changes in individual forcing parameters to assess model sensitivity, as well as a sub-daily downscaled climate projection under the Relative Concentration Pathway 8.5 scenario, on changes in lake thermal structure and mixing regime. Model results demonstrate that Lago Llanquihue is expected to warm slower than many similar deep, temperate, monomictic systems in the Northern Hemisphere provided that current levels of lake clarity (light attenuation) are maintained in the future. This is largely on account of the lower predicted rates of atmospheric warming in the Southern Hemisphere. The role of water clarity in

[3] This manuscript is being submitted to the *Journal of Great Lakes Research* for publication.

preserving the northern Patagonian lakes, underscores the importance of land use management in this region.

4.1 Introduction

Anthropogenic climate change has rapidly altered the surface heat fluxes and water budgets which regulate the equilibrium conditions of lake ecosystems (Adrian et al., 2009). Some of the most pronounced physical changes include reductions in ice cover (Butcher et al., 2015; Latifovic & Pouliot 2007), changing precipitation/evapotranspiration patterns (Zamani et al., 2021), increasing surface water temperatures (Pilla et al., 2020), shoaling of seasonal thermoclines (Darko et al., 2019), and shifting mixing regimes (Woolway et al., 2020). Deep temperate lakes in the Northern Hemisphere (NH) have experienced increased thermal stability and reduced frequency of deep convective mixing due to the differential warming rates of surface and deep waters (Livingstone 2003). As a result, many oligomictic systems are forecasted to become permanently stratified (Sahoo et al., 2013; Fenocchi et al., 2018) while monomictic systems will experience incomplete winter mixing (Schwefel et al., 2016; Straile et al., 2003). A change in a lake's mixing regime can have significant ecological implications: reducing downwelling of oxygenated surface waters (Jane et al., 2021) and upwelling nutrient-rich hypolimnetic waters to the surface (Yankova et al., 2017). Additionally, warming lake surface temperatures alter the phenology, abundance and composition of phytoplankton and zooplankton communities (de Senerpont Domis et al., 2013; Shimoda et al., 2011), which can be further exacerbated by land use change, leading to the proliferation of harmful cyanobacteria blooms (Paerl and Huisman 2009; Rigosi et al., 2014).

Though air temperatures are increasing globally, lake warming rates are highly variable, with the most pronounced increases observed in North America and Central Europe (Fink et al., 2014), while lakes in the Southern Hemisphere (SH) have warmed more slowly. Schneider and Hook (2010) calculated warming trends of 167 globally distributed large lakes from 1985-2010 and found that NH surface waters warmed on average 0.05-0.08 °C yr^{-1}, while temperate SH lakes warmed at a rate of 0.012 °C yr^{-1} (non-significant trend), albeit from a much smaller set of lakes. A global reconstruction of lake surface water temperatures during the 20th century similarly found that temperate NH lakes, on average, warmed three times faster than temperate SH lakes from 1980-2010 (Piccolroaz et al., 2020).

In the northern Patagonian (NP) region of central Chile, studies have provided conflicting evidence of lake warming trends. Lake surface water temperatures, derived from satellite imagery, showed an increase of 0.01 °C yr^{-1} from 2000-2016 in 14 NP lakes (Aranda et al., 2021). In contrast, surface temperatures directly measured in the field indicate a cooling trend over the past 20 years, possibly linked to the accelerating rate of glacial melting (Pizarro et al., 2016). Due to the absence of high-frequency lake monitoring data, the current and future trajectory of these lakes remains uncertain.

Numerous numerical modeling studies have assessed the sensitivity of the lakes to climatic changes by primarily altering air temperatures and precipitation projections (Butcher et al., 2015; Hetherington et al., 2015). Although warming air temperatures are widespread, the relationship between air and lake temperature trends is not globally or evenly regionally consistent as various meteorological and morphometric factors regulate a system's heat budget and mixing regime (O'Reilly et al., 2015). Meteorological variables, such as radiation, cloud cover, and wind can act to amplify or suppress climate-induced lake warming by altering the contribution of individual heat flux terms (Ayala et al., 2023). In Lake Tahoe, USA, for example, forecasted decreasing wind speed and increasing longwave radiation will act in conjunction with higher air temperatures to warm the lake (Sahoo et al., 2013). In New Zealand, Lakes Wanaka and Wakatipu are predicted to warm due to increased air temperatures, but higher wind speeds will counterbalance increases in thermal stratification and continue to facilitate annual overturn (Bayer et al., 2013b). A lake’s response to atmospheric warming is also impacted by water clarity which can be affected by changes in basin activity that alter sediment and nutrient loads, invasive species, shifts in aquatic community structure, and water temperatures (Lottig et al., 2014). Decreased water clarity limits the penetration of shortwave radiation and the depth of the seasonal thermocline and alters surface heat fluxes. However, variations in water clarity are rarely considered in long-term climate change lake modeling studies (Rose et al., 2016).

While one-dimensional (1D) models are frequently employed to investigate lake response to climate change, studies utilizing three-dimensional (3D) models are rare due to high computational cost and longer run times (Wahl & Peeters, 2014). However, 1D models require extensive site-specific calibration to integrate the complex interactions of basin morphology, wind, and surface forcings into a one-dimensional framework. The relationship between these different factors cannot be determined *a priori* and thus requires calibration to parameterize the observed net effect of internal processes during the calibration period. Long-term simulations, where lake stratification regimes shift, can alter the internal wave field and mixing rates. Consequently, 1D models calibrated to current conditions may produce unrealistic predictions of lake mixing in the future (Zamani et al., 2021). Furthermore, though 1D models can accurately simulate water temperatures in deep lakes, they are predicated on the assumption that horizontal gradients are small, so lake mixing can be described as a 1D process. This simplification precludes mechanistic modeling of deep water mixing since both internal waves, the primary energy pathway for turbulence into the deep hypolimnion (Imberger 1998), and boundary mixing (Goudsmit et al., 1997) require a horizontal dimension to be described mechanistically. In addition, 1D models cannot account for rotational effects in large lakes (>500 km^2, Herdendorf, 1990). These limitations can be overcome with 3D models, which can resolve seiche activity (Hodges et al., 2000; Rueda et al., 2003), spatially heterogeneous geometries, and the effects of differential cooling, which can contribute to deep water renewal (Zamani et al., 2021). Though 3D models require calibration as well, their ability to resolve temporal and spatial variability wave dynamics that drive mixing energetics, suggests that a well-calibrated model will continue to perform reasonably under changing lake thermal regimes. Furthermore, 3D lake models can be coupled with regional climate models to better resolve heat fluxes between lakes and local climate (Y. Song et al., 2004).

Several studies have used 3D models to investigate the effects of changing meteorological forcing on deep lake hydrodynamics. Using a 3D model of Lake Biwa forced by global climate model (GCM), Yamashiki (2010) predicted increasing epilimnion thickness and warmer hypolimnion temperatures would cause potential catastrophic ecosystem degradation. Wahl and Peeters (2014) employed a 3D model to conduct a sensitivity analysis on the effects of changing meteorological conditions on stratification and deep water renewal in Lake Constance. However, both studies primarily consider climate change through the lens of altered air temperatures. Studies incorporating sensitivity analysis in conjunction with fully downscaled climate projections are needed to understand the individual and integrated effects of projected changes in a range of meteorological and in-lake parameters.

In this study, a 3D hydrodynamic model (Si3D) is calibrated and validated to simulate the thermal structure of Lago Llanquihue, one of 23 large, deep monomictic NP lakes. The results of the 3D model are compared against the output of a 1D model to highlight the difference when representing deep water mixing as a three-dimensional process. We employ the 3D model to evaluate the sensitivity of the lake's response to changes in air temperature, wind speed, and clarity. The evolution of Llanquihue's thermal structure over the 21st century is then evaluated using downscaled data from the REGCM4 regional climate model under a Representative Concentration Pathway (RCP) 8.5 emissions scenario. Based on modeling studies of similar large monomictic/oligomictic lakes in the Northern Hemisphere and New Zealand, we hypothesize that 1) amplified surface heating will promote increased water temperature, heat storage, and thermal stability and 2) the lake will shift from a monomictic to oligomictic state as the intensity and duration of winter overturn weakens. We then discuss how predicted changes for Llanquihue compare to other lakes globally. Finally, we discuss the water quality and ecological implications of the results of climate-induced changes in lake thermal structure.

4.2 Materials and Methods

4.2.1 Study Site

Lago Llanquihue (-41.132°, -72.819°) is a deep, glacier-fed, temperate lake located at an elevation of 51 m.a.s.l at the base of the western side of the Andes Mountain Range in the Los Lagos region of Chile (**Figure 4.1**). With a surface area of 871 km^2 and a volume of 159 km^3, it is the second-largest lake in Chile (Campos 1988). Llanquihue is a warm, monomictic system, historically stratifying from October through June and reaching near-isothermal conditions from late July through early September (Campos 1988). Due to its great depth (Z_{mean} = 190 m; Z_{max} = 320 m) and its mild climate, the lake never experiences ice cover. Relative to its surface area, the lake has a comparatively small drainage basin (1605 km^2), receiving approximately 50% of its input from precipitation and 50% from a network of small streams that flow down from the Andes Mountains into the lake's eastern shoreline (IFOP 2020). In contrast, the lake has only one outflow – the Maullin River – which discharges from the lake's southwestern shoreline. As a result of its low inflow rate and large volume, the lake has a long residence time of 74 years (Soto & Campos, 1995). Lago Llanquihue is an ultra-oligotrophic system in part due to its low watershed-to-surface area ratio (1.8:1) and the minimal rates of anthropogenic activities historically conducted in the watershed. Water clarity remains high with a mean Secchi depth of approximately 21 m and a range of 8 – 30 m (Abarca et al., 2023). The lake provides various beneficial uses for the regional economy including freshwater supply, greywater disposal, housing juvenile fish farms for the pisciculture industry (which have been reduced in recent years) and significant tourism (Donoso 2018). However, studies have indicated the lake could become mesotrophic because of increasing nutrient loads and land use changes in recent decades (De Los Ríos-Escalante & Soto, 2007). The lack of high-frequency monitoring data though has limited the ability to forecast the trajectory and the long-term evolution of the lake's trophic and physical state.

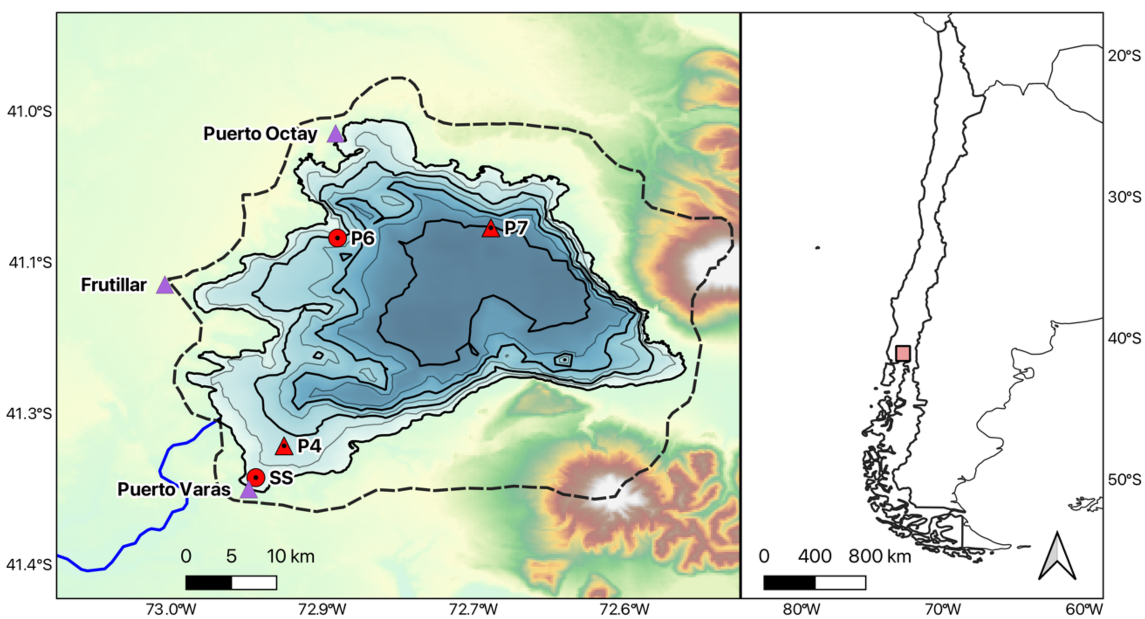

Figure 4.1. *Lago Llanquihue site map indicating locations of thermistor chains (red markers) and meteorological stations (triangles). Black and grey contours indicate 100 m and 50 m isobaths. Dashed line is the watershed boundary.*

Previous hydrodynamic modeling studies have investigated Llanquihue's nearshore current dynamics (Universidad San Sebastian, 2022), and internal wave field (Abarca et al., 2023) to determine the fate and transport of illicit discharges to the lake. However, these studies primarily focused on the dynamics of the bays near the population centers of Puerto Varas and Puerto Octay and the hydrodynamics of the epilimnion in offshore regions. To our knowledge the only temperature measurements of Llanquihue's deep hypolimnion include discontinuously collected monthly measurements (Campos et al., 1988).

4.2.2 Lake Monitoring Program

Since August 2021, Lago Llanquihue has been instrumented with thermistor chains deployed from three buoys in the southern (P4), western (P6), and northern (P7) regions of the lake (**Figure 4.1**). The instruments stations were manufactured and installed by Innovex® (https://www.innovex.cl) and are comprised of thermistors (resolution 0.01°C) and dissolved oxygen (DO) sensors (resolution 0.01 mgL^{-1}). Thermistors were spaced approximately every 10 m from the surface down to 100 m, and at 50 m intervals at greater depths. P7 also has a thermistor at 1 m depth recording lake surface temperature. One DO sensor was placed in the epilimnion and the hypolimnion at each buoy. Data from a surface monitoring buoy on the lake's southern shoreline, operated by the Universidad San Sebastian (SS), was used to fill in occasional data gaps. Data were downloaded to a server via a cell modem on each buoy. Meteorological stations (recording wind speed [WS] and direction, air temperature [T_{air}], atmospheric pressure [$AtmP$], and humidity [RH]) at 2 m above the water surface were located on the P4 and P7 buoys since

October 2021 and February 2022, respectively. These data were supplemented with data from terrestrial meteorological stations in Puerto Varas, Puerto Octay, Frutillar, and the Puerto Montt Airport operated by the Meteorological Directorate of Chile (DMC). The thermistors, DO, and on-water met stations recorded data every 10 minutes, while on-land met stations recorded data every 60 minutes.

Table 4.1. *Thermistor chain array description. All depths are in meters.*

Site	Lat / Lon	Z_{max}	Thermistor	DO
P4	-41.282 / -72.938	80	10,20,30,40,50,60,70,80	10, 80
P6	-41.076 / -72.885	100	10,20,30,40,50,60,70,80,90,100	10, 100
P7	-41.066 / -72.733	320	1,5,10,20,30,40,65,100,150,200,250,300	200, 300
SS	-41.315 / -72.967	80	3	3

4.2.3 3D Hydrodynamic Model (Si3D)

Lake hydrodynamics were simulated with Si3D (P. Smith, 2006), a semi-implicit, finite-difference 3D hydrodynamic model which has been employed to model baroclinic motions (Rueda and Schladow 2003), internal wave fields (Rueda et al., 2009), bivalve dispersion (Hoyer et al., 2015), fate and transport of river plumes (F. J. Rueda & MacIntyre, 2010) and upwelling dynamics in rotationally influenced deep lakes (Valbuena et al., 2021). The model is based on the continuity equation for incompressible fluids, the Reynolds-averaged form of the Navier-Stokes equations for momentum, the transport equation for temperature, and an equation of state relating temperature and pressure to fluid density (Gill, 1982). For the vertical turbulence closure of the Reynolds stress, the

2.5 Mellor and Yamada k-ε scheme is used, while the Smagorinsky method is utilized to parameterize horizontal diffusion. Further details on the governing equation and numerical methods incorporated in Si3D can be found in Rueda and Schladow (2003) and Smith (2006).

Wind drag (C_D) and light extinction coefficient (k_d) were selected as calibration parameters as these terms had the most significant influence on surface heat fluxes and thermocline depth. Initial temperature conditions were based on measurements at 00:00 on August 20, 2021 from the P7 thermistor chain, while the velocity field was initialized at 0. A rectilinear gridded bathymetry of the lake was generated from depth-point measurements collected approximately 1000 m apart (Servicio Hidrografico Oceanografico de la Armada de Chile, 2003). A horizontal grid resolution of 400 m was selected as a compromise to minimize computational time for multi-year simulations in a large domain and to sufficiently resolve Lago Llanquihue's bathymetry. It has been previously suggested that the choice of grid size is unlikely to significantly impact simulated water temperatures and deep water exchange in 3D large lake models (Wahl & Peeters, 2014). A constant vertical grid size of 2 m was used across the full depth of the lake, and a timestep of 50 s was employed to satisfy the Courant-Friedrichs Lewy criteria for model stability while preventing numerical instabilities in the hypolimnion observed at smaller timesteps. Model results were output at an hourly resolution. Daily lake level data were unavailable during the monitoring period. However, monthly observations from 1996-2019 recorded annual fluctuations of <0.5 m and given that the 1-year modeling period was significantly shorter than the lake's 74 year resident time, lake level was assumed constant. On account of the long residence time, inflows/outflows were excluded from the simulations.

After comparing measurements across multiple meteorological stations, surface boundary conditions were considered uniform across the entire surface of the lake. On-water and terrestrial meteorological stations had intermittent data gaps during the one-year monitoring period. $AtmP$, T_{air}, and RH, normalized to height of 10 m, were averaged from the P4 and P7 met stations, while shortwave radiation (Φ_{SW}) was only measured at terrestrial stations. Incoming longwave radiation (Φ_{LW}) was not directly measured and was calculated from the Stefan-Boltzmann law modified by atmospheric emissivity to account for cloud cover (Martin and McCutcheon 1999). Hourly cloud cover was estimated as the ratio of the observed Φ_{SW} to extraterrestial $\Phi_{SW,}$ calculated from the lake's latitude, time of day, and the declination of the sun (Tennessee Valley Authority 1972). On-water wind speeds measured at the P4 buoy were considered representative of wind conditions across the entire water surface. Before this station was installed, wind observations were obtained from the Puerto Varas ESSAL wastewater treatment plant, located approximately 500 m off the lake's southern shoreline. Wind speeds increase across the transition from land to water (Hsu 1981; Rueda et al., 2009), so on-land wind measurements blowing offshore were multiplied by a factor of 2.46, calculated from a linear regression between wind speeds in Puerto Varas and at P4. This factor is consistent with an on-water wind correction factor for Llanquihue previously determined by Mesa (2018).

4.2.4 1D Hydrodynamic Model (GLM)

3D model results were compared to those generated by the 1D hydrodynamic General Lake Model (GLM), an open-source code widely used within the limnological research community (Hipsey et al., 2019). GLM is derived from the earlier DYRESM model. GLM has previously been applied to simulate broad range of aquatic systems, from wetlands and ponds to deep lakes (Fenocchi et al., 2018, 2019). GLM assumes that temperatures are horizontally uniform and simulates a water body as a series of vertical layers, each of which is defined as a control volume that can contract or expand in response to inflows, outflows, and mixing with adjacent layers. To solve the energy balance, GLM quantifies the amount of turbulent kinetic energy available for surface mixing and deep mixing (i.e., below the thermocline) separately. In the surface layer, the available kinetic energy driving mixing and the deepening of the thermocline is calculated from the energy imparted from wind stirring, convective overturn, shear production, and Kelvin-Helmholtz billowing. Hypolimnetic turbulent diffusivity was parametrized by the Weinstock model (Weinstock, 1981) which calculates the vertical diffusivity as a function of the strength of stratification and an assumed rate of turbulent dissipation. The model domain was set up with a vertical grid size of 2 m. The GLM package in R (Bueche et al., 2020) includes an autocalibration procedures that utilizes an evolutionary Covariance Matrix Adaptation Evolution Strategy (Ladwig et al., 2018), which iteratively adjusted light attenuation and scaling factors for wind and longwave radiation to minimize the root mean square error between simulated and measure temperature profiles. Using this procedure, the model was calibrated and validated against the observed temperature at the P7 buoy for the same one-year time span evaluated for the 3D model calibration. A comparison of calibrated model specifications is shown in **Table 4.2**.

Table 4.2. *Specification of model parameters*

	GLM	**Si3D**
Dx/Dy	N/A	400 m
Dz	2 m	2 m
Dt	3600 s	50 s
C_D	0.0019	0.0013
k_d	0.17	0.085
WS Factor	0.96	1
Φ_{LW} Factor	1.07	1
Turbulence Closure	Weinstock	k-ε model

4.2.5 Calibration and Validation

Model performance of Si3D and GLM was evaluated by quantifying the agreement between measured and simulated water temperatures with four metrics: Root Mean Square Error (*RMSE*), Model Skill Score (*SS*), (Murphy & Epstein, 1989), *I1* and *I2* error norms (Rueda & Schladow 2003). These terms are defined as:

$$\mathrm{RMSE} = \frac{\sqrt{\sum_{i=1}^{N}\left(y_i - \hat{y}_i\right)^2}}{N} \tag{4.1}$$

$$\mathrm{I1} = \frac{\sum_{i=1}^{N}|y_i - \hat{y}_i|}{\sum_{i=1}^{N}|y_i|} \tag{4.2}$$

$$\mathrm{I2} = \frac{\left[\sum_{i=1}^{N}\left(y_i - \hat{y}_i\right)^2\right]^{\frac{1}{2}}}{\left[\sum_{i=1}^{N}\left(y_i\right)^2\right]^{\frac{1}{2}}} \tag{4.3}$$

$$\mathrm{SS} = 1 - \frac{\mathrm{RMSE}}{\sigma_{y_i}} \tag{4.4}$$

where N is the number of samples, y_i and $\hat{y}_i$ are the observed and modeled water temperatures at time i and σ_{y_i} is the standard deviation of the observed water temperature. Models were calibrated and validated against one year of field observations between August 20, 2021 and August 20, 2022 with a three-day model spin-up time.

4.2.6 Forecasted Meteorological Data

We first assessed the sensitivity of lake thermal structure to changes in T_{air} (+0.2–1.4 °C), WS (±10%), k_d (±50%), by modifying each parameter independently in the baseline (2021 – 2022) simulation. These ranges were determined from the predicted change in meteorological conditions forecasted under the RCP 8.5 scenario (see Section 4.3). We then assessed the net effects of changes in all meteorological forcing parameters using an output from a downscaled climate scenario. Changes in precipitation patterns and river inflows were not considered, as a robust analysis of Llanquihue's water budget has not been conducted and no inflow gaging data were available. Forecasted meteorological data based on climate projections for the 21st century in NP were obtained from the Center for Climate Resilience Research (CR^2) simulation platform (https://simulaciones.cr2.cl) which provides publicly available climate forecasts for Chile at various spatial and temporal scales. Climate models provide superior predictions to linear regional trend analyses as they contain internally consistent sets of meteorological forcing variables and can reveal changes in tipping points (i.e., shifts in mixing regime) that cannot be resolved by linear trends alone (Zamani et al., 2021).

From the five available regional climate models (RCMs), the 10 km gridded REGCM4 was selected because of its daily forecast outputs, relatively high spatial resolution and ability to accurately simulate regional climatic patterns over Chile's complex terrain features, such as the Andes Mountains and Pacific coastline (Bozkurt et al., 2019a). Climate projections from the IPCC's highest RCP scenario (RCP 8.5) were utilized in this analysis. This pathway represents a "worst case" scenario in which increasing greenhouse gas emissions continue to occur unabated through 2100, resulting in an additional 8.5 W m^{-2} of heat trapped in the atmosphere compared to preindustrial conditions (Riahi et al., 2011).

Daily forecasts for January 1, 2007 through December 31, 2099 were averaged across six model grid cells that encompassed Lago Llanquihue's surface. A monthly bias correction offset was applied to minimize the difference between modeled and observed daily meteorological conditions during the 2021-2022 monitoring period and then the forecasted data were normalized to the baseline conditions using the change factor or 'delta method' (Diaz-Nieto & Wilby, 2016). Lastly, daily data were downscaled to an hourly timestep to account for subdaily variability. A detailed description of the downscaling methodology can be found in **Appendix C.1**. To assess the significance of long-term trends in meteorological parameters, a non-parametric Mann-Kendall test (MKT) was utilized as the datasets did not meet normality assumptions. The magnitude of the linear trend was calculated by the Sen's slope estimator. This method was used instead of a simple linear regression as it is less susceptible to outliers. The mean and standard deviation of projected climate trends were calculated for six combinations of GCMs and RCMs to provide an estimate of the uncertainty in predictions (**Appendix C.2**). Eight scenario runs were performed, running for 730 days each (i.e., two years), from which year one was used as a spin-up period to eliminate the effects of initial conditions, while results from year two were evaluated for comparison. Each scenario represented the meteorological conditions at the start of the decade from 2021 to 2091. To assess the possible effects of a concurrent decline in trophic status, we compared results from scenarios where k_d remained constant with those in which k_d declined at rate 1% per year (Lottig et al., 2014).

4.2.7 Characteristics of Thermal Stratification

Changes in lake mixing regime were assessed by evaluating shifts in the timing and duration of the summer stratified and winter mixing seasons. The thermally stratified season was defined as when the temperature difference between epilimnion, less than 30 m depth, and hypolimnion, greater than 200 m depth, exceeded 1 °C (Engelhardt & Kirillin, 2014; Wilhelm & Adrian, 2008). The winter mixing period was defined as beginning when the hypolimnion temperature cooled by more than 0.02 °C, indicating vertical convective mixing throughout the water column, and ended when the vertical difference between the top and bottom layers exceeded 0.1 °C. To quantify the degree of stratification, we calculated the Schmidt stability (S_T [J m^{-2}]) , the resistance to mixing due to energy stored within the lake, using the LakeAnalyzer toolbox in MATLAB® (Read et al., 2011). Thermocline depth (Z_{thermo}), metalimnion (h_{meta}) and epilimnion (h_{epi}) thickness were calculated via the equations described in Imberger and Patterson (1989). Derivations each of these limnological parameters can be found in the **Appendix C.4**.

The effects of climate change on the lake's surface heat flux (Q_{net}) were assessed by quantifying the net shortwave radiative (Q_{sw}) and net longwave (Q_{lw}), latent (Q_e) and sensible (Q_h) heat fluxes via the Lake Heat Flux Analyzer toolbox in MATLAB® (Woolway et al., 2015). The efficiency of wintertime vertical mixing was evaluated through numerical tracer experiments following the methods of Wahl and Peeters (2014).

For these experiments, the model was initialized on May 1 with a vertical linear gradient of a passive tracer wherein layers below 300 m had a maximum concentration, and surface layers had a tracer concentration of 0. Mixing from hydrodynamic model outputs was evaluated during the winter by quantifying the mixing index (M_{idx}) defined as:

$$M_{idx} = \frac{\sigma_{t1} - \sigma_{ti}}{\sigma_{t1}} \tag{4.5}$$

where σ_{t1} and σ_{ti} are the standard deviations of the vertical tracer concentration on May 1 and i^{th} day of winter respectively evaluated at the mid-lake station. M_{idx} equals 0 when there is no mixing, whereas $M_{idx} = 1$ when complete mixing occurs.

4.3 Results

4.3.1 Lake Observational Data

One year of temperature (P7) and deep water DO (P4) observations from Lago Llanquihue are shown in **Figure 4.1**. Thermistor chain recorded surface temperatures varying from a minimum of 10.8 °C in September to 19 °C at peak stratification in early February. Hypolimnion temperatures remained relatively stable, gradually increasing from 10.65 °C to 10.74 °C from September to July. The lake was thermally stratified from mid-October through the end of June, initially forming a thermocline at 30 m, which progressively deepened to 80 m throughout the summer and early fall. During winter, surface temperatures cooled until the lake reached near homothermal conditions at the end of July. When vertical convective mixing reached the bottom of the lake, hypolimnion temperatures cooled from 10.74 °C to 10.44 °C as a series of sudden drops in hypolimnion temperature throughout August. This cooling denoted the duration of the winter mixing period before the lake began to restratify in mid-September. When stratified, hypolimnetic DO decreased by -0.08 mgL^{-1} $mnth^{-1}$ from 8.81 to 8.30 mgL^{-1} but quickly rebounded to near-saturated conditions during winter.

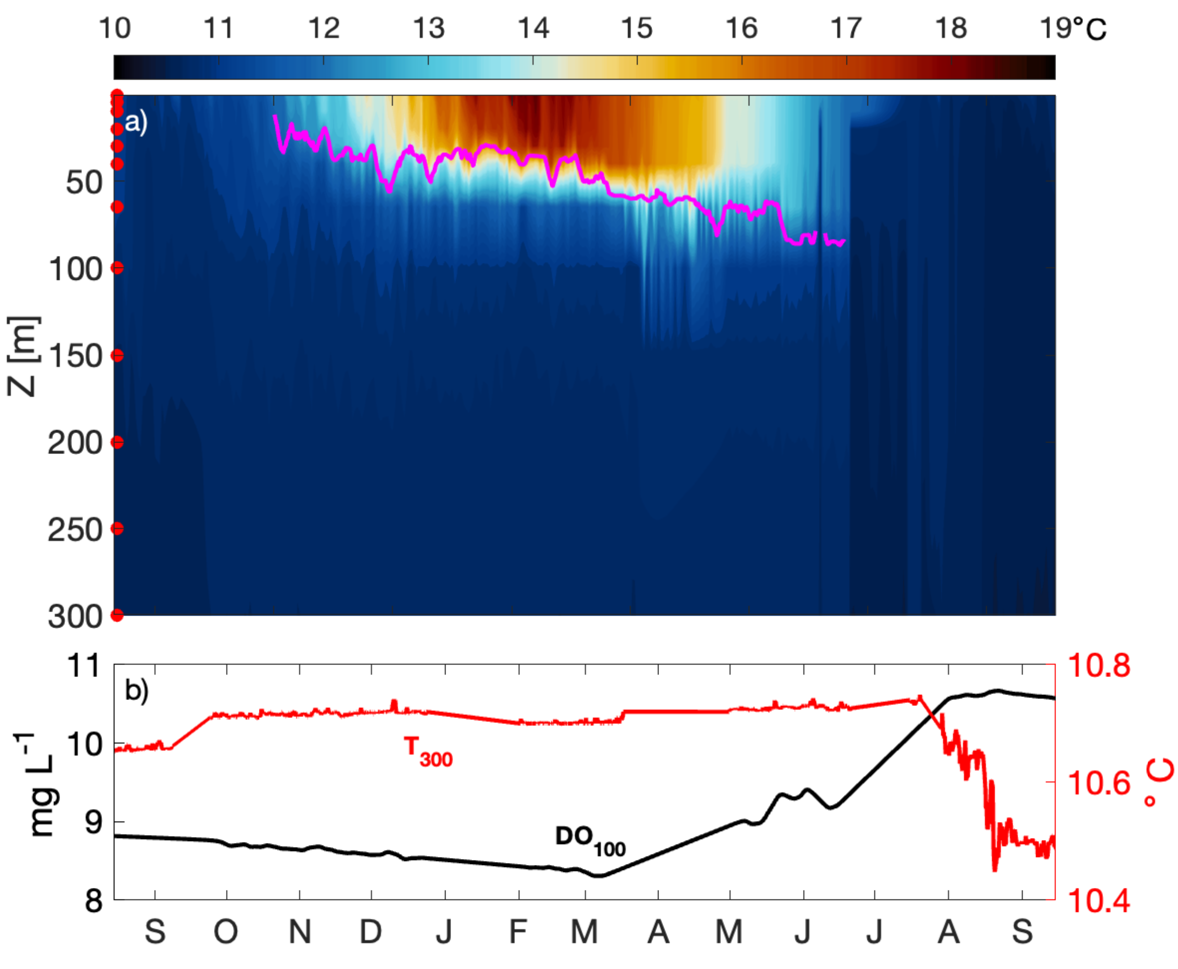

Figure 4.2. *a) Contour plot of the observed temperature at P7 during 2021-2022 deployment. Missing data was gap filled with data from P4 and P6 when possible and linearly interpolated otherwise. Magenta line indicates thermocline depth. Red dots on y-axis indicate location of thermistors. b) Time series of DO at 100 m at P4 and temperature at 300 m at P7.*

4.3.2 Model Calibration and Validation

verall, there was good agreement between between measured water temperatures and those simulated by Si3D. Model runs with $C_D = 1.3\text{x}10^{-3}$ and $k_d = 0.085\ \text{m}^{-1}$ produced the best results (**Figure 4.3**). While light extinction is likely higher in the summer when a greater concentration of organic matter in the water column reduces clarity, we chose to use this constant value as it improved model performance compared with larger values. The average *RMSE* across all sites increased from 1.1°C with a $k_d = 0.17\ \text{m}^{-1}$ to 0.47 °C at the calibrated value.The *RMSE* of the depth-integrated water temperature ranged from 0.31 – 0.65 °C (**Table 4.3**) across the three stations during the calibration period (Aug 23 2021 – Feb 20 2022), comparable with the range of errors published in previous numerical modeling studies of deep lakes (Laborde et al., 2010; Rueda et al., 2003; Valbuena et al., 2022). Skill scores, calculated for the upper 50 m of the water column at each site, were all above 0.8, indicating "excellent" model performance (Scheu et al., 2018), while the *I1* and *I2* norms were all within an acceptable range of 0-0.06 (Laborde et al., 2010; Morillo et al., 2008). Model performance was slightly better during the validation period (Feb 21 2022 - Aug 22 2022) with lower *RMSE*s (0.18 – 0.41 °C) , higher skill scores (0.97 – 0.99) and *I1* and *I2* metrics were still within a valid range found in the literature. The most significant deviation between modeled and observed temperatures occurred in the metalimnion, between 40-70 m depth, where the seasonal thermocline forms. As a result of the large vertical temperature gradients of ~0.5 °C m^{-1} in this region, comparatively small displacements of the thermocline can result in large temperature differences (Wahl & Peeters, 2014).

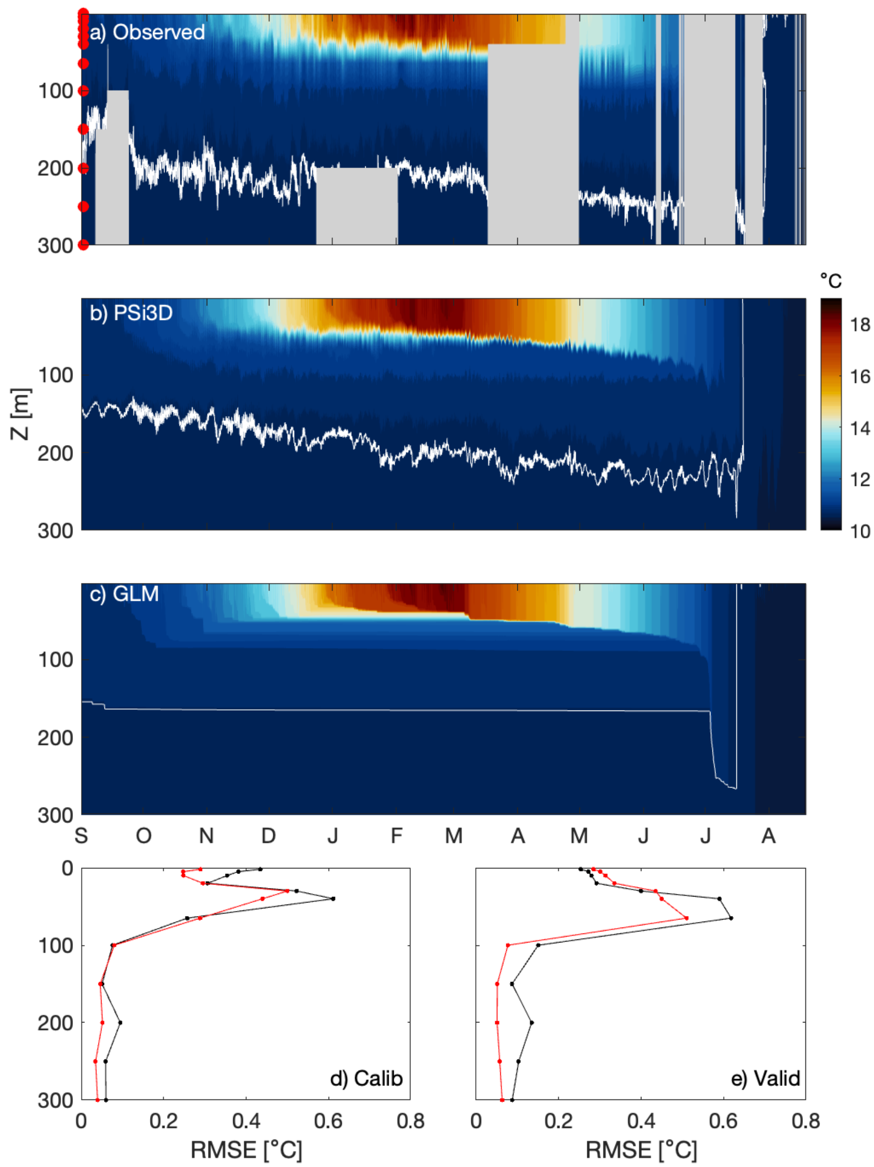

Figure 4.3. *Comparison of a) observed vertical temperature structure at P7 with b) calibrated Si3D and c) GLM simulations from September 2021 to August 2022. Red dots indicate locations of thermistors. White line denotes 10.75 ℃ isotherm. RMSE of Si3D (red) and GLM (black) at thermistor depths during d) calibration and e) validation period.*

The model accurately estimated both the onset (October 19) and the end of the stratification period (June 24) within two days of observation. The calibrated model was validated by determining the extent to which the occurrence and duration of winter turnover events were correctly identified. The onset of turnover (July 26) was simulated as occurring 3 days earlier than observed while the end of the winter mixing period was simulated 5 days later than observed, thus the duration of the winter mixing period was overestimated by about a week. The discrepancy between the model and observed temperatures during the winter was due to a faster rate of surface cooling predicted by the model in the late winter. Consequently, Si3D slightly overestimated the degree of bottom water cooling by 0.15 °C during winter mixing.

Table 4.3. *Comparison of performance metrics during calibration and validation of Si3D and GLM.*

		Calibration				Validation			
		Aug 23 2021 – Feb 20 2022				Feb 20 2022 – Aug 20 2022			
		RMSE	**SS**	**I1**	**I2**	**RMSE**	**SS**	**I1**	**I2**
Si3D	P4	0.65	0.87	0.014	0.050	0.41	0.98	0.013	0.034
	P6	0.45	0.83	0.002	0.034	0.33	0.97	0.013	0.029
	P7	0.31	0.92	0.008	0.023	0.18	0.99	0.005	0.016
GLM		0.27	0.80	0.004	0.047	0.27	0.84	0.004	0.053

As with the 3D simulation, water temperatures simulated by GLM were in good agreement with the observed data. The mean RMSE during both the calibration and validation periods was 0.27 °C while the skill scores were lower than the Si3D simulation, 0.80 and 0.84 (**Table 4.3**). The onset and end of stratification were accurate to within three days of observations and thus surface heat fluxes and the thermal structure of the well-mixed epilimnion were reproduced reasonably well with the 1D model. However, the 1D model produced higher errors than the 3D model between 30 m and 40 m, with the largest error observed at 40 m, $RMSE$ = 0.62 °C. While Si3D can simulate vertical thermocline displacements on the order of 10 m in the metalimnion, associated with internal wave activity, GLM models a horizontally homogenous thermocline depth. In the underlying hypolimnion (i.e., below 100 m), the 3D model continued to perform better than the 1D model, as Si3D was able to better resolve both periodic temperature oscillations and the long-term warming trend of the hypolimnion caused by vertical turbulent mixing (+0.0044 °C $mnth^{-1}$). Turbulent mixing in the deep hypolimnion of lakes and oceans can result from various inherently 3D processes including horizontal penetration of shear produced over later slopes of the lake (Lemmin, 2020), breaking of progressive internal waves (Garret, 2003; Gregg, 1987) and frictional decay of inertial motion (Alford 2016), thus 3D models are necessary to accurately resolve the dynamics at these depths. Furthermore, GLM overestimated the duration of the winter mixing period by 3 weeks, simulating the date of turnover 14 days earlier and end of the mixing period 7 days later than observed. Consistent with observations, Si3D simulated bottom water cooling as a series of discrete sharp drops in bottom temperature, while GLM simulated the bottom cooling as a continuous process. The ability of Si3D to better resolve the timing of mixing events and the evolution of hypolimnion temperature demonstrates that 3D models provide superior performance for simulating deep water temperature dynamics, particularly during the convective cooling period. These observations agree with a comparative analysis conducted by Man et al (2021), which found that 3D lake models were better able to simulate periods when the thermal structure is dynamically changing. Due to its ability to better resolve the thermal evolution of both the metalimnion during the stratified season and the hypolimnion during turnover, Si3D was selected for future climate change scenario analyses.

4.3.3 Downscaled Climate Forecast Data

Daily to hourly downscaling methods performed well with correlation coefficients (r) >0.85 between hourly observed and modeled measurements for all parameters except for north-south and east-west wind-components, $r = 0.83$ and $r = 0.65$ respectively (**Appendix C.1**). The results demonstrate that forecasted hourly meteorological data can be accurately downscaled from daily predictions that are typically output from GCMs but also highlight the limitations in forecasting winds, which remains challenging due to inherent variability at small scales (Dupré et al., 2020). Predicted changes from the 10 km REGCM4 simulation were generally consistent with the average trend across the RCP 8.5 simulations for all parameters, except for RH and east-west wind component, indicating that this was a suitable model for simulating the mean climate trajectory in northern Patagonia (**Appendix C.2**). Discrepancies in RH and wind projections between the 10 km and coarser resolution models may be due to differences in the spatial extent of the model domains. Mann-Kendall test indicates significant (p-value <0.001) increasing trends for T_{air} and Φ_{LW} and significant decreasing trends for WS and Φ_{SW} (**Figure 4.4**). The Sens slope estimates an increase in the mean annual T_{air} at a linear rate of 0.2 ± 0.08 (S.D.) °C decade^{-1} with no sign of weakening throughout the century while Φ_{LW} wil increase by 1.4 ± 0.43 W m^{-2} decade^{-1}. Correlation between annual T_{air} and Φ_{LW} is r = 0.84, highlighting the dependence of incoming longwave radiation on atmospheric temperature. In contrast, annual mean WS is forecasted to decline at a rate of -0.03 ± 0.048 m s^{-1} decade^{-1} (-6% by 2099). While the change in Φ_{SW} of -0.3 W m^{-2} decade^{-1} is statistically significant, the total decline is <1% from baseline conditions and would have a minor impact on the lake's annual heat budget. Likewise, the change in RH was not statistically significant and was not included in the sensitivity analysis.

Seasonally, the largest increases in T_{air} are forecasted to occur between December and January (+0.20 – 0.22 °C decade^{-1}) while T_{air} from February through July (+0.18 to 0.19 °C decade^{-1}) will warm less rapidly (**Figure 4.5**). Consequently, the rate of Φ_{LW} increase in December (+2.2 W m^{-2} decade^{-1}) is projected to be more than three times as

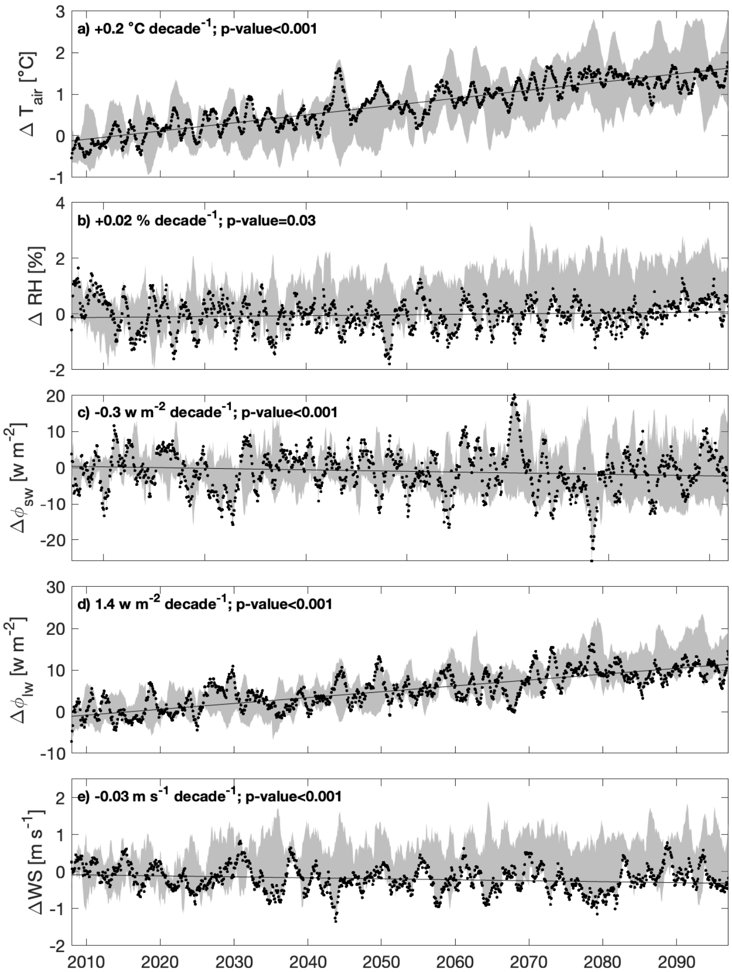

Figure 4.4. *Predicted change in 12 month running mean relative to 2007-2021 baseline for a) air temperature, b) relative humidity, c) incoming shortwave radiation, d) incoming longwave radiation, and e) wind speed in Lago Llanquihue from REGCM4 RCP 8.5 simulation. Shaded grey region denote range across all six GCM RCM combinations. Black lines indicate the Sens slope estimate of the linear trend.*

fast as in June (+0.6 W m^{-2} decade^{-1}). Changes in *WS* also show a strong seasonal pattern with declining speeds projected during the austral summer and autumn months and increasing wind speeds forecasted during the winter and spring.

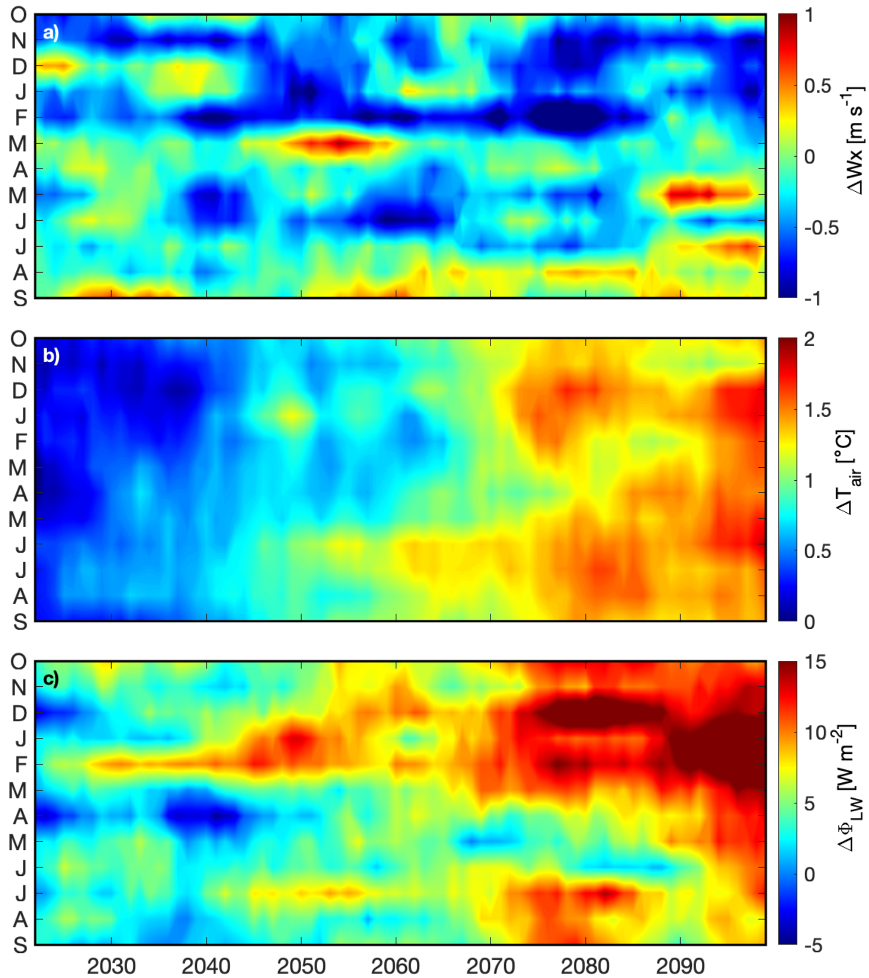

Figure 4.5. *Seasonal variation in projected changes a) wind speed, b) air temperature, c) incoming longwave radiation under RCP 8.5 scenario relative to 2021-2022 baseline.*

4.3.4 Sensitivity Analysis

The results of the sensitivity analysis of effects of variation in air temperature (+0 to 1.4 °C), wind speed (WS ± 10%), and clarity (k_d ± 50%) on lake temperature and seasonal mixing regime are shown in **Table 4.4**. The analysis found that warming air temperatures had the greatest impact on lake temperatures, with increases in T_{air} of +1.4 °C resulting in a +0.32 °C increase in the volume-averaged lake temperature. While temperatures rose at all depths, surface waters (+0.66 °C) warmed more than twice as fast as bottom waters (+0.29 °C). Due to the differential rate of warming between the epilimnion and the hypolimnion, there was an increase in the vertical temperature gradient and intensifying stratification, resulting in an annual average Schmidt stability increase of 15% (3,333 J m^{-2}) and a decrease in the depth of seasonal thermocline by 2.7 m. Stronger stabilities reduced vertical exchange through the metalimnion and resulted in the stratified season persisting 13 days longer. Consequently, the date of overturn was shifted 30 days later in the winter, and the duration of winter mixing period declined by 34 days.

Increasing k_d by +50% (i.e. lower clarity) resulted in average lake temperatures cooling of -0.21 °C. While surface temperatures increased at higher k_d values, deep water temperatures declined resulting in a net cooling throughout the water column. Lower clarity shifted the stratified season a week earlier in the year but had minimal effects on its duration. Furthermore, the seasonal thermocline depth was strongly dependent on k_d with variations in Z_{thermo} >8.5 m depending on the direction of k_d change.

In contrast variations in wind speed up to ±10% had comparatively little effect on lake temperature or seasonality of the mixing regime, as averaged lake temperatures change by <0.1 °C. For example, while a decrease in wind speed of 10% warmed surface temperatures by +0.29 °C, deep water temperatures warmed by only +0.06 °C. As wind speeds primarily influence surface heating in lakes through sensible and latent heat transfer, heat transfer to the deep hypolimnion was relatively insensitive to variations in wind.

Table 4.4. *Sensitivity of lake temperature, stratification strength, thermocline depth and duration of stratified and mixing seasons to changes in air temperature, clarity, and wind speed.*

	T_{air} +0.2 °C	T_{air} +0.6 °C	T_{air} +1 °C	T_{air} +1.4°C
T_{avg} [°C]	+0.05	+0.13	+0.22	+0.32
T_{surf} / T_{bot} [°C]	+0.10 / +0.03	+0.29 / +0.12	+0.48 / +0.20	+0.66 / +0.29
Strat Onset / End	0 / +1	-1 / + 3	-7 / +5	-7 / +6
Strat Season [days]	+1	+4	+12	+13
Mix Onset / End	+2 / -6	+15 / -4	+13 / - 0	+ 30 / -4
Mix Season [days]	-8	-19	-13	-34
S_T [J m^{-2}]	+477	+1409	+2374	+3333
Z_{thermo} [m]	-0.2	-1.3	-2.0	-2.7
	k_d -50%	***k_d -25%***	***k_d +25%***	***k_d +50%***
T_{avg} [°C]	+0.24	+0.12	-0.10	-0.21
T_{surf} / T_{bot} [°C]	-0.08 / +0.16	-0.04 / + 0.07	+0.04 / -0.08	+0.10 / -0.14
Strat Onset / End	+4 / +6	+3 / +4	-1 / -4	-7 /-6
Strat Season [days]	+2	1	-3	+1
Mix Onset / End	+18 / +3	+5 / -7	-6 / -6	-9 / -8
Mix Season [days]	-14	-12	0	1
S_T [J m^{-2}]	+546	+455	-386	-1061
Z_{thermo} [m]	+9.8	+6.2	-3.6	-8.7
	WS -10%	***WS -5%***	***WS +5%***	***WS +10%***
T_{avg} [°C]	+0.04	+0.02	-0.01	-0.01
T_{surf} / T_{bot} [°C]	+0.29 / +0.06	+0.14 / +0.01	-0.13 / -0.02	-0.26 / -0.04
Strat Onset / End	-1 / +4	0 / +2	+1 / -1	+2 /-2
Strat Season [days]	+5	+2	-2	-4
Mix Onset / End	+4 / -10	-2 / 0	1 / -12	-4 / -12
Mix Season [days]	-14	+2	-13	-7
S_T [J m^{-2}]	+ 770	+505	-299	-629
Z_{thermo} [m]	-3.4	-1.3	+2.0	+4.6

4.3.5 Forecasted Changes in Lake Thermal Structure

Results from the REGCM4 RCP 8.5 simulation predict that while atmospheric warming will impact the lake's stratification regime, the lake is not projected to become oligomictic during the 21st century under a worst-case emissions scenario. The volume-averaged annual lake temperature is forecasted to warm at an average rate of +0.07 °C decade^{-1} increasing by +0.29 °C in 2041 and by +0.54 °C in 2091 relative to the baseline scenario (**Figure 4.6**). As expected, the most significant temperature increase occurred in the upper 30 m of the water column (+0.13 °C decade^{-1}), warming by +1.01 °C by 2091. The hypolimnion warmed at approximately half this rate (+0.06 °C decade^{-1}) increasing by +0.50 °C by 2091. Differential rates of warming between the epilimnion and the hypolimnion resulted in great thermal stability, with an increase in the resistance to mechanical mixing at a rate of 430 J m^{-2} decade^{-1}. Comparing monthly average temperatures in the 2091-92 scenario against the baseline simulation (**Figure 4.7**) demonstrates that seasonally, surface warming will be most pronounced between October and January (+1.04 - 1.72 °C) while surface temperatures from March and April are forecasted to remain the same and winter surface temperatures will warm less (+0.37 - 0.75 °C). In contrast, at 50 m deep, temperatures are projected to be cooler from November through April. Hypolimnetic waters are projected to be warmer year-round, though the most significant difference can be observed in August when bottom waters are forecasted to cool by only -0.04 °C during turnover compared to a decrease of -0.25 °C in the baseline simulation.

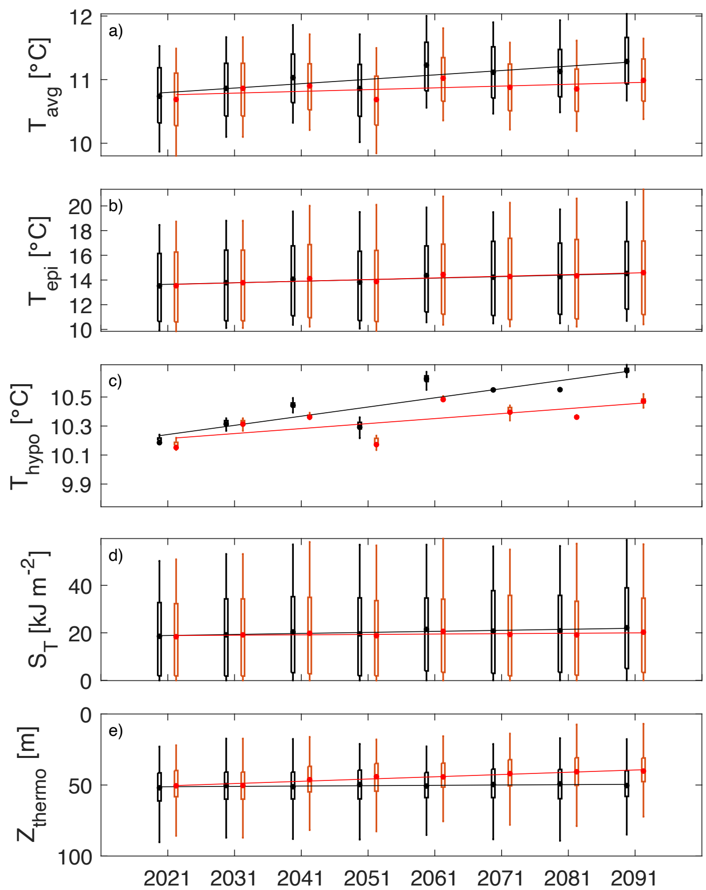

Figure 4.6. *Comparison of forecasted a) volume-averaged lake temperature, b) epilimnion temperature between 1-20 m, c) hypolimnion temperature below 100 m, d) Schmidt Stability, e) thermocline depth for REGCM4 RCP 8.5 simulations using a constant k_d (black) and k_d increasing + 1% yr^{-1} (red). Boxes and whiskers indicate quartile ranges for one year of simulation data, dots indicate mean and solid lines indicate linear trend determined via linear regression.*

Warmer surface temperatures in the spring shifted the onset of the stratified season earlier in the year by approximately +1 day decade^{-1} while the end of the stratified season moved later in the year by +3 days decade^{-1}, resulting in the stratified season persisting 10 days longer by 2041 and 25 days longer by 2091 (**Figure 4.8**). During the stratified period, the temperature difference between the epilimnion and hypolimnion increased by +0.06 °C decade^{-1}.

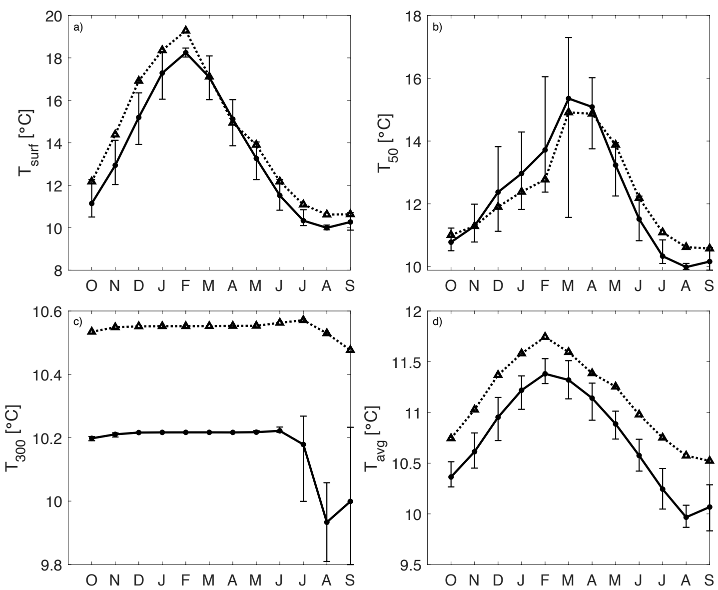

Figure 4.7. *Monthly mean temperatures at a) surface b) 50 m c) 300 m and d) volume-averaged for 2021-2022 baseline (solid line with circles) and 2091-92 RCP 8.5 projection (dotted line with triangles). Error bars show the maximum and minimum of the baseline simulation.*

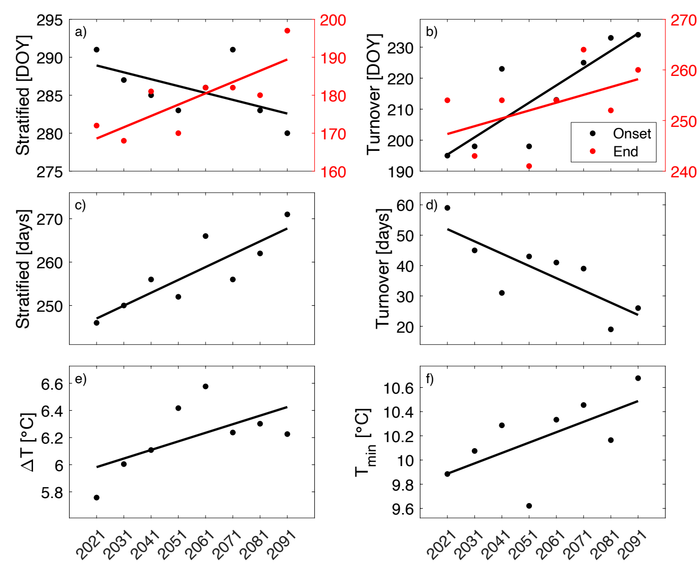

Figure 4.8. *Projections of long-term changes in a) onset (black) and end (red) of stratified season, b) onset (black) and end (red) of winter mixing period, c) duration of stratified season, d) duration of winter mixing period, e) temperature difference between epilimnion and hypolimnion during stratified season, f) minimum bottom temperature during mixing for RCP 8.5 projection. Solid lines indicate linear trend calculated via linear regression.*

Error! Reference source not found. depicts how the thermal structure of the lake during t he stratified season will be altered by the end of the century. Throughout the stratified season the thermocline in 2091-92 simulation remained predominately shallower than in the baseline scenario. In November, the forecasted Z_{thermo} was initially 5 m shallower, however this difference

decreased through time so that from December through February there was no consistent offset between the baseline and forecasted Z_{thermo}.

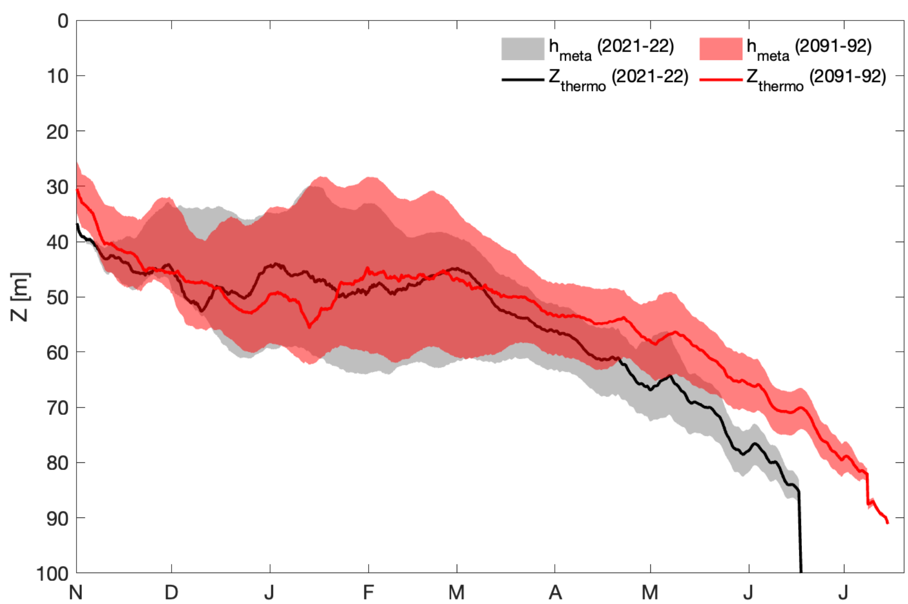

Figure 4.9. *Comparison of depth of thermocline (Z_{thermo}) and thickness of metalimnion (h_{meta}) in baseline (black) and 2091-92 (red) RCP 8.5 simulation.*

From March through the end of the stratified season, the baseline thermocline deepened at a faster rate than in the 2091-92 simulation resulting in the forecasted thermocline depth lying 15 m above the baseline position by early June. On average the thermocline depth is forecasted to shoal at a rate of 0.25 m decade^{-1} (**Figure 4.6**). The mean thickness of the metalimnion from November to June is predicted to increase by 1.9 m with the largest width of 33.5 m reached in mid-January. In contrast, the largest width of the metalimnion on the baseline simulation was 31 m and occurred in February. The increase in the h_{meta} is primarily driven by a shoaling of the upper metalimnion boundary.

As a consequence of a longer stratified season and greater average thermal stability, the onset of winter turnover was shifted later in the winter at a rate of +5.5 days decade^{-1} while the end of winter mixing period was shifted back +1.5 days decade^{-1} later, shortening the duration of the winter mixing season by -4 days decade^{-1} (**Figure 4.8**). Thus, by the end of the century the duration of the winter mixing period is forecasted to decline by ~30 days, lasting for three weeks from late August through September. The minimum bottom temperature during turnover increased from 9.88 °C to 10.68 °C reflecting a milder winter climate and a shorter mixing period when the bottom of the lake is actively mixing with cool surface waters. Numerical tracer experiments demonstrate, that despite a decline in the duration of the winter mixing period, Llanquihue will continue to completely mix annually during this century (**Figure 4.10**). In all simulated winter seasons, $M_{idx} = 1$ by mid-August indicating the duration of the winter mixing season will continue to be sufficient to facilitate deep mixing throughout the entire water column each year.

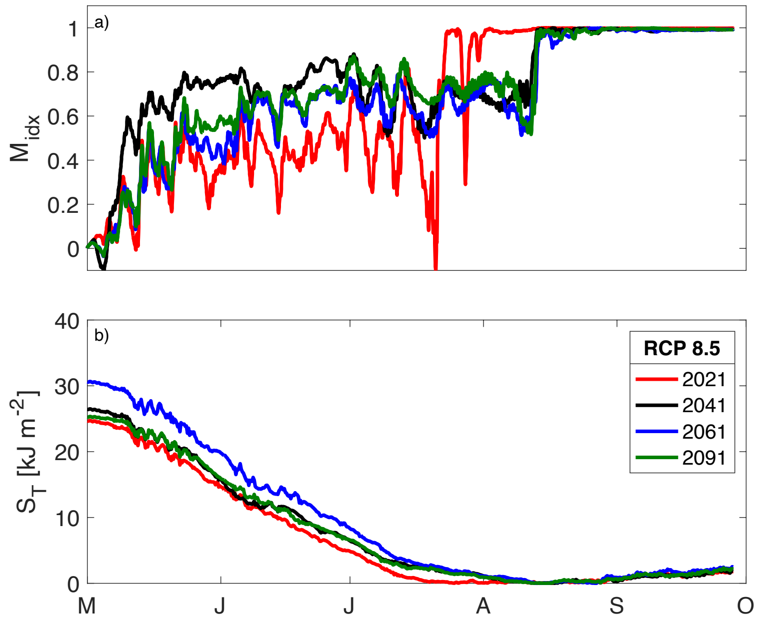

Figure 4.10. *Results of wintertime numerical tracer experiments. A): Mixing Index (M_{idx}) and b) Schmidt Stability (S_T) for selected winters in RCP 8.5 simulation.*

4.3.6 Impacts of Clarity

An additional set of forecasts runs with light extinction coefficient (k_d) increasing by +1% yr^{-1} were conducted to simulate how the lake's thermal response to climate change would be altered were trophic status to decline concurrently (**Figure 4.6**) shows that reduced lake clarity can counteract much of the projected warming in Lago Llanquihue. While average surface temperatures warmed at comparative rates with both constant and increasing k_d, the hypolimnion warmed slower in the low clarity scenarios resulting in a lower volume-average warming rate of +0.028 °C decade^{-1}. Furthermore, the thermocline depth shoaled faster in the low clarity scenarios at a rate of 1.59 m decade^{-1}. As k_d declined, peak summer surface temperatures increased dramatically. In the baseline simulation the

99% percentile surface temperature was 18.4 °C. By the end of the century this temperature was exceeded in 13% of days.

4.4 Discussion

4.4.1 Model Performance and Limitations

Si3D successfully simulated the thermal structure of Lago Llanquihue over a one-year period at three locations across the lake, validating model performance in both space and time. The 3D model more accurately resolved the seasonal evolution of stratification, the timing of overturn and the warming/cooling of the hypolimnion than a 1D model. While temperatures near the thermocline were predicted with greatest uncertainty in both models, errors produced by Si3D at this depth were lower due to the model's ability to resolve internal seiche activity. In contrast, GLM simplifies the hydrodynamic processes that govern vertical mixing and transport and thus poorly represents variations in thermocline depth and heat fluxes into the deep hypolimnion. There was good agreement between 3D simulated and observed temperatures (as indicated by the high values of a range of performance metrics) despite model simplifications including the use of a spatially uniform wind field and the neglect of inflows and outflows. Prevailing winds are predominantly along a north-south axis, enabling a simplified wind field to be used as a model input. While changes in catchment runoff can impact lake thermal structure (Zamani 2021), Llanquihue's long residence time suggests that the impact of changing inflows on vertical mixing would be relatively minor. Calibrated C_D and k_d terms fell within realistic ranges from the published literature, though both values likely vary throughout the year in response to environmental conditions. The attenuation of light, for example, will fluctuate seasonally due to phytoplankton succession (Schanz 1994) while wind drag varies temporally as both a function of the wind speed and the roughness of the water surface. However, time-invariant constants used in this study produced sufficiently accurate results. The performance of Si3D in this study is comparable with results reported by others in 3D hydrodynamic lake models (Amadori et al., 2021; Reiss et al., 2020; Wahl and Peeters 2014).

Despite the overall good performance and reasonable model errors, the results inevitably include some degree of uncertainty. The meteorological forecasts provided by REGCM4, may contain errors in the estimation of the local climate (Koutsoyiannis et al., 2008). However, these uncertainties can be reduced with the bias correction and downscaling techniques described in the methods section. Although the climate trends simulated by REGCM4 were largely consistent with the average of the six RCP 8.5 simulations, there is considerable uncertainty when predicting changes in winds, which are much more localized. Likewise, current GCMs do not fully capture the extreme climatic events that are expected to be a feature of future climatic conditions. All scenarios were initialized with this same starting condition (i.e., thermistor chain measurements in

August 2021) and were run for a relatively short time period of two years. To eliminate the effects of the initial conditions, only data from the second year were evaluated for comparison. It is possible Llanquihue has not completely equilibrated to the climate perturbations after only one year (Perroud & Goyette, 2010). Therefore, warming rates, particularly in the gradually warming hypolimnion (Fenocchi et al., 2018), are likely conservative estimates of long-term warming rates. While a longer running simulation may be preferred, with the limited available data, it was not possible to assess model performance over a longer time span. In the absence of robust historical record of lake monitoring data these model results provide the first quantitative estimates of the long-term trajectory of a deep northern Patagonian lake.

4.4.2 Climate Change Effects on Heat Fluxes and Mixing Regime

The energy flux between a lake and the atmosphere is regulated by shortwave and longwave radiative fluxes, as well as sensible and evaporative heat fluxes. The RCP 8.5 scenario predicted that there would be no significant changes in incoming shortwave radiation throughout the 21st century. However, it is uncertain how accurately regional climate models can predict changes in cloud cover, which would affect daily Φ_{SW} (Enriquez-Alonso et al., 2017). In comparison, the RCM predicts a long-term decline in wind speed, and increases in air temperature reducing latent and sensible heat losses and increased incoming longwave radiation. In the RCP 8.5 scenario, the correlation of annual average lake water temperature with T_{air} was $r = 0.94$, $p < 0.001$ and with Φ_{LW} was $r = 0.90$, p-value < 0.01 after detrending. Thus, both were significantly correlated with the increase in water temperature, though T_{air} was slightly more significant. While increased air temperature was important to the lake's changing net thermal budget, T_{air} was less closely correlated with hypolimnion temperatures ($r = 0.71$, $p < 0.001$). This finding suggests that the temperature of the hypolimnion integrates the combined effects of winter cooling and mixing during stratification. Thus, while winter air temperatures are an important factor influencing deep water cooling during winter mixing in Llanquihue, is not necessarily determinative.

Hydrodynamic simulations evaluated the sensitivity of the lake's thermal structure to changes in air temperatures, wind speed, and clarity through simple modifications of the baseline forcing data. Increased air temperature up to +1.4 °C resulted in a longer duration of summertime stratification and reduced the duration of wintertime turnover. In comparison, the impacts of variations in wind speed by ±10% are more complex because wind acts both on sensible and latent heat exchange and provides kinetic energy to the lake surface to drive turbulent transport. Lower wind speeds increased heating throughout the water column, thermal stability and reduced Z_{thermo}. However, the duration of the mixed season did not change linearly in response to wind speed. The impacts of wind speed on the volume-average lake temperature were relatively minor compared to T_{air}.

This finding is expected given that predicted changes in wind speeds will have the most pronounced impact on shallow lake mixing regimes (Woolway and Merchant 2019). Lake warming was also sensitive to variations in clarity. A higher light extinction coefficient limits the penetration depth of radiative heat so that more heat is absorbed near the surface and less heat is transferred to deeper layers. Thus, as k_d increased, hypolimnion waters cooled while surface layers warmed. Given the impact that variations in k_d, independent of climatic change, can have on lake heat fluxes suggests that temporally variable light extinction coefficient should be incorporated into long-term climate models of lakes to assess uncertainty (Rose et al., 2016).

Increased surface heating due to climate change can impact lake mixing regime by increased water temperatures, altering the apportionment of the water column between epilimnion, metalimnion and hypolimnion, shifting the duration of stratification and mixing, and changing the overall strength of stratification. These factors are interrelated and depend on how seasonally uniform or varied the change in meteorological forcings are. In addition, the change in the strength and duration of stratification may not be directly related to one another; if for example the largest increase in surface fluxes primarily occurred during winter months, the annual average S_T might increase, but the duration of stratification would be relatively unaffected. In the case of Llanquihue, the most significant increase in monthly heat fluxes (**Figure 4.11**) is projected to occur from

January through March as result of lower latent and sensible heat loss. Both heat flux components are forecasted to decline in summer due to seasonal changes in atmospheric temperature and lower summer wind speeds. Thus, the forecasted increase in S_T and stratified season duration are highly correlated ($r = 0.97$, $p < 0.01$).

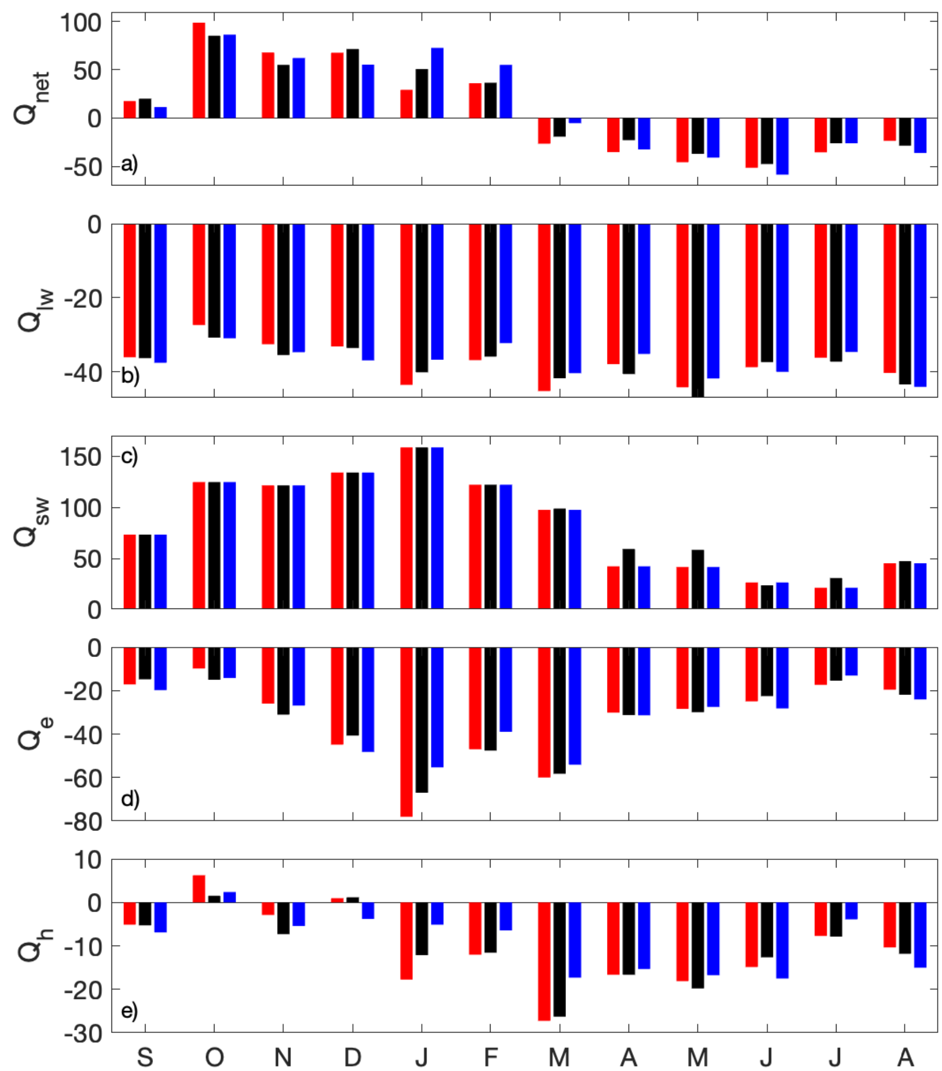

Figure 4.11. *Comparison of monthly cumulative heat fluxes in mJ m^{-2} for baseline (red), 2041-42 (black) and 2091-92 (blue) RCP 8.5 simulations. a) Q_{net} is net surface, b) Q_{LW} is net longwave radiative, c) Q_{SW} is net shortwave radiative, d) Q_e is latent, e) Q_h is sensible heat flux.*

Outputs of the downscaled RCP 8.5 scenario exhibited higher rates of surface (+ 0.11 °C decade^{-1}) and bottom (+0.06 °C decade^{-1}) warming and a greater increase in the duration of the stratified season than when T_{air} was altered individually (**Table 4.4**). The discrepancy between the results from the air temperature sensitivity analysis and the RCP 8.5 simulation demonstrate the importance of utilizing a full set of internally consistent forecasted climate parameters in predicting lake thermal structure. These higher rates of warming can partially be attributed to the inclusion of forecasted lower wind speeds.

Warming air temperatures resulted in an increase in modeled lake temperatures at all depths, with the most significant warming observed in the epilimnion, whereas deep water warmed slower. Epilimnetic warming rates were approximately 70% of the modeled increases in air temperature, consistent with observations and modelling studies of other deep temperate lakes (Perroud and Goyette 2010; Wood et al., 2016). In contrast, deep ice-covered lakes are warming more rapidly than regional air temperatures (Austin and Colman 2007; Hampton et al., 2008; O'Reilly et al., 2015) as reduced ice coverage promotes a positive ice-albedo feedback loop that enhances lake surface water temperature warming. Warming, because of increased air temperatures, led to an equally earlier onset and later break up of thermal stratification in Lago Llanquihue

Warming of hypolimnetic waters, is indirectly driven by surface warming in a so called "deep water cascade" (Anderson 2021). The increased duration of the summer stratified season delays the onset of winter turnover and shortens the length of the subsequent well-mixed period when the hypolimnion is mixing with plunging convectively cooled surface waters. Thus, a shorter well-mixed period results in less winter-time cooling in the hypolimnion and a higher annual minimum bottom temperature. The difference between the downscaled simulation and those based on simple linear offsets also reflects the seasonal variability in the change of atmospheric forcings. For example, seasonal projections of lower summer winds and higher winter winds (**Figure 4.5**) suggest that changes in wind intensity will act to both enhance stability during the stratified season and continue to support cooling and convective mixing during winter.

4.4.3 Comparison to Forecasted Warming of Deep Lakes

Temperate NH lakes are warming more than twice as fast as Lago Llanquihue is predicted to warm under a worst-case emissions scenario (**Table 4.5**). Bayer (2013) similarly forecasted that two deep New Zealand lakes will warmer slower than comparative systems in the NH. The study attributed this variation to lower atmospheric warming rates at temperate latitudes in the SH than in the NH, as well as the cooling effect of increased inflows. Local air temperatures are forecasted to increase by +1.4 – 2 °C in New Zealand and northern Patagonia by 2090 compared to +1.5 – 5.7 °C predicted for lakes in Europe and North America. Since 1980, the NH, on average, has warmed at a faster rate than the SH (Morice et al., 2012) and models forecast approximately 1 °C difference in temperature by 2099 (Friedman et al., 2013). The cause of this interhemispherical asymmetrical warming has been primarily attributed to the greater coverage of ocean in the SH, resulting in a higher effective heat capacity in the SH relative to the NH (Bryan et al., 1988). Disproportionate melting of arctic sea ice also drives a positive ice-albedo feedback further amplifying the warming in the NH (Friedman et al., 2013). Ocean currents, that transport warmer waters from the SH across the equator (e.g. the Gulf Stream), may also contribute to temperature differences between the hemispheres (Feulner et al., 2013). While the interhemispheric temperature asymmetry is considered an emerging feature of global climate change (Friedman et al., 2013), interhemispheric variation in lake warming rates has received comparatively little attention. The majority of long-term limnological monitoring programs have been conducted in European and North American lakes where many of the most extreme changes in lake thermal structure and mixing regime have been observed (Jane et al., 2021). Due the absence of high-resolution observational data for many SH lakes, the magnitude of their change has not been well defined. In lieu of long-term lake monitoring, predictive modeling studies, like this, are essential for determine the future and current trajectory of these understudied systems. The study indicates that the impacts of climate change on deep temperate SH lakes during the 21st is likely significantly less severe than in analogous NH systems.

Table 4.5. *Comparison of modeled and observed response of deep lakes to climate change.*

Lake	Model / Observed	Hemi-sphere	Years of simulation / observation	Predicted / Observed ΔT_{air} [°C]	ΔT_{epi} [°C decade^{-1}]	ΔT_{hypo} [°C decade^{-1}]	Δ dt Stratification	Model	Paper
Wanaka	M	S	2090 (+2 °C/ + 5% wind)	2	0.1	0.03	+5 days	DYRESM	Bayer 2013
Wakataipu	M	S	2090 (+2 °C/ + 5% wind)	2	0.1	0.02	+5 days	DYRESM	Bayer 2013
Llanquihue	M	S	2021 - 2091 (+1.4 °C)	1.4	0.09	0.04	+13 days	Si3D	This study
Llanquihue	M	S	2021 - 2091 (RCP 8.5)	1.4	0.11	0.06	+25 days	Si3D	This study
Crater	M	N	2006 - 2099 (RCP 8.5)	5.2 - 5.72	0.31	0.01 - 0.02	--	DYRESM	Wood et al 2016
Geneva	M	N	2071 - 2100	4.13	0.41	0.23	> 3 weeks	SIMSTRAT	Perroud & Goyette 2010
Geneva	O	N	1970 - 2003	0.4 - 0.7	0.4	0.27	Becoming meromictic	SIMSTRAT	Perroud & Goyette 2010
Zurich	O	N	1947 - 1993	0.4-0.7	0.24	0.13	+2-3 weeks	N/A	Livingstone 2003
Tahoe	O	N	1970 - 2002	0.15	0.23	0.2	No earlier	N/A	Coats 2005
Tahoe	M	N	2000 - 2041	4-5.5	0.21	0.11	--	LCM	Sahoo 2011
Shinagawa	M	N	2081 - 2100	3.3	0.34	0.28	+36 days	Lake Specific	Komatsu et al 2007
Mondsee	M	N	2071 – 2100	4.1	0.76 (Summer)	0.10 (Summer)	+63 days	PROBE	Jones et al 2010
Constance	M	N	1961 - 2011 (+2 °C)	+2	0.34	0.2	--	Deflt3D	Wahl & Peeters 2014
US Great Lakes	O	N	1979 - 2006	1.6	0.1-1.1	N/A	13.5 days	N/A	Austin & Colman 2007
Stechlinsee	M	N	2006 - 2100	1.5	0.14	0.1	+17 days	FLake	Shatwell 2019
Qiandao	O	N	1951 - 2012	1.2	0.13	--	--	N/A	Zhang 2014
Maggiore	O	N	2006 - 2085	1.44	0.66	0.1-0.12	Becoming meromictic	GLM	Fenochi 2018

4.4.4 Potential Implications for Lake Ecosystem and Water Quality

Forecasted changes in thermal stratification, temperature, and mixing regime can influence many aspects of lake ecosystems. An earlier onset of stratification can promote earlier spring phytoplankton blooms (e.g., Lake Washington, Shimoda et al., 2011). Under the RCP 8.5 scenario, the onset of stratification is forecasted to occur a week earlier by the end of the century and is not likely to significantly alter the timing of the spring phytoplankton bloom. Warming surface temperatures increase metabolic rates of primary producers, promoting greater biomass accumulation if nutrient availability is sufficient (Winder and Sommer 2012). Though Llanquihue is currently oligotrophic, increasing trends in summertime nitrogen and phosphorus concentrations were observed from 2012 – 2019 (Instituto De Fomento Pesquero, 2020), suggesting that further watershed development would increase nutrient loads to the lake and support greater phytoplankton growth. Warmer surface waters can also increase the risk of harmful cyanobacteria blooms, which have higher growth rates than other phytoplankton groups when water temperatures exceed 20 °C (Paerl and Otten 2013). While surface temperatures do not presently reach this threshold, simulations predict that surface waters will exceed 20 °C, between 7 (constant k_d) and 28 days each summer (k_d +1% yr^{-1}), increasing the risk of cyanobacteria blooms. Furthermore, changes in water temperature may affect the spatial-temporal distribution of fish species (Pandit et al., 2017)

Increased thermal stability and stratification duration can intensify hypolimnetic oxygen depletion and promote internal phosphorus loading, increased methane emissions and impact fish hatchery operations (Foley et al., 2012; Grasset et al., 2018; Laval and Lawrence 2004; North et al., 2014). While Llanquihue's stratified season is projected to extend 3 weeks longer by the end of the century, under the lake's current hypolimnetic oxygen depletion rate (0.08 mgL^{-1} $mnth^{-1}$), the lake would need to remain consistently stratified for ~5 years for DO decline to hypoxic (<3.5 mgL^{-1}) levels. Given that the lake is forecasted to remain monomictic this century, increased risk of hypolimnetic anoxia in not likely to occur under the lake's current trophic status. Due to similar regional climate and hydrodynamic characteristics, the results of this study qualitatively pertain to other NP lakes and, to a lesser extent, to other deep temperate SH lakes.

4.5 Conclusions

Coupled regional climate and hydrodynamic models can serve as prognostic tools to investigate the limnological impacts of climate change. While there are inherent uncertainties in forecasts estimates, calibration and validation of lake models and bias correction of meteorological forecasts can minimize errors. A comparison of 3D and 1D model simulations for a deep, Southern Hemisphere lake demonstrated the advantages in simulating deep lake hydrodynamics with 3D simulations. While many studies focus on air temperature as the primary driver of changes we demonstrated that shifts in water clarity can also drive changes in lake thermal regime. This points to the importance of controlling watershed land use practices in order to help counter the impacts of climate change.

Increased air temperature and longwave radiation will warm the surface waters faster than the hypolimnion promoting a longer stratified season, stronger thermal stratification, and shorter well winter mixing period. However warming rates in Lago Llanquihue are predicted to be much slower than in analogous large, deep NH lakes, largely due to lower predicted rates of atmospheric warming in the SH. As a result, Llanquihue, and the lakes of northern Patagonia generally, are likely to remain monomictic during this century and will continue to be resilient to climate change during the 21st century, provided clarity levels are maintained. These results highlight that in the absence of climate-induced degradation, sustainable land use management policies can effectively protect these pristine systems for future generations.

References

Abarca, J., Ulloa, H. N., & Niño, Y. (2023). Basin-scale hydrodynamics and physical connectivity in a great Patagonian Lake. *J. Great Lakes Res.* , *49*(1), 172–189.

Adrian, R., O'Reilly, C. M., Zagarese, H., Baines, S. B., Hessen, D. O., Keller, W., Livingstone, D. M., Sommaruga, R., Straile, D., Van Donk, E., Weyhenmeyer, G. A., & Winder, M. (2009). Lakes as sentinels of climate change. *Limnol. Oceanogr.*, *54*(6), 2283–2297.

Amadori, M., Giovannini, L., Toffolon, M., Piccolroaz, S., Zardi, D., Bresciani, M., Giardino, C., Luciani, G., Kliphuis, M., van Haren, H., & Dijkstra, H. A. (2021). Multi-scale evaluation of a 3D lake model forced by an atmospheric model against standard monitoring data. *Environ. Model. Soft.*, *139*(105017).

Anderson, E. J., Stow, C. A., Gronewold, A. D., Mason, L. A., McCormick, M. J., Qian, S. S., Ruberg, S. A., Beadle, K., Constant, S. A., & Hawley, N. (2021). Seasonal overturn and stratification changes drive deep-water warming in one of Earth's largest lakes. *Nature Communications*, *12*(1).

Aranda, A. C., Rivera-Ruiz, D., Rodríguez-López, L., Pedreros, P., Arumí-Ribera, J. L., Morales-Salinas, L., Fuentes-Jaque, G., & Urrutia, R. (2021). Evidence of climate change based on lake surface temperature trends in south central Chile. *Remote Sens.*, *13*(22).

Austin, J. A., & Colman, S. M. (2007). Lake Superior summer water temperatures are increasing more rapidly than regional temperatures: A positive ice-albedo feedback. *Geophys. Res. Lett.*, *34*(6).

Ayala, A. I., Jones, I. D., Goyette, S., Pierson, D. C., Mesman, J. P., De Eyto, E., & Jennings, E. (2023). Climate change impacts on surface heat fluxes in a deep monomictic lake. *JGR: Atmospheres*, *128*(11).

Bayer, T. K., Burns, C. W., & Schallenberg, M. (2013). Application of a numerical model to predict impacts of climate change on water temperatures in two deep, oligotrophic lakes in New Zealand. *Hydrobiologia*, *713*(1), 53–71.

Biemond, B., Amadori, M., Toffolon, M., Piccolroaz, S., Van Haren, H., & Dijkstra, H. A. (2021). Deep-mixing and deep-cooling events in Lake Garda: Simulation and mechanisms. *J. Limnol.*, *80*(2).

Bozkurt, D., Rojas, M., Boisier, J. P., Rondanelli, R., Garreaud, R., & Gallardo, L. (2019). Dynamical downscaling over the complex terrain of southwest South America: Present climate conditions and added value analysis. *Clim. Dyn.*, *53*(11), 6745–6767.

Bryan, K., Manabe, S., & Spelman MJ. (1988). Interhemispheric asymmetry in the transient response of a coupled ocean–atmosphere model to a CO2 forcing. *J. Phys. Oceanogr.*, *18*(6), 851–867.

Bueche, T., Wenk, M., Poschlod, B., Giadrossich, F., Pirastru, M., & Vetter, M. (2020). GlmGUI v1.0: An R-based graphical user interface and toolbox for GLM (General Lake Model) simulations. *Geosci. Model Dev.*, *13*(2), 565–580.

Butcher, J. B., Nover, D., Johnson, T. E., & Clark, C. M. (2015). Sensitivity of lake thermal and mixing dynamics to climate change. *Climatic Change*, *129*(1–2), 295–305.

Campos, H., Steffen, W., Aguero, G., Parra, O., & Zuniga, L. (1988). Limnological study of Lake Llanquihue (Chile): morphometry, physics, chemistry, plankton and primary productivity. *Archi. Hydrobiol., Supplementband 81*, *1*, 37–68.

Darko, D., Trolle, D., Asmah, R., Bolding, K., Adjei, K. A., & Odai, S. N. (2019). Modeling the impacts of climate change on the thermal and oxygen dynamics of Lake Volta. *Journal of Great Lakes Research*, *45*(1), 73–86.

De Los Ríos-Escalante, P., & Soto, D. (2007). Eutrophication and dominance of daphnids (Crustacea) in a deep Patagonlan lake (Lake Llanquihue, Chile). *Polish Journal of Ecology*, *55*(1), 191–193. https://www.researchgate.net/publication/289603041

De Senerpont Domis, L. N., Elser, J. J., Gsell, A. S., Huszar, V. L. M., Ibelings, B. W., Jeppesen, E., Kosten, S., Mooij, W. M., Roland, F., Sommer, U., Van Donk, E., Winder, M., & Lürling, M. (2013). Plankton dynamics under different climatic conditions in space and time. *Freshw. Biol.*, *58*(3), 463–482.

Diaz-Nieto, J., & Wilby, R. L. (2016). A comparison of statistical downscaling and climate change factor methods: Impacts on low flows in the River Thames, United Kingdom. *Clim. Change*, *69*, 245–268.

Donoso, G. (Ed.). (2018). *Water Policy in Chile (Global Issues in Water Policy)* (Vol. 21). Springer.

Dupré, A., Drobinski, P., Alonzo, B., Badosa, J., Briard, C., & Plougonven, R. (2020). Sub-hourly forecasting of wind speed and wind energy. *Renewable Energy*, *145*, 2373–2379.

Engelhardt, C., & Kirillin, G. (2014). Criteria for the onset and breakup of summer lake stratification based on routine temperature measurements. *Fundamental and Applied Limnology*, *184*(3), 183–194.

Enriquez-Alonso, A., Calbó, J., Sanchez-Lorenzo, A., & Tan, E. (2017). Discrepancies in the climatology and trends of cloud cover in global and regional climate models for the Mediterranean region. *JGR: Atmospheres*, *122*, 11664–11677.

Fenocchi, A., Rogora, M., Morabito, G., Marchetto, A., Sibilla, S., & Dresti, C. (2019). Applicability of a one-dimensional coupled ecological-hydrodynamic numerical model to future projections in a very deep large lake (Lake Maggiore, Northern Italy/Southern Switzerland). *Ecol. Model.*, *392*, 38–51.

Fenocchi, A., Rogora, M., Sibilla, S., Ciampittiello, M., & Dresti, C. (2018). Forecasting the evolution in the mixing regime of a deep subalpine lake under climate change scenarios through numerical modelling (Lake Maggiore, Northern Italy/Southern Switzerland). *Clim. Dyn.*, *51*(9–10), 3521–3536.

Feulner, G., Rahmstorf, S., Levermann, A., & Volkwardt, S. (2013). On the origin of the surface air temperature difference between the hemispheres in earth's present-day climate. *J. Clim.*, *26*(18), 7136–7150.

Fink, G., Schmid, M., Wahl, B., Wolf, T., & Wüest, A. (2014). Heat flux modifications related to climate-induced warming of large European lakes. *Water Resour. Res.*, *50*(3), 2072–2085.

Foley, B., Jones, I. D., Maberly, S. C., & Rippey, B. (2012). Long-term changes in oxygen depletion in a small temperate lake: Effects of climate change and eutrophication. *Freshw. Biol.*, *57*(2), 278–289.

Friedman, A. R., Hwang, Y. T., Chiang, J. C. H., & Frierson, D. M. W. (2013). Interhemispheric temperature asymmetry over the twentieth century and in future projections. *J. Clim.*, *26*(15), 5419–5433.

Garret, C. (2003). Mixing with latitude. *Nat.*, *422*, 477–478.

Gill, A. E. (1982). *Atmosphere-Ocean Dynamics*. Academic Press.

Goudsmit, G. H., Peeters, F., Gloor, M., & Wuest, A. (1997). Boundary versus internal diapycnal mixing in stratified natural waters. *J. Geophys. Res.*, *102*(C13), 27903–27914.

Grasset, C., Mendonça, R., Saucedo, G. V., Bastviken, D., Roland, F., & Sobek, S. (2018). Large but variable methane production in anoxic freshwater sediment upon addition of allochthonous and autochthonous organic matter. *Limnol. Oceanogr.*, *63*, 1488–1501.

Gregg, M. C. (1987). Diapycna Mlixing in the Thermocline: A Review. *Journal of Geophysical Research: Oceans*, *92*(C5), 5249–5286.

Hampton, S. E., Izmest'eva, L. R., Moore, M. V., Katz, S. L., Dennis, B., & Silow, E. A. (2008). Sixty years of environmental change in the world's largest freshwater lake - Lake Baikal, Siberia. *Glob. Change Biol.* , *14*(8), 1947–1958.

Herdendorf, C. E. (1990). Distribution of the World's Large Lakes. In C. Tilzer Max M. and Serruya (Ed.), *Large Lakes: Ecological Structure and Function* (pp. 3–38). Springer Berlin Heidelberg.

Hetherington, A. L., Schneider, R. L., Rudstam, L. G., Gal, G., DeGaetano, A. T., & Walter, M. T. (2015). Modeling climate change impacts on the thermal dynamics of polymictic Oneida Lake, New York, United States. *Ecol. Model.*, *300*, 1–11.

Hipsey, M. R., Bruce, L. C., Boon, C., Busch, B., Carey, C. C., Hamilton, D. P., Hanson, P. C., Read, J. S., De Sousa, E., Weber, M., & Winslow, L. A. (2019). A General Lake Model (GLM 3.0) for linking with high-frequency sensor data from the Global Lake Ecological Observatory Network (GLEON). *Geosci. Model Dev.*, *12*(1), 473–523.

Hodges, B. R., Imberger, J., Laval, B., & Appt, J. (2000). Modeling the hydrodynamics of stratified lakes. *Hydroinformatics 2000 Conference*, *July*, 23–27.

Hoyer, A. B., Schladow, S. G., & Rueda, F. J. (2015). Local dispersion of nonmotile invasive bivalve species by wind-driven lake currents. *Limnol. Oceanogr.*, *60*(2), 446–462.

Hsu, S. A. (1981). Models for estimating offshore winds from onshore meteorological measurements. *Boundary-Layer Meteorol.*, *20*, 341–351.

Imberger, J. (1998). Flux paths in a stratified lake: A review. In *Physical Processes in Lakes and Oceans* (Vol. 54, pp. 1–18).

Imberger, J., & Patterson J. (1989). Physical Limnology. In *Advances in Applied Mechanics* (Vol. 27, pp. 303–475). Elsevier.

Instituto De Fomento Pesquero. (2020). *Collection and Analysis of Background Information for the Review of the Secondary Standard of Water Quality of Lago Llanquihue.*

Jane, S. F., Hansen, G. J. A., Kraemer, B. M., Leavitt, P. R., Mincer, J. L., North, R. L., Pilla, R. M., Stetler, J. T., Williamson, C. E., Woolway, R. I., Arvola, L., Chandra, S., DeGasperi, C. L., Diemer, L., Dunalska, J., Erina, O., Flaim, G., Grossart, H. P., Hambright, K. D., ... Rose, K. C. (2021). Widespread deoxygenation of temperate lakes. *Nat.*, *594*(7861), 66–70.

Koutsoyiannis, D., Efstratiadis, A., Mamassis, N., & Christofides, A. (2008). On the credibility of climate predictions. *Hydrol. Sci. J.*, *53*(4), 671–684.

Laborde, S., Antenucci, J. P., Copetti, D., & Imberger, J. (2010). Inflow intrusions at multiple scales in a large temperate lake. *Limnol. Oceanogr.*, *55*(3), 1301–1312.

Ladwig, R., Furusato, E., Kirillin, G., Hinkelmann, R., & Hupfer, M. (2018). Climate change demands adaptive management of urban lakes: model-based assessment of management scenarios for Lake Tegel (Berlin, Germany). *Water*, *10*(188), 1–23.

Latifovic, R., & Pouliot, D. (2007). Analysis of climate change impacts on lake ice phenology in Canada using the historical satellite data record. *Remote Sens. Environ.*, *106*(4), 492–507.

Laval, B. E., Lawrence, G., Pawlowicz, R., & Pieters, R. (2004). Physical mechanisms leading to upwelling of anoxic bottom water in Nitinat Lake. *17th ASCE Engineering Mechanics Conference.* https://www.researchgate.net/publication/229000700

Lemmin, U. (2020). Insights into the dynamics of the deep hypolimnion of Lake Geneva as revealed by long-term temperature, oxygen, and current measurements. *Limnol. Oceanogr.*, *65*(9), 2092–2107.

Livingstone, D. M. (2003). Impact of secular climate change on the thermal structure of a large temperate central European lake. *Clim. Change*, *57*, 205–225.

Lottig, N. R., Wagner, T., Henry, E. N., Cheruvelil, K. S., Webster, K. E., Downing, J. A., & Stow, C. A. (2014). Long-term citizen-collected data reveal geographical patterns and temporal trends in lake water clarity. *PLoS ONE*, *9*(4).

Man, X., Lei, C., Carey, C. C., & Little, J. C. (2021). Relative performance of 1-D versus 3-D hydrodynamic, water-quality models for predicting water temperature and oxygen in a shallow, eutrophic, managed reservoir. *Water (Switzerland)*, *13*(1).

Martin, J., & McCutcheon, S. (1999). *Hydrodynamics and Transport for Water Quality Modeling* (1st ed.). Taylor and Francis.

Mesa, J. A. (2018). *Modelacion Hidrodinamica del Lago Llanquihue.* Santiago De Chile.

Morice, C. P., Kennedy, J. J., Rayner, N. A., Jones, P. D., Morice, C. :, Kennedy, J. J., Rayner, N. A., & Jones, P. D. (2012). Quantifying uncertainties in global and regional temperature change using an ensemble of observational estimates: The HadCRUT4 data set. *JGR: Atmospheres*, *117*(D8), 8101.

Morillo, S., Imberger, J., Antenucci, J. P., & Woods, P. F. (2008). Influence of wind and lake morphometry on the interaction between two rivers entering a stratified lake. *J. Hydraul. Eng.*, *134*(11), 1579–1589.

Murphy, A., & Epstein, E. (1989). Skill scores and correlation coefficient in model verification. *Monthly Weather Review*, *117*, 572–581.

North, R. P., North, R. L., Livingstone, D. M., Köster, O., & Kipfer, R. (2014). Long-term changes in hypoxia and soluble reactive phosphorus in the hypolimnion of a large temperate lake: Consequences of a climate regime shift. *Glob. Change Biol.* , *20*(3), 811–823.

O'Reilly, C. M., Rowley, R. J., Schneider, P., Lenters, J. D., Mcintyre, P. B., & Kraemer, B. M. (2015). Rapid and highly variable warming of lake surface waters around the globe. *Geophys. Res. Lett.*, *42*, 10773–10781.

Paerl, H. W., & Huisman, J. (2009). Climate change: A catalyst for global expansion of harmful cyanobacterial blooms. *Environ. Microbiol. Rep.*, *1*(1), 27–37.

Paerl, H. W., & Otten, T. G. (2013). Harmful Cyanobacterial Blooms: Causes, Consequences, and Controls. *Microbial Ecology*, *65*(4), 995–1010.

Perroud, M., & Goyette, S. (2010). Impact of warmer climate on Lake Geneva water temperature profiles. *Boreal Environ. Res.*, *15*(2), 255–278. https://www.researchgate.net/publication/267793741

Piccolroaz, S., Woolway, R. I., & Merchant, C. J. (2020). Global reconstruction of twentieth century lake surface water temperature reveals different warming trends depending on the climatic zone. *Clim. Change*, *160*, 427–442.

Pilla, R. M., Williamson, C. E., Adamovich, B. V., Adrian, R., Anneville, O., Chandra, S., Colom-Montero, W., Devlin, S. P., Dix, M. A., Dokulil, M. T., Gaiser, E. E., Girdner, S. F., Hambright, K. D., Hamilton, D. P., Havens, K., Hessen, D. O., Higgins, S. N., Huttula, T. H., Huuskonen, H., ... Zadereev, E. (2020). Deeper waters are changing less consistently than surface waters in a global analysis of 102 lakes. *Sci. Rep.*, *10*(20514).

Pizarro, J., Vergara, P. M., Cerda, S., & Briones, D. (2016). Cooling and eutrophication of southern Chilean lakes. *Sci. Total Environ.*, *541*, 683–691.

Read, J. S., Hamilton, D. P., Jones, I. D., Muraoka, K., Winslow, L. A., Kroiss, R., Wu, C. H., & Gaiser, E. (2011). Derivation of lake mixing and stratification indices from high-resolution lake buoy data. *Environ. Model. Soft.*, *26*(11), 1325–1336.

Reiss, R. S., Lemmin, U., Cimatoribus, A. A., & Barry, D. A. (2020). Wintertime coastal upwelling in Lake Geneva: An efficient transport process for deepwater renewal in a large, deep lake. *JGR: Oceans*, *125*(8), 1–18.

Riahi, K., Rao, S., Krey, V., Cho, C., Chirkov, V., Fischer, G., Kindermann, G., Nakicenovic, N., & Rafaj, P. (2011). RCP 8.5-A scenario of comparatively high greenhouse gas emissions. *Clim. Change*, *109*(1), 33–57.

Rigosi, A., Carey, C. C., Ibelings, B. W., & Brookes, J. D. (2014). The interaction between climate warming and eutrophication to promote cyanobacteria is dependent on trophic state and varies among taxa. *Limnol. Oceanogr.*, *59*(1), 99–114.

Rose, K. C., Winslow, L. A., Read, J. S., & Hansen, G. J. A. (2016). Climate-induced warming of lakes can be either amplified or suppressed by trends in water clarity. *Limnol. Oceanogr. Lett.*, *1*, 44–53.

Rueda, F. J., & MacIntyre, S. (2010). Modelling the fate and transport of negatively buoyant storm-river water in small multi-basin lakes. *Environ. Model. Soft.*, *25*(1), 146–157.

Rueda, F. J., & Schladow, S. G. (2003). Dynamics of large polymictic lake. II: numerical simulations. *J. Hydraul. Eng.*, *129*(2), 92–101.

Rueda, F. J., Schladow, S. G., & Pálmarsson, S. Ó. (2003a). Basin-scale internal wave dynamics during a winter cooling period in a large lake. *JGR: Oceans*, *108*(3), 1–16.

Rueda, F. J., Schladow, S. G., & Pálmarsson, S. Ó. (2003b). Basin-scale internal wave dynamics during a winter cooling period in a large lake. *Journal of Geophysical Research: Oceans*, *108*(3), 1–16.

Rueda, F., Vidal, J., & Schladow, G. (2009). Modeling the effect of size reduction on the stratification of a large wind-driven lake using an uncertainty-based approach. *Water Resour. Res.*, *45*(3).

Sahoo, G. B., Schladow, S. G., Reuter, J. E., Coats, R., Dettinger, M., Riverson, J., Wolfe, B., & Costa-Cabral, M. (2013). The response of Lake Tahoe to climate change. *Clim. Change*, *116*(1), 71–95.

Schanz, F. (1994). Oligotrophication of Lake Zurich as reflected in Secchi depth measurements. *Annls. Limnol.*, *30*(1), 57–65.

Scheu, K. R., Fong, D., Monismith, S. G., & Fringer, O. B. (2018). Modeling sedimentation dynamics of sediment-laden river intrusions in a rotationally-influenced, stratified lake. *Water Resour. Res.*, *54*(6), 4084–4107.

Schneider, P., & Hook, S. J. (2010). Space observations of inland water bodies show rapid surface warming since 1985. *Geophys. Res. Lett.*, *37*(22).

Schwefel, R., Gaudard, A., Wüest, A., & Bouffard, D. (2016). Effects of climate change on deepwater oxygen and winter mixing in a deep lake (Lake Geneva): Comparing observational findings and modeling. *Water Resour. Res.*, *52*(11), 8811–8826.

Servicio Hidrografico Oceanografico de la Armada de Chile. (2003). *Hydrographic Survey of Lago Llanquihue*.

Shimoda, Y., Azim, M. E., Perhar, G., Ramin, M., Kenney, M. A., Sadraddini, S., Gudimov, A., & Arhonditsis, G. B. (2011). Our current understanding of lake ecosystem response to climate change: What have we really learned from the north temperate deep lakes? In *Journal of Great Lakes Research* (Vol. 37, Issue 1, pp. 173–193).

Smith, P. (2006). A semi-implicit, three-dimensional model for estuarine circulation. *USGS Report*, 176.

Song, Y., Semazzi, F. H. M., Xie, L., & Ogallo, L. J. (2004). A coupled regional climate model for the Lake Victoria Basin of East Africa. *Int. J. Clim.*, *24*(1), 57–75.

Soto, D., & Campos, H. (1995). *Los lagos oligrotorficos asociados al bosque templado del sur de Chile*.

Straile, D., Jöhnk, K., & Rossknecht, H. (2003). Complex effects of winter warming on the physicochemical characteristics of a deep lake. *Limnol. Oceanogr.*, *48*(4), 1432–1438.

Tennessee Valley Authority (1972). Heat and mass transfer between a water surface and the atmosphere. *0-6803*.

Universidad San Sebastian. (2022). *Estudio Hidrodinámico Para La Calidad Del Agua En La Bahía Puerto Varas*.

Valbuena, S. A., Bombardelli, F. A., Cortés, A., Largier, J. L., Roberts, D. C., Forrest, A. L., & Schladow, S. G. (2022). 3D flow structures during upwelling events in lakes of moderate size. *Water Resour. Res.*, *58*(3).

Wahl, B., & Peeters, F. (2014). Effect of climatic changes on stratification and deep-water renewal in Lake Constance assessed by sensitivity studies with a 3D hydrodynamic model. *Limnol. Oceanogr.*, *59*(3), 1035–1052.

Weinstock, J. (1981). Vertical turbulence diffusivity for weak or strong stable stratification. *J. Geophys. Res.*, *86*(C10), 9925.

Wilhelm, S., & Adrian, R. (2008). Impact of summer warming on the thermal characteristics of a polymictic lake and consequences for oxygen, nutrients and phytoplankton. *Freshw. Biol.*, *53*(2), 226–237.

Winder, M., & Sommer, U. (2012). Phytoplankton response to a changing climate. *Hydrobiologia*, *698*(1), 5–16.

Wood, T., Wherry SA, Piccolroaz S, & Girdner SF. (2016). Simulation of deep ventilation in Crater Lake, Oregon, 1951–2099: U.S. Geological Survey Scientific Investigations Report 2016–5046. In *Climatic Change* (Vol. 69).

Woolway, R. I., Jones, I. D., Hamilton, D. P., Maberly, S. C., Muraoka, K., Read, J. S., Smyth, R. L., & Winslow, L. A. (2015). Automated calculation of surface energy fluxes with high-frequency lake buoy data. *Environ. Model. Soft.*, *70*, 191–198.

Woolway, R. I., Kraemer, B. M., Lenters, J. D., Merchant, C. J., O'Reilly, C. M., & Sharma, S. (2020). Global lake responses to climate change. *Nat Rev Earth Environ*, *1*, 388–403.

Woolway, R. I., & Merchant, C. J. (2019). Worldwide alteration of lake mixing regimes in response to climate change. *Nat. Geosci.*, *12*(4), 271–276.

Yamashiki, Y., Kato, M., Takara, K., Nakakita, E., Kumagai, M., & Jiao, C. (2010). Sensitivity Analysis on Lake Biwa under the A1B SRES climate change scenario using Biwa-3D Integrated Assessment Model: *Hydrol. Res. Lett.*, *4*, 45–49.

Yankova, Y., Neuenschwander, S., Köster, O., & Posch, T. (2017). Abrupt stop of deep water turnover with lake warming: Drastic consequences for algal primary producers. *Sci. Rep.*, *7*.

Zamani, B., Koch, M., & Hodges, B. R. (2021). A potential tipping point in the thermal regime of a warm monomictic reservoir under climate change using three-dimensional hydrodynamic modeling. *Inland Waters*, *11*(3), 315–334.

5 SUMMARY & CONCLUSIONS

This dissertation has focused on analyzing the factors that influence vertical mixing in lakes both presently and under future climate scenarios. In addition, the effects of stratification and mixing on dissolved oxygen dynamics and internal nutrient loading were investigated. The overarching aim of this work was to apply novel observational and modelling methods to deepen our understanding of the drivers and impacts of vertical mixing processes across temperate lakes of varying depth. To this end, three manuscripts were presented investigating lakes that encompass a spectrum of aquatic environments from a shallow, hypereutrophic system that overturns multiple times each year to a deep, oligotrophic system that overturns sporadically every few winters. While these lakes contrast starkly in their geographic setting, morphometry, and watershed development history, each study highlights the central role that vertical mixing plays in regulating lake ecological health. Across all three systems, results demonstrate that simple one-dimensional modelling approaches that neglect horizontal variations in bathymetry and temperature may fail to accurately resolve important transport and mixing processes that will be increasingly important to deep water renewal as climate change alters the frequency of turnover events. This dissertation underscores the necessity for high-frequency observations and three-dimensional models to capture the complex dynamics of lake systems, in turn enhancing our capacity to manage and protect these vital freshwater resources for future generations.

Chapter 2 Concluding Remarks

While the impacts of stratification on hypolimnetic dissolved oxygen concentrations have been investigated extensively over recent decades, determining the timing and extent of hypolimnetic hypoxia in eutrophic, polymictic lakes remains challenging due to the rapidity of hypolimnetic DO depletion during stratification and the frequent occurrence of mixing events. In such systems, redox-dependent release of sedimentary P can delay lake restoration efforts and promote excessive phytoplankton growth. Nevertheless, internal P loads in polymictic systems are frequently ignored or calculated only at seasonal scales due to challenges in accurately capturing dynamic variations in thermal structure and hypolimnetic DO. Chapter 2 detailed a comprehensive observational study conducted between 2019 and 2021 at Clear Lake—the largest natural freshwater body completely situated within California, which yielded the first detailed insights into both the timing and interannual variations of hypolimnetic hypoxia in this system. Given its complex, multi-basin geometry and dynamic thermal structure, accurate estimate of internal nutrient loads, critical to understanding interannual cyanobacteria variability, demanded thorough data collection and analytical efforts. Throughout the study period, summertime increases in hypolimnion P, provided clear evidence of wide-spread internal loading in the system. Annual estimates of internal P loading for each of the lake's arms were calculated via two methods: a water column mass balance and experimental sediment P release rates. Comparisons between external and internal P contributions revealed that internal sources dominated nutrient cycling in Clear Lake, accounting for an extraordinary 70-95% of annual total P input—an unparalleled figure within the existing limnological literature. Mixing events were found to promote cyanobacteria growth by transporting nutrient-enriched waters into the epilimnion and shifting nutrient limitation from P to N in favor of N-fixing cyanobacteria in the early summer. Subsequent blooms of non-N-fixing cyanobacteria were observed in the early fall due to the increasing availability of N in the water column. These observations underscore the central role that stratification and mixing dynamics play in regulating nutrient cycling and, consequently, cyanobacterial blooms in shallow, polymictic systems.

A significant contribution of this study is the development of a framework for evaluating the benefits and drawbacks of various internal loading estimation methods. A water column mass balance approach is typically the most widespread method employed, as estimates are directly derived from observations and water samples can be collected with relative ease. However, the accuracy of these estimates is limited by sample frequency, and infrequent sampling events may fail to capture peak nutrient concentrations resulting in underestimations. Moreover, this method provides an aggregate measure that cannot distinguish between various internal and external nutrient sources. Alternatively, estimates based on hypolimnetic DO observations and sedimentary P release experiments allow for a direct quantification of the timing and magnitude of redox-sensitive P releases, albeit being more labor-intensive and potentially not capturing the spatial and temporal variability of sedimentary P pools through individual core experiments. While the mass balance approach is generally suitable for long-term monitoring and tracking lake restoration progress, an in-depth understanding of the impacts of lake hydrodynamics on biogeochemical cycling and ecosystem dynamics necessitates insights provided by *in situ* temperature and DO measurements.

In addition, this study underscores the need for comprehensive nutrient accounting within lake systems as part of broader basin-scale nutrient budget While internal loading mechanisms are well-documented in scientific literature, policymakers and environmental regulations have historically focused on limiting watershed-based nutrient inputs to mitigate lake eutrophication. This study emphasizes the importance of recognizing contribution of internal nutrient loads alongside external ones. In particular the findings highlight intermittent stratification and mixing events can regulate nutrient cycling at temporal scales relevant for phytoplankton growth cycles. Thus, it is imperative that future nutrient reduction strategies embrace a more holistic approach, integrating watershed and in-lake measures, to effectively foster environmental and socio-economic benefits of impaired waterbodies in both the immediate and long-term. Furthermore, by demonstrating that Clear Lake was N-limited each summer, this study highlights the importance in managing both P and N for effective mitigation of eutrophication in freshwater lakes.

Chapter 3 Concluding Remarks

Climate change has altered the mixing regimes of lakes globally with many oligotrophic lakes predicted to become permanently thermally stratified by the end of this century. Despite such global trends, half a century of monitoring data suggests that the frequency of turnover in oligomictic, Lake Tahoe has remained remarkably consistent throughout recent decades. Deep mixing events, albeit infrequent, play a central role in maintaining the productivity and ecological health of deep lakes. However, their episodic nature and unpredictability make direct observation a challenge. Motivated by the need to better understand the drivers and dynamics of these important deep mixing events, Chapter 3 investigated the evolution of Lake Tahoe's thermal structure across multiple turnover winters.

Analysis of multi-decadal winter meteorological data, coupled with recordings of the lake's thermal structure, revealed a key insight: it is the timing of winter storms, rather than broad climatic oscillations, that predominantly dictate the depth of winter mixing. Specifically, the study found that turnover events were catalyzed by cold fronts serendipitously passing over the lake in February, when the lake was most weakly stratified. While surface mixed layer deepening can, to an extent, be conceptualized as a one-dimensional vertical process, complex three-dimensional transport phenomena can contribute to deep water renewal. A volumetric scaling analysis indicated that density currents generated by differentially cooled littoral waters, not plunging stream inflows, likely transported cold water to the lake bottom. The absence of a long-term decline in turnover frequency, as well as the identification of these three-dimensional renewal processes, suggest that Lake Tahoe is less susceptible to climatic eutrophication during the 21st century than previously predicted. This research underscores the limitation of relying on one-dimensional lake models forced by downscaled climate projections for forecasting the long-term evolution of lake mixing regime.

Though turnover events in deep lakes have been previously documented with periodic profiling measurements, this is the first study to provide continuous *in situ* temperature and oxygen measurements throughout multiple deep mixing events in an oligomictic system, providing valuable new insights into the evolution of winter thermal structure of deep lakes. In each of the four winters following turnover, the bottom of the lake continued to cool while the overlying water column restratified, suggesting that deep water renewal is not solely attributed to vertical buoyancy-driven mixing processes. Observations of cooler surface waters in the shallow, littoral zone relative to the lake interior throughout the winter indicated the potential for differential cooling to induce plunging density currents. While climate change will likely continue to increase lake stability and reduce the intensity of winter vertical mixing, this study highlights that deep water renewal does not necessarily require isothermic conditions in the water column.

Furthermore, this study underscores that a singular, unpredictable event such as a timely storm during a near-isothermic period can significantly impact the interannual variability of a lake's ecological state, overshadowing the influence of longer-term climatic patterns. This finding reveals a dichotomy: while climate scenarios are adept at forecasting broad-scale, seasonal, and annual trends, they are unable to accurately predict the precise timing of stochastic events like storms, which play a pivotal role in determining lake turnover. The critical role of such unpredictable events points to the need to reevaluate how long-term forecasts of mixing regime of oligomictic systems are conducted, particularly incorporating a greater degree of stochasticity in the outputs of climate models.

Chapter 4 Concluding Remarks

While climate change-driven alterations to lake mixing regime have been widely investigated across Northern Hemisphere lakes, Southern Hemisphere systems have received less attention in part due to the lack of long-term monitoring data. Nonetheless, the northern Patagonia region of South American contain some of the largest pristine lakes on the planet. Motivated by the need to better understand the current and future trajectory of these systems in the context of climate change and proposed development, a limnological monitoring program was initiated in 2021 in one of the largest lakes in the region, Lago Llanquihue. Field observations were used to calibrate a 3D numerical model (Si3D) which was then employed to evaluate changes to lake mixing regime under a future climate scenario and a future development scenario when lake clarity declined. Model results indicate that this deep Southern Hemisphere lake will warm slower than analogous systems in the Northern Hemisphere during the 21st century, largely due lower predicted increases in air temperature. Changes in clarity were shown to be as important climatic perturbations in influencing lake thermal structure, highlighting the importance of advocating for sustainable watershed development.

This study provided the first high-resolution climate modelling study for a deep South American lake. By temporally downscaling climate change scenario forecasts, we were able to force the model with an internally consistent set of sub-daily meteorological parameters, an improvement over simple sensitivity analysis studies. The downscaling methodology serves as a framework to develop additional long-term meteorological forecasts at timescales relevant to lake mixing processes. The relatively small rates of change in lake temperature, stratification, and mixing were consistent with those estimated for lakes in New Zealand. The findings of this study further support the growing body of evidence demonstrating the asymmetrical impacts of climate change between the Northern and Southern Hemispheres. While this phenomenon has been extensively discussed in the climatological research community, it has often been overlooked in limnological research due to a lack of long-term lake monitoring programs in regions like South America. Ultimately, this study fills a critical knowledge gap in the scientific literature by providing a comprehensive assessment of climate change impacts on a deep South Hemisphere lake.

Moreover, model results demonstrate that long-term changes in water clarity, which are often caused by increasing human activities in the watershed, can amplify surface warming and suppress warming of deep waters. This emphasizes the importance of considering changes in water clarity in long-term lake simulation, as they can be as important as climate changes in influencing changes in lake stability and mixing regimes. While climate modeling studies often evaluate a range of potential GHG emissions scenarios, few lake simulations incorporate a range of clarity scenarios in their projections. Therefore, incorporating an assessment of the potential impacts of both anthropogenic and climatic factors can provide a more comprehensive understanding of the range of possible outcomes for lakes and inform the development of effective management strategies for these ecosystems.

Further Research

The findings in this dissertation serve to advance understanding of the physical processes and water quality impacts during stratification and vertical mixing events in lakes of varying depth. Nonetheless, this research opens up a wide range of possibilities for further research on this subject.

The results presented in Chapter 2 indicate that internal P loading in Clear Lake represents the most substantial contribution to the annual P budget of any lake detailed in the limnological literature. Internal loads estimated from both water column mass balance and experimental sediment P release rates are similar in magnitude, but large differences in estimates were observed in the Upper Arm – the lake's largest and shallowest subbasin. While arm-specific loading rates accounted for inter-basin variations in temperature and dissolved oxygen, this discrepancy suggests that other biological, mechanical, and chemical processes may be contributing to increased P released in this arm. Specifically, the role of sediment resuspension due to benthic bioturbation and wave action on internal P release could be investigated through field experimentation. In addition, the contribution of internal P loads released from the vegetated littoral zone should be studied further. By quantifying the relative contribution of each of these mechanisms, a holistic conceptual model of in-lake P cycling processes could be developed to facilitate more targeted restoration strategies.

Furthermore, while this study demonstrates how intermittent summertime mixing events facilitate cyanobacteria bloom growth by altering nutrient limitation in favor of N-fixers, the dynamics of cyanobacteria blooms in Clear Lake remain poorly understood due to the complexity of the cyanobacteria community. Seasonal succession from N-fixers to non-N-fixers appears to routinely occur but the role of zooplankton succession and iron-cycling is understudied. Future research would benefit from developing ecological models to disentangle the drivers and progression of cyanobacteria succession within this ecosystem.

Chapter 3 demonstrates that deep water renewal in oligomictic Lake Tahoe is likely driven by three-dimensional transport processes. While a volumetric scaling analysis suggests that differential cooling in littoral areas can drive density currents that facilitate this renewal, this hypothesis should be corroborated with future field deployments. Current profiles arrayed along the lake's shallow shelves could help to identify the occurrence, timing, and magnitude of such flows. These measurements could be complemented with three-dimensional numerical simulations to resolve the depth to which these flows plunge.

The hydrodynamic model developed in Chapter 4 lays the groundwork for much needed further research on the lakes of northern Patagonia. This region is undergoing dramatic social and land use as Chileans move from the populated north of the country to the pastoral south. This hydrodynamic model could serve as a valuable tool to evaluate potential watershed development scenarios and provide science-based policy recommendations to guide sustainable development. However, much remains unknown about nutrient cycling within the lake and its watershed. A watershed model should be developed, and a water quality model should be coupled with the calibrated lake model to enable scientists to explore how the ecological health of the lake will be impacted by development. Moreover, remote sensing tools could be applied to extrapolate the modeling results obtained for Lago Llanquihue across all the understudied lakes of northern Patagonia.

~

Appendix A – Chapter 2 Supplemental Information

A.1 Historical Metrological and Nutrient Data

Figure A.1. *Long term trends in summer (circle) and winter (triangle) Clear Lake surface temperatures from 1970 – 2020 (California Department of Water Resources).*

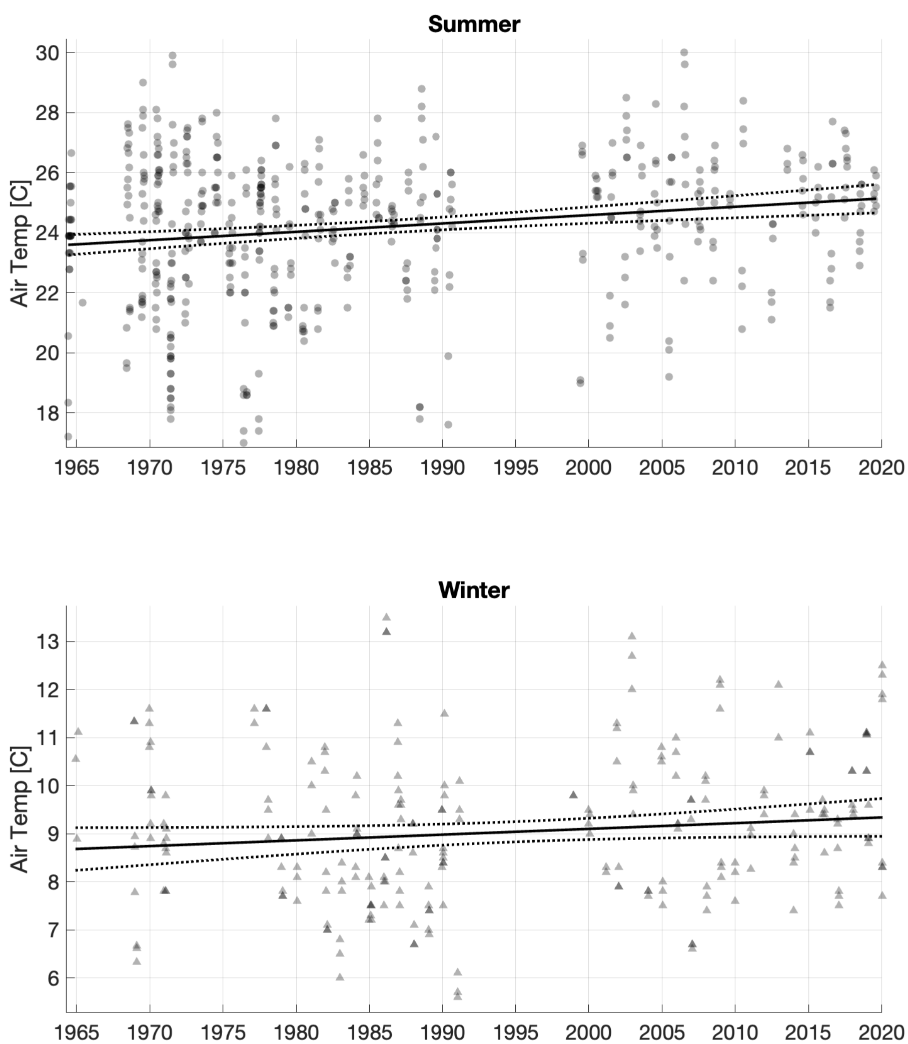

Figure A.2. *Dissolved inorganic nitrogen (DIN, nitrate plus ammonium) to orthophosphate (OP) molar ratio, concentrations of nitrate, ammonium, orthophosphate in mmol/L, Redfield ratio (N:P = 16:1), and N:P ratio = 25:1. (Source – Department of Water Resources).*

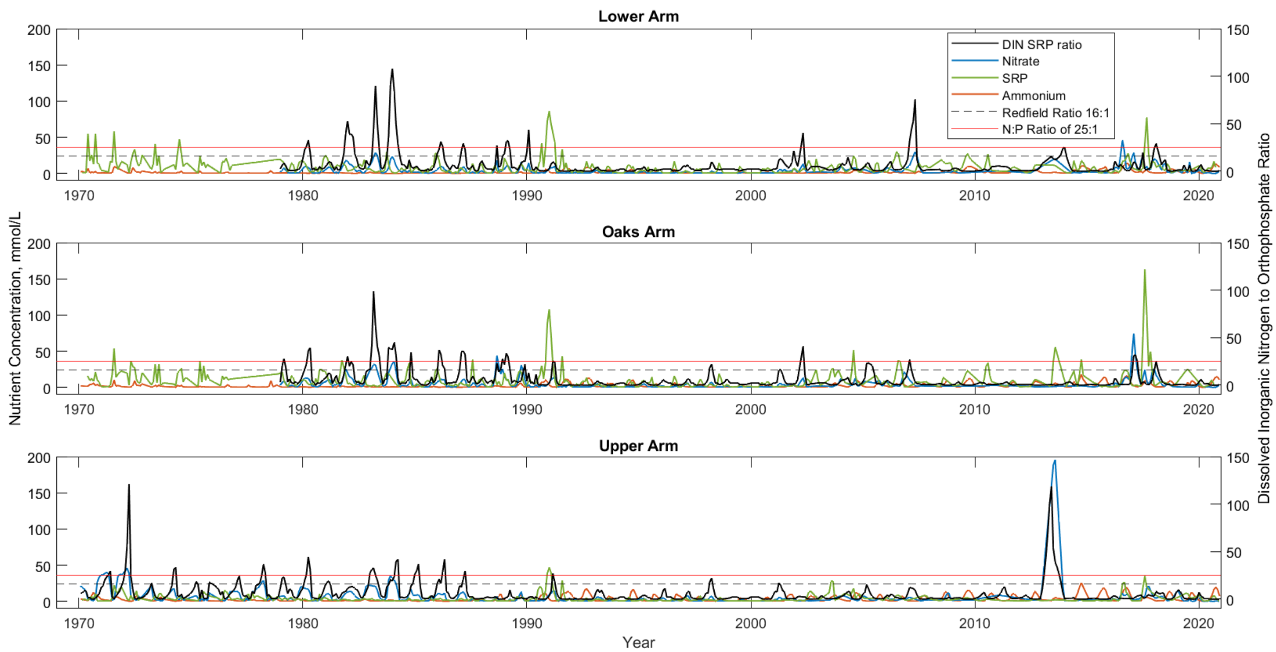

A.2 Lake Temperature and Dissolved Oxygen Data

Each instrumentation mooring is comprised of a vertical array of RBR solo^{3}T thermistors (0.002^{o}C accuracy; 0.0002^{o}C resolution), spaced ~1 m apart, that record water temperatures every 10 seconds (s). The 3 deepest moorings in each basin (LA-03, OA-04, UA-06) also contained 2 RBR codaT.ODO dissolved oxygen or RBR-DO sensors (accuracy 0.26 mgL^{-1}; resolution <0.03 mgL^{-1}) positioned 0.5 m and 2 m off the bottom that record near-bed oxygen concentrations at 30 s intervals. PME miniDOT dissolved oxygen sensors (accuracy 0.3 mgL^{-1}; resolution 0.01 mgL^{-1} resolution) were deployed in the epilimnion, ~4-5 m below the water surface. The other 4 moorings contained one RBR-DO sensor each, positioned at 0.5 off the bottom. All optical DO sensors were equipped with wipers to prevent biofouling. An Onset HOBO U20-001-01 water depth sensor was attached to each mooring line to determine the depth of each logger and track fluctuations in lake water level during the study period.

Figure A.3. *Hourly temperature data measured by moored thermistor chain at LA-03 and hypolimnetic DO measured 0.5m off lakebed (Apr 2019 – Dec 2021).*

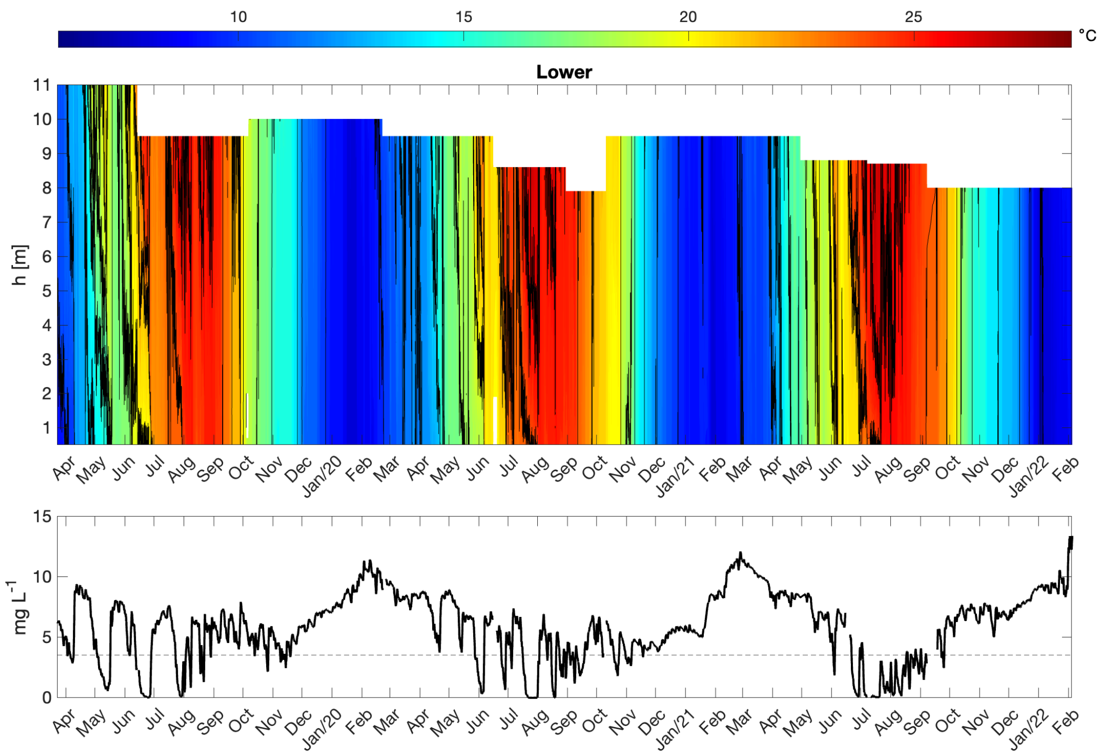

Figure A.4. *Hourly temperature data measured by moored thermistor chain at OA-04 and hypolimnetic DO measured 0.5 m off lakebed (Apr 2019 – Dec 2021).*

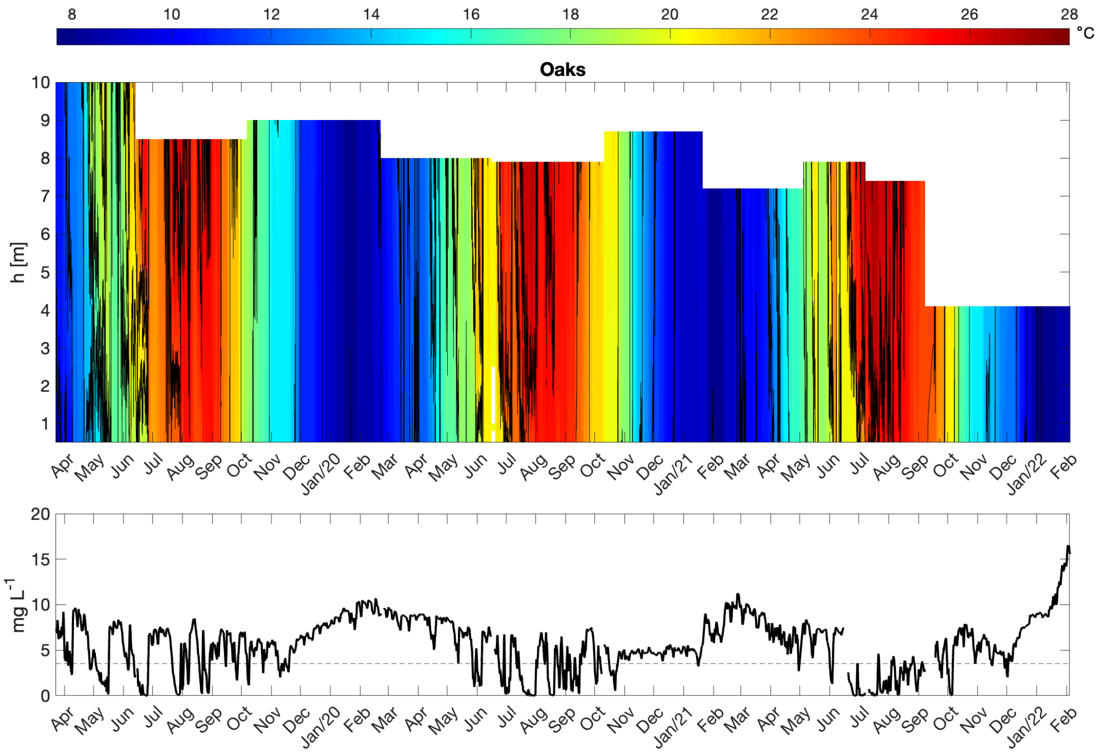

Figure A.5. *Hourly temperature data measured by moored thermistor chain at UA-06 and hypolimnetic DO measured 0.5 m off lakebed (Apr 2019 – Dec 2021).*

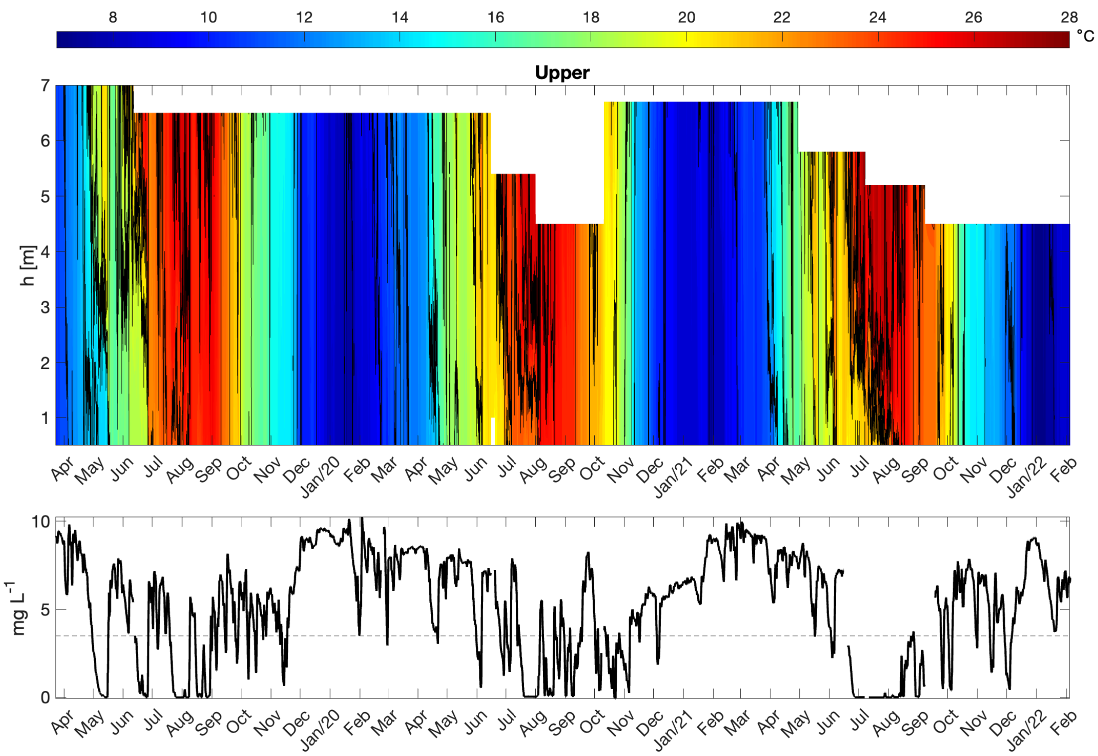

A.3 Constituents Analyzed During Water Quality Monitoring.

Table A.1. *Constituents analyzed during water quality monitoring. Laboratory analytical methods are outlined in* Liston et al. 2013 *and* Rice et al. 2012.

Category	*Constituent*	*Description*
Nitrogen	*NO3 + NO2*	*Dissolved Nitrite and Nitrate*
	NH4	*Ammonium*
	DKN	*Dissolved Kjeldahl Nitrogen*
	PN	*Particulate Nitrogen*
Phosphorus	*SRP*	*Soluble Reactive Phosphorus*
	TDP	*Total Dissolved Phosphorus*
	PP	*Particulate Phosphorus*
Carbon	*DOC*	*Dissolved Organic Carbon*
	PC	*Particulate Carbon*
Chlorophyll	*Chl-a*	*Chlorophyll-a*
Phytoplankton	*Phyto*	*Specifies identification and enumeration*

A.4 Clear Lake Cyanobacteria Index

Figure A.6. *Monthly averaged 10-day running maximum modified cyanobacteria index for May – October (2019-2021).*

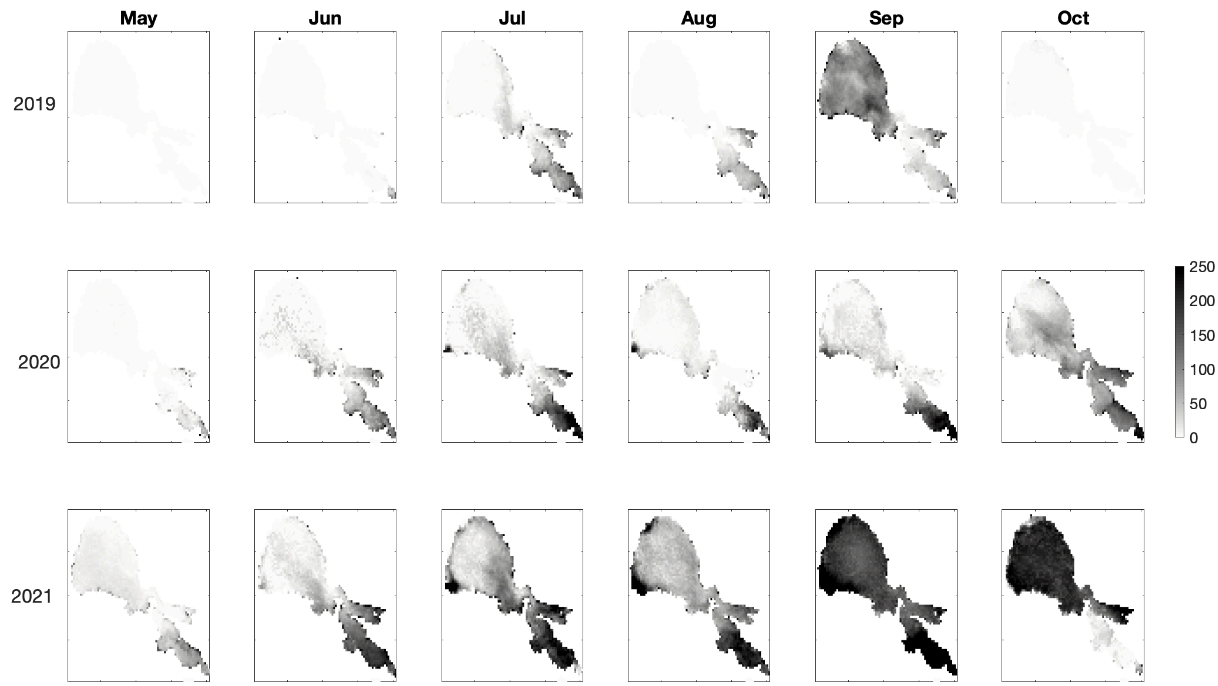

Figure A.7. *Scatter plots comparing observed cyanobacteria biovolume and chlorophyll a concentration in surface grab samples against 10-day running maximum modified cyanobacteria index from March 2019 – December 2021.*

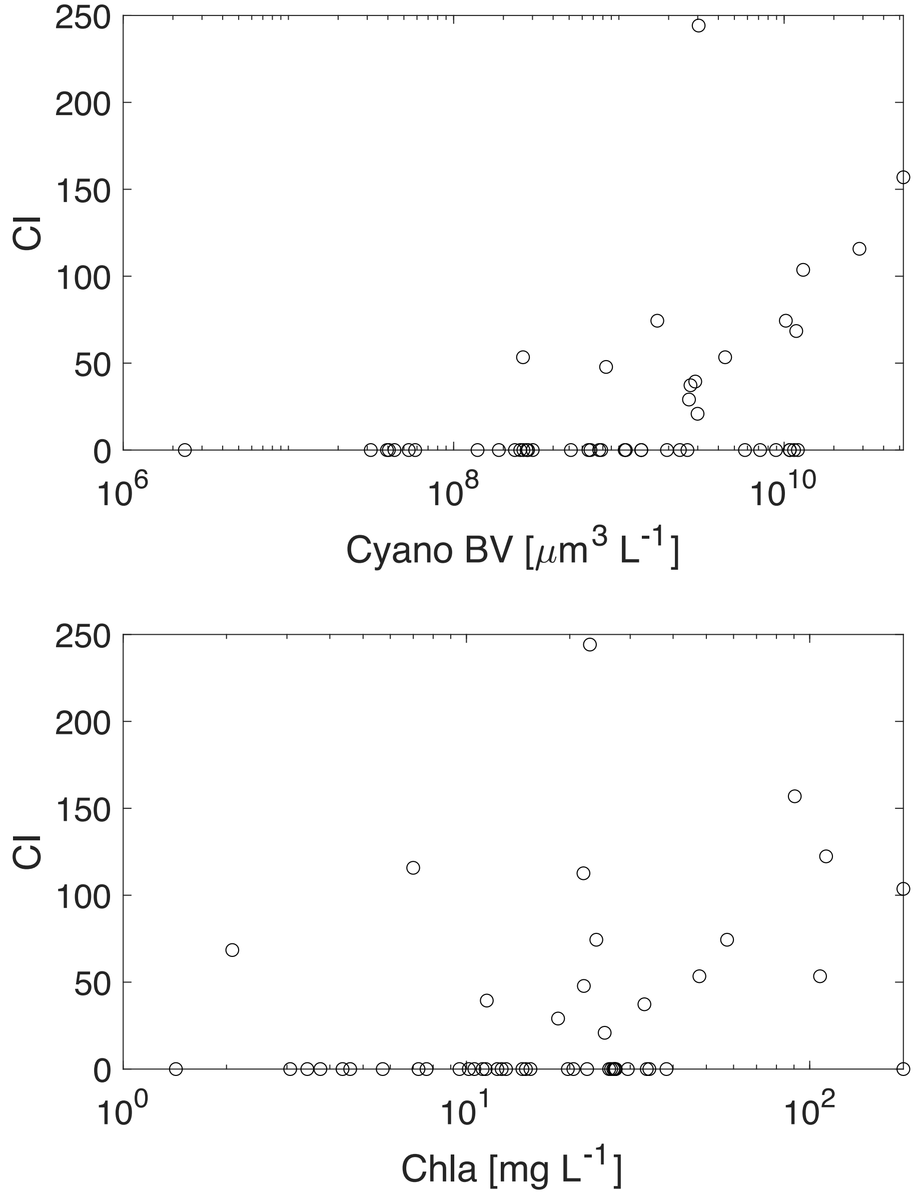

A.5 Stream External Loading Calculations

Figure A.8. *Left) Stream-specific linear regressions relating flow to TP concentration from Lake County Water Resources Department routine stream sampling program (2008-2018). Right) Daily and hourly hydrographs for gaged streams from January 2019 – December 2021.*

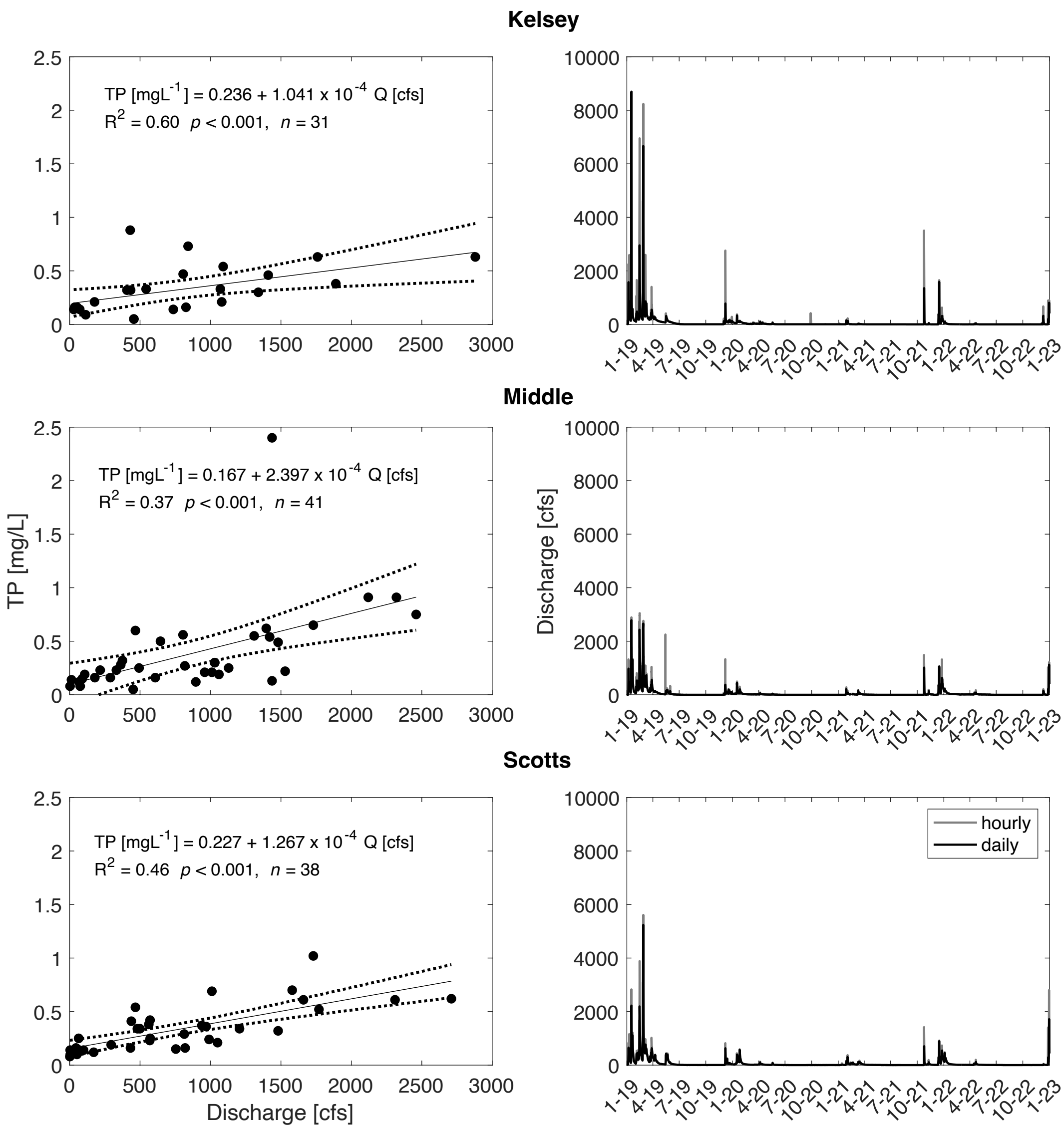

A.6 Clear Lake Meteorology

Figure A.9. *Frequency Distribution of observed summertime wind speeds (April – October) across Clear Lake subbasin from 2019-2021.*

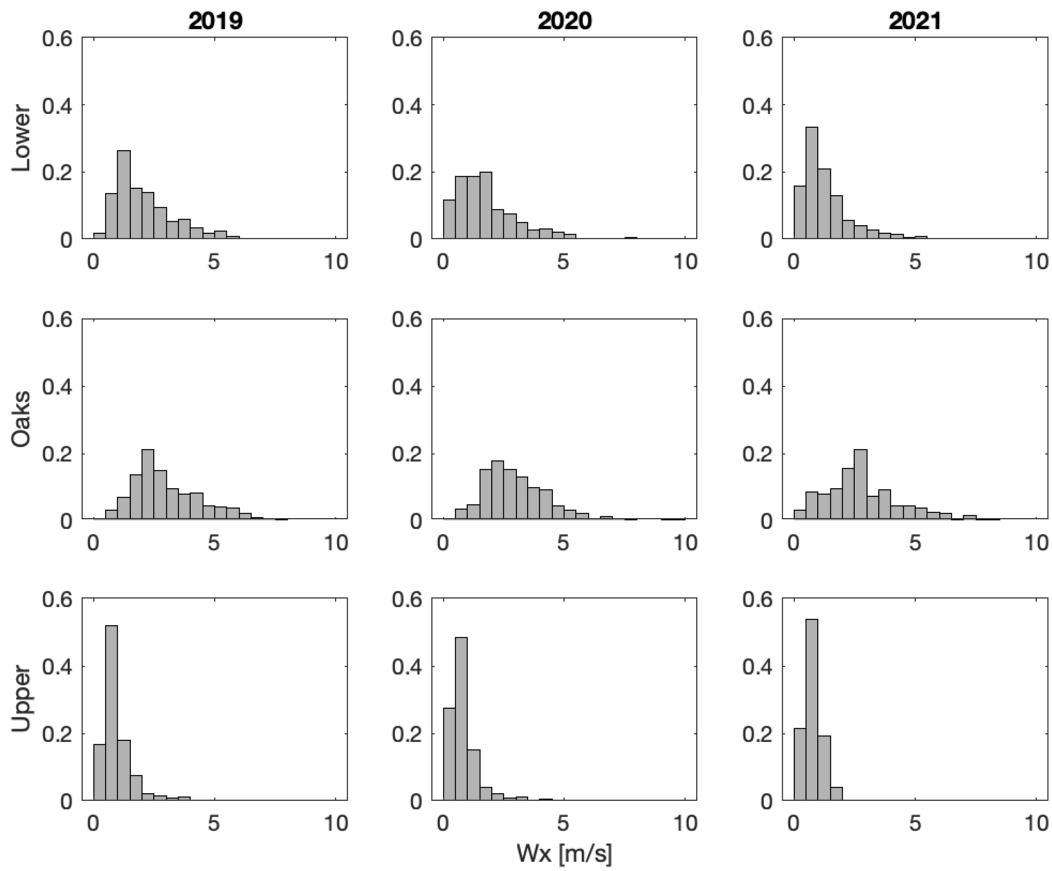

Figure A.10. *10 Day trailing average wind speed (a) and air temperature(b) and lake surface water temperature (c) measured at BKP station and 3 Day trailing average buoyancy frequency for UA from May to November 2019 – 2021.*

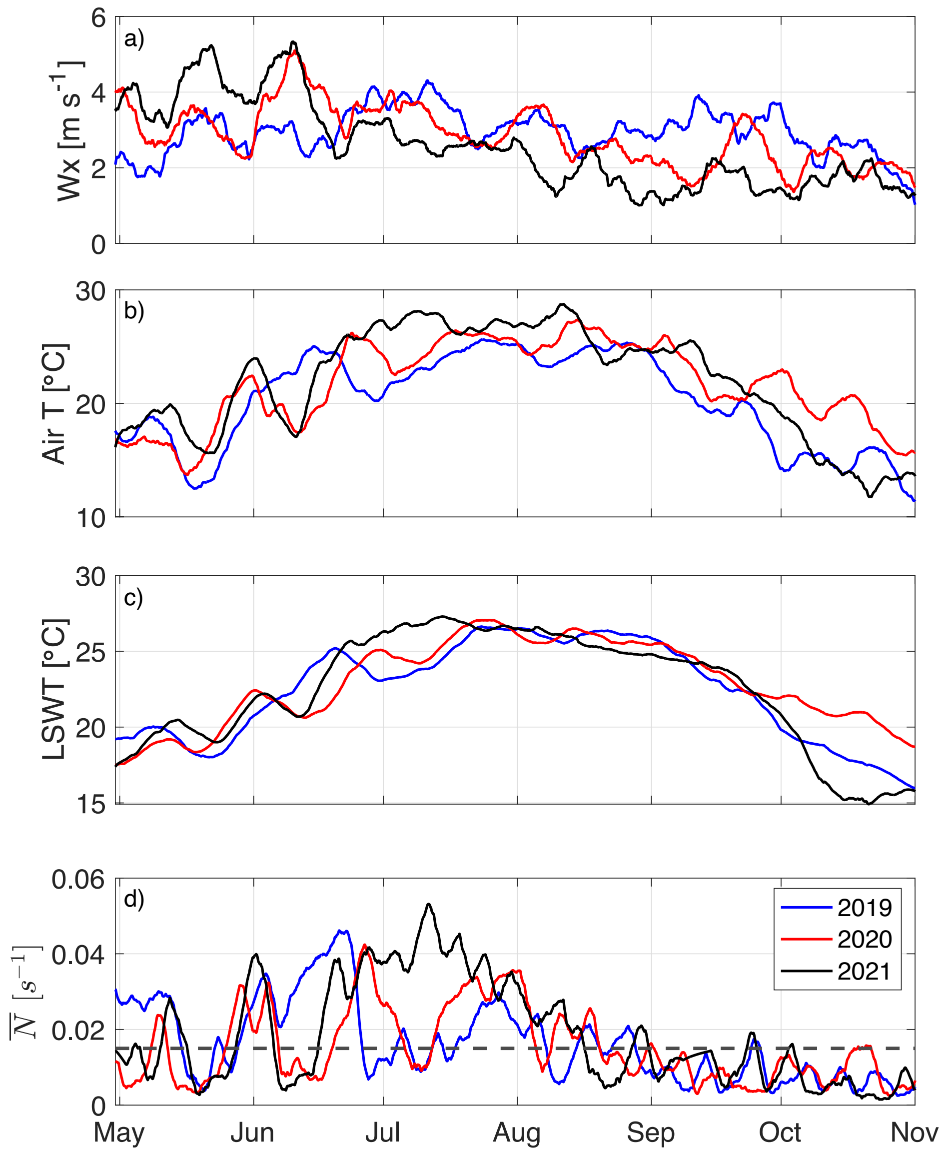

A.7 Time Series Decomposition of Spatially-averaged CI

Figure A.11. *Time series of spatially averaged CI across Clear Lake and three sub-basins. Plots show observed (blue), long term trend (orange), seasonal trend (yellow) and residuals (purple).*

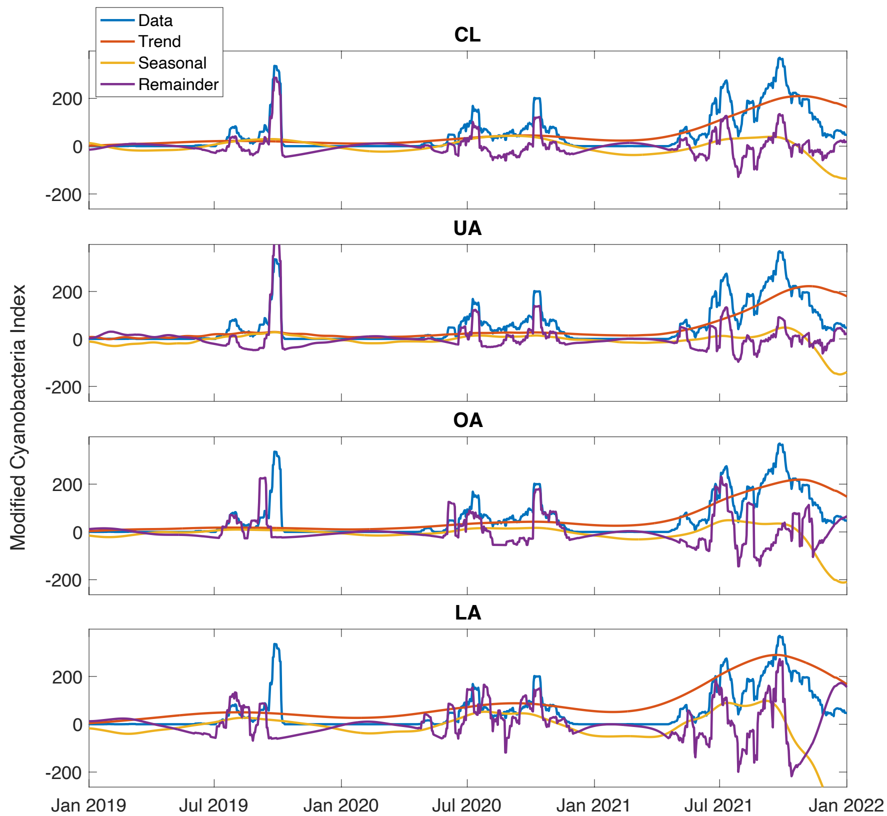

Table A.2. *Variance and Strength of long term (F_T) and seasonal (F_S) trends*

Basin	***Var (Trend)***	***Var (Seasonal)***	***Var (Residual)***	***F_T***	***$_FS$***
Clear Lake (CL)	*3571*	*1088*	*1889*	*0.66*	*0.41*
Upper (UA)	*3695*	*810*	*2884*	*0.56*	*0.28*
Oaks (OA)	*3971*	*1610*	*2992*	*0.58*	*0.38*
Lower (LA)	*6331*	*5605*	*4794*	*0.58*	*0.53*

A.8 Distribution of Submersed Aquatic Vegetation in Clear Lake

Figure A.12. *Aquatic vegetation bio-volume in Clear Lake, Sept-2002 (ReMetrix 2003). Majority of vegetation is located along the western and northern banks of UA.*

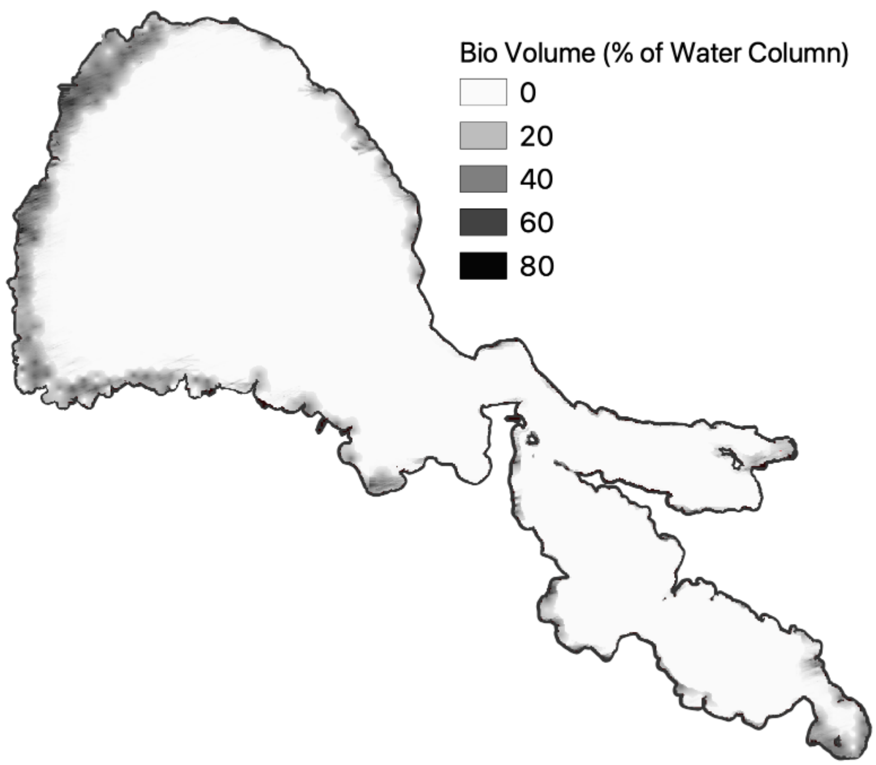

References

Liston, A., Hammel, T., Edirveerasingam, V., Allen, B., Hackley, S., Reuter, J., & Schladow, G. (2013). *Laboratory Procedure, Field Protocol and Quality Assurance Manual,.*

Rice, E. W., Bridgewater, L., & American Public Health Association. (2012). *Standard methods for the examination of water and wastewater* (Vol. 10). American public health association.

Appendix B – Chapter 3 Supplemental Information

B.1 Characterization of Mixing and Water Column Stability

Water column stability can be evaluated as the square of the Brunt-Väisälä buoyancy frequency as defined in Imberger and Patterson 1989 as:

$$N^2 = -\frac{\frac{g}{\rho}\partial\rho}{\partial z}$$

where N^2 (s^{-2}) is the square of the buoyancy frequency, g ($m\ s^{-2}$) is gravitational acceleration, ρ ($kg\ m^{-3}$) is the water density at depth z (m). Density was calculated as function of conductivity, temperature and depth based on methods described in Chen and Millero 1986.

The work required to mix the entire water column from density stratified condition to a uniform density can be estimated using the Schmidt Stability Index (S_T) as defined by Idso 1973 as:

$$S_T = g/A_0 \int_0^{z_{max}} A_z(z - z_{\bar{\rho}})(\rho_z - \bar{\rho})\, dz$$

where S_T ($J\ m^{-2}$) is the Schmidt stability index, A_o (m^2) is the surface area of the lake, z_{max} (m) is the maximum depth, A_z (m^2) is the area at depth z, $z_{\bar{\rho}}$ (m) is the depth of the volumetric mean density, ρ_z ($kg\ m^{-3}$) is the density at depth z and $\bar{\rho}$ ($kg\ m^{-3}$) is the volumetric mean density which can be calculated via the following equation.

$$\bar{\rho} = \frac{1}{\int_0^{z_{\max}} A_z dz}\int_0^{z_{\max}} \rho_z A_z dz.$$

The depth of the volumetric mean density can be calculated as:

$$z_{\overline{\rho}} = \frac{1}{\int_0^{z_{\max}} \rho_z A_z dz} \int_0^{z_{\max}} z \rho_z A_z dz.$$

The relative strength of the stratification compared to the destabilizing force of wind stress can be evaluated using the dimensionless Wedderburn Number (W) as defined in Imberger and Patterson 1989 as:

$$W = \frac{g\, \Delta\rho h^2}{\rho_o u_*^2 L}$$

where $\Delta\rho$ is the density difference between the epilimnion and the hypolimnion, h (m) is the depth of the top mixed layer, ρ_o (kg m^{-3}) is the density of the surface mixed layer u_*^2 is the square of the wind shear stress (m s^{-1}) and L *(*m*)* is the effective fetch length. W << 1 indicate strong wind stress relative to the stabilizing buoyancy force while W > 10 indicate the stratification dominates over wind stress with limited wind-driven mixing the upper epilimnion.

The Lake Number (L_N) is analogous to Wedderburn number but is an integral representation of the dynamic stability of water column which directly takes into account the bathymetry of lake. L_N can be calculated as Robertson and Imberger 1994:

$$L_N = \frac{S_T \left(1 - \frac{Z_T}{Z_{(\max)}}\right)}{\rho_s u_*^2 A_o^{0.5} (1 - \frac{z_{\overline{\rho}}}{z_{\max}})}$$

B.2 Monitoring Metadata

***Table B.1**. Description of monitoring sites used in this study*

Site Name	Site ID	Category	Parameters Measured	Deployment
Glenbrook	GBTC	Thermistor chain	Water T, DO	2013-02 to present
Mid-Lake	MLTP	Thermistor chain	Water T	1998-11 to 1999-06
		profiling site	Water T, DO, conductivity	2006 to present
Homewood	HWTC	Thermistor chain	Water T	2014 to present
Tahoe Buoy 1	TB1	Met	Wx, Air T, Atm P, RH, LSWT	2006 to present
Tahoe Buoy 2	TB2			
Tahoe Buoy 3	TB3			
Tahoe Buoy 4	TB4			
Lake Tahoe US Coast Guard Station	USCG	Met	Wx, Air T, Atm P, RH, SWin, LWin	1998-11 to present
Tahoe City (USC00048758)	TC	Met	Air T	1910 to present
Homewood Nearshore	HWNS	Nearshore	Water T	2016 to present
Tahoe City Nearshore	TCNS	Nearshore	Water T	2016 to present
Glenbrook Nearshore	GBNS	Nearshore	Water T	2016 to present

Table B.2. Thermistor deployment configuration and deployment log

Site	Type	Height Above Bottom Logger	Deployment Notes
HWTC	RBR Concerto3 Thermistor string	105	
		100	
		95	
		90	
		85	
		80	
		75	
		70	
		60	
		50	
		40	
		30	
		20	
		15	
		10	
		5	
	Concerto3 (T,DO)	0	
GBTC	TR1060, SoloT	455	TR1060: Feb 2013 - Jun 2016 / SoloT: Jul 2016 - present
	TR1060, SoloT	440	TR1060: Feb 2013 - Jun 2016 / SoloT: Jul 2016 - present
	TR1060, SoloT	435	TR1060: Nov 2013 - June2016 / SoloT: Jul 2016 - present
	SoloT	430	
	SoloT	420	
	SoloT	400	
	SoloT	380	
	SoloT	360	
	SoloT	340	
	SoloT	300	
	SoloT	260	
	TR1060, SoloT	220	SoloT: Feb 2013 - Apr 2018 / TR1060: Apr 2018 - Dec 2019 SoloT: Oct 2020 - present
	SoloT	180	SoloT: Feb 2013 - Jun 2016 / TR1060: July 2016 - present
	SoloT	140	
	SoloT, TR 1060	100	SoloT: Feb 2013 - Jun 2016 / TR1060: July 2016 - present
	SoloT, TR 1060	60	SoloT: Feb 2013 - Jun 2016 / TR1060: July 2016 - present
	SoloT, TR 1060	20	SoloT: Feb 2013 - Jun 2016 / TR1060: July 2016 - Dec 2019 SoloT: Oct 2020 - present
	SoloT	0	
	Concerto (CTD-DO)	0	
MLTP	OEI 9311	459	
	OEI 9311	449	
	TR-1000	439	
	TR-1000	419	
	OEI 9311	409	
	OEI 9311	389	
	TR-1000	379	
	OEI 9311	369	
	TR-1000	359	
	OEI 9311	349	
	OEI 9311	329	
	OEI 9311	309	
	OEI 9311	289	
	OEI 9311	259	
	OEI 9311	229	
	OEI 9311	199	
	OEI 9311	159	
	OEI 9311	119	
	OEI 9311	79	
	OEI 9311	39	
	OEI 9311	0	

B.3 Thermistor Chain and CTD Data

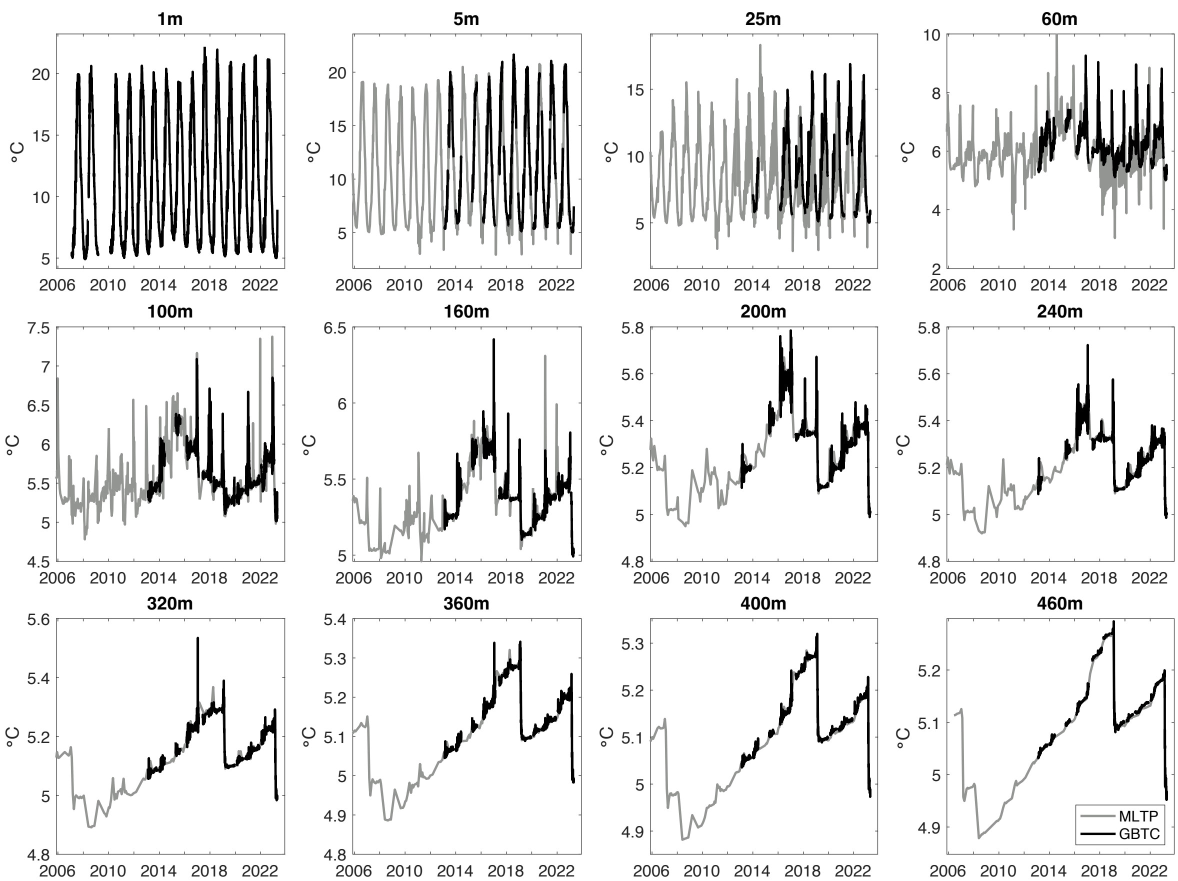

Figure B.1. *Time series of temperature measured at discrete depths in Lake Tahoe recorded at MLTP profiling site (grey) and GBTC thermistor chain (black). Deep mixing events occurred in the winters of 2007, 2008, 2011, 2019, and 2023.*

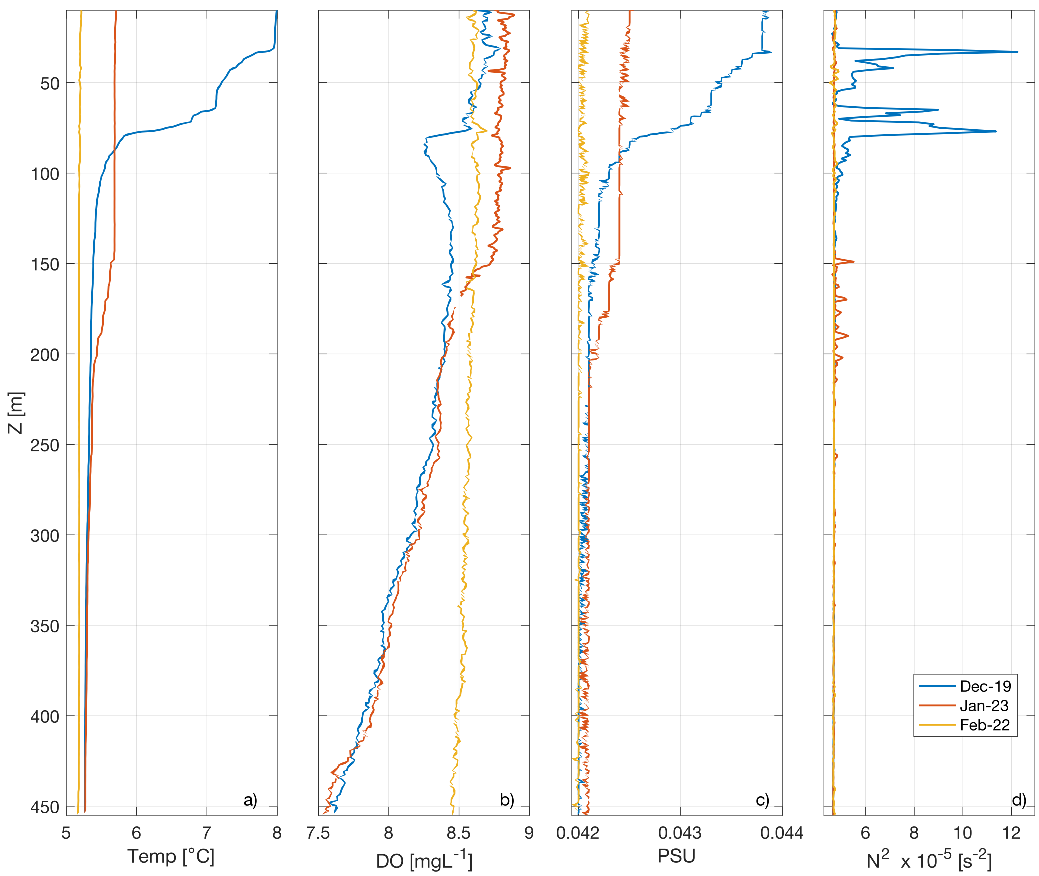

Figure B.2. *Profiles of temperature and DO collected at MLTC monitoring site and calculated buoyancy frequency (N^2) before and after turnover on February 10 2019.*

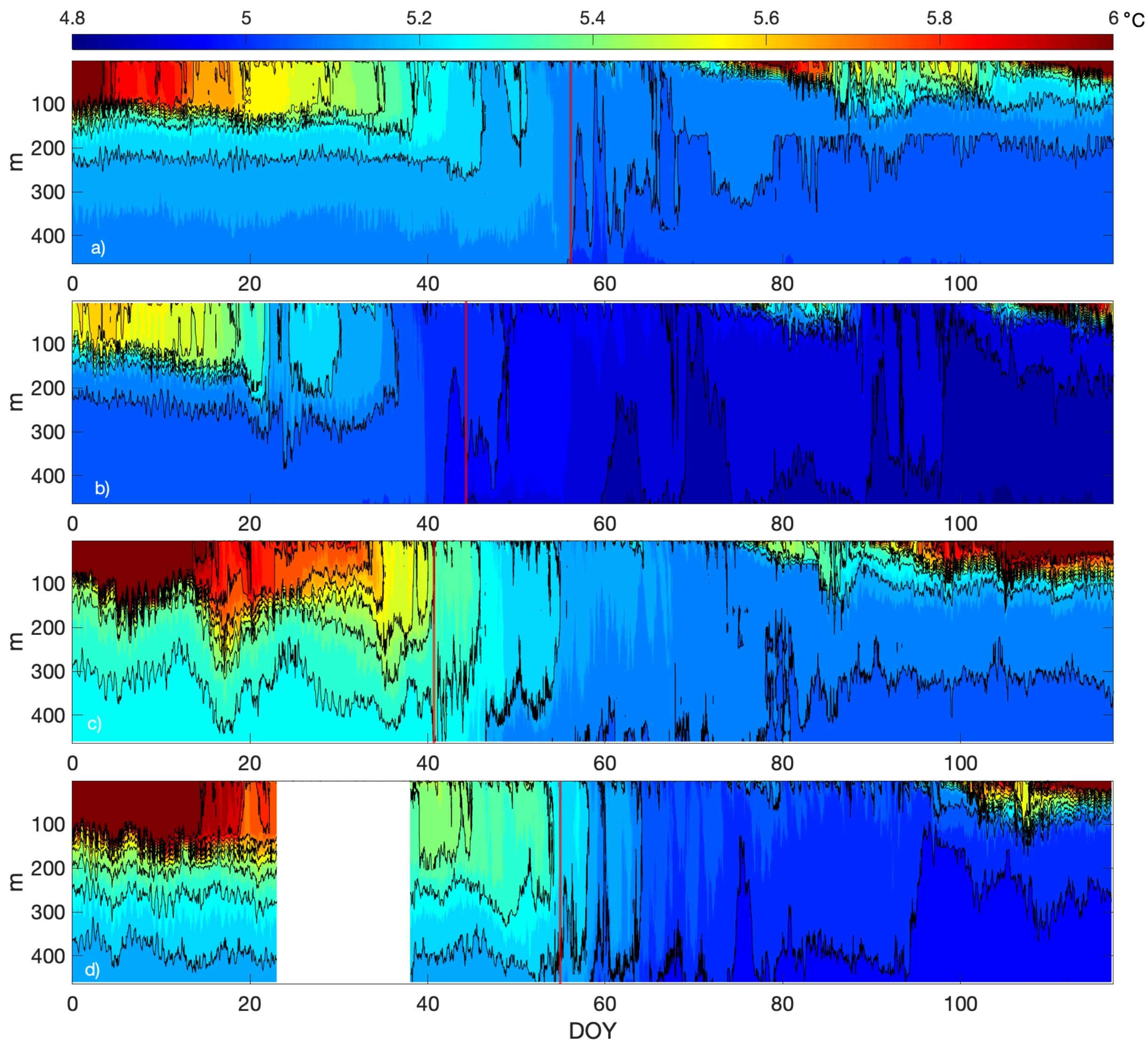

Figure B.3. *a-d) Thermal structure of Lake Tahoe events during deep mixing in the winters of 1998,1999,2019,and 2023. Red vertical lines indicate onset of turnover. Black lines show 0.05 °C isotherms.*

B.4 Historical Observations

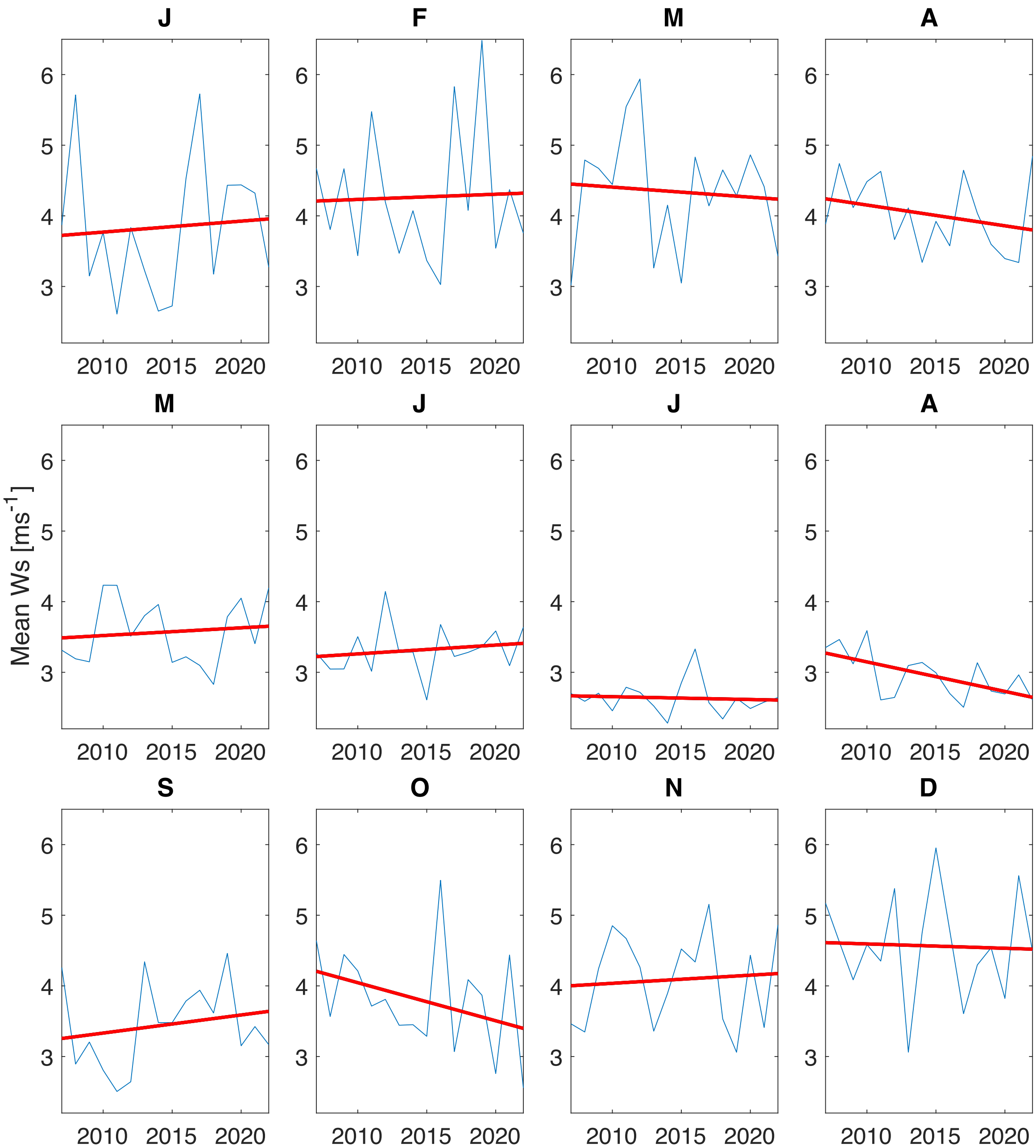

Figure B.4. *Monthly average wind speeds measured by on-water buoys at Lake Tahoe 2006-2022. Red lines indicate linear trend line.*

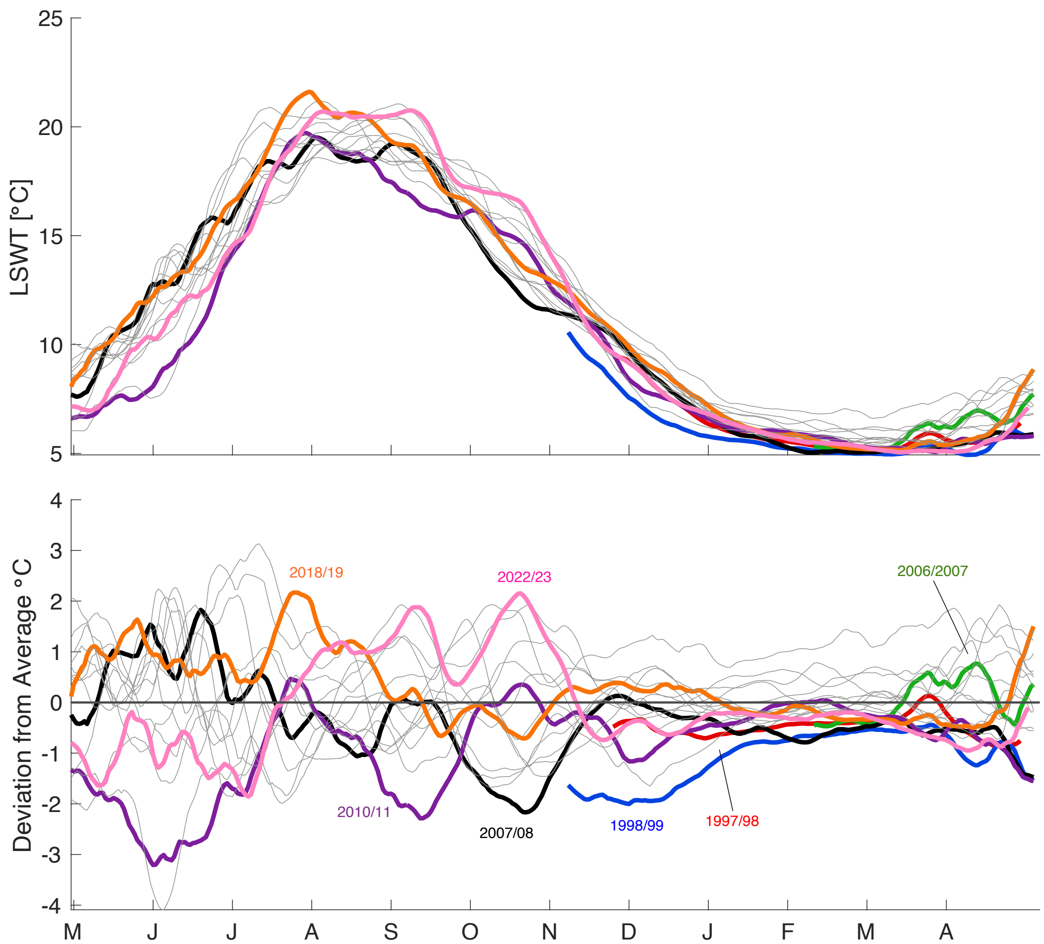

Figure B.5. *Comparison of daily average surface temperature from May 1 – Apr 30 (1997-1999 and 2008 – 2023). Colored lines denote deep mixing winters.*

Appendix C – Chapter 4 Supplemental Information

C.1 Meteorological Data Downscaling Procedure Future Meteorological Data

Forecasted meteorological data for northern Patagonia was obtained from the Center for Climate Resilience Research (CR2) simulation platform (https://simulaciones.cr2.cl). This platform was developed to support informed public policy by providing regional scale climate forecasts across Chile from 2006 – 2094. Of the 10 available model projections, only three produced outputs at a daily timestep. The regional climate model, REGCM4, was selected from this subset because of its relatively high spatial resolution (10 km grid size) and ability to simulate regional climatic patterns over complex terrain features such as the Chile Andes (Bozkurt et al., 2019a). REGCM4 describes soil-plant-atmosphere interactions and is driven by the MPI-ESM-MR global climate model at its lateral boundaries. Climate projections from the IPCC's highest greenhouse gas emission scenario (representative pathway 8.5) were utilized in this analysis. This representative pathway represents a "worst case" scenario where increasing GHG emissions continue to occur through 2100 with minimal emission mitigation policies implemented (Riahi et al. 2011). From this projection, daily values for the following parameters were selected: average air temperature, maximum air temperature, minimum air temperature, relative humidity, cloud cover, shortwave radiation, longwave radiation, atmospheric pressure, north-south wind speed, and east-west wind speed. Daily parameter values were calculated as the average of the grid cells that cover Lago Llanquihue's surface.

Temporal Down-Scaling Methods

While future projected meteorological data was generated at a daily timestep, the lake model requires surface boundary condition inputs at sub-daily values to accurately represent the hydrodynamic response to diurnal weather patterns. To this end, daily data was downscaled to an hourly timestep following the procedure outlined in Birt et al. (2021). Downscaling performance was evaluated by comparing observed and down-scaled hourly data.

Air Temperature

Hourly air temperature was calculated as a function of the maximum and minimum air temperature for a given day of the year. Air temperature oscillates in a regular diurnal pattern which can be numerically represented by two functions: a sine function during the day and exponential decreasing function at night (Birt et al., 2021; Ephrath et al., 1996). The daytime air temperature was modeled by the equation,

$$T_{a(t)} = T_{n(min)} + \left(T_{n(max)} - T_{n(min)}\right) * S_{(t)} \tag{1}$$

where $T_{a(t)}$ is the air temperature at time t, $T_{n(min)}$ and $T_{n(max)}$ are the daily maximum and minimum temperatures. $S_{(t)}$ is a sine function at time t defined as:

$$S_{(t)} = \sin(\pi \frac{t - SM + \frac{DL}{2}}{DL + 2P}) \tag{2}$$

where DL is the day length for the study site, SM is the time of the solar maximum (observed to be 15:00) and P is the delay between SM and $T_{n(max)}$, (~3 hours). After sunset, the temperature declines exponentially from the sunset temperature to the lowest temperature of the following day, just before dawn. This night time temperature function is defined as:

$$T_{a(t)} = \frac{T_{n+1(min)} - \left(T_{ss} * e^{-\frac{24-DL}{\tau}}\right) + \left(\left(T_{ss} - T_{n+1(min)}\right) * e^{-\frac{t-t_{ss}}{\tau}}\right)}{1 - e^{-(24-DL)/\tau}} \tag{3}$$

where T_{ss} and t_{ss} are the temperature and time of sunset respectively, $T_{n+1(min)}$ is the minimum air temperature during the following night, and τ is the time coefficient calibrated for the field site to minimize error between modeled and observed temperatures. $T_{n+1(min)}$ occurs on either the following day for hours between sunset and midnight or on the current day for nighttime hours before sunrise. All temperatures and times are measured in degrees Celsius and hours, respectively.

Relative Humidity (RH)

RH in decimal form can be calculated from the ratio of actual vapor pressure in the air (VPA) and the saturated vapor pressure (e_s) in the equation:

$$RH(\%) = 100 * \frac{VPA}{e_s} \tag{4}$$

where VPA is a function of the air temperature (T_a)

$$VPA = 6.107 * e^{\frac{17.4*T_a}{239+T_a}} \tag{5}$$

and e_s is analogously related to the calculated dew point temperature (T_d) for a given pair of humidities and temperatures.

$$e_s = 6.107 * e^{\frac{17.4*T_d}{239+T_d}} \tag{6}$$

Since RH is a function of temperature, it too follows a diurnal pattern. To calculate a daily average T_d, equations 4-6 were rearranged to formulate equation 7.

$$0 \cong 6.107 * e^{\frac{17.4*T_d}{239+T_d}} - \frac{e_s * RH}{100} \tag{7}$$

In this equation there are two estimates for VPA: one derived from daily average T_a and RH values and another estimated for a range of possible T_d values. The T_d value that minimized the difference between these two terms was selected as a constant daily average value from which hourly RH values were calculated. This method would occasionally result in RH values greater than 100%, which cannot be accepted as boundary conditions in the model, so these values were set to 100%.

Downwards Shortwave Radiation (Φ_{sw})

Hourly shortwave radiation was estimated with a sine function which takes solar declination (δ in radians), solar elevation (β), latitude (L in radians) , day of year (n) , time of day of the solar maximum (SM) and day length (DL) as inputs. Solar declination was calculated as a function of the day of year in the equation below.

$$\delta = -23.45 * \frac{\pi}{180} * \cos(\frac{2\pi}{365} * (172 - n)) \tag{8}$$

Next seasonal offset (SD) and amplitudes (CD) of the sine wave were calculated with the following equations.

$$SD = \sin(L) * \sin(\delta) \tag{9}$$

$$CD = \cos(L) * \cos(\delta) \tag{10}$$

These terms were then used to calculate the sin of the solar elevation and integral of the solar radiation from sunrise to sunset (DSBE) as defined below.

$$\sin(\beta) = SD + (CD * \cos\left(\pi * \frac{t - SM}{12}\right)) \tag{11}$$

$$\text{DSBE} = \arccos\left(-\frac{SD}{CD}\right) * \frac{24}{\pi} * \left(SD + C * SD^2 + \frac{C * CD^2}{2}\right) + 12 * CD * (2 + 3 * C * SD) * \frac{\left(\sqrt{1 - \left(\frac{SD}{CD}\right)^2}\right)}{\pi} \tag{12}$$

Finally the incoming solar radiation at hour t ($\phi_{SW,t}$) was defined in the following equation:

$$\phi_{sw,t} = \phi_{sw,a} * \sin(\beta) * \frac{1 + (C * \sin(\beta))}{DSBE * 3600} \tag{13}$$

where $\phi_{sw,a}$ is total global radiation, j day^{-1}, and C is a meteorological variable characterizing dependence of transmissivity on solar height, approximately equal to 0.4 (Spitters et al., 1986).

Downwards Longwave Radiation (ϕ_{Lw})

Hourly longwave radiation was calculated as a function of downscaled air temperature and hourly estimates effective emissivity calculated from cloud cover. LW_{in} is frequently calculated via the Stefan-Boltzmann equation.

$$\phi_{Lw} = E_{eff}\sigma T_{eff}^{4} \tag{14}$$

where E_{eff} is effective emissivity (dimensionless), T_{eff} is the air temperature (°K), and σ is the Stefan-Boltmann constant (5.670367 x 10^{-8} kg s^{-3} k^{-4}). Clear sky emissivity (e_{clr}) was calculated from vapor pressure (e_a) via the Angstrom 1918 equation which estimated ϕ_{Lw} on a clear day.

$$e_{clr} = 0.83 - (0.18 * 10^{-0.067\, e_a}) \tag{15}$$

Finally, the effective emissivity, accounting for cloud cover influence was calculated using the Unsworth and Monteith 1975 equation where Cf is the daily predicted cloud cover (decimal) from forecasted simulations.

$$E_{eff} = (1 - 0.84Cf)e_{clr} + 0.84\, Cf \tag{15}$$

Wind

Wind speed (Wx) and direction ($WDir$) varies both cyclically and stochastically in time, producing a signal with random noise around a more predictable diurnal cycle that is driven by changes in atmospheric pressure and geostrophic wind. To model the deterministic component of the wind patterns, a wave function that varies from minimum to maximum wind speeds over the course of the day was used. Since the climate projections produced daily average data for eastward and northward wind components, the two wind components were modeled independently, from which wind speed and direction were subsequently determined.

$$W_t = W_a + \left(\frac{1}{2} * W_a * \cos\left(\frac{\pi * (t - H_{\max})}{12}\right)\right) \tag{17}$$

Here W_t is the hourly wind speed, W_a is the daily average wind speed, t is the hour of the day and H_{max} is the time of maximum wind speed for each component (14th and 3rd hour of the day for northward and eastward wind components respectively).

Air Pressure (AtmP)

When comparing hourly to daily averaged air pressure data, sub-daily variability was small when compared to fluctuations at longer timescales. As a result, a constant daily air pressure was used in the down-scaled model.

Downscaling Performance

The performance of the downscaling methods is shown in **Figure C.1** and **Table C.1.** Down-scaled air temperatures produced greater deviations from the mean towards the minimum and maximum. The temperature model performed well during the summer, but errors were introduced during the winter months when the diurnal, sinusoidal pattern was less pronounced in the observations. However, the root mean squared error (RMSE) of 1.2 °C and the high correlation coefficient (r) of 0.98 demonstrates that this method accurately resolves hourly temperature variation. Down-scaled RH tended to produce overestimates at high humidity values (i.e. above 85%) but performed much better at modeling lower values. The RMSE of 7.8% and r of 0.87 indicates that this model provides a sufficient estimate of sub-daily variation in RH. Downscaled shortwave radiation captured the diurnal signal in solar input but tended to underestimate the peak daily solar maximum as well as under-predicting times of no incoming radiation. The latter error is likely a result of the hourly time step employed which obfuscates the exact times of sunrise and sunset. This method produced a comparatively low RMSE of 78.6 W m^{-2} and a high r of 0.95. Downscaled ϕ_{Lw} radiation was compared against estimates derives from hourly cloud cover values calculated from the difference between extraterrestrial and observed incoming solar radiation. Downscaled ϕ_{Lw}tended to dampen the diurnal signal, producing values closer to the daily average and underestimating daily minimums and maximums. However, with a RMSE of 21.7 W m^{-2} and a $r = 0.84$ this method performed sufficiently. Atmospheric pressure was the only parameter not downscaled from daily averages but the high correlation between daily averages with hourly values ($r = 0.91$) demonstrates that sub-daily fluctuations in this parameter are negligible.

The wind speed downscaling method did not perform as well at capturing hourly variations when compared with the other parameters and tended to underestimate periods of low wind speed (i.e., less than 1 m s^{-1}) and overestimate the frequency of wind speeds greater than 5 m s^{-1} The winds across Llanquihue blow predominantly along a north-south axis running parallel to the west slope of the Andes and while the strong N-S wind component was sufficiently resolved ($r = 0.83$), smaller fluctuations in the E-W component were not captured as well (r = 0.60). This was due to the fact that E-W winds tended to fluctuate around 0, so that small daily average wind speeds dampened the diurnal oscillation in this component. Overall, the downscaled wind magnitude has a RMSE of 2.21 m s^{-1} s and $r = 0.83$. While the mode down-scaled and observed wind directions agree with on another (180-210°), the correlation is low (r = 0.46) and the RMSE of 73° is high. Thus, while down-scaled values generally capture the frequency distribution, the wind direction is not accurately resolved at an hourly timescale.

Across all the down-scaled parameters, there was good agreement between observed and modeled data at hourly timescales. Most had low RMSE and high correlations indicating that sub-daily variation required for model input was sufficiently represented.

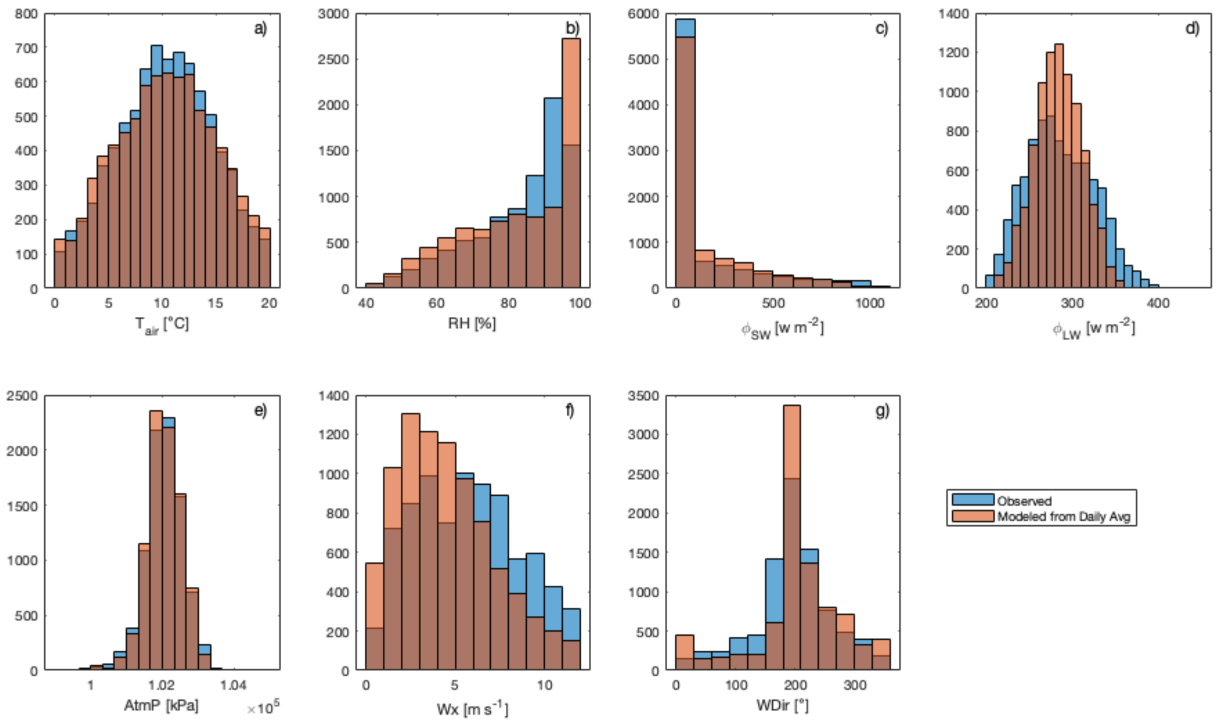

Figure C.1. *Frequency plots comparing observed and down-scaled hourly data for a) air temperature, b) relative humidity, c) incoming shortwave radiation, d) longwave radiation, e) atmospheric pressure, f) wind speed and g) wind direction.*

Table C.1. *Correlation coefficient and root mean squared error (RMSE) between observed and down-scaled hourly meteorological data.*

Meteorological Parameter	*Correlation coefficient*	*RMSE*
Air Temperature	0.98	1.25 °C
Relative Humidity	0.87	7.8 %
Incoming Shortwave	0.95	78.6 W m^{-2}
Incoming Longwave	0.84	21.7 W m^{-2}
Atm Pressure	0.91	211.5 kPa
E-W Wind Velocity	0.65	2.4 m s^{-1}
N-S Wind Velocity	0.83	2.7 m s^{-1}
Wind Mag	0.83	2.98 m s^{-1}
Wind Direction	0.53	68 °

C.2 Evaluating Uncertainty in Climate Projections

The CR2 RegCM4 regional climate model (RCM), gridded at a 10 km resolution and forced by the MPI-M-MPI-ESM-MR global climate model (GCM) at its lateral boundaries, was selected as the optimal model to forecast the regional climate of south-central Chile based. Bozkurt (2019) demonstrated that simulations at 10 km spatial resolution improved the resolution of climate gradients imposed by complex topography in the costal-valley Andes transition zone in Chile. Decadal trends from this RCP 8.5 simulation were compared with trends from 5 other 50 km resolution simulations (**Table C.2**) in order to quantify the uncertainty in forecasted projections. Except for relative humidity, the 10 km CR2 RegCM4 RCM trend lines fell within the average range across all five simulations

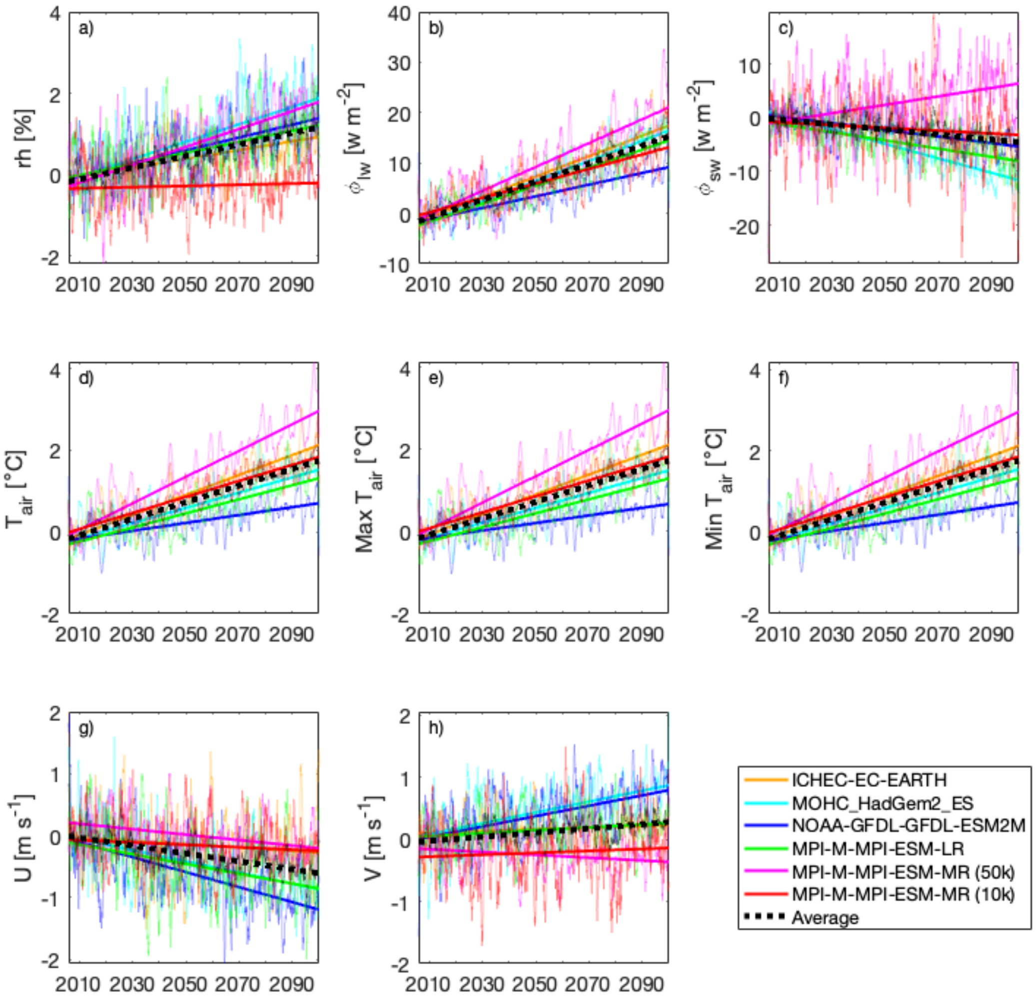

Figure C.2. *Projected trends in monthly meteorological conditions for Lago Llanquihue under RCP 8.5 emissions scenario relative to 2006 to 2016 baseline. Six combinations of GCMs, RCMs and domains are shown in various color. Parameters shown include a) relative humidity, b) incoming longwave radiation, c) incoming shortwave radiation, d) average air temperature, e) maximum air temperature, f) minimum air temperature, g) zonal wind component, f) meridional wind component. Average of all simulation results is indicated by black dotted line.*

Table C.2. *Comparison of average decadal trends in meteorological parameters for Lago Llanquihue across multiple GCM and RCM combinations. Mean (μ), standard deviation (σ) and coefficient of variation (cv) are show in three columns on right.*

Domain	**SAM44 (50 km)**					**CR2-RegCM4-10K**	**Statistics**		
RCM	**SMHI-RCA4**				**CR2-RegCM4-6**				
GCM	**ICHEC-EC-EARTH**	**MOHC-HadGem 2-ES**	**NOAA-GFDL - ESM2M**	**MPI-M-MPI-ESM-LR**	**MPI-M-MPI-ESM-MR**	**MPI-M-MPI-ESM-MR**	**μ**	**σ**	**cv**
Rh [%]	+0.11	+0.21	+0.16	+0.14	+0.22	+0.01	+0.14	0.08	0.54
LWin [W m^{-2}]	+2.02	+1.99	+1.15	+1.78	+2.35	+1.44	+1.79	0.43	0.24
SWin [W m^{-2}]	-0.62	-1.37	-0.64	-0.79	+0.80	-0.26	-0.48	0.72	-1.51
T_{air} [°C]	+0.24	+0.19	+0.09	+0.17	+0.32	+0.20	+0.20	0.08	0.37
Max T_{air} [°C]	+0.24	+0.18	+0.09	+0.17	+0.32	+0.19	+0.20	0.08	0.39
Min T_{air} [°C]	+0.24	+0.19	+0.10	+0.17	+0.32	+0.20	+0.20	0.07	0.36
U mag [m s^{-1}]	-0.03	-0.09	-0.12	-0.08	-0.04	-0.02	-0.06	0.04	-0.63
V mag [m s^{-1}]	+0.01	+0.09	+0.08	+0.02	-0.02	+0.02	+0.03	0.04	1.30

C.3 Observed Temperature and DO Data from Lago Llanquihue (2021 – 2022)

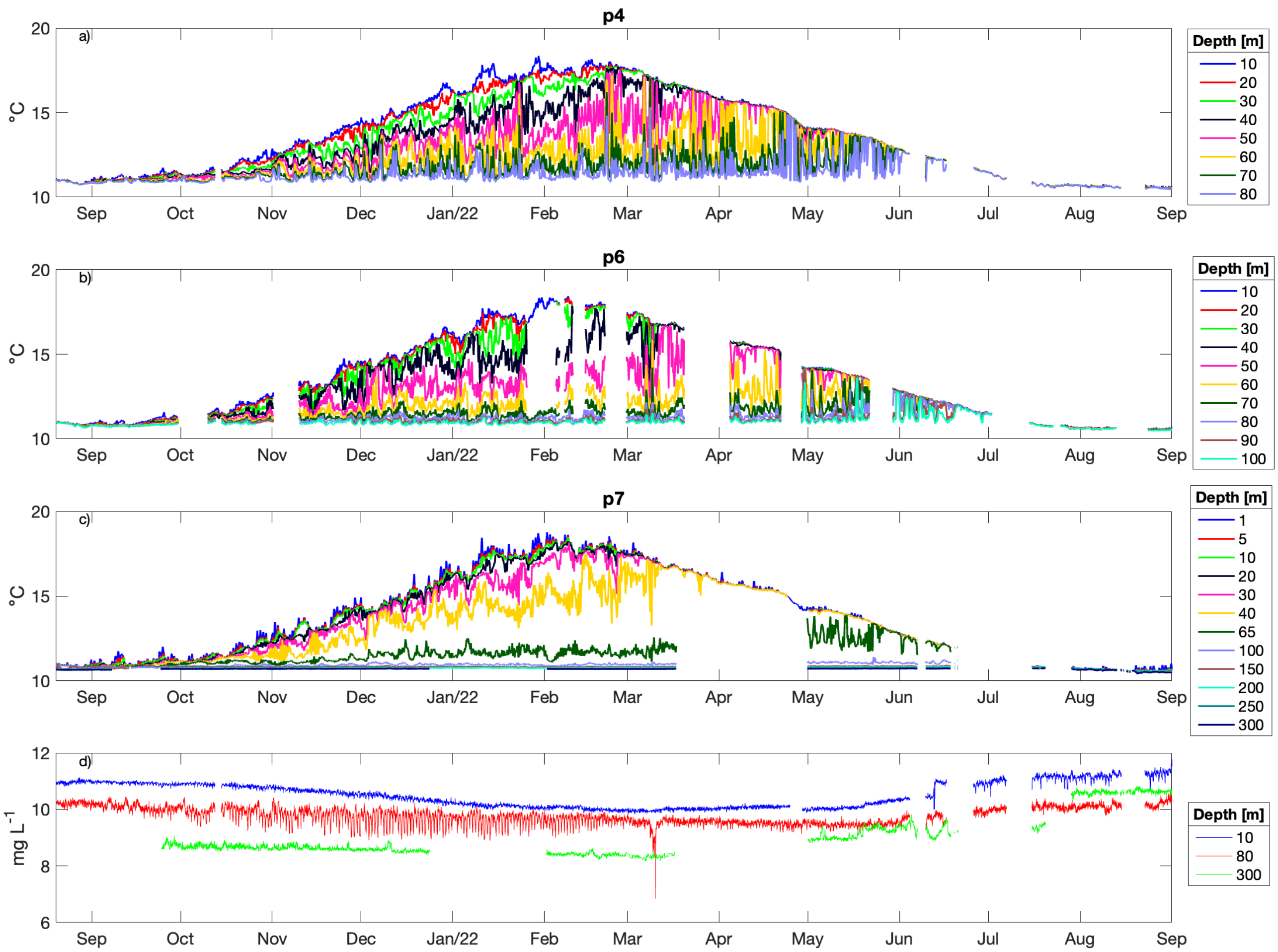

Figure C.3. *Observed temperature data from moored instrument arrays at a) p4, b) p6, and c) p7 buoys and d) observed DO fluctuations at three discrete depths. DO measurements from both depths at the p6 buoy and at 200 m from p7 buoy are not shown due to erroneous measurements and data gaps. White areas indicate periods when data was not properly transmitted.*

C.4 Characterization of Mixing and Water Column Stability

Definitions of Brunt-Väisälä buoyancy frequency, Schmidt Stability, thermocline depth, and top and bottom of the metalimnion follow the conventions outlined in Read et al. (2011). Water column stability can be evaluated as the square of the Brunt-Väisälä buoyancy frequency as defined in Imberger and Patterson 1989 as:

$$N^2 = -\frac{\frac{g}{\rho}\partial\rho}{\partial z}$$

where N^2 (s^{-2}) is the square of the buoyancy frequency, g (m s^{-2}) is gravitational acceleration, ϱ (kg m^{-3}) is the water density at depth z (m). Density was calculated as function of conductivity, temperature and depth based on methods described in Chen and Millero 1986.

The work required to mix the entire water column from density stratified condition to a uniform density can be estimated using the Schmidt Stability Index (S_T) as defined by Idso 1973 as:

$$S_T = g/A_0 \int_0^{z_{max}} A_z(z - z_{\bar{\rho}})(\rho_z - \bar{\rho})\, d$$

where S_T (J m^{-2}) is the Schmidt stability index, A_o (m^2) is the surface area of the lake, z_{max} (m) is the maximum depth, A_z (m^2) is the area at depth z, $z_{\bar{\rho}}$ (m) is the depth of the volumetric mean density, ρ_z (kg m^{-3}) is the density at depth z and $\bar{\rho}$ (kg m^{-3}) is the volumetric mean density which can be calculated as:

$$\overline{\rho} = \frac{1}{\int_0^{z_{\max}} A_z dz} \int_0^{z_{\max}} \rho_z A_z dz.$$

The depth of the volumetric mean density can be calculated as:

$$z_{\overline{\rho}} = \frac{1}{\int_0^{z_{\max}} \rho_z A_z dz} \int_0^{z_{\max}} z \rho_z A_z dz.$$

The thermocline depth is determined based on the depth of the maximum density gradient. In a discretized vertical domain the density gradient from layers i=1 *to I = k-1* is defined as:

$$\frac{\partial \rho}{\partial z_{i\Delta}} = \frac{\rho_{i+1} - \rho_i}{z_{i+1} - z_i} \; where \; z_{i\Delta} \; (z_{i+1} + z_i)/2$$

The top of the metalimnion (*metaT*) is defined as the base of mixed layer via a user defined minimum density gradient threshold ($\delta_{\min}$) which was set as 0.01 kg m^{-3} per m for the simulations.

$$z_e = z_{i\Delta} = \frac{\left(\delta_{min} - \frac{\partial \rho}{\partial z_{i\Delta}}\right)(z_{i\Delta} - z_{i\Delta+1})}{\frac{\partial \rho}{z_{i\Delta}} - \frac{\partial \rho}{z_{i\Delta+1}}}$$

Likewise the base of the metalimnion (*metaB*), the theoretical division between the metalimnion and the hypolimnion, can be found where $\frac{\partial \rho}{z_{i\Delta}} \leq \delta_{\min}$.

References

Birt, D., Wain, D., Slavin, E., Zang, J., Luckwell, R., & Bryant, L. D. (2021). Stratification in a reservoir mixed by bubble plumes under future climate scenarios. *Water*, *13*(18).

Bozkurt, D., Rojas, M., Boisier, J. P., Rondanelli, R., Garreaud, R., & Gallardo, L. (2019a). Dynamical downscaling over the complex terrain of southwest South America: Present climate conditions and added value analysis. *Clim. Dyn.*, *53*(11), 6745–6767.

Bozkurt, D., Rojas, M., Boisier, J. P., Rondanelli, R., Garreaud, R., & Gallardo, L. (2019b). Dynamical downscaling over the complex terrain of southwest South America: present climate conditions and added value analysis. *Climate Dynamics*, *53*(11), 6745–6767.

Chen, C. T. A., & Millero, F. (1986). Precise thermodynamic properties for natural waters covering only the limnological range. *Limnol. Oceanogr.*, *31*(3), 657–661.

Ephrath, J. E., Goudriaanb, " J, & Marani', A. (1996). *Modelling Diurnal Patterns of Air Temperature, Radiation Wind Speed and Relative Humidity by Equations from Daily Characteristics* (Vol. 51, Issue 4).

Idso, S. B. (1973). On the concept of lake stability. *Limnol. Oceanogr.*, *18*, 681–683.

Imberger, J., & Patterson J. (1989). Physical Limnology. In *Advances in Applied Mechanics* (Vol. 27, pp. 303–475). Elsevier.

Read, J. S., Hamilton, D. P., Jones, I. D., Muraoka, K., Winslow, L. A., Kroiss, R., Wu, C. H., & Gaiser, E. (2011). Derivation of lake mixing and stratification indices from high-resolution lake buoy data. *Environ. Model. Soft.*, *26*(11), 1325–1336.

Riahi, K., Rao, S., Krey, V., Cho, C., Chirkov, V., Fischer, G., Kindermann, G., Nakicenovic, N., & Rafaj, P. (2011). RCP 8.5-A scenario of comparatively high greenhouse gas emissions. *Clim. Change*, *109*(1), 33–57.

Spitters, C., Toussaint, H., & Goudriaan, J. (1986). Separating the diffuse and direct component of global radiation and its implications for modeling canopy photosynthesis Part I. Components of incoming radiation. *Agricultural and Forest Meteorology*, *38*(1–3), 217–229.